Université du Québec

INRS — Institut national de la recherche scientifique

Universite du Quebec
Institut National de la Recherche Scientifique
Centre Energie, Materiaux et Telecommunications

Surface and atomic modification of stable alkali metal anode: towards high-utilization alkali metal batteries

Par

Tingzhou Yang

These presentee pour l'obtention du grade

de Philosophiae Doctor (Ph.D.)

en sciences de l'énergie et des matériaux

Jury d'évaluation

Président du jury et examinateur interne	Prof. Shuhui Sun INRS-EMT Université du Québec
Examinateur externe	Prof. Jérôme Claverie Département de chimie Université de Sherbrooke
Examinateur externe	Prof. Mickaël Dollé Département de chimie Université de Montréal
Directeur de recherche	Prof. Federico Rosei INRS-EMT Université du Québec

REMERCIEMENTS

It is my great honor to accomplish my Ph.D. program at the Centre Énergie Matériaux Télécommunications in Institut National de la Recherche Scientifique, University of Québec, Canada. Many people have offered me valuable help in this thesis, and I would like to express my gratitude to those people who had, in different ways, contributed to its construction.

First and foremost, I would like to express my heartfelt gratitude to my supervisor, Prof. Federico Rosei, for offering me the opportunity to undertake my Ph.D. studies in his research group. An old Chinese proverb says, "A teacher for a day is a father for a lifetime (一日为师，终身为父)". It is one of the most valuable experiences in my life being able to study under his supervision. I learn a lot from his dedication, leadership, and scientific insight. Personally, Prof. Rosei has always been a strong supporter when I need help. Professionally, he not only provided me systematic guidance on my research projects, but also created a warm and free research environment allowing me to explore my interest in the forefront and fascinating scientific field. Without whom, I would not be able to accomplish my goal.

I also express my gratitude to Prof. Chenglin Yan and Dr. Tao Qian, for their patience, motivation, enthusiasm, and immense knowledge. They give me many useful suggestions in terms of research direction and detail, where I need to explore deeper. They have made vital contributions to most of my work and given me invaluable help and comments on my thesis writing and research.

I would like also to thanks all our group members and collaborators in NanoFemtoLab and Soochow University, for their help throughout the duration of my Ph.D. I also acknowledge Dr. Benetti Daniele for his assistance, comments, and discussions and Prof. Jun Zhong, from Soochow University, for the measurement in the field of synchrotron radiation, and Prof. Haiguang Zhao for his help during my application for the scholarship. I am grateful to all my friends who have made the last four years so enjoyable: Jie Liu, Mengfan Wang, Jinqiu Zhou, Xiaowei Shen, Na Xu, Li Shi, Faying Li, Xin, Liu, Zhengkang Wang, Lei Jin, Maria Elena Lombardo, Gurpreet Singh Selopal, and Wanderlei Mendes Ferreira. They always are with me and support me to get over the difficulties I confronted along the journey.

Last but not least, I would like to give special thanks to my family: my parents Guanghe Yang and Qingfeng Ji, for their continuing love and heartily support during my entire Ph.D. study period. I

RÉSUMÉ

En raison de leurs densités d'énergie gravimétriques et volumétriques plus élevées, les batteries au lithium-ion (Li-ion) sont la technologie dominante dans le domaine du stockage d'énergie. Cependant, les batteries Li-ion commerciales à base d'anode de graphite, dont la capacité théorique limitée est inférieure à 300 Wh kg^{-1}, ne peuvent pas répondre à la demande croissante de véhicules électriques modernes et de réseaux intelligents. Le fabricant mondial de batteries suscite un immense intérêt pour l'augmentation des densités d'énergie à plus de 500 W h kg^{-1}. De plus, le lithium n'est pas un élément naturellement abondant. Le prix du carbonate de lithium est passé de 5,180 dollars américains par tonne métrique en 2010 à 13,000 dollars américains par tonne métrique en 2019. Par conséquent, les ressources limitées en lithium et la forte demande de hautes densités d'énergie élevées dans les véhicules électriques ont motivé le développement des batteries rechargeables de nouvelle génération afin de remplacer les batteries Li-ion actuelles.

Parmi toutes les possibilités, l'anode au lithium métal (Li métal) est fortement considérée en guise de l'alternative de l'anode à base de graphite, en raison de son faible potentiel redox (-3.04V vs SHE) et de sa capacité spécifique théorique élevée (3860 mAh g^{-1}). Malheureusement, la formation incontrôlée de dendrites, le grand changement de volume et l'interface instable pendant le cycle électrochimique entravent les applications des anodes métalliques Li, ce qui réduit la durée de vie du cyclage et entraîne des risques pour la sécurité, notamment des courts-circuits internes et un emballement thermique. De nombreux efforts ont été consacrés à la résolution des défis mentionnés ci-dessus de l'anode en métal Li, tels que le collecteur de courant poreux tridimensionnel (3D), les additifs d'électrolyte, la couche d'interphase d'électrolyte solide artificielle (SEI) et le contrôle du dépôt spatial.

Dans mon premier chapitre, comme alternative à la feuille de Li plane, une mousse de Li métallique poreuse en 3D, autoportante accompagnée d'une couche de SEI inhérente, a été construite par gravure chimique. La matrice poreuse servant de squelette rigide conduit à une distribution de charge plus uniforme et oriente ainsi le dépôt de Li. La couche SEI artificielle peut supprimer la formation de dendrites de Li et les réactions secondaires. Le deuxième chapitre a dans l'objectif de concevoir et de synthétiser un collecteur de courant basé sur des groupes ou des sites d'atomes uniques pour anode en métal alcalin. La dispersion uniforme des atomes simples et des agrégats d'Au sur un tissu de charbon actif guide uniformément le dépôt de Li / Na, limitant ainsi

la croissance des dendrites. En raison d'une distribution optimisée du champ électronique, les atomes et les clusters uniques d'Au favorisent non seulement le dépôt de Li / Na avec un surtension de nucléation nulle similaire aux nanoparticules Au, mais ils ont également une grande affinité et des interactions avec les ions Li / Na dans l'électrolyte, offrant des positions d'adsorption stables pour Atomes de Li / Na. Dans le troisième chapitre, le collecteur de courant basé sur un seul atome de Zn a été synthétisé par pyrolyse et absorption entre les particules de Zn et les ligands imidazolate. Les sites d'atomes uniques de Zn, qui servent d '«aimant» puissant pour les ions Na, peuvent guider la nucléation uniforme du Na métallique et exempts de court-circuit induit par la dendrite.

Mots-clés : Stockage d'énergie, batterie lithium-ion, batterie sodium-ion, batterie lithium-métal, batterie sodium métal, anodes en métal alcalin, structure poreuse 3D, atomes uniques, utilisation élevée.

ABSTRACT

Due to its higher gravimetric and volumetric energy densities, lithium-ion (Li-ion) batteries are the dominant technology in the field of energy storage. However, the commercial Li-ion batteries based on graphite anode with a limited theoretical capacity of less than 300 Wh kg^{-1} cannot fulfill the increasing demand for modern electric vehicles and smart grids. There is immense interest around the global battery manufacturer to increase the energy densities to more than 500 W h kg^{-1}. Furthermore, lithium is not a naturally abundant element. The price of lithium carbonate is increased from 5180 U.S. dollars per metric ton in 2010 to 13000 U.S. dollars per metric ton in 2019. Hence, the limited lithium resources and strong demand for high energy densities in electric vehicles have motivated the development of next-generation rechargeable batteries to replace current Li-ion batteries.

Among all the possibilities, lithium metal (Li metal) anode is strongly considered as the alternatives to the graphite-based anode, owing to its low redox potential (-3.04 V vs SHE) and high theoretical specific capacity (3860 mAh g^{-1}). Unfortunately, the uncontrolled formation of dendrites, the large volume change, and the unstable interface during electrochemical cycling hinder the applications of Li metal anodes, which reduce the cycling life and lead to safety hazards including internal short circuits and thermal runaway. Many efforts have been devoted to addressing the above challenges of Li metal anode, such as three dimensional (3D) porous current collector, electrolyte additives, artificial solid electrolyte interphase (SEI) layer, and spatial deposition control

In my first chapter, as an alternative to planar Li foil, freestanding 3D porous Li metal foam accompanied by an inherent SEI layer has been constructed via chemical etching. Porous matrix served as a rigid backbone leads to more uniform charge distribution and thus orients the Li deposition. The artificial SEI layer can suppress the formation of Li dendrites and side reactions. The second chapter intends to design and synthesize cluster-based or single atom site-based current collectors for alkali metal anode. The uniform dispersion of Au single atoms and clusters on activated carbon cloth was reported to guide Li/Na deposition uniformly, thereby constraining the growth of dendrites. Due to an optimized electron field distribution, Au single atoms and clusters not only favor Li/Na deposition with zero nucleation overpotential similar to Au nanoparticles, but also have great affinity and interactions with Li/Na ions in the electrolyte, providing stable

adsorption positions for Li/Na atoms. In the third chapter, the single Zn atom sites based current collector was synthesized by pyrolysis and absorption between Zn particles and imidazolate ligands. Single Zn atom sites, which serve as a strong "magnet" for Na ions, can guide the metallic Na uniform nucleation and free from dendrite-induced short circuit.

Keywords: Energy storage, Lithium-ion battery, Sodium-ion battery, Lithium metal battery, Sodium metal battery, Alkali metal anodes, 3D porous structure, Single atoms, High utilization.

SOMMAIRE RÉCAPITULATIF

Modification surfacique et atomique d'anode alcaline stable :

vers des batteries alcalines à forte utilisation

La forte utilisation de l'énergie traditionnelle des fossiles accélère le développement du réchauffement climatique et de nombreux problèmes environnementaux tels que les précipitations acides, la destruction des forêts, l'appauvrissement de la couche d'ozone et la pollution de l'air. Avec le développement des énergies renouvelables, les sources d'énergie idéales dérivées de l'énergie solaire, de l'hydroélectricité, de l'énergie marémotrice ainsi que de la chaleur géothermique fournissent un flux d'énergie continu. Afin de répondre aux besoins des différentes conceptions et alimentations en énergie de conserver une bonne quantité d'énergie, il est désormais implacable de trouver de nouveaux dispositifs de stockage d'énergie commercialisables, peu coûteux et naturellement abondants, tels que les supercondensateurs et les batteries lithium-ion. Les demandes énergétiques en augmentation constante exigent un développement des techniques de batteries au lithium-ion, qui offrent une stabilité de cyclage à long terme, une densité d'énergie élevée et une capacité de débit élevé. Cependant, la batterie Li-ion actuellement commercialisée composée d'un hôte Li-ion et d'une électrode en graphite avec une capacité théorique limitée ne peut répondre à la demande croissante de véhicules électriques modernes et de réseaux intelligents. Actuellement, les batteries Li-ion commerciales à base d'anode en graphite sont limitées aux batteries dont la densité d'énergie est inférieure à 300 Wh kg^{-1}. Le fabricant mondial de batteries suscite un immense intérêt pour augmenter les densités d'énergie à plus de 500 W h kg^{-1}. Parmi toutes les possibilités, le Li métallique est fortement considéré comme l'alternative de l'anode en graphite en raison de son potentiel redox extrêmement faible (-3.04 V vs SHE) et de sa capacité spécifique théorique dix fois plus élevée (3860 mAh g^{-1}) que celle du graphite. Les applications des batteries à base de métal Li sont limitées par plusieurs défis sérieux qui ont intrigué les chercheurs pendant un demi-siècle. En tant qu'électrode «sans hôte», le processus de placage / décapage de Li facilitera l'énorme expansion de volume qui peut facilement fissurer le SEI, ce qui se traduit par un flux d'ions local accru et un dépôt de Li dendritique irrégulier. Les dendrites de Li connectent non seulement électroniquement l'anode et la cathode, ce qui entraîne des risques de

sécurité tels qu'un court-circuit interne, mais facilite également les réactions secondaires après exposition à l'électrolyte. Les produits des réactions secondaires isoleront l'anode métallique Li de la matrice conductrice, produisant du «Li mort» avec une décroissance rapide de la capacité, et résultant en une grande polarisation, une durée de vie médiocre et une faible efficacité coulombique.
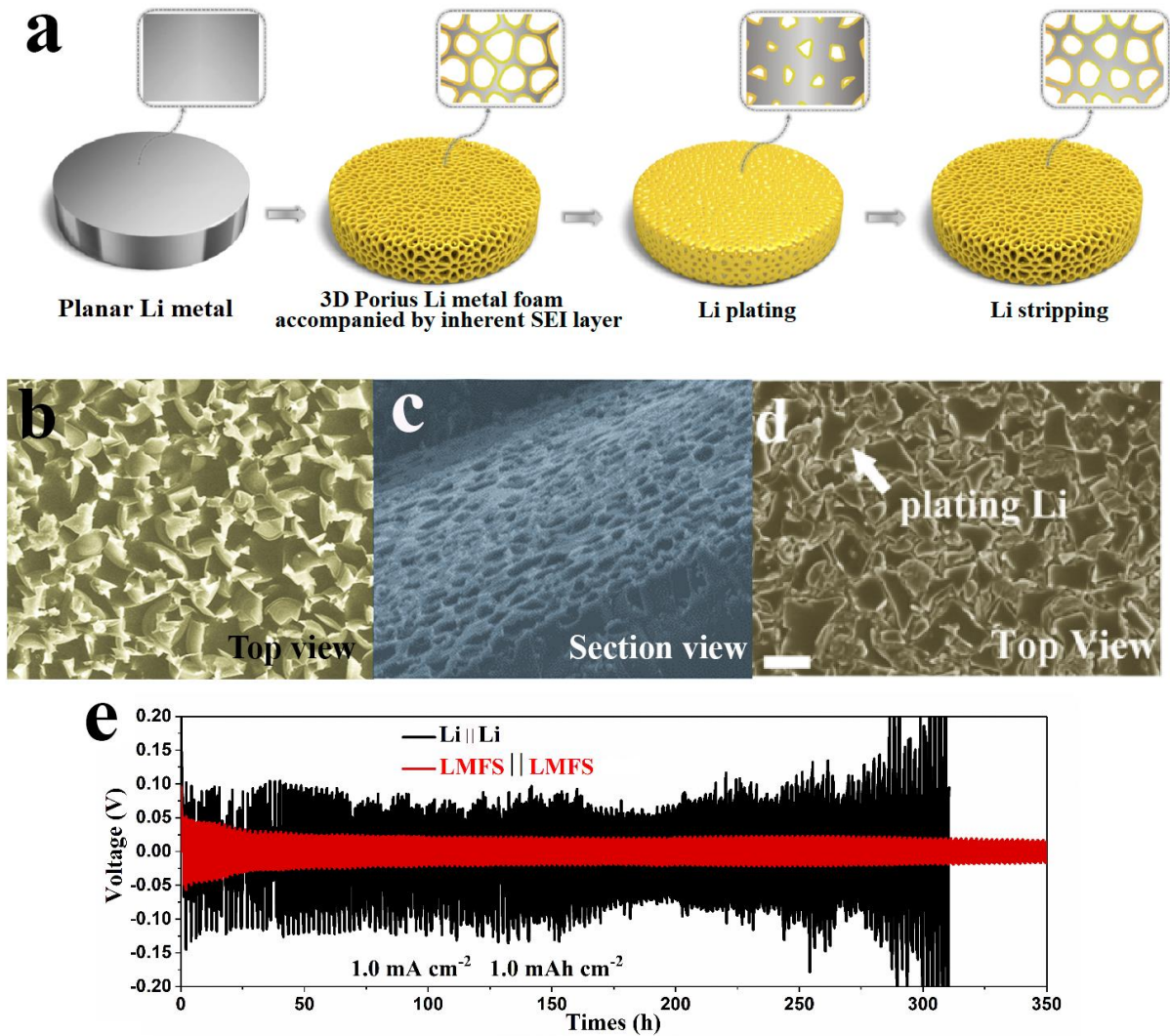

Figure R1. (a) Configuration schématique de la structure et des fonctions de l'anode LMFS avant et après les cycles. (b) La vue de dessus et (c) vue en coupe des images SEM de LMFS. (d) Images SEM de LMFS après placage Li, qui est rempli de placage Li. (e) Profils tension-temps des cellules symétriques utilisant une anode métallique plane en Li et une anode LMFS à une densité de courant de 1.0 mA cm^{-2} avec une capacité de placage/dénudage de 1.0 mAh cm^{-1}.

De nombreux efforts ont été déployés à relever les défis mentionnés ci-dessus concernant l'anode métallique Li. Un certain nombre de travaux se concentrent sur un collecteur de courant poreux tridimensionnel (3D) pour inhiber la croissance des dendrites de Li. La grande surface spécifique du squelette 3D permet une distribution uniforme des charges positives, et la sténose poreuse peut accueillir Li pendant le processus de placage, atténuer l'énorme changement de volume et supprimer la croissance des dendrites. A titre d'exemple, un certain nombre d'œuvres mettent en œuvre un collecteur de courant en cuivre poreux (Cu) 3D comme hôte de Li, où une grande zone hautement électroactive peut favoriser la nucléation et le dépôt uniformes du métal Li. Néanmoins, le prix et le poids du collecteur de courant 3D Cu sont plus élevés que la feuille de Cu, ce qui entraîne une faible densité d'énergie et un coût d'emballage élevé. Récemment, le développement des composants électrolytiques et des additifs a été perçu comme une voie possible pour homogénéiser le flux d'ions Li pendant le processus de placage et stabiliser les couches SEI. A contrario, les couches SEI obtenues ne peuvent toujours pas s'adapter au changement morphologique pendant le processus répété de placage / décapage. Par conséquent, certaines couches SEI artificielles comme les barrières mécaniques et les électrolytes à l'état solide ont été explorées dans l'objectif d'inhiber la formation de dendrite de Li.

Dans mon premier chapitre, comme alternative à la feuille de Li plane, une mousse de lithium métal poreuse 3D autoportante accompagnée d'une couche SEI inhérente (LMFS) a été construite par gravure chimique d'une feuille de Li à l'aide d'acide 4-dodécylbenzène sulfonique (DBSA) pour une batterie Li métallique haute performance.(**Figure R1**) La matrice poreuse servant de squelette rigide conduit à une distribution de charge plus uniforme et oriente ainsi le dépôt de Li. Les couches LDBS en tant que couche SEI conforme peuvent supprimer la formation de dendrites de Li et les réactions secondaires. De plus, les anodes LMFS présentent d'excellentes performances électrochimiques lorsqu'elles sont couplées par une cathode $LiNiCoMnO_2$ avec les différentes charges actives jusqu'à 20.4 mg cm^{-2}. En outre, nous avons activé des anodes de Li métal à haute performance, profondément cyclables à des capacités de surface élevées de 15,0 ou 20,0 mAh cm-2, et un processus de placage / décapage stable à long terme de cellules symétriques avec une hystérésis à basse tension sur 350 heures est révélé, ce qui en outre démontre que notre stratégie peut réduire considérablement la décomposition de l'électrolyte, empêcher les dendrites de se propager et supprimer le processus de gazage, démontrant la fiabilité et la sécurité de la batterie. Ces résultats fournissent des informations supplémentaires indispensables sur les structures

poreuses / micro et la protection SEI compatible pour l'anode métallique Li, en particulier après une innovation et une amélioration supplémentaires.
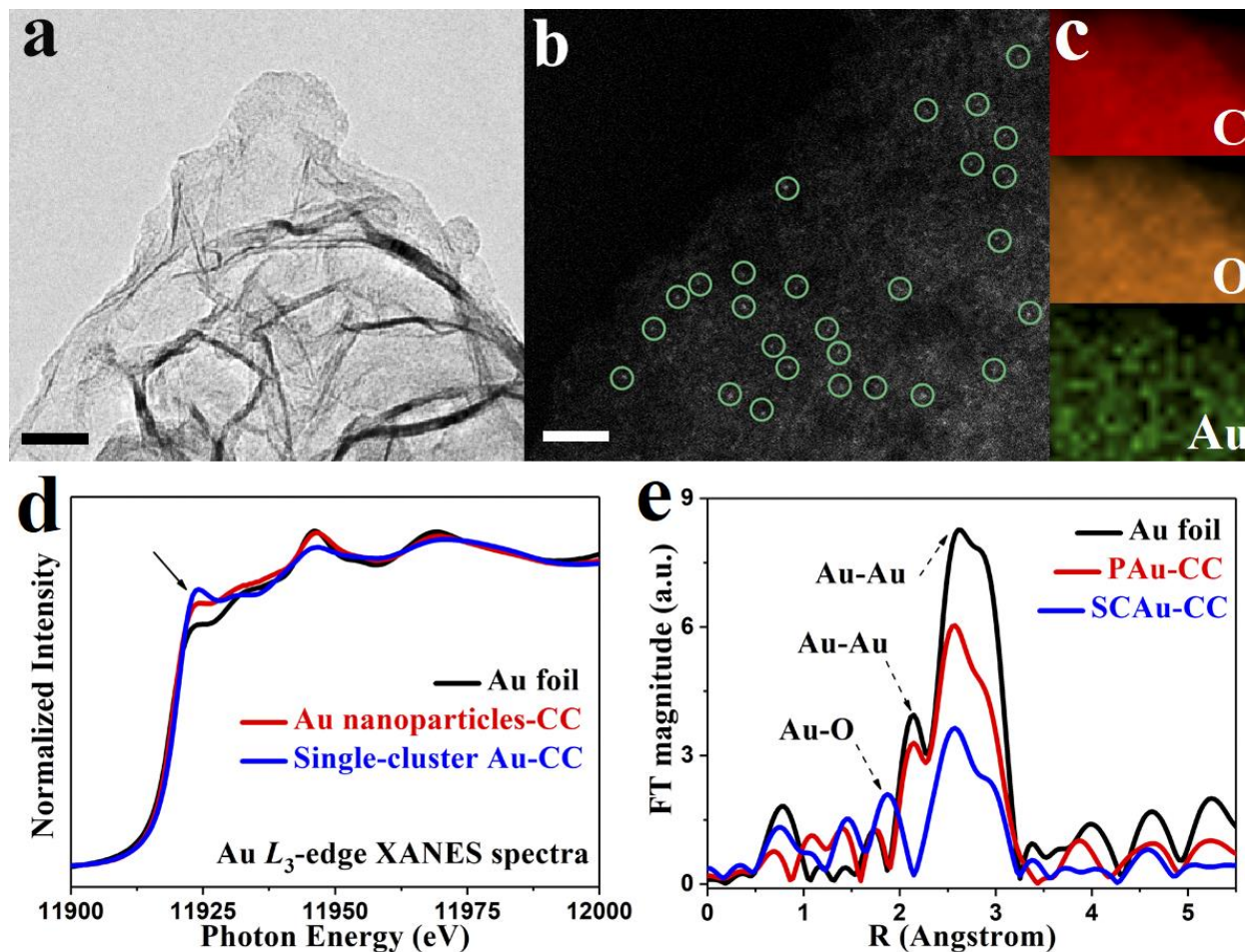

Figure R2. (a) Images TEM de SCAu-CC. Barre d'échelle, 50 nm. (b) L'image HAADF-STEM de SCAu-CC et l'Au à un seul cluster sont mis en évidence dans des cercles verts. Barre d'échelle, 2 nm. (c) L'examen de la cartographie EELS correspondante de C, O et Au révèle la distribution homogène de l'Au mono-amas sur le squelette carboné. (d) Spectres XANES de bord Au L3 des échantillons. (e) Spectres EXAFS pondérés k3 transformés de Fourier.

Récemment, Cui et ses collègues ont travaillé sur les surpotentiels de divers matériaux (Au, Ag, Mg, Zn, Cu, Ni, Pt, Si, C, Al, etc.) sur la nucléation de Li et ont conclu que la formation d'une solution solide avec du lithium aiderait la nucléation du lithium en raison de l'énergie interfaciale Li / hôte réduite, où aucun surpotentiel n'était nécessaire pour nucléer le métal Li sur Au, Ag, Zn

ou Mg. Les particules Au et Ag fournissent une nouvelle façon de croissance ensemencée hétérogène pour contrôler le placage de Li sur les substrats désignés, ce qui entraîne une faible barrière de nucléation pour le dépôt d'ions Li. Les hôtes métalliques nobles pour le métal Li sont censés remédier à l'imperfection de la croissance des dendrites et à l'instabilité de l'interface de l'anode, présentant le grand potentiel de développement de l'anode en métal Na. Toutefois, étant l'un des métaux nobles les plus courants, l'Au et l'Ag sont si chers qu'ils sont inabordables en tant que substrats de batteries métalliques. La réduction de la taille des métaux noblesà des atomes individuels ou à des groupes d'atomes constitue un moyen efficace de réduire le dosage Au/Ag et de maximiser l'efficacité d'utilisation atomique. Les anodes métalliques modifiées à un seul atome ou à amas sont analogues à une anode en feuille de métal noble, or, contrairement à de nombreuses anodes métalliques, la réaction au niveau du site actif peut être comprise avec des détails atomistiques sur une anode métallique modifiée à un seul atome. En conséquence, la conception d'une matrice de dépôt Na/Li avec des atomes uniques convient mieux à l'anode en métal alcalin. Le fait de guider le dépôt de Na/Li au niveau atomique et d'inhiber la croissance incontrôlée des dendrites Na/Li aux stades de nucléation peut ouvrir une nouvelle dimension pour la conception d'anodes de métal alcalin sûres et efficaces.

Le deuxième chapitre a pour but de concevoir et de synthétiser un collecteur de courant basé sur des grappes ou des sites d'atomes uniques pour l'anode métallique Li. Dans ce chapitre, il a été rapporté que la dispersion uniforme d'atomes uniques et d'amas Au sur un tissu de charbon actif (SCAu-CC) guidait le dépôt de Li de manière uniforme, limitant ainsi la croissance des dendrites.(**Figure R2**) En vertu d'une distribution optimisée du champ électronique, les atomes simples et les clusters d'Au favorisent non seulement le dépôt de Li avec une surtension de nucléation nulle similaire à celle des nanoparticules d'Au, mais ils ont également une grande affinité et des interactions avec les ions Li dans l'électrolyte, fournissant des positions d'adsorption stables pour les atomes de Li. Des anodes métalliques Li stables et réversibles ont été obtenues grâce à un seul cluster d'Au, présentant une excellente stabilité de cyclage pendant plus de 900 cycles avec une efficacité coulombique de presque 100% et un comportement profondément cyclable à une capacité surfacique élevée allant jusqu'à 20 mA h cm^{-2}. En tirant parti du dépôt de Li guidé et d'une utilisation maximale du Li, nous avons constaté que les batteries au Li métal dotées de cathodes à forte charge offrent également des performances électrochimiques

exceptionnelles, ce qui est prometteur pour les futures technologies de batteries rechargeables Li métal.
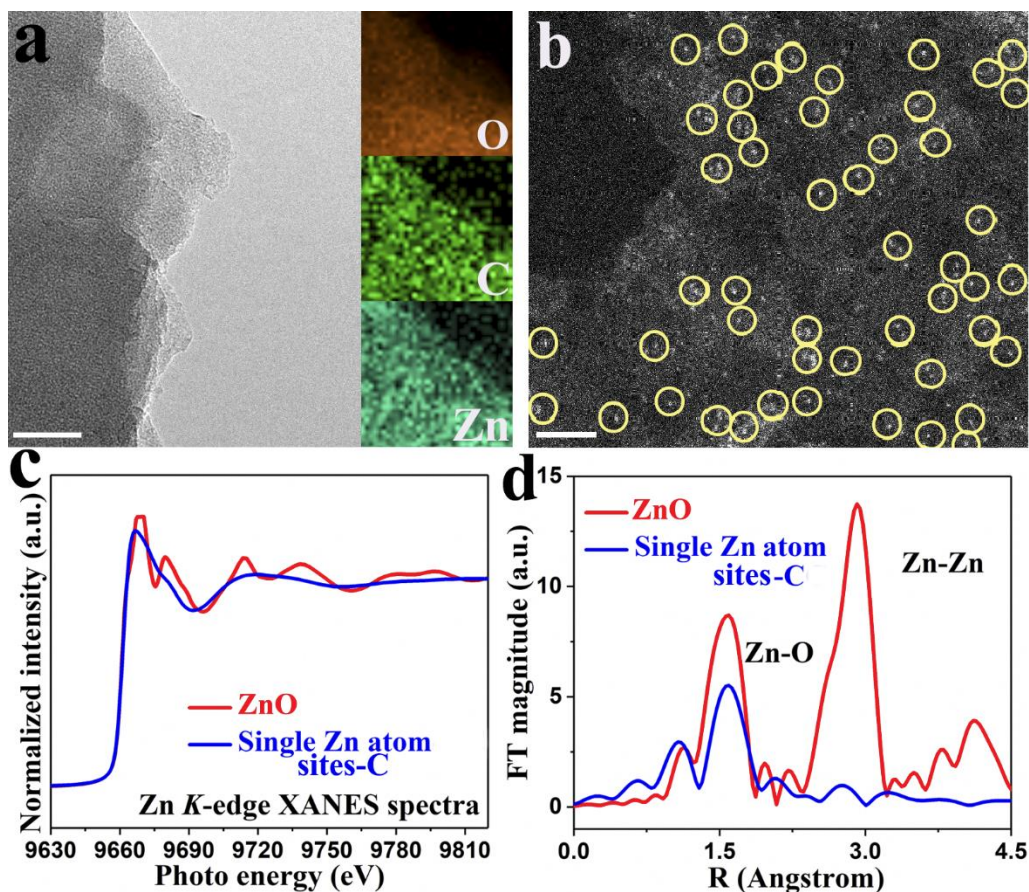

Figure R3. Caractérisation de la morphologie de sites uniques d'atomes de Zn. (a) Image TEM et résultats de mappage élémentaire correspondants pour Zn$_{SA}$-N-C. Barre d'échelle, 50 nm. (b) L'image HAADF-STEM de Zn$_{SA}$-N-C et les atomes de Zn simples sont mis en évidence dans des cercles jaunes. Barre d'échelle, 2 nm. (c) Spectres Zn K-edge XANES des échantillons. (d) Spectres EXAFS transformés par Fourier Zn K-edge.

Nous utilisons en outre SCAu-CC pour préparer l'anode en métal Na. Nous avons découvert que l'introduction d'Au mono-atome et de cluster sur le substrat peut homogénéiser le flux ionique pour guider le dépôt d'ions Na et supprimer la formation de dendrites Na pendant le processus de placage/décapage à long terme. Aucun surpotentiel de nucléation n'est nécessaire pour nucléer le métal Na sur SCAu-CC, menant à une solution efficace pour réguler ou encapsuler le dépôt d'ions

Na au niveau atomique. Une telle électrode SCAu-CC avec des dépôts limités de Na présente une hystérésis stable et basse tension sur 400 heures, et l'efficacité coulombique se maintient à 99,73% même après 300 cycles. De plus, la cellule pleine Na-SCAu-CC‖NVP avec un minimum de dépôts de Na peut être cyclée pendant plus de 1000 cycles avec une rétention de capacité élevée et une efficacité coulombique élevée. Le présent travail fournit un aperçu de la synthèse de la nouvelle anode métallique Na au niveau atomique et propose des idées sur la conception d'une anode métallique avancée via différents atomes individuels.

Quand à la production commercialisée, il est très souhaitable de développer des matériaux rentables pour le stockage d'énergie à grande échelle. En tant que l'un des métaux nobles les plus courants, les Au sont si chers qu'ils sont inabordables comme les substrats de batteries métalliques. Dans le troisième chapitre, le collecteur de courant fondé sur un seul atome de Zn a été synthétisé en deux étapes, dont la synthèse de Zn-ZIF et le traitement thermique. Les sites d'atomes uniques de Zn ont été obtenus par pyrolyse et absorption entre des particules de Zn et des ligands imidazolate. De surcroît, nous utilisons la microscopie électronique à transmission (TEM), la microscopie électronique à balayage (SEM) et la microscopie électronique à transmission électronique à balayage à champ noir à grand angle (HAADF-STEM) afin de discerner la différence entre les atomes uniques et les Zn-ZIF.(**Figure R3**) En confirmant la réussite de la synthèse de sites d'atomes uniques, la structure électronique locale et son interaction avec les substrats ont été étudiées plus en détails par des spectres normalisés d'absorption des rayons X près de la structure des bords (XANES) et des spectres de structure fine d'absorption des rayons X étendus (EXAFS) pour Zn K-bords avec la comparaison avec une feuille ZnO standard. Les sites d'atomes uniques de Zn qui servent d '«aimant» puissant pour les ions Na, peuvent guider la nucléation uniforme du Na métallique et exempts de court-circuit induit par la dendrite. Il s'avère que l'efficacité coulombique de l'électrode basée sur un site d'atome de Zn unique peut se maintenir à 99.8% pendant 350 cycles, et la polarisation de l'anode en métal Na est limitée à 56 mV avec une durée de vie ultra-longue pendant plus de 1000 h. De manière impressionnante, l'électrode avec un minimum de dépôts de Na exerce des fonctions similaires à celles d'une feuille de Na et indique une bonne stabilité de cyclage, qui présente en outre une utilisation élevée de presque 100% avec une source de Na limitée.(**Figure R4**) En ce qui concerne la durée de vie et l'utilisation de Na, notre stratégie dépasse de loin les anodes métalliques au Na, qui sont à la pointe de la technologie.
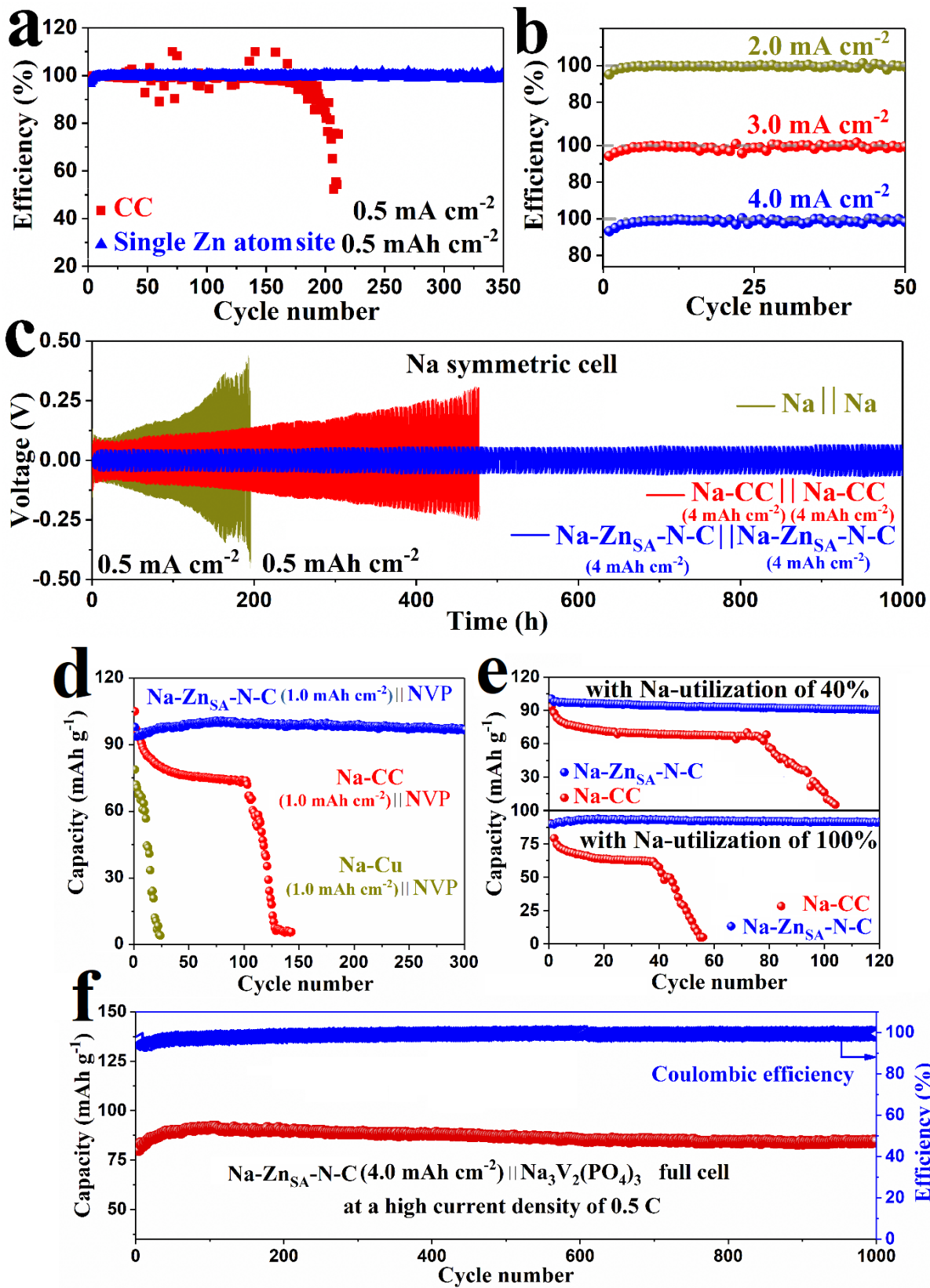
Figure R4. (a) Efficacité coulombique avec capacité surfacique de 0.5 mAh cm^{-2} à une densité de courant de 0.5 mA cm^{-2}. (b) Comparaison de l'efficacité coulombique du stripping / placage de Na à haute densité de courant de 2.0, 3.0 et 4.0 mA cm^{-2}. Pour évaluer la stabilité du cyclage et l'hystérésis de tension, 4 mAh cm^{-2} Na est d'abord pré-déposé sur le Zn$_{SA}$-N-C en demi-cellules. (c) Profils de tension de cellules symétriques avec deux électrodes identiques à une densité de courant de 0.5 mA cm^{-2}, présentant une excellente stabilité cyclique sur 1000 h. (d) Comparaison des performances de cycle de différentes électrodes (1.0 mAh cm^{-2}) à 0,2 C. (e) Performances de cyclage de l'anode Na-Zn$_{SA}$-N-C et de l'anode Na-CC avec une utilisation élevée de Na de 40% (en haut) et 100% (bas). (f) Longue stabilité de cyclage avec une efficacité coulombique élevée de presque 100% à 0.5 C.

TABLE DES MATIÈRES

LISTE DES FIGURES

LISTE DES TABLEAUX

LISTE DES ABRÉVIATIONS

Abbreviation	Meaning
3D	Three dimensional
AFM	Atomic force microscope
Ag	Sliver
Al	Aluminium
Au	Gold
CC	Carbon cloth
Cd	Cadmium
Co	Cobalt
CO_2	Carbon dioxide
Cu	Copper
DEC	Diethyl carbonate
DFT	Density functional theory
EC	Ethylene carbonate
EDS	Energy-dispersive X-ray spectroscopy
EIS	Electrochemical impedance spectroscopy
EXAFS	Extended X-Ray absorption fine structure
FEC	Fluoroethylene carbonate

GGA	Generalized gradient approximation
HAADF	High angle annular dark field
Hg	Mercury
LCO	$LiCoO_2$
LFP	$LiFePO_4$
Li	Lithium
LTO	$Li_4Ti_5O_{12}$
mAh	Megawatt hour
Mg	Magnesium
Mn	Manganese
MOF	Metal-organic frameworks
N₂	Nitrogen gas
Na	Sodium
NCA	$LiNiCoAlO_2$
NCM	$LiNiCoMnO_2$
Ni	Nickel
NVP	$Na_3V_2(PO_4)_3$
O₂	Oxygen gas
PAu	Gold particles

Pb	Lead
PC	Propylene carbonate
PSI	Pounds per square inch
Pt	Platinum
SA	Single atom
SCAu	Single-atom and cluster gold
SCE	Saturated calomel electrode
SEI	Solid electrolyte interphase
SEM	Scanning electron microscope
SHE	Standard hydrogen electrode
STEM	Scanning transmission electron microscopy
TEM	Transmission Electron Microscopy
XANES	X-ray absorption near edge structure
XAS	X-ray absorption spectroscopy
XPS	X-ray photoelectron spectrometry
XRD	X-ray diffraction
ZIF	Zeolitic imidazolate frameworks
Zn	Zinc

1 INTRODUCTION

1.1 Renewable energy

The global industrial sector energy use will increase by more than 30% and transportation energy consumption will increase by nearly 40% between 2018 and 2050. By then, global industrial energy consumption will reach about 315 quadrillion British thermal units (Btu).[1-8] Currently, fossil fuels, including oil shales, coal, natural gas, petroleum, and heavy oils, provide more than 85% of the world's energy requirement, which continues to remain the world's leading source of energy. Fossil fuels and the environment have an undeniable link, where the biggest environmental challenges associated with the burning of fossil fuels result in many environmental problems, such as thermal pollution and the greenhouse effect. Global warming leads to climate change, which will make widespread flooding and extreme weather more common.[4-8] The substantial increase of carbon dioxide (CO_2) in the atmosphere caused by the combustion of fossil fuels is a major contributing factor to human-induced global warming. Furthermore, fossil fuels are a nonrenewable resource, which is formed by decomposing plants and animals over millions of years.

Now, to make sure there are enough energy and a suitable environment to sustain human life and activities in the future, engineers and researchers around the world have been looking for ways to find solutions to fossil fuel problems and to find an alternative for fossil fuel. Renewable energy is an incredible way to fuel, heat, and power our community by solar, biomass, wind, hydropower, geothermal, and ocean energy. (**Figure 1.1**)[9-15] In 2019, 11.4% of total U.S. energy consumption was provided by renewable energy. 17% of total U.S. electricity was generated by renewable energy sources. As more fossil fuel power stations retire and more intermittent renewables enter the market. More than half of total U.S. renewable energy consumption was consumed by the electric power sector. According to the International Energy Agency, renewables accounted for more than 28% of global electricity generation in the first quarter of 2020. A major impediment to the uptake of renewable energy has been its price tag, but its costs have decreased significantly with the fast development of technologies. The cost of solar panel technology, onshore wind, and offshore wind dropped 82%, 40%, and 20% during the last decade, respectively. The development of reliable energy systems is needed to design corresponding energy storage devices for energy storage and transmission. In order to meet the increasing demand for energy

storage systems by electric vehicles and portable electronic products, naturally-abundant, large-scale, and low-cost producible electrical energy storage systems, such as lithium-ion (Li-ion) batteries, sodium-ion (Na-ion) batteries, and super-capacitors, have attracted extensive attention.[16-19] These technologies have great potential for smoothing out the electricity supply from these renewable energy technologies and maintaining the power balance between supply and demand.

Figure 1.1 Renewable energy is derived from replenishable sources such as solar energy, wind power, hydroelectric power, biofuels, geothermal energy, and tidal power.

1.2 Energy storage devices

Energy storage is a very important part of our daily life, which can be used to help balance a power system with the time-variable renewable energy source. Energy comes in many forms, such as chemical, high temperature, electricity, radiation, kinetic and gravitational potential. Energy can be stored in several different ways, involving converting energy from difficult storage mode to more convenient or economical modes.[18-19] Energy storage devices have been widely used in many portable devices, power grids, electric vehicles, and electronic equipment, which can store energy in different forms including electrochemical, chemical, thermal, potential, and pressure.[20-24] Pumped storage hydropower is known as the world's largest battery technology, and contains two water reservoirs at different elevations, which can generate power by a turbine as water moves down and draw power as it pumps water to the upper reservoir. The pumped storage hydropower is an ideal complement to modern clean energy storage systems, and the pumped storage can alleviate the defects of wind and solar power such as seasonality and intermittency. Now, over 95% of large-scale electricity storage systems use pumped hydro dams, but they are not suitable for distributed applications due to the limitation of geography. Furthermore, the molten salt can store the thermal energy produced for use at night or during periods with less sunlight. They use the sunlight to heat the salts and put the formed molten salts close to water via a heat exchanger, where the hot steam can be used to turn the turbines.

Figure 1.2 Photograph of different kinds of cells for energy storage.

The battery is an important energy storage system, which can convert chemical energy directly into electrical energy. (**Figure 1.2**)[25] The batteries work on the redox reactions of the electrolyte with metals. On the side of the reduction reaction, the electrode gets positively charged called anode. Due to the oxidation reaction, the electrode gets negatively charged called cathode. Batteries can be connected to each other in a series circuit or a parallel circuit. They are extremely important in our daily life, where the large batteries are used to start cars and the small ones can power the children's toys. There are two kinds of batteries on the market: the primary and the secondary battery. Primary batteries, also known as non-rechargeable batteries, are single-use batteries because the electrochemical reaction is not reversible and cannot be recharged. A conventional primary battery is the dry cell zinc-carbon battery, where the zinc anode serves as both the negative electrode and the container, a carbon rod as the cathode is used to collect the current from the manganese oxide-based electrode, and the electrolyte is an aqueous mixture paste of zinc chloride and ammonium chloride solution. (**Figure 1.3a**)[26-30] The discharging mechanism is according to the reaction as follows:

$$2MnO_2 + 2NH_4Cl + Zn \rightarrow Zn^{2+} + Mn_2O_3 + 2NH_2 + H_2O + 2Cl^-$$
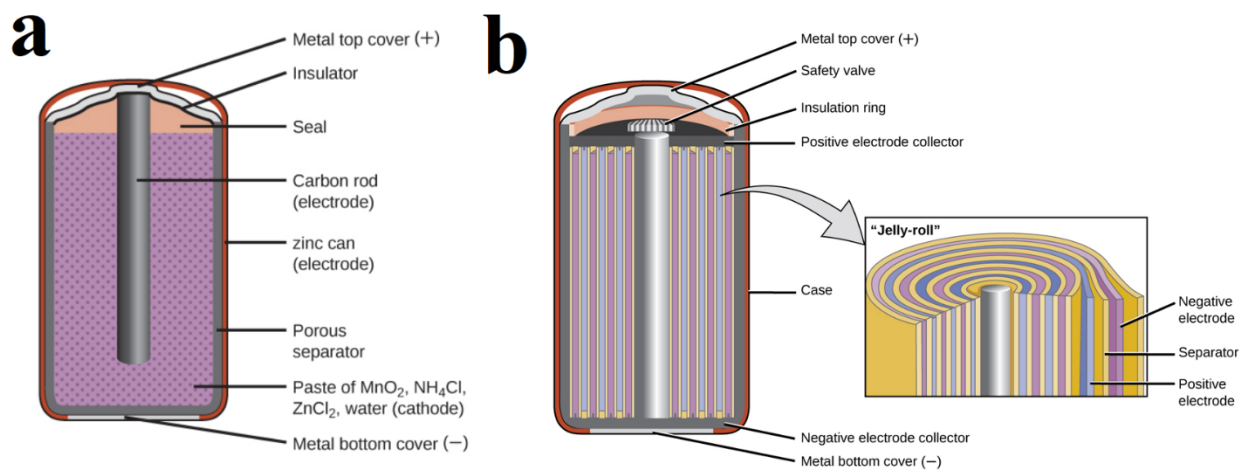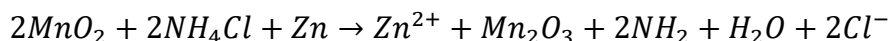
Figure 1.3. (a) The schematic diagram of the zinc-carbon battery. (b) The schematic diagram of the nickel-cadmium battery.[26]

To address the performance challenges with zinc-carbon dry batteries, alkaline batteries were launched on the market in the 1950s. The reaction mechanism can be represented as:

$$2MnO_2 + Zn \rightarrow ZnO + Mn_2O_3$$
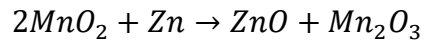
which uses potassium hydroxide as the electrolyte.[26-30] Primary batteries are now the market leader, which makes up about 90% of the $50 billion battery market, but secondary batteries have great potential to gain market share. In principle, secondary batteries are more economical to use than primary batteries. Secondary batteries are rechargeable batteries, which can be charged and discharged many times. With the rise in electric vehicles and portable electronic products such as power tools, iPad, cell phones, cordless vacuum cleaners, and laptops, the need for secondary batteries has grown substantially in the last hundred years. In 1859, Gaston Plante firstly invented the lead-acid cell, and it is the earliest type of secondary battery. Now, secondary batteries with different shapes and sizes can be found easily on the market, including lead-acid batteries, Zinc-air batteries, Li-ion batteries, Na-ion batteries, and nickel-metal hydride (NiMH) batteries.[30-64]

Different rechargeable batteries exhibit different reversible reaction mechanisms. For distributed energy storage applications, lead-acid storage devices have aroused attention.[36-40] The lead-acid type battery is a relatively simple energy storage device based on the sulfuric acid electrolyte and this kind of device accounts for more than half of the global market in 2018 with a total production of about 600 gigawatt-hours. The total reactions are

$$\text{Discharge process: } PbO_2 + Pb + 2H_2SO_4 \rightarrow 2PbSO_4 + 2H_2O$$

$$\text{Charge process: } 2PbSO_4 + 2H_2O \rightarrow PbO_2 + Pb + 2H_2SO_4$$
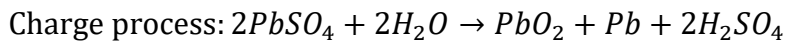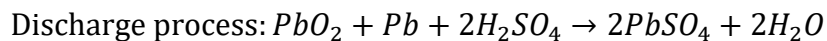
This battery can be used as an independent 12 V supply to support lighting and power module even in the event of a high-voltage battery disconnect and under cold conditions. However, the lead-acid type presents also big drawbacks: during the discharging/charging processes, the constant dissolution and redeposition of electrodes lead to morphological changes of the active materials and the corrosion of electrode grids, which affect the material utilization efficiency and battery cycle life.[38,39] Furthermore, lead-acid type batteries pose a potential threat to the environment and human body if improperly discarded as lead is a heavy metal and a strong poison. The lead and sulfuric acid in the lead-acid batteries can as well contaminate solid and groundwater. Lead is

very harmful to the human body, especially for children, where lead can damage all of the body systems. Sulfuric acid is highly corrosive. Add some sentences to connect here the change to another type of battery. Nickel-cadmium batteries are assembled by the cadmium-plated anode, nickel-plated cathode, and a potassium hydroxide electrode (**Figure 1.3b**).[31-35] The total reactions are

$$Discharge\ process: NiO_2 + Cd + 2H_2O \rightarrow Cd(OH)_2 + Ni(OH)_2$$

$$Charge\ process: Cd(OH)_2 + Ni(OH)_2 \rightarrow NiO_2 + Cd + 2H_2O$$
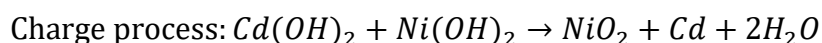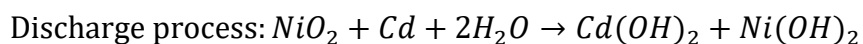
When properly treated, a nickel-cadmium battery can exhibit an excellent cycling performance more than 1000 times. The nickel-cadmium battery is the first widely available rechargeable battery, but it still suffers from an inherent obstacle, known as the memory effect. After using, they must be fully discharged. Moreover, cadmium is one of the toxic heavy metals, so these nickel-cadmium batteries need to be sealed for their whole life. Then, nickel-metal hydride batteries are used to replace the nickel-cadmium battery, due to their higher capacity and minimal memory effect.[31-40]
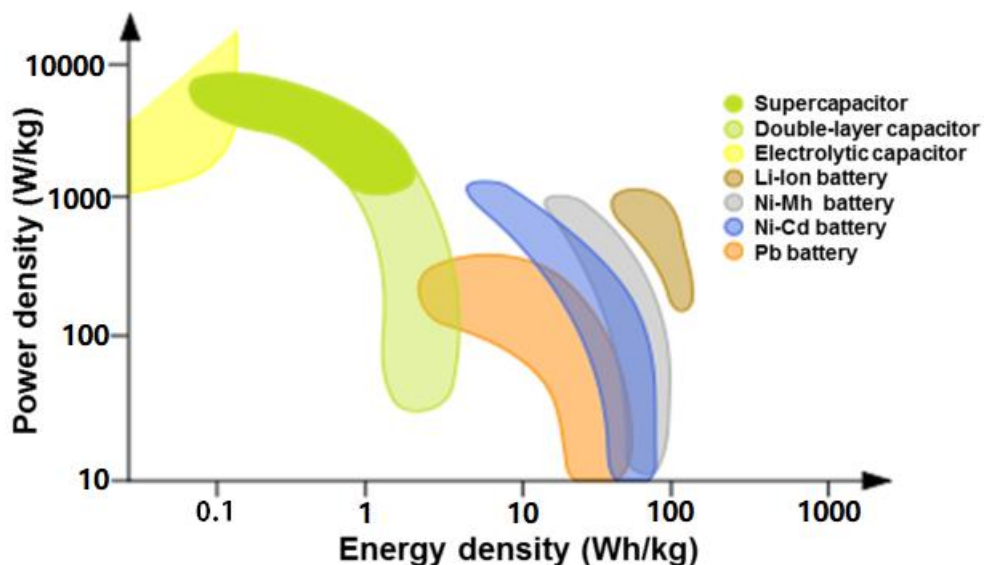
Figure 1.4. The energy density and power density of different kinds of energy storage devices. Copyright 2016 Royal Society of Chemistry.

6

Among the various existing energy storage devices (**Figure 1.4**), Li-based and Na-based batteries currently outperform other systems due to their long cycling performance, relatively high energy density, and design flexibility. However, current energy storage technology is still far from meeting the demands of new technological developments.[41-57] The demand to further improve the safety, increase the energy density and reduce the cost, as well as the growing concern related to natural resource needs for Cobalt (Co) ions and Li ions have accelerated the investigation of so-called nest generation energy storage technologies.[57-64]

1.3   Lithium ion battery

As a typical secondary battery (rechargeable batteries), the Li-ion battery uses lithium ions as a key component of its electrochemistry.[65-67] In 1985, Akira Yoshino developed the prototype Li-ion battery based on earlier research by Koichi Mizushima, John B. Goodenough, Rachid Yazami, and M. Stanley Whittingham. In 1991, Sony in Japan commercialized the first rechargeable Li-ion batteries, and today these improved Li-ion batteries have become the most fastest-growing and promising energy storage devices on the market. Today, the capacity of 18650 cylindrical cells rose from 1100 mAh to over 3000 mAh, and the price dropped from $10 to ~$2.[68-73] Cost reduction, the absence of toxic material, and increase in specific energy paved the road to make Li-ion batteries serve as the universally acceptable battery for electro vehicles and portable application, first in the consumer industry and now increasingly also in heavy industry. Compared with conventional battery technology, Li-ion batteries exhibit a faster charge ability and a long cycle life and have a higher power density for more battery life in a lighter package. During the discharging process, Li atoms in the side of the anode are ionized and detached from the anode. The generated Li-ions leave the anode and transfer through the electrolyte to the cathode. On the side of the cathode, they recombine with the electrons and electrically neutralize. During the charging process, the Li-ions move from the cathode and transfer through the electrolyte until they come back to the anode. A micro-permeable separator is placed between the cathode and anode to prevent an electrical short circuit, and the formed Li-ions are small enough to be able to shuttle back and forth through the separator.[65-73]

7
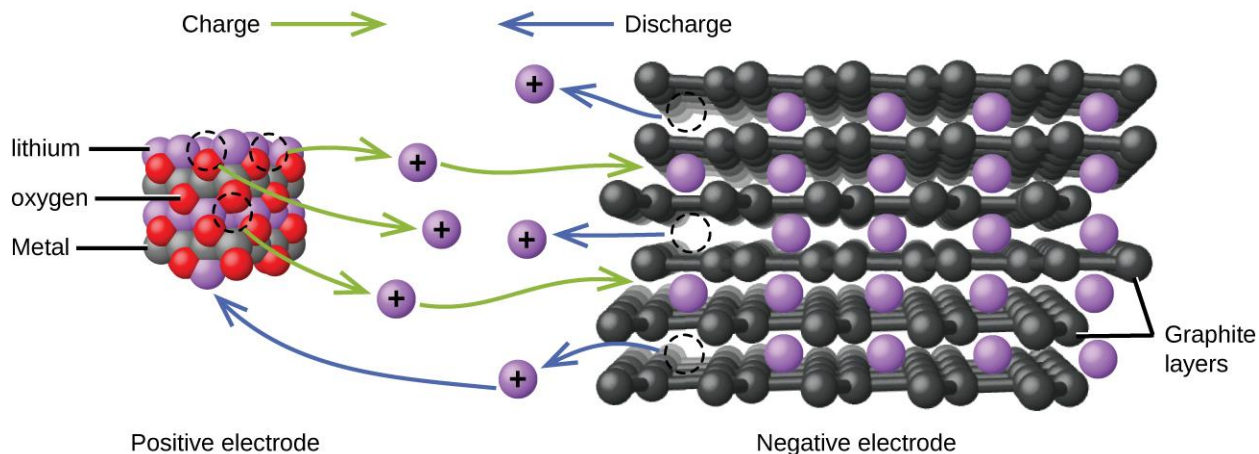
Figure 1.5. In the Li-ion battery, lithium ions move from the cathode through an electrolyte to the anode during the charging process, and back when discharging.

Compared to other elements, lithium has the lowest reduction potential, further allowing Li-ion batteries with the highest possible cell potential. Furthermore, as the third lightest element on earth Li element possesses the smallest ionic radii compared with any other single charged ion, allowing Li-based batteries to have a high volumetric and gravimetric capacity. Similar to the lead- and nickel-based batteries, Li-ion batteries contain a negative electrode (anode), a positive electrode (cathode), and an electrolyte as the conductor. For the cathode, Li ions can be stored in the intercalation cathode, which is a solid host network composed of transition multi-metal oxides, metal chalcogenides, and polyanion compounds.[73-77] Take LiCoO₂ (LCO) as the example (**Figure 1.5**),[78-81] the total reactions of the discharging process is

$$\text{Anode: } 6C + xLi^+ + xe^- \rightarrow Li_xC_6$$

$$\text{Cathode: } LiCoO_2 \rightarrow Li_{1-x}CoO_2 + xLi^+ + xe^-$$

and the total reactions of the charging process is

$$\text{Anode: } Li_xC_6 \rightarrow 6C + xLi^+ + xe^-$$

$$\text{Cathode: } Li_{1-x}CoO_2 + xLi^+ + xe^- \rightarrow LiCoO_2$$
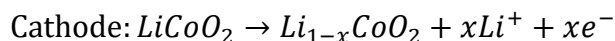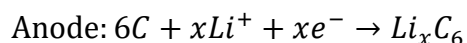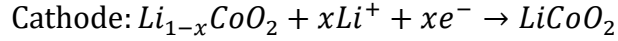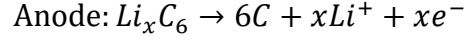
For LiFePO$_4$ （LFP) cathode,[82-86] the total reactions of the discharging process are

$$\text{Anode: } 6C + xLi^+ + xe^- \rightarrow Li_xC_6$$

$$\text{Cathode: } LiFePO_4 \rightarrow Li_{1-x}FePO_4 + xLi^+ + xe^-$$

and the total reactions of the charging process is

$$\text{Anode: } Li_xC_6 \rightarrow 6C + xLi^+ + xe^-$$

$$\text{Cathode: } Li_{1-x}FePO_4 + xLi^+ + xe^- \rightarrow LiFePO_4$$
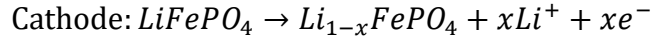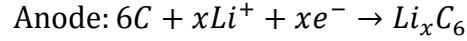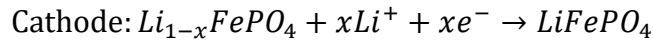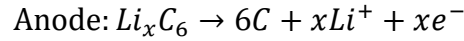
Due to their stable crystal structures and large application potential, commercial intercalation materials such as lithium iron phosphate (LFP), lithium cobalt oxide (LCO), lithium titanium oxide (LTO), lithium nickel cobalt manganese oxide (NCM), and lithium nickel cobalt aluminum oxide (NCA) have become the most prominent battery chemistries for energy storage. (**Figure 1.6**)[87] To develop new cathode materials, researchers have developed a range of new cathode materials, including a sulfur-based cathode, selenium-based cathode, tellurium-based cathode, iodine cathode, polyanion compounds, fluorine compounds, and chlorine compounds.

For anode materials, coke was firstly served as the anode by Sony in Li-ion batteries, and since 1997 almost all Li-ion batteries use conductive carbon materials or carbon-based derivatives as the anode to attain a flatter discharge curve.[88-110] Now, conventional carbon anodes can be largely divided into two types: graphitic carbon and hard carbon.[96] Nano-structured lithium titanium oxide as anode material has been successfully commercialized due to their high rate, long cycle life, relatively high volumetric capacity, superior thermal stability, and excellent low-temperature performance, but they still suffer from the high cost of titanium, low cell voltage, and low capacity. Recently, silicon (Si)-based alloys have been considered as one of the most attractive materials for the anode due to their high gravimetric (4,200 mAh g^{-1}) capacity and high volumetric (2,400 mAh cm^{-3}) capacity. During the plating process, Li-ions can react with graphite to form LiC$_6$ alloy, but

for Si only, to form $Li_{22}Si_5$ alloy.[88] However, the cycling performance of Si-based anode is very poor, still hindering the practical application of Si-based anode materials.
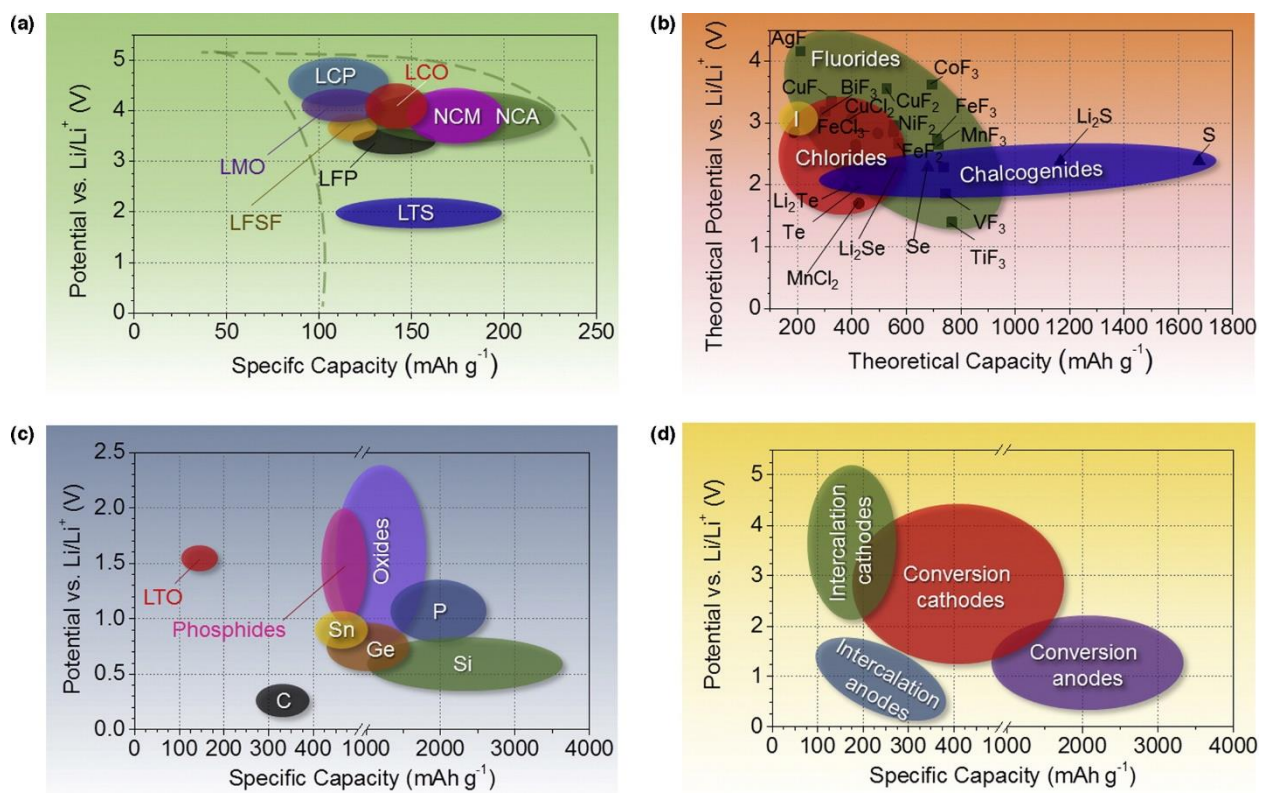
Figure 1.6. Approximate range of average discharge potentials and specific capacity of some of the most common (a) intercalation-type cathodes (experimental), (b) conversion-type cathodes (theoretical), (c) conversion type anodes (experimental), and (d) an overview of the average discharge potentials and specific capacities for all types of electrodes. Copyright 2015 Elsevier.

Optimizing the electrolyte is one of the most important directions to improve the electrochemical performance of the Li-ion batteries, especially in the field of rate capability, cell cyclability, safety, ionic conductivity, and life-span.[111-118] The electrolyte acts as the storehouse for Li-ions, and can facilitate the diffusion of Li ions between the anode and cathode. The electrolyte must be low viscosity and a high dielectric constant, which can dissolve Li salts and enable the Li-ions to

transport freely. Under the open charging voltages, the organic electrolyte is thermodynamically and electrochemically unstable, and the decomposition of electrolytes results in the formation of solid electrolyte interphase (SEI) layer on the surface of the anode, accompanied by an irreversible loss of Li ions.[46, 47] Traditional commercial electrolyte systems use a mixture of linear carbonate esters, such as dimethyl carbonate and diethyl carbonate, and cyclic carbonate esters, such as propylene carbonate and ethylene carbonate as the solvents, and $LiPF_6$ or $LiBF_4$ as the Li salts.[112-114] The alkyl carbonates were used as the solvents, because of their high polarity, lithiated graphite, low toxicity, and acceptable anodic stability for the 4 V cathodes. For Li salts, $LiPF_6$ salt is widely used in commercial electrolytes. Other conventional Li salts have too many disadvantages: $LiBF_4$ is problematic on the negative side; $LiSO_3CF_3$ has a very low conductivity; $LiAsF_6$ is poisonous; $LiClO_4$ is explosive.

Due to its high energy density, the most common battery type in modern electric vehicles is the Li-ion battery. According to the United States Department of Energy,[117] the mileages of electric vehicles have increased to 171.23% in the last 7 years, which increased from 73 miles in 2011 to 125 miles in 2018. More than 95% of electric vehicles are equipped with or directly powered by Li-ion batteries, mitigating environmental pollution and reducing energy use. By 2019, sales of electric vehicles in the world topped 2.1 million, outdistancing 2018-already a record year-to boost the stock to 7.2 million electric vehicles, and 47% of which were in China. The global electric vehicle batteries market is expected to reach $35.36 billion in 2023.[118] Such huge Li-ion battery demand will result in considerable consumption of resources for their manufacture. In Li-ion batteries, Li and Co are in greater demand than other metals due to their low relative abundance and high price. According to the United States Geological Survey, only 80 million tons of Li resources have been found with the continuing exploration, and the average export price of battery-grade lithium carbonate was increased to $13,000 per metric ton in 2019. While the 82% average cost of Li-ion battery has already been reduced from 2012 to 2020, the increasing demand for Li commodity chemicals combined with geographically constrained Li mineral reserves will drive up prices. Further reductions and recycling are the key factors to increasing the competitiveness and wider adoption of Li-ion batteries for electric vehicles and grid storage. In addition to the cost, the theoretical capacity of a Li-ion battery is only 372 mA h g^{-1} in the case of the graphite-based anode, corresponding to the energy density of 250-300 Wh kg^{-1}. Limited resources and strong demand for

high energy densities in electric vehicles and portable electronic products have motivated the fast development of next-generation rechargeable batteries to replace current Li-ion batteries.

1.4 Sodium ion battery

Table 1. Lithium vs sodium characteristic.

Category	Sodium	Lithium
Cation radius (Å)	1.06	0.76
Atomic weight	23 g mol^{-1}	6.9 g mol^{-1}
E^o (vs. Li/Li$^+$)	0.3 V	0
Cost, carbonates	$150/ton	$5000/ton
Capacity	1166 mAh g^{-1}	3860 mAh g^{-1}
Coordination preference	Octahedral and prismatic	Octahedral and tetrahedral

Recently, rechargeable batteries offer efficient electrical energy storage of electrical energy and off-peak electric power generated by wind, solar, fossil fuels, and nuclear, but Li-ion batteries are still too expensive for application in the field of the large-scale energy storage system. Unlike Li, sodium (Na) element is the most abundant of the alkali group of metals and is the fourth most abundant element on earth, comprising about 2.6% of the earth's crust. Supplies of sodium-containing precursors are vast, and the average price of sodium carbonate is only $150 per ton, which is much lower than that of lithium carbonate (around $5000/ton). Due to their low cost and wide availability, Na-ion batteries have the potential for meeting the increasing demands for the

large-scale energy storage system, which exhibit similar chemistry with Li-ion batteries. The redox potential of sodium (-2.71 V vs. S.H.E.) is similar to lithium (-3.04 V vs. S.H.E.), and the theoretical specific capacity of metallic sodium (1166 mAh g^{-1}) is less low than that of metallic lithium (3860 mAh g^{-1}).[119-122] Recent reports have even shown that Na-based batteries can compete with Li-based batteries in terms of energy density. (**Table 1**) The cell construction and working principle of Na-based batteries are almost identical to those of the Li-based battery types, with the primary difference being that the lithium-based compounds are exchanged with sodium-based compounds.[123-125]
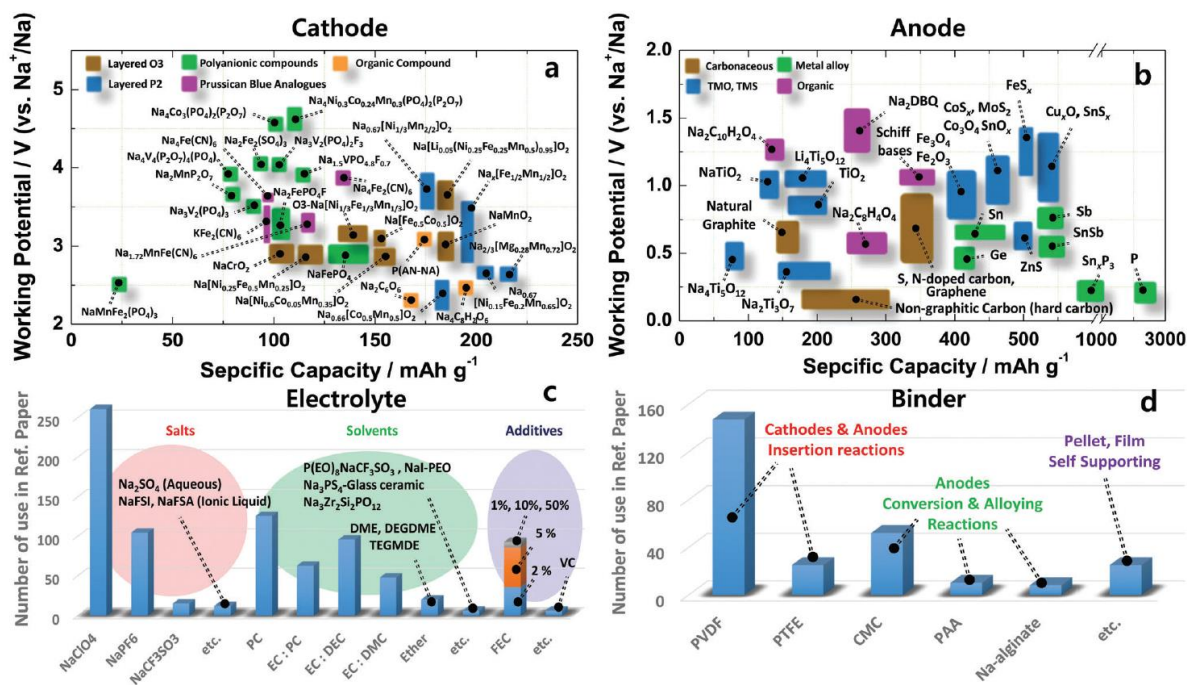
Figure 1.7. Recent research progress in sodium-ion batteries: (a) cathode, (b) anode, (c) electrolyte and (d) binder. Copyright 2017 Royal Society of Chemistry.

Early research in the field of Na-ion batteries mainly focused on Na-NiCl$_2$ batteries and Sodium Sulfur (Na-S) batteries operated at the ultra-high temperature (>300 °C) to maintain the sodium species in a liquid state with a solid ceramic electrolyte. All of these devices delivered a high energy density but poor power density at the expense of harsh terms and complicated implementation. By the early 1990s, the research community quickly lost interest in Na-ion batteries due to their lower energy density and the fast development of Li-ion batteries.[122] However, the improvement of Li-ion battery systems cannot address the rarity of lithium resources, leading to a risk that Li-ion batteries for electric vehicles will no longer be affordable with their exhaustive usage. Therefore, Na-ion batteries in ambient conditions have received international attention and commercial interest in the 2010s and 2020s as a possible substitute for Li-ion batteries.[119-122] The increasing of energy density for room temperature Na-ion batteries can be revived by increasing the working potential of the cathode or decreasing the working potential of the anode, producing active materials with densely packed particles, and increasing specific electrode capacities.

To date, various cathode materials have been well investigated, where the appropriate cathode can reversibly accommodate sodium cations with a voltage larger than +2.0 V to that of sodium metal.[123-138] The ideal cathode for Na-ion batteries should have a small volume change during the cycles and exhibit appropriate property if they function as a host material for sodium. Whittingham et al. and Hagenmuller et al. found that Na ions can be intercalated into layered MoS$_2$, TaS$_2$, TiS$_2$, Na$_x$CoO$_2$, and Na$_x$MnO$_2$. Sodium inclines to form a 6-coordination, prismatic arrangement, or octahedral arrangement, where tetrahedral coordination is limited in inorganic materials, posing a limited structure for the design of cathode materials.[123-138]

After that, various Na-ion cathode materials have been reported, such as transition metal fluorides, transition metal sulfides, layered metal oxides, tunnel metal oxides, polyanionic compounds, Prussian blue analogues, and polymers. (**Figure 1.7**)[139-148] Here, we choose the Na$_3$V$_2$(PO$_4$)$_3$ (NVP) as the cathode materials to exhibit the charging and discharging process as follows:

$$\text{Discharge process:} \; Na_3V_2(PO_4)_3 \rightarrow 2Na^+ + 2e^- + NaV_2(PO_4)_3$$

$$\text{Charge process:} \; 2Na^+ + 2e^- + NaV_2(PO_4)_3 \rightarrow Na_3V_2(PO_4)_3$$
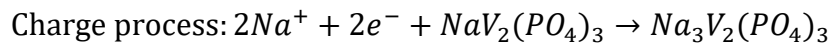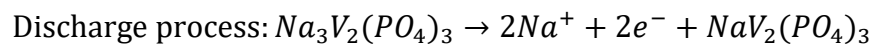
However, the search for an appropriate anode for Na-ion batteries with a large reversible capacity, appropriate Na voltage storage, and high structural stability remains an obstacle due to the limited capacity of the traditional anode materials in the field of Li-ion batteries. Materials with lower voltages (< 2.0 V, Na^+ vs. Na) are best defined as the anode for Na-ion batteries. Graphite-based derivatives, which are a common anode material in the field of Li-ion batteries, are electrochemically irreversible and cannot intercalate Na-ions to any appreciable extent. In 2000, Dahn's group firstly found that the improved hard carbon can realize the electrochemical reversibility of Na^+ insertion at room temperature. Hard carbon anodes, which are considered as the first-generation anode, still exhibit low Coulombic efficiency, poor rate capability, and low capacity. Furthermore, high capacities can be achieved by alloy and metal chalcogenide anodes, but still suffer from high cost, large volume change, and relatively high redox potential, which limit their applicability in Na-ion batteries.[122-148] The challenges of the anode materials need to be overcome before such Na-ion batteries can become a practical, commercial reality.

An appropriate electrolyte system for Na-ion batteries must be in conjunction with anode advances, and the discovery of an electrolyte system is a great research opportunity.[149-157] Traditional electrolyte systems for Na-ion batteries use carbonate ester solvents as the electrolyte solution and $NaPF_6$ or $NaClO_4$ as the sodium salts. Unfortunately, the high reactivity between the metallic sodium and organic electrolyte will lead to continuous corrosion of Na anode, rather than forming a stable SEI layer. Some additives, such as fluoroethylene carbonate, *trans*-difluoroethylene carbonate, vinylidene carbonate, and ethylene sulfate, are used to improve the cycling stability.[149-157] In general, the research in the field of Na-ion batteries has increased dramatically and is in full swing to address these challenges and thereby enable this new energy storage technology based on sodium ions to become available in the coming years.

1.5 Lithium metal battery

Over the past three decades, Li-ion batteries have displaced other secondary batteries as the market leader in the field of large-scale energy storage systems, such as consumer electronics, portable electronic products, electric vehicles, and grid energy storage.[16,17,157] However, the energy density of commercial Li-ion batteries (such as graphite/LFP cell and graphite/NCM cell) has increased from 80 to 300 Wh kg^{-1}, approaching their physicochemical limits.[158] High energy densities Li-ion batteries, such as Li metal batteries, become the study focus owing to the merits of its extremely low redox potential (-3.04 V vs S.H.E.) and high theoretical specific capacity (~3860 mAh g^{-1}), where the capacity is ten times higher than that of graphite.[158-164] Once the conventional graphite-based anode material is replaced by the metallic Li or Li metal anode, the cell assembled with an LMO cathode can achieve high specific energy of ~440 Wh kg^{-1}. Moreover, transition to Li metal-air battery and Li metal-S battery can further increase the specific energy to ~950 Wh kg^{-1} and ~650 Wh kg^{-1}, respectively.[165-168]
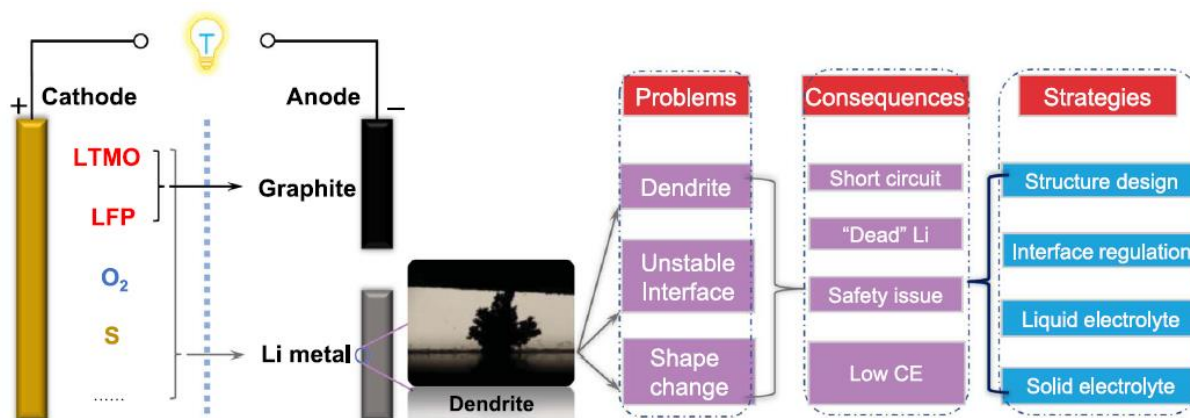
Figure 1.8. Schematic illustration of Li-ion battery and Li metal batteries; the failure mechanism of Li metal batteries and the practical strategies to suppress dendrites. Copyright 2018 Elsevier.

The high energy density achieved by replacing graphite with Li metal anode has promoted persistent motivations to realize Li metal batteries in practical applications. At first, Exxon used metallic Li in the infancy of Li-based battery research in the early 1970s. Until now, the improved Li-I$_2$ based primary batteries developed by Exxon are still widely used in the field of cardiac pacemakers. In the 1980s, the Li metal batteries assembled with MoS$_2$ cathode were commercialized by Moli Energy.[162] In subsequent years, the safety issues still hinder the large-scale applications of Li metal-based batteries, even after 500,000 tests by NEC and Mitsui. Until Sony developed coke as the anode to replace metallic Li, and the commercialization of Li metal anodes was terminated. Until now, traditional Li-ion batteries based on carbonaceous anode are approaching their limited capabilities, and the reviving Li metal anode is becoming a necessity.[164]

There are some intractable barriers limiting the large-scale applications of Li metal anode (**Figure 1.8**). The low Coulombic efficiency, large volume change, unstable solid electrolyte interphase (SEI) layer, and uncontrolled formation of dendrites during the charging/discharging processes still hinder the practical applications of Li metal anodes, which further result in capacity fading and reduce the cycling life. The growth of Li dendrites can pierce the polymer separator, leading to safety hazards including thermal runaway and internal short circuits.[165] To further realize the practical applications of Li metal batteries, appropriate strategies and mechanistic insights are imperative demands to intelligently solve the following challenges.

1. SEI layer. The SEI layer is instantaneously and spontaneously formed by the parasitic reactions between the organic electrolytes and Li metal anode in the initial cycles. A good SEI layer serves as the passivation layer on the surface of the Li metal anode, which is permeable to Li-ions and impermeable to electrons and electrolytes. An excellent SEI layer can effectively prevent the electrolyte from further decomposition. Degradation and broken of SEI layer negatively impact the whole battery life. Components of SEI, such as Li alkoxide salts and Li alkyl carbonates, are sensitive to moisture and thermally unstable. Decomposition can cause SEI to dissolve/evolve/peel off during the charging and discharging processes, leading to continuous corrosion of anode material. The extra issues, such as gas evolution, volume changes, and solvent co-intercalation, also accelerate the degradation process of the anode, leading to the additional growth of the SEI

17

layer and the increasing diffusion barrier for the Li-ions. In summary, the growth of SEI directly contributes to an increase in power fade, battery impedance, and capacity fade.[166-171]

2. Lithium dendrites. Li metal anode was constantly changing during the repeated stripping and plating processes, which leads to ineluctable stress concentrations on the preformed protection layers. This phenomenon became more severe after the growth of the Li dendrites on the surface. The growth of Li dendrites further induces unwanted side reactions that reduce energy density and Coulombic efficiency, at worst, cause internal shorting of the Li metal batteries that can lead to fires or explosions.[172-182]

3. Infinite relative volume change. During the cycles, all materials in the battery undergo volume change. The conventional graphite exhibits a volume change of 10%, and the Si-based anode exhibits a much greater volume change of 400%. The relative volume change of a Li anode is virtually infinite, owing to its hostless nature. From a practical perspective, the areal capacity of a single-sided commercial electrode needs to reach at least 3 mAh cm^{-2}, equivalent to a relative change in thickness of $\sim$14.6 μm for Li. This imposes formidable challenges on the stability of the SEI layer.[183-209]

Extensive works, including electrolyte additives, 3D matrix composites, spatial deposition control, porous structural host, and artificial SEI layers, have been carried out to significantly suppress the formation of dendritic structure and push the Coulombic efficiency in corrosive carbonate-based electrolytes up to 98%. (**Figure 1.9**)[210-213] For example, various mechanical protective layers, such as poly(dimethylsiloxane) film diamond-like carbon film, and the alloy-LiCl coating layer, have also been proposed to inhibit the Li dendrite growth during repeated stripping/plating processes. Among various approaches, 3D host structures, such as carbon paper and copper (Cu) foam, have attracted considerable interest, as they can regulate the metal deposition, inhibit the dendrite growth, reduce the local current density, and homogenize the ion flux. However, Li deposition in 3D Cu or Carbon-based structure is hampered by their poor affinity for Li-ions, where lithium shows poor wettability on these substrates and the nucleation overpotential occurs during Li plating, further indicating the unfavorable Li deposition behavior on Cu/Carbon-based substrates. Some works use the modified 3D porous copper substrates to prepare the Li metal anode, where a large number of protuberant tips serve as a favorable host of Li. The protuberant tips provide a large and highly electroactive area, and a regulated electric field to promote

homogeneous nucleation and deposition of Li. The optimization of the electrolyte components and additives can homogenize the Li$^+$ flux during lithium plating and improve the stability of the SEI layers.[166-212]
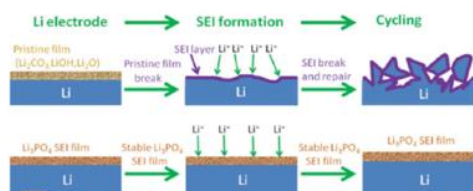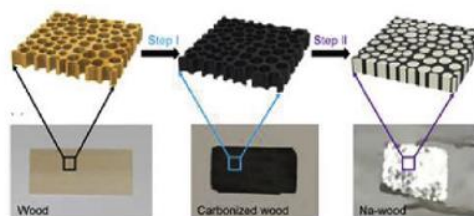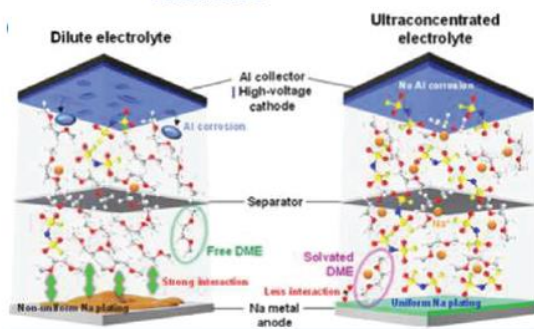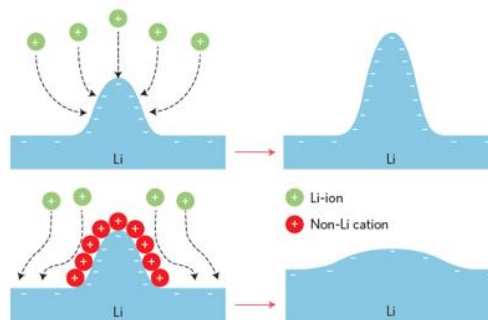
Figure 1.9. Schematic illustration of different methods to revive the Li metal anode. Copyright 2017 American Chemical Society.

1.6 Sodium metal batteries

Similar to the lithium metal battery, Na metal batteries have become appealing choices for high energy-density energy storage devices due to their low cost and high energy densities.[213-216] Na metal anode is an ideal alternative for conventional anode materials of Na-ion battery, due to its low redox potential (-2.71 V vs S.H.E.) and relatively high theoretical specific capacity (1165 mAh g^{-1}). The assembled room temperature Na-O$_2$ or Na-S battery system based on Na metal anodes and oxygen (O$_2$) or sulfur (S) cathodes can exhibit high theoretical specific energies of 1605 Wh kg^{-1} and 1274 Wh kg^{-1}, which are ten times higher than that of conventional Na-ion battery (~120 Wh kg^{-1}) and triple or quadruple times larger than that of corresponding Li-graphited based batteries.[214-220] Owing to the severe shortage of Li-containing resources, Na metal-based systems have drawn a wide range of interest due to their similar chemistry with Li metal-based chemistry. Furthermore, Na minerals are more available and abundant than Li resources. Benefiting from the low cost and wide distribution of sodium-based resources, it is possible to design low cost, high energy density, high safety, and high power energy storage devices by Na metal batteries.[221-225]
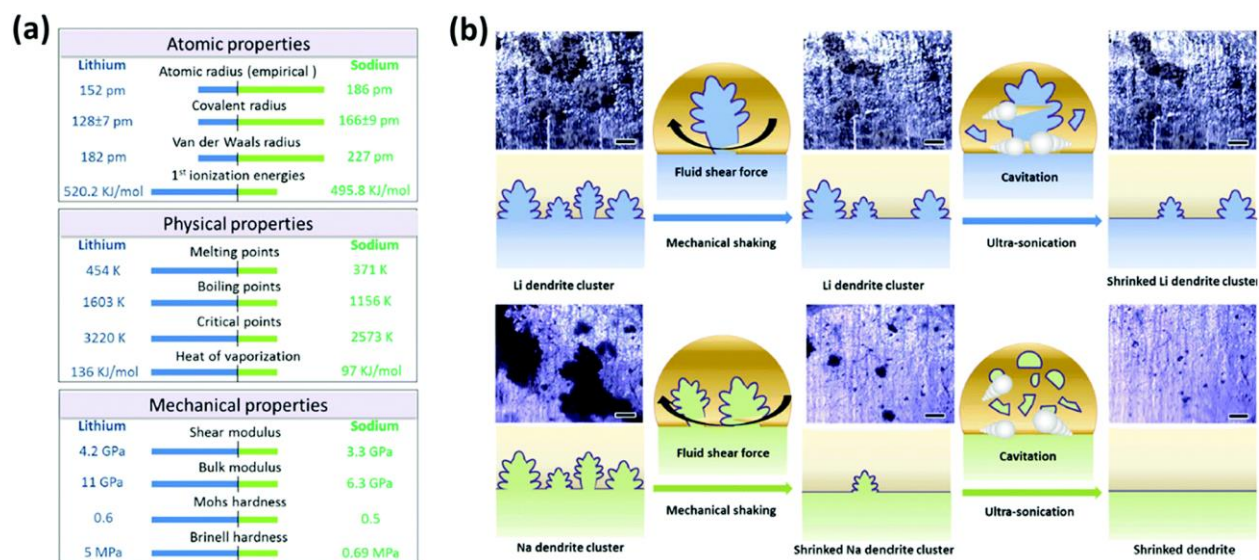
Figure 1.10. (a) Various properties of Li and Na. (b) mechanically stability under the quasi-zero electrochemical field for Li and Na dendrites. Copyright 2018 Elsevier.

Although the Na metal anode has great potential for next-generation energy storage devices, their commercial applications are still encountered by tremendous challenges, which is even more problematic than for Li metal anode (**Figure 1.10**). Metallic Na can easily react with carbonate electrolytes, leading to the formation of weak SEI layers. The broken of unstable SEI layer will lead to the continuous consumption of the Na ions and electrolyte, further promoting the growth of Na dendrites. The consumption of the Na ions and electrolyte will reduce the Coulombic efficiency and shorten the lifetime of Na metal batteries. Owing to its uncontrollable side reactions, high reactivity, and continuous consumption of both Na and electrolyte can cause poor electrochemistry performance and uncontrolled Na dendritic growth, leading to safety hazards such as internal short-circuiting, thermal runaway, or explosion. Furthermore, the host-less nature of the Na metal anode leads to large volume changes during repeated Na stripping/plating processes.[226-229]

In initial studies in the field of Na metal batteries, most of the works focus on the development of other cell components, and the important role of the Na metal anode has been significantly neglected. To overcome the above challenges, many strategies have been devoted to improving the electrochemical performance of Na metal batteries by suppressing the growth of sodium dendrites, which is inspired by the improvement of the Li metal anode. (**Figure 1.11**) For example, a stable SEI layer with high flexibility, small thickness, sufficient density, and high ionic conductivity was used to inhibit the formation of Na dendrites. The properties and composition of the SEI layer are mainly determined by the different sodium salts, organic solvents, and electrolyte additives. In addition to the spontaneous formation of the SEI layer on the surface of Na metal anode by the reaction between the metallic Na and organic electrolyte, the modification of surface structure by artificial SEI layers is considered as the effective strategy to suppress the growth of Na dendrites and protect Na metal anodes. Furthermore, it is urgent for Na metal anode to produce a uniform Na^+ flux, where the spatial inhomogeneity of Na^+ distribution on the surfaces contributes to the growth of Na dendrites. Therefore, the current collectors with a large surface area can dissipate the local current density. Furthermore, to overcome the infinite volume change, some works use nanostructured host materials to prepare the Na metal anode. Different from the traditional 3D substrates, these modifications are very important for the commercial application of stable Na metal anodes in the field of room temperature Na metal-Air batteries and Na metal-S batteries, where the cathode materials lack prestored Na. [230-249]
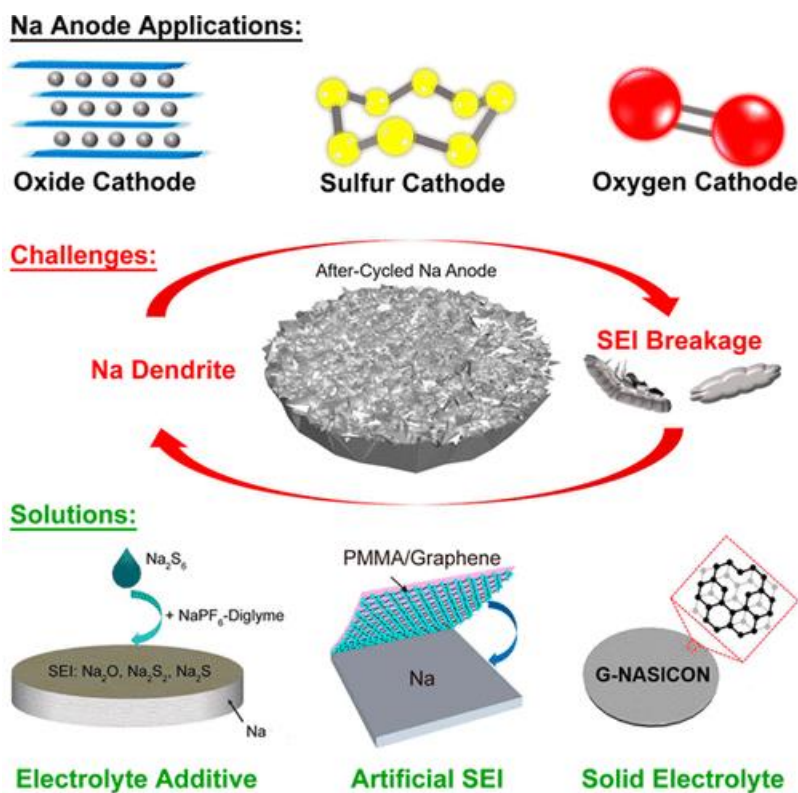
Figure 1.11. Schematic diagram of the high energy Na metal batteries with various cathode choices, the three major challenges upon repeated stripping and plating cycles of the Na metal anode, and the three major solutions to enable safe Na metal battery. Copyright 2019 American Chemical Society.

1.7 Selective deposition of alkali metal

Recently, Cui and co-workers studied the overpotentials of various nanomaterials (Zn, Au, Ag, Mg, Cu, Ni, Si, Pt, C, Al, and so on) on Li nucleation and concluded that the formation of a solid solution with lithium would help lithium nucleation because of the reduced Li/host interfacial energy.[250] The Li metal nucleation overpotential on Cu, Al, Pt, Ni, Sn, and C is 40 mV, 5 mV,

8 mV, 30 mV, 16 mV, and 14 mV, respectively. (**Figure 1.12**) No nucleation overpotential was needed to nucleate Li ions on Zn, Ag, Au, or Mg. After galvanostatic deposition, Li was selectively and preferentially deposited on the surface of Au strips, but not on the surface of bare Cu foil. Au and Ag particles providing a new way of heterogeneous seeded growth to control Li plating on the appointed substrates, resulting in a low nucleation barrier for Li-ions deposition.[250-257]
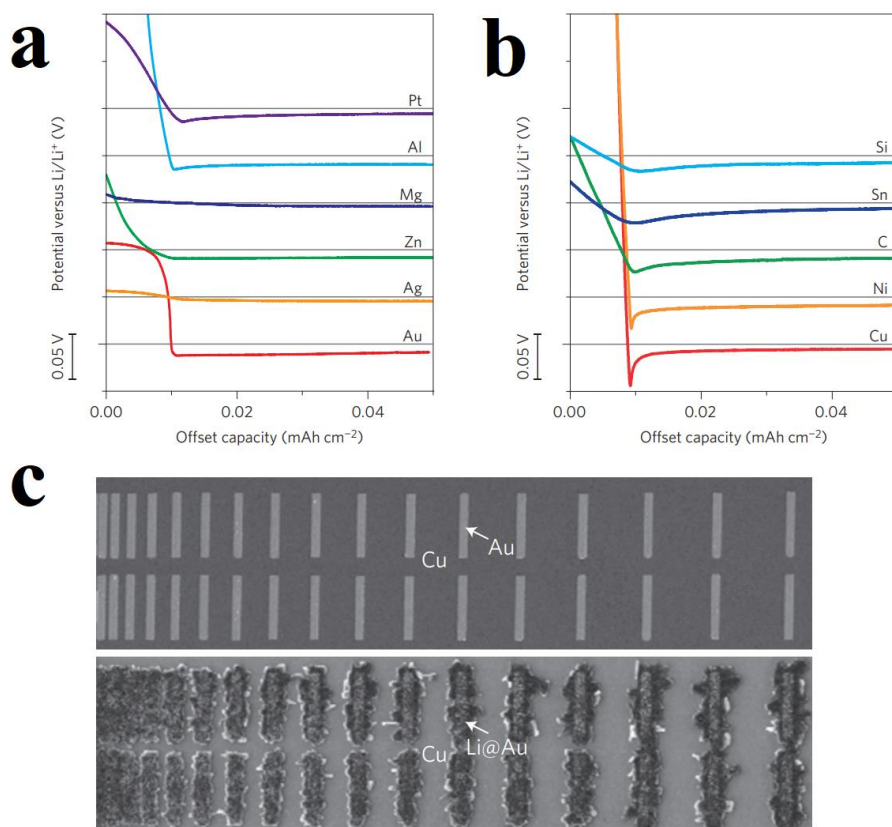
Figure 1.12. (a-b) Voltage profiles of various materials during Li deposition. (c) SEM images of a gold strip array with various separations before (top) and after (bottom) Li deposition. Copyright 2016 Springer Nature Limited.
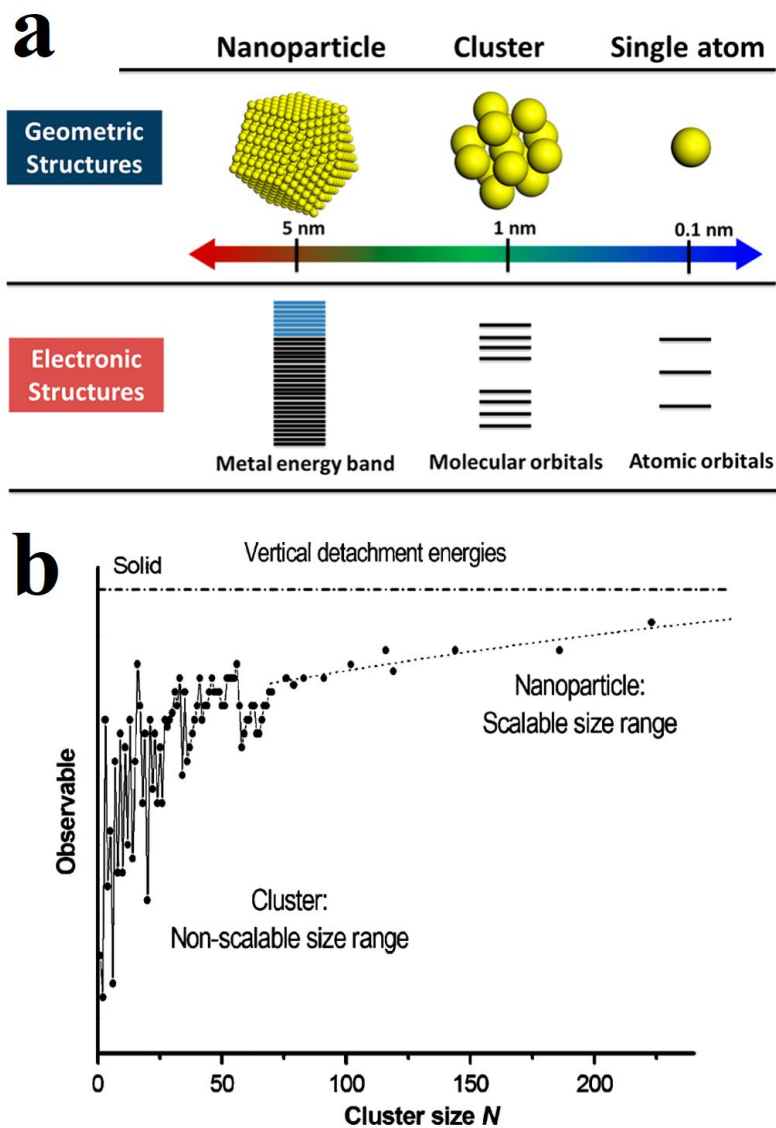
Figure 1.13. (a) Geometric and electronic structures of single atoms, clusters, and nanoparticles. Copyright 2018 American Chemical Society. (b) Work function obtained from ultraviolet photoelectron spectroscopy of Au clusters with different atomicity. Copyright 1992 AIP Publishing LLC.

Noble metal-based current collectors for Li metal are expected to address the imperfection of interface instability and dendrite growth, exhibiting the great development potential for Na metal anode. However, as one of the most common noble metals, Au and Ag are so expensive that they

would be unaffordable as the substrates of metal batteries for large-scale production. Downsizing noble metals to single atoms or clusters provides an effective way to decrease Au/Ag dosage and maximize atomic utilization efficiency. [258-260] At the maximum limit of metal dispersion, using single atom and cluster-based materials as nucleation seeds to induce alkali metal deposition generates great interest, due to their closer structural resemblance, maximized atomic utilization efficiency, and increased active sites. (**Figure 1.13a**)[261-267] The metal species with different sizes exhibit different catalytic behavior for different reactions. Many published works show that some factors (such as metal-solvent interaction, chemical composition, shape, particle size, and metal-support interaction) can significantly change the properties of metal catalysts. Taking Au as an example, the work function for Au cluster with less than 30 atoms varies greatly with the atomicity, while the work function for Au nanoparticles with more than 70 atoms remains constant and increases slowly with the growth of particle size. (**Figure 1.13b**) When the nanoparticles become smaller, especially metal clusters or even single atoms supported on size, shape, solid carriers, and the electronic properties of the metal will also depend on the surface arrangement and electronic structure of the support. Integrating single atoms or clusters on appropriate conductive substrates can significantly alter the reactivity and optimize the electronic property, which tends to be more active and helpful to regulate the deposition of the alkali metal with controllable morphology and position.[268,269]

1.8   Thesis objective

This project aims to develop novel surface or atomic modification of current collector for stable alkali metal anode, which can guide alkali metal ion deposition uniformly and prevent the growth of dendrite structure. Specifically, different kinds of alkali metal anode with long-term cycling stability, dendrite-free structure, and record-high utilization and will be designed, synthesized, and investigated.

Part I: The first part is mainly devoted to the synthesis and design of freestanding three dimensional (3D) porous lithium metal foam accompanied by an artificial SEI layer

Li metal anode is among the most promising candidates as the ultimate anode materials for the next-generation rechargeable Li-based batteries. However, large volume expansion and uneven dendrite formation still hinder the development of Li metal anode. Herein, different from the conventional Li foil, freestanding lithium metal anode with 3D porous foam structure accompanied by inherent LDBS layer (artificial SEI layer) has been constructed by in situ chemical etching using 4-dodecylbenzene sulfonic acid. Porous matrix served as a rigid backbone leads to more uniform charge distribution and thus orients the deposition of Li ions. The LDBS layers as the conformal SEI layer can suppress the side reactions and the formation of Li dendrites. Moreover, the Li metal anodes exhibit excellent electrochemical performance when assembled by LiNiCoMnO$_2$ cathode with a high active material loading up to 20.4 mg cm^{-2}. In addition, we have enabled deeply cyclable performance at a high area capacity of more than 20.0 mAh cm^{-2}, and stable long-term plating/stripping process of symmetric cells with low voltage hysteresis over 350 hours are revealed, which further demonstrate that our strategy can greatly prevent dendrites from shooting out, prevent the electrolyte decomposition, and suppress the gassing process, demonstrating the reliability and security of the battery.

Part II: The second part is mainly devoted to the design and synthesis of single-atom and cluster Au as the nucleophilic site for deeply cyclable Li/Na metal anodes.

The practical application of alkali metal anodes still faces some serious challenges, among which the uncontrolled growth of the dendritic structure is prominent. Herein, we demonstrated that the unfirm dispersion of single-atom and cluster Au (SCAu) on the surface of functionalized carbon cloth (CC) as the current collector to uniformly guide alkali metal deposition, thereby inhibiting the growth of dendritic structure. Single-atom and cluster Au not only serves as the stable adsorption sites for Li/Na atoms with minimized nucleation barriers, but also has great affinity and interaction with Li/Na ions in the electrolyte, leading to the uniform alkali metal deposition. When used in Li metal anode, SCAu-CC substrate exhibits a high average Coulombic efficiency of 99.82% for more than 900 cycles under 1.0 mAh cm^{-2} and reversible deeply cyclable capacity at high

current density with high areal capacities of 15.0 and 20.0 mAh cm^{-2}. In addition, the corresponding Na metal anodes achieve high Coulombic efficiency of 99.73% for more than 250 cycles and a long lifespan of more than 400 h with low overpotential. Moreover, the Li metal batteries and Na metal batteries are successfully assembled, which shows the high Li/Na-utilization and feasibility of the anodes.

Part III: The third part presents the optimization of synthesis of single Zn atom sites based current collector for Na metal anode, aiming at designing and realizing a Na metal battery system with high utilization, high safety, and long cycling stability.

Low utilization of active Na metal and uncontrollable growth of Na dendrites remain significant challenges for the commercial application of Na metal batteries. In this part, long-term cycling stability and record-high utilization of Na metal anode are reported, using single Zn atoms distributed carbon substrate as the current collector. Single Zn atoms, like a strong magnet for Na ions, guide the metallic Na nucleation, causing the uniformly Na metal deposition on the substrate surface, free from dendrite-induced short circuit or safety hazards. Compared with the bare carbon substrate and traditional Cu foil, the single Zn atom modified Na metal anode demonstrates significantly enhanced cycling stability. The resultant Na metal anode exhibits a stable voltage response with an ultralow overpotential after cycling for 1000 h and a high average stripping/plating Coulombic efficiency of 99.8% over 350 cycles. Superior long-term cycling stability of more than 1000 cycles was achieved by the full cell assembled by resultant Na metal anode with matched Na loading and Na$_3$V$_2$(PO$_4$)$_3$ cathode. This work sheds fresh light on the application of single-atom metal doping in the rational design of Na metal anodes, and provides new insight into further development of next-generation rechargeable batteries.

1.9 Thesis organization

This thesis is divided into six parts and organized as follows:

Chapter 1 Introduction: This chapter generally introduces the general background, motivation, and basics of my projects.

Chapter 2 Materials and characterization: This chapter describes experimental details regarding the structural characterization and electrochemical measurement for alkali metal anode. We further clarify the sample preparation and mechanism in corresponding parts.

Chapter 3 Results: Lithium dendrite inhibition via 3D porous lithium metal anode accompanied by inherent SEI layer: This chapter presents the design of 3D porous Li metal anodes with an artificial SEI layer, which can buffer the volume change, guide Li deposition inside its porous structure, uniform the diffusion of Li-ion on the interface and enable deeply deposited Li metal. The publication related to this chapter is:

Tingzhou Yang, Yawen Sun, Tao Qian, Jie Liu, Xuejun Liu, Federico Rosei, Chenglin Yan, Lithium dendrite inhibition via 3D porous lithium metal anode accompanied by inherent SEI layer – Energy Storage Materials, 2020, 26, 385-390.

Chapter 4 Results: Single-atom and cluster Au as an usher for deeply cyclable Li/Na metal anodes: This chapter presents the design of deeply cyclable Li/Na metal anodes by single-atom and cluster Au modified current collector and the investigation on their electrochemical performance by Li/Na metal batteries. The publication related to this chapter is:

Tingzhou Yang, Tao Qian, Xiaowei Shen, Mengfan Wang, Sisi Liu, Jun Zhong, Chenglin Yan, Federico Rosei. Single-cluster Au as an usher for deeply cyclable Li metal anodes - Journal of Materials Chemistry A, 2019, 7, 14496-14503.

Yawen Sun, **Tingzhou Yang** (**Co-first author**), Haoqing Ji, Jinqiu Zhou, Zhenkang Wang, Tao Qian, Chenglin Yan, Boosting the Optimization of Lithium Metal Batteries by Molecular Dynamics Simulations: A Perspective – Advanced Energy Materials, 2020, 10, 2002373.

Chapter 5 Results: Mega high utilization of sodium metal anodes enabled by single zinc atom sites: This chapter illustrates the optimization of Na metal anode by carbon-substrate-supported nitrogen-anchored zinc (Zn) single atoms. The in situ measurement and electrochemical measurement are further investigated to demonstrate the advantages and high utilization of Na metal anode. The publication related to this chapter is:

Tingzhou Yang, Tao Qian, Yawen Sun, Jun Zhong, Federico Rosei, Chenglin Yan, Mega high utilization of sodium metal anodes enabled by single zinc atom sites – Nano Letters, 2019, 19, 7827-7835.

Chapter 6 Conclusions and perspectives: This chapter briefly summarizes the most important contributions of these works and presents the perspectives of future improvement.

An appendix is followed the main part of this thesis, which summarizes this dissertation in French based on INRS policy.

2 MATERIALS AND CHARACTERIZATION

2.1 Chemicals and reagents

Table 2. Summary of the reagents.

Name	Linear Formula	Assay	Company
Gold(III) chloride trihydrate	$HAuCl_4. 3H_2O$	$\geq 99.9\%$	Sigma-Aldrich
Sodium chloride	$NaCl$	$\geq 99.5\%$	Sigma-Aldrich
Ammonium metavanadate	NH_4VO_3	$\geq 99.0\%$	Sigma-Aldrich
2-Methylimidazole	$C_4H_6N_2$	99%	Sigma-Aldrich
Zinc nitrate hexahydrate	$Zn(NO_3)_2.6H_2O$	$\geq 99\%$	Aladdin
Ammonium dihydrogen phosphate	$NH_4H_2PO_4$	$\geq 98.0\%$	Aladdin
Sodium carbonate	Na_2CO_3	$\geq 99.5\%$	Aladdin
Methanol	CH_4O	$\geqslant 99.9\%$	Aladdin
Dopamine hydrochloride	$C_8H_{11}NO_2 \cdot HCl$	98%	Aladdin
Sulfuric acid	H_2SO_4	95%	Sigma-Aldrich
Hydrochloric acid	HCl	37%	Sigma-Aldrich
Nitric acid	HNO_3	70%	Sigma-Aldrich

The carbon paper and carbon cloth were obtained from CeTech Co., Ltd. All of the electrolyte (1 M lithium hexafluorophosphate ($LiPF_6$) in diethyl carbonate (DEC)/ethylene carbonate (EC) (1:1 by volume) and 1 M sodium perchlorate ($NaClO_4$) in dimethylcarbonate (DMC)/ethylene carbonate (EC) (1:1 by volume) with 5 wt % fluoroethylene carbonate (FEC)) and lithium foil (25 μm) were obtained from DodoChem Ltd. All chemicals were used as purchased.

2.2   Material characterizations

2.2.1   Scanning electron microscope

As a widely used electron microscope, the scanning electron microscope (SEM) can be used to examine the morphology of powder samples by scanning them with a focused beam of electrons in a raster scan pattern. Compared with traditional optical microscopes, where the image magnification is achieved through a system of lenses under visible light, SEM produces images by the interaction between the electrons from the focused beam and the atoms in the sample. The use of electrons allows obtaining images with higher resolution (up to 10 nm) and greater depth of field. When the electrons strike the sample, the various generated signals including secondary electrons, visible light, characteristic X-rays, diffracted backscattered electrons, backscattered electrons, and heat, produce an image of the sample surface and its elemental composition along with energy dispersive X-rays (EDX). The secondary electrons are used to exhibit the topography and morphology of the sample, while the function of the backscattered electron illustrates the contrasts of composition in different multiphase samples. (**Figure 2.1**) Under radiation of characteristic X-rays, the inelastic collisions between the incident electrons and the electrons in discrete orbitals of atoms occur, in this case, the different elements in the samples can be distinguished accurately. Furthermore, SEM analysis is considered to be non-destructive, where X-rays generated by electron interactions do not result in the volume loss of the materials.[270]

During the sample preparation, a clean sample is important for image clarity and characterization. We can use ultrasonic baths to avoid the accumulation of the materials and clean the samples.

However, ultrasonic baths need to be carefully treated to avoid damaging the sample. Metal-based materials and some carbon-based materials don't need to be pre-processed due to their inherent electrical conductivity. Some non-metal materials and polymers are required by coating a conductive layer (gold or platinum layer) with a sputter-coater. Before transferring to a high vacuum environment in SEM, the sample must be thoroughly dried, where the residual water vaporization will obstruct the electron beam as well as lead to low image clarity. Conductive double-coated carbon tape can be used to adhere the sample to the stubs or supports. Before coating by a conductive layer, the sample needs to be mounted on the specimen stage so that both the sample and plug receive the coating.
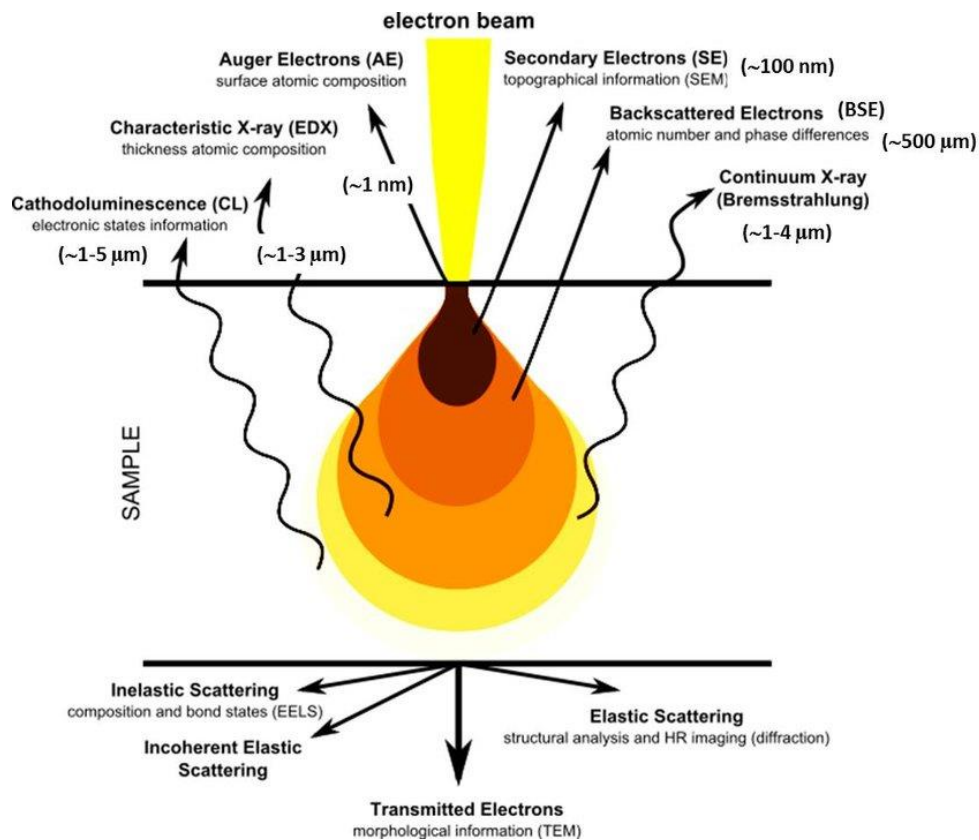
Figure 2.1. Signals generated from the interaction between the electron beam and specimen under study in SEM.[270]

2.2.2 Transmission electron microscope

The transmission electron microscope (TEM) is another type of conventional electron microscope, which is a very powerful tool for material science. The basic principles of TEM are similar to the optical microscope, but the light is replaced by electrons. The electron wavelength is much smaller than the light wavelength, so the optimal resolution obtained by TEM is many orders of magnitude higher than that of an optical microscope. In conventional TEM, the sample must be thin enough (less than 100 nm) to allow excited electrons to pass through it and form an image with minimum energy loss. The electron source and electromagnetic lenses in TEM that generate and focus the beam are similar to those described for the SEM, and the sample is bombarded by a highly focused beam of single-energy electrons. The focused beam must have enough energy to enable the electrons to be transmitted through the sample, and a series of electromagnetic lenses are used to magnify the transmitted electron signal, which can be observed by amplitude-contrast imaging, electron diffraction, or phase-contrast imaging. TEM has a much higher resolution than SEM. TEM is a major analytical method in the chemical, biological, and physical sciences, which can be used to investigate the corresponding defects, composition, and growth of layers in semiconductors. High-resolution TEM can be used to explore the size, quality, density, and shape of quantum dots, wells, and wires.[271]

During the sample preparation of carbon-based materials, these materials can be easily dispersed in different organic solvents, including ethanol, isopropyl alcohol, dichloromethane, hexane, and so on. The organic solutions containing dispersed carbon materials must be ultrasonicated for at least 30 min to disperse uniformly. Then, a drop of the dispersed solution is dropped onto carbon-coated TEM grids and viewed under the microscope. If the sample is very thin (such as graphene), we can choose the ultra-thin carbon film supported Cu mesh or Cur mesh microgrid as the TEM grids. Before transferring in a high vacuum environment, the sample must be thoroughly dried. For other thick materials, these specimens after being fixed and dehydrated can be embedded in resin to withstand the high vacuum in the chamber of the instrument called an ultramicrotome and make them easier to cut into electron transparent thin sections (100 nm or thinner). (**Figure 2.2**) TEM specimens are also treated with heavy metals to increase the level of contrast in the final image. The parts of the specimen that interact strongly with the metals exhibit darker areas. We

can use an optical microscope to ensure that samples are successfully loaded on the surface of the TEM grids.
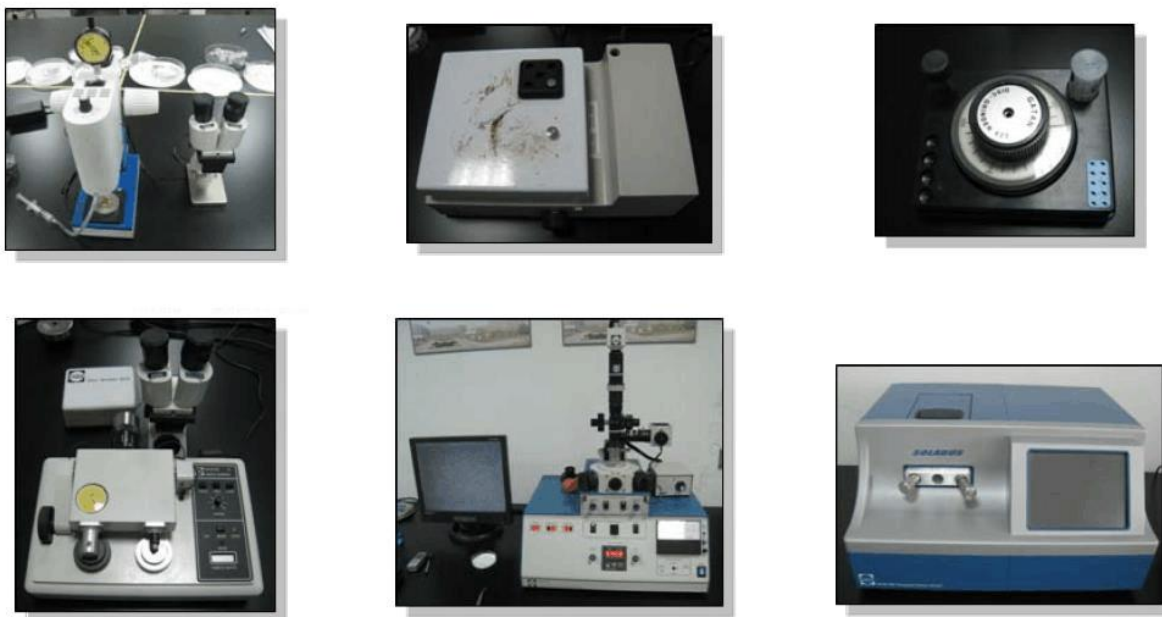
Figure 2.2. The equipment that can be used for the sample preparation.

2.2.3 High-angle annular dark-field scanning transmission electron microscopy

High-angle annular dark-field (HAADF) scanning transmission electron microscopy (STEM) is a type of STEM method. In HAADF-STEM, they use an annular dark-field detector (~50 to sufficiently high angle) to receive inelastically scattered electrons or thermal diffuse scattering at high angles. STEM is a type of TEM. For STEM, a highly focused electron beam or probe is raster-scanned across the sample surface, which is adjusted by the microscope lenses. The various signals (transmitted electrons at a high scattering angle) are collected point-by-point to form chemically sensitive, high-resolution, atomic number (Z^-) contrast images. When the electron probe is scanned

across the sample surface, Z-contrast images are formed by mapping the intensity of high-angle scattered electrons. It can provide crystal information and elemental composition at the atomic scale. The difference with SEM is that one has to prepare ultrathin specimens of 200 nm or less so that the accelerated beam of electrons passes through the sample. HAADF is a STEM method that receives thermal diffuse scattering or inelastically scattered electrons at a very high angle by an annular dark-field detector. In the HAADF image, the intensity is proportional from a square to 1.4 square of the atomic number, so this method is highly sensitive to variations in the atomic number of atoms in the specimen, where the light atoms are difficult to be observed and heavy atoms are observed brighter. (**Figure 2.3**)[272]
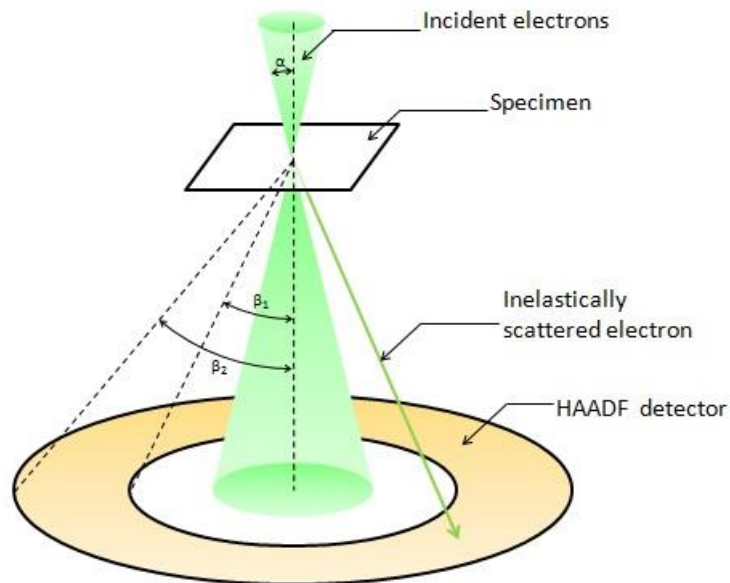
Figure 2.3. Relationship between the convergence semi-angle of the incident electron beam and acceptance semi-angles of the detector for HAADF-STEM.[272]

In the HAADF image, due to the small scattering cross-section of thermal diffuse scattering at high angles used for the imaging, no multiple scattering signals arise. Furthermore, the interference effect of electrons does not take place for non-interference imaging. For the dark-field imaging from traditional TEM, an objective aperture is used in order to collect scattered electrons that pass through the specimen. In a sharp contrast, the dark-field imaging formed by STEM uses an annular detector to selectively collect the scattered electrons rather than using an aperture to differentiate the scattered electrons from the main beam. Consequently, conventional dark-field imaging and STEM dark-field exhibit a different contrast mechanism.

2.2.4   X-ray photoelectron spectroscopy
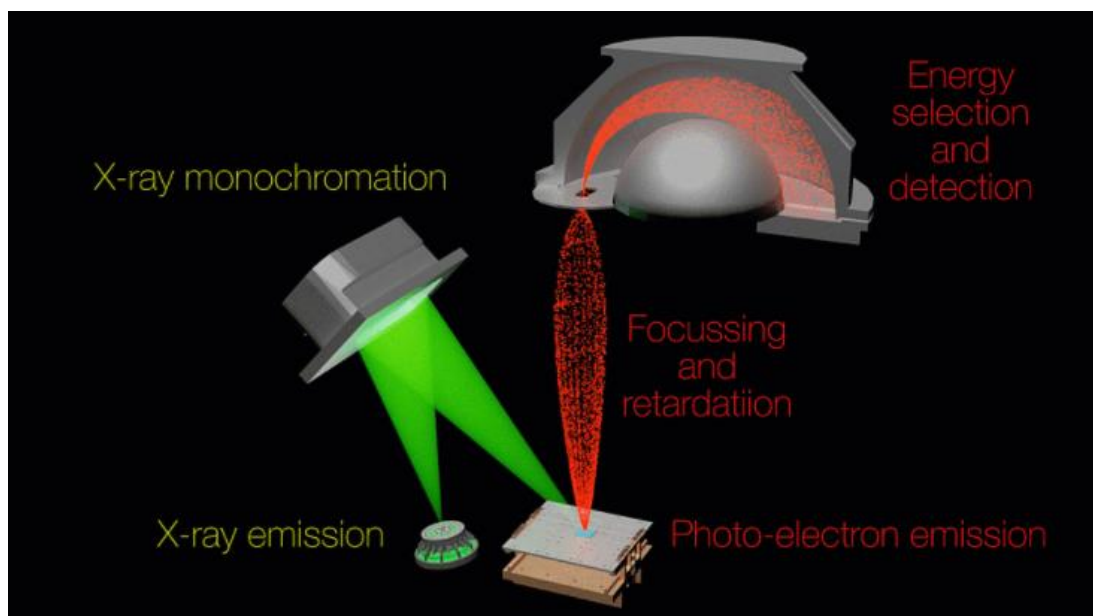
Figure 2.4. Schematic diagram of the working principle of XPS.

With the increasing demand for high-performance materials, surface engineering has an important role to play in chemistry, tribology, and physics. The surface of the material is the contact area with other materials and the external environment; therefore, many issues associated with advanced materials and different compositions can be solved by making full sense of chemical and physical interactions that occur at the interfaces of the surface. X-ray photoelectron spectroscopy (XPS) is an important technique used to explore surface chemistry characterization, which can measure the chemical state, electronic state, empirical formula, and elemental composition of each element within a material. For XPS spectra, a beam of X-rays are irradiating a solid surface and the kinetic energy of electrons is measured simultaneously, where the top 1-10 nm of the material is analyzed. (**Figure 2.4**) The photoelectron spectrum can be recorded by counting ejected electrons with a range of electron kinetic energies. The characteristic peaks appear in the photoelectron spectrum, which is generated by emitting electrons from atoms with a particular characteristic energy. The kinetic energy of the emitted photoelectron is measured and the atomic core level binding energy of the sample is determined by：

$$E_B = \hbar v - E_K - \Phi$$

Where the value of Φ is the work function depends on both the material and spectrometer, hv is the energy of the incident X-ray, E_B is the binding energy of the core electron, and E_K is the kinetic energy of the photoelectron as measured by the instrument. The intensities and energies of the characteristic peaks enable the quantification and identification of all surface elements (except hydrogen and helium).

An XPS spectrum can provide the relative frequencies of binding energies of electrons detected, which is measured in electron volts. Each element has a set of its own characteristic XPS peaks, which are attributed to the electron configuration of the electrons within the atoms, such as 1s, 2s, 2p, 3s, etc. The surface sensitivity of XPS makes it a valuable tool in the study of graphene, which can provide quantitative information such as the number of layers, functional groups, and identification of impurities. Some works use XPS to identify the formation of carbon materials from CVD growth processes and metal impurities, further exploring the chemical states on the surface of different carbon-based materials in approximate order of increasing binding energy, such as amine, alcohol, ketone, organic ester, carbide, silane, carbonate, monofluoro-hydrocarbon, trifluorocarbon, difluoro-hydrocarbon, and methylene/methyl/hydrocarbon.

Figure 2.5. The vacuum chamber for the XPS instruments.

During the sample preparation, the specimens that can be analyzed by XPS are all solids ranging from powders and films to frozen liquids including metal alloys, semiconductors, polymers, carbon-based materials, inorganic compounds, and many others. There are a few universally accepted methods for sample preparation in XPS. As a surface technique, the specimens are particularly susceptible to contamination, which needs to be prepared carefully. Gloves and clean tweezers must be used during the preparation process and any glassware must be thoroughly cleaned before use. Due to the ultra-high vacuum conditions, the volatile or loose material on the surface can contaminate the instrument. The most favored method for sample preparation is to fix the materials into clean Al foil by double sides adhesive tape and tablet press. Alternatively, Alternatively, the materials can be dissolved in an appropriate solvent, and the mixture is dropped on the surface of the silicon wafer. Then, the sample is pasted on the test bench. Magnetic and non-magnetic samples need to be separated in the different test benches. The preparation processes of Li metal anode and Na metal anode-based materials are finished in the glove box and transferred to the XPS instruments by a vacuum chamber. (**Figure 2.5**)

2.2.5 X-ray absorption near-edge structure

As a subset of X-ray absorption spectroscopy (XAS), X-ray absorption near-edge structure also has another name called the near-edge X-ray absorption fine structure (NEXAFS). XAS is a broadly used method to investigate the electronic, structural, and magnetic properties by using synchrotron radiation. In 1895, the X-ray is discovered by Wilhelm Röntgen via passing electrical currents through a partially evacuated glass tube, which is a penetrating form of high-energy electromagnetic radiation with a short wavelength between 0.01 and 100 Å. In general, any charged particle which moves in a curved path or is accelerated in a straight-line path will emit electromagnetic radiation. Synchrotron radiation is the name given to the radiation which occurs when charged particles are accelerated in a curved path or orbit. (**Figure 2.6**) A linear accelerator is first used to accelerate the charged particles, and then by a booster ring. During the accelerating, X-rays with a broad spectrum of energies are generated and emitted by the electrons, which are directed toward "beamlines" that surround the storage ring. Each beamline can be used and designed with a specific technique for different research.[273,274]
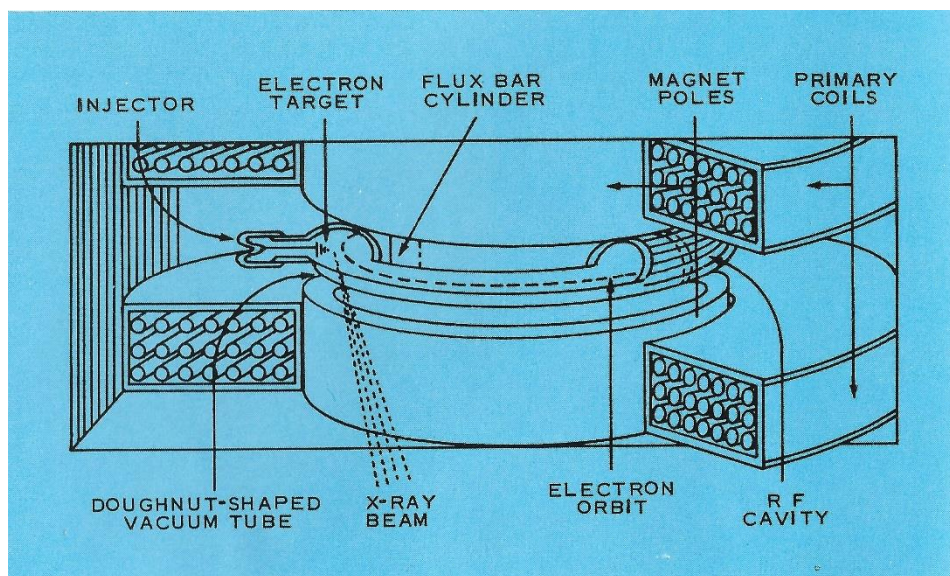
Figure 2.6. Scheme of a synchrotron and the particle trajectory inside it.
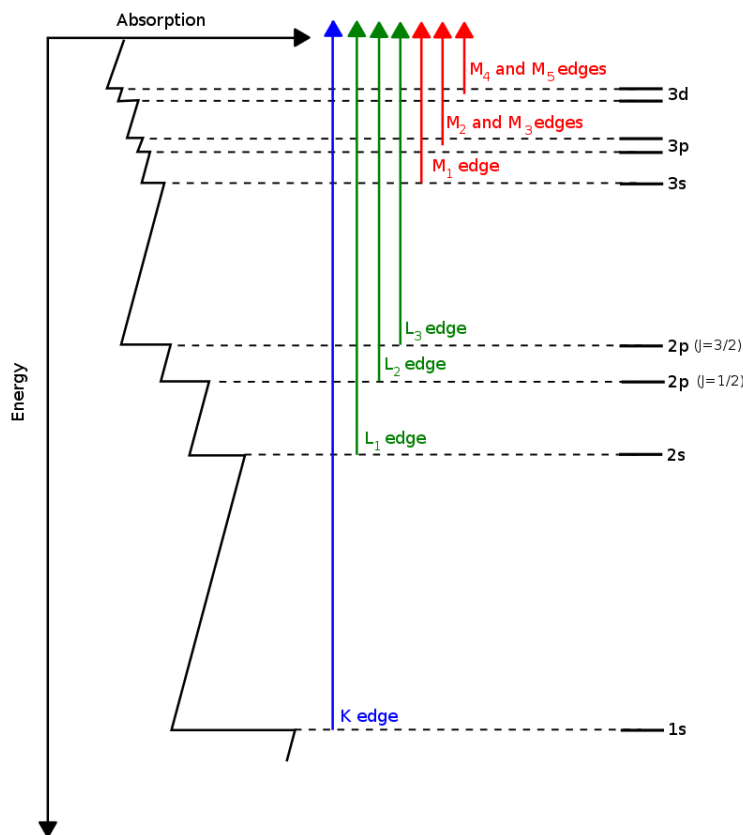
Figure 2.7. Transitions that contribute to XAS edges.[273]

Among them, the X-ray with the energy produced span 1000 eV or more is more suitable for XAS measurements. For XAS, the X-ray strikes an atom in the sample and excites a core electron, which is usually coming from the 1 s or 2 p shell with the energy of thousands of electron volts. (**Figure 2.7**) The wavelength of X-ray obtained at synchrotron facilities is on the same order of magnitude as atom-atom separation in molecular structure, so XAS can be used to deduce the local structure of atoms. XAS is also a useful tool to analyze materials based on their characteristic X-ray absorption "fingerprints", which can deduce the local atomic environment of each atom.

For XANES, it is a local bonding-sensitive and element-specific spectroscopic analysis, which can be used to determine the partial density of the empty states of a molecule and elucidate the local electronic structure of an atom. In XANES, the photon can be absorbed, and then, the electrons

41

are excited from the original core state to an empty state. The energy of the photon must be higher than or equal to the binding energy of a given core level to excite an electron, which will open a new absorption channel. The energy of an absorption edge is attributed to the energy of the core level, so XANES is an element-selective technique. The high oxidation-states are corresponding to short bond lengths in molecules, where the increasing of edge energies leads to the increasing of oxidation states. Due to its oxidation sensitivity, XANES can be used to determine the 3D structure of the absorbing atom to its environment. (**Figure 2.8**)
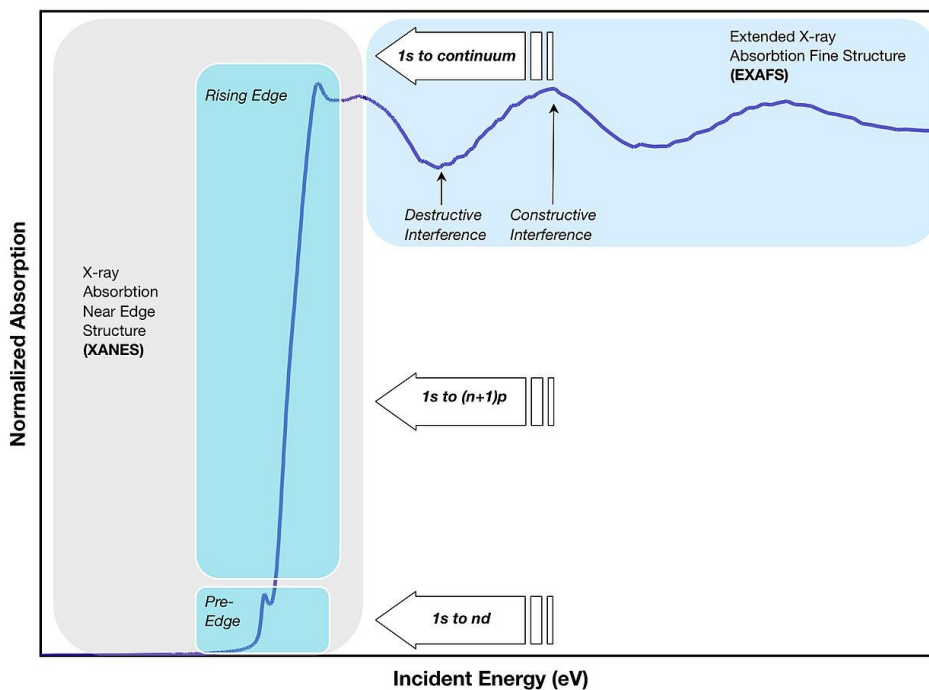
Figure 2.8. Three regions of XAS data.[273]

During the sample preparation process for XAS, the first method is using Kapton tape and a sample holder to prepare a homemade mold, as shown in **Figure 2.9a**. We should use the mortar to grind

the sample for more than 30 min to ensure our sample is a fine powder. After that, the sample holder is filled with powder. The powder is pressed by a spatula to ensure that the sample is as compact as possible. The second method is adding a solid sample on one side of the Kapton table, and then the sample is dispersed along with the Kapton table by one finger. The finger should be slid several times to apply pressure to form a uniform and complete covering film. (**Figure 2.9b**) We further use the tweezers to fold the film until obtaining 8 layers.
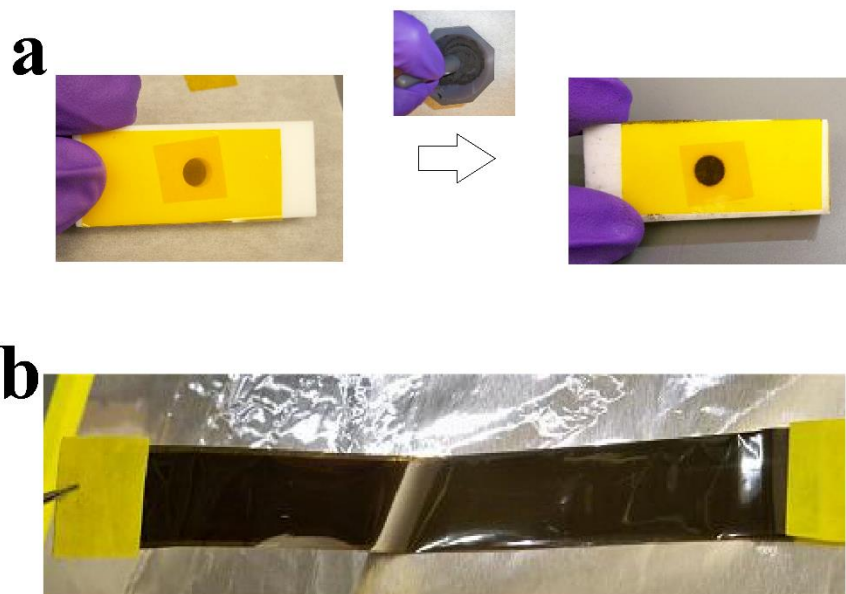
Figure 2.9 (a) The method for the sample preparation of solid materials. (b) The method for the sample preparation process by films.

2.2.6 Extended X-ray absorption fine structure
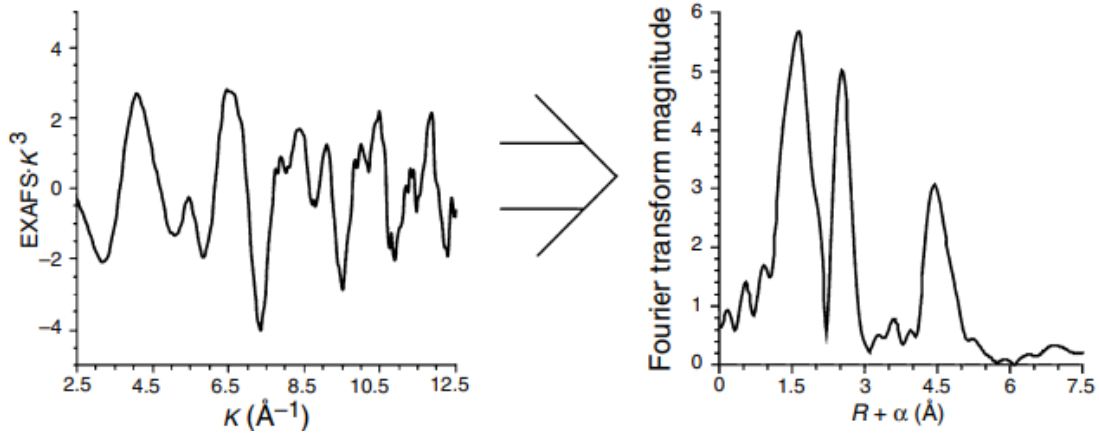
Figure 2.10. EXAFS data (left) and its Fourier transform (right). The Fourier transform clearly shows three distinct peaks, reflecting the presence of three distinct absorber-scatterer interactions.

Extended X-Ray absorption fine structure (EXAFS), along with XANES, is a subset of XAS. EXAFS can be used to analyze the structure and composition of the active surface species, such as the geometry and nature of ascorbates and coordination sites, which is based on the measure of the variation of the X-ray absorption coefficient for different materials. The X-ray absorption coefficient of a given specimen with a range energy of 500-1000 eV can be displayed by EXAFS spectra, which are usually normalized to unit step height. The wavelength of the photoelectron depends on the phase and energy of the backscattered wave, which exists at the central atom. The photoelectron has greater kinetic energy with a shorter wavelength at higher X-ray energy, leading to a local minimum and destructive interference in the photoabsorption cross-section. [273,274]

For the quantitative analyses, EXAFS can be described by an equation as follows:

$$x(k) = \sum_{s} \frac{N_S A_S(k) S_0^2}{k R_{as}^2} \exp(-2R_{as}/\lambda(k) \exp(-2k^2 \sigma_{as}^2) \cdot \sin(2kR_{as} + \emptyset_{as}(k))$$

44

Where the R_{as} is the absorber-scatterer distance, N_S the number of scattering atoms is, $\emptyset_{as}(k)$ is the phase shift, and $A_S(k)$ is the energy dependence of the photoelectron scattering. The above equation provides a complete description of EXAFS oscillation, but cannot provide a particularly convenient way to reveal the information content of a spectrum, where Fourier transformation can be used to decompose a k-space signal into its different constituent frequencies. (**Figure. 2.10**) In 1971, Sayers et al. exhibited that Fourier transformation is a mathematical transform and results in a radial distribution function, as follows:

$$\text{FT(R)} = \frac{1}{\sqrt{2\pi}} \int_{k_{min}}^{k_{max}} k^n x(k) e^{i2kR} dk$$

Since the Fourier transform is a complex mathematical function, both imaginary and real parts can be obtained, where the imaginary parts are very important for the analysis of EXAFS data with an accurate determination of the discovery of unknown contributions and absorber-scatterer distance.

2.3 Electrochemical measurements

2.3.1 The preparation of the electrode

The preparation of the alkali metal anode in this thesis was based on electrochemical deposition. Electrochemical deposition, known as electroplating, is regarded as a simple and powerful method, which can accumulate one material onto the surface of another material by the repeated oxidation and reduction reactions. The appropriate electrode and electrolyte are extremely important during the electrochemical deposition process, where no electrochemical reaction will occur if we choose the wrong materials. Also, the polarity of the electrodes must be correct, linking to the corresponding positive and negative terminals.

During the electrochemical deposition process, the reference electrode, counter electrode, and working electrode are dipped into the electrolytic solution. Then, the electricity is introduced to the system through the electrodes, and the ions of the deposition material in the electrolyte or

stripped from the counter electrode adhere to the working electrode via oxidation and reduction reaction. This process can achieve very strong bonds between two materials, and the thickness of the deposited layer can be controlled by the time and current density. There are two main reasons to use the electrochemical deposition process:

1. Low cost and aesthetic appeal. The direct use of some metals is very expensive. One way to obtain a cheaper metal with a similar look to the noble metal is to plate it with a thin layer of platinum, silver, or gold, which is very common in the jewelry industry.

2. Protective layer. Many automotive components are made of Zinc-plated steel, where the surface of the steel component is uniformly coated by a Zinc protective layer using the electrochemical deposition process.
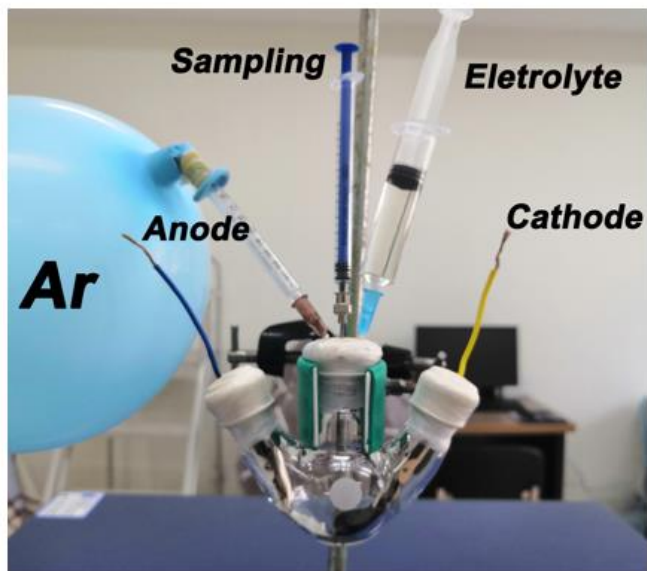
Figure 2.11. The homemade electrolytic tank for the preparation of alkali metal anode.

Here, in my thesis, we use a two-electrode system to prepare the alkali metal anode. (**Figure 2.11**) The different current collectors are used as the working electrode, and the bare Na foil and Li foil are servicing as the counter electrode. It is suggested that all of the electrochemical deposition processes are carried out in a high purity argon-filled glove box, which can effectively suppress the side reactions caused by moisture, nitrogen, and oxygen. Also, we can assemble the working electrode and counter electrode in a CR2032-type coin cell in the glove box filled with argon, and use an electrochemical workstation to realize the electrochemical deposition. After electrochemical deposition processes, the prepared Li/Na metal anodes are washed by PC, EC, DME, or DOL solvents, and dry thoroughly in the glove box.

Figure 2.12 The photograph of the mixing hollander and planetary ball mills in our lab.

The preparation of cathode in this thesis was based on my previous works. Firstly, the active material, the conductive acetylene black, and the binder (polytetrafluoroethylene, 60 wt% dispersion in water) in a ratio of 8:1:1 is added in the agate mortar with the continuous grinding for more than 30 min. Then, NMP as the solvent is dropped in the mixture to prepare the ink. The mass fraction of solid in ink is depending on the nature of the binder and solvents. Another way to prepare the ink is using mixing Hollander or planetary ball mills at 400 r/min for more than 2 hours. (**Figure 2.12**). Finally, the ink is added on one side of the coating machine using bare aluminum foil as the current collector. The thickness of the coating layer is 25-100 μm, and we can change the loading of active materials by increasing the height of the doctor blade. (**Figure 2.13**) For example, the height of the doctor blade is 300 μm, leading to a dry residue with a thickness of ~70 μm. The area capacity of the electrode is about 2.0-4.0 mAh cm^{-2}. To remove the N-methyl-2-pyrrolidone from the ink, the electrode needs to dry at 100 °C in a vacuum oven for more than 48 hours. The moisture in the electrode can lead to the decomposition of the electrolyte, further reducing the cycling performance of the battery. Finally, the electrode is cutting by the slicer in the form of a small wafer. (**Figure 2.14**) The electrodes are finally weighed, listed, and stored in an argon-filled glove box. The mass of the bare current collector is subtracted from the measured mass of the electrodes in order to calculate their grammage.

Figure 2.13. The coating process of the ink by the coating machine using Al foil as the current collector.
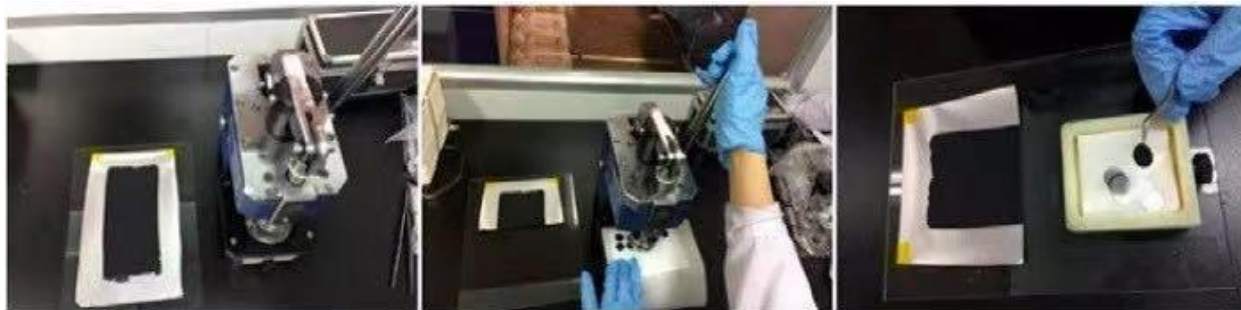
Figure 2.14. The cutting processes of the electrode.

2.3.2 The assembly of the battery

In this thesis, we mainly use the CR2032-type coin cell and CR2025-type coin cell to assemble the Li metal batteries and Na metal batteries. In the market, the CR2025 cell is a lithium coin that is 20mm diameter x 2.5mm thickness. Both CR2025 cells and CR2032 cells have a high working voltage of 3V. CR2032 cell has a capacity of 225mAh, while the average CR2025 can nominally only deliver 160mAh. A CR2032 cell is a non-rechargeable lithium coin that is 20mm diameter x 3.2mm thickness, and the CR2032 is the most common lithium cell battery. In terms of technology, both CR2025 cell and CR2032 cell have the same voltage, chemistry, and diameter, which can be used to power small devices like laser pens, smart carport keyless entry devices, toys, and calculators. The obvious difference between the two cells would be the thickness, where the CR2032 cell is 0.7mm thicker than the CR2025 cell. Here, both CR2025-type and CR2032-type coin cells can be used for the assembly of Li metal batteries, buy Na metal batteries only use CR2032-type coin cells before sealing.

During the assembling, the prepared cathode electrode, obtained as described in section previous, is affixed in the middle of the positive electrode and covered the button cell by a drop of the corresponding electrolyte. (**Figure 2.15**) Then, a polypropylene separator (Celgard®2400, 25 µm) is fully covered by the whole positive cover, and the electrode is soaked by 100 µL electrolyte. A disc of metallic lithium anode is then deposited in the middle of the separator, which is acting as the reference electrode and the counter electrode. A stainless steel shim is further added on the

metallic Li anode side with a total thickness of more than 1.5 mm. A stainless steel spring is added in order to maintain the contact and pressure of the different components in the cell. Finally, the cell is transferred to the sealing mold by the anti-static tweezers, and the cell is sealing under the pressure of 800 MPa for more than 5 seconds. (**Figure 2.16**) The packaged cell needs to be aged for more than one days before testing. If the voltage between the two sides is near 0 V, the cell is a short circuit.

Figure 2.15 The assembling process of Li-ion battery based on a CR2032-type coin cell in an argon-filled glove box.

Figure 2.16. The finally sealing process of the Li-ion battery is based on a CR2032-type coin cell in an argon-filled glove box.

2.3.3 Polarization properties

In electrochemistry, the performance of the alkali metal battery is limited by the polarization properties of the alkali metal anode. Polarization is defined as the collective term of mechanical side-effects during the electrochemical process caused by the barriers at the electrolyte-electrode interface. These side effects critically affect the reaction mechanisms, as well as metal deposition and the chemical kinetics of corrosion. The ideal polarizable electrode is the electrode where no charge transfer occurs across the electrolyte-electrode interface. Actually, we cannot find any ideal polarizable electrodes in the battery system. When a faradaic current passes through the cell, the departure of the electrode potential from the equilibrium value is called polarization.[275] The extent of polarization can be measured by the overpotential, as follow：

$$\eta = E - E_{eq}$$

The polarization curves are the current-potential curves obtained under steady-state conditions. Polarization can be divided into three categories:

1. Ohmic polarization. Ohmic polarization or ohmic drop or IR drop (ΔE_{ohm}) is referred to the resistance of the media during the flow of electrical current through the cell.

2. Electrochemical polarization. Electrochemical polarization is measured in the range of millivolts (mV) or volts (V) by galvanostatic plating/stripping processes, which is also called cathode polarization. The negative variation is caused by the movement of electrons, which should be consumed in the reaction and transfer toward the cathode.

3. Concentration polarization. Concentration polarization occurs when the concentration of a specific component is increasing or decreasing at the boundary layer close to the membrane surface due to the selective transport through the membrane.
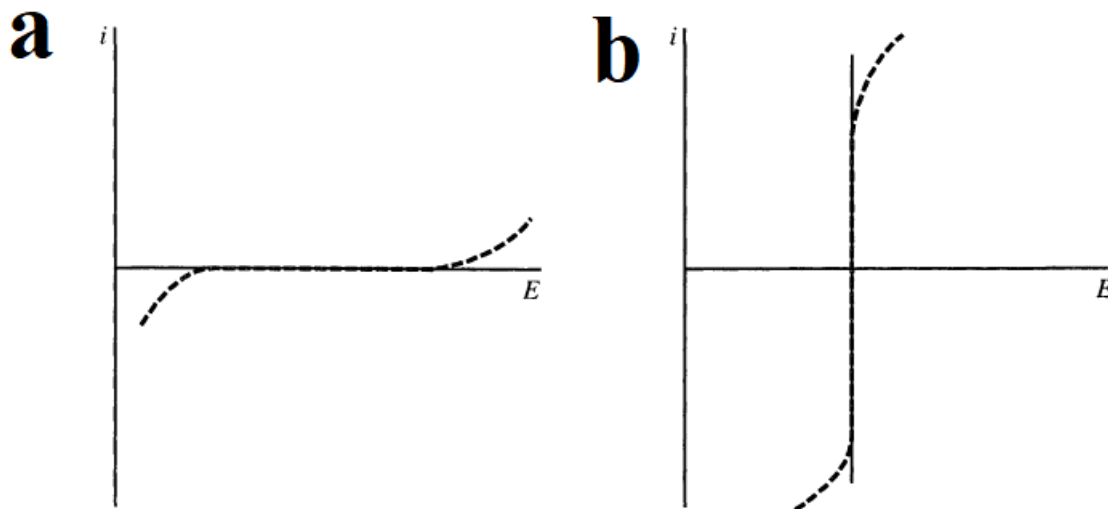
Figure 2.17. Current-potential curves for ideal (a) polarizable and (b) nonpolarizable electrodes. Dashed lines show the behavior of actual electrodes that approach the ideal behavior over limited ranges of current or potential.

Another important index is nucleation overpotential. Electrochemical deposition of an alkali metal onto an appropriate conductive current collector usually occurs by an island growth mechanism. The key characteristics during island growth for Li/Na ions (M) on a conductive substrate (S) are that the onset potential for deposition is shifted negative from the equilibrium potential for the metal ion couple. The nucleation overpotential can be defined as:

$$\eta_n(M^+/S) = \left| U_n(M^+/S) - U_{eq}(M^+/M) \right|$$

The value of nucleation overpotential is proportional to the nucleation barrier, which is a fundamental limitation to achieving control of island shape.[275] If the value of nucleation overpotential is less than 100 mV, the island growth can proceed under kinetic control and the island shape can be controlled. If the value of nucleation overpotential is more than 100 mV, island growth after nucleation is very fast. The diffusion of island growth is limited and the island shape cannot be controlled. In this case, the instabilities during the growth can lead to deposit fast on the protuberances, further promoting the growth of dendrites.

In this thesis, the polarization curves were measured by the repeated galvanostatic charging/discharging processes at the same time. The overpotential is calculated by the difference between 0 V and peak voltage of charging or discharging curves. Here, the symmetric cells were used to study the alkali metal stripping/plating behaviors by assembling two identical alkali metal anode into 2,032-type coin cells. For symmetric cells, they have the same alkali metal anode as the negative electrode and positive electrode, where the average voltage of these cells is zero. Symmetric cells can give vast information about reactions between electrode materials and electrolytes.

2.3.4 Electrochemical resistance

A simple battery system includes three different parts: the electrolyte, a negative electrode, and a positive electrode, which is used to transfer the metal ions. The current will be generated in the

battery due to the different dissolving efficiency between positive and negative electrodes in the electrolyte. The dissolved atoms enter the electrolyte in the form of the positive ions, leaving some excess electrons on the electrode. When a wire is used to connect the cathode and anode outside the battery, the generated electrons redistribute themselves and some of them flow through the wire to another side, thereby producing an electric current. All conductors intrinsically have some resistance built-in, and all the batteries are no exception. If a voltage is placed between the ends of the electrode, a current will flow through the electrode, which is proportional to the magnitude of the voltage. In 1826, Ohm came up with Ohm's law to describe this behavior:

$$V = I \times R$$

Where R is the resistance, I is current, and V is the voltage. If we use the superconductor as the electrodes, the device will get the voltage directly. This is the idealistic case, and it doesn't occur in real life. The voltage is dropped across the element when the battery is powering, rather than voltage drop by the battery itself. According to Ohm's law, the higher the resistance, the greater the voltage drop. The electrolytes and electrodes are not 100% conductive, so all of them have resistances.[275] The resistance of the 3.6 V Li-ion battery is 320 mΩ.

In my thesis, I use the electrochemical impedance spectroscopy (EIS) measurement system to measure the resistances of different alkali metal batteries and full cells. (**Figure 2.18**) In my opinion, EIS is a multi-frequency AC electrochemical measurement technique, which measures the value of the resistance in a wide range of frequencies from 1 MHz to 10 kHz by the external field's interaction with the dipole moment. We use the Nyquist plot to represent the information obtained from the EIS measurement, where curves are plotted according to the negative imaginary component of impedance (y-axis) and the real component of impedance (x-axis). In the Nyquist plot of an ideal battery,(**Figure 2.19**) we can see that the R_b, R_{SEI}, R_{CT}, and W is corresponding to the SEI resistance, internal resistance, Warburg impedance, and charge-transfer resistance.

R_b. R_b is the internal resistance value of the bare materials in the cell, including the current collector, separator, and electrolyte, which can be observed in the Z-real. The internal resistance can not be changed with the state of charge, but the internal resistance increases as temperature drops or the continuous cycling, due to the formation of micro-crack on the electrode and the consumption of the electrolyte.

R_{SEI}. R_{SEI} is the SEI resistance, where the first semicircle in the EIS spectrum is defined as the SEI resistance. SEI layer plays an important role in electrolyte consumption, cycling stability, Coulombic efficiency, and battery safety. During the charging process, the Li ions are moving from the cathode to the anode through the electrolyte. When electrolyte contact with anode materials and Li-ions, the reactive elements in the electrolyte undergo reductive reactions due to the thermodynamically and electrochemically instability of the electrolyte. The decomposition of lithium salts and electrolytes leads to the SEI layer's formation at the surface of the anode, accompanied by an irreversible loss of Li ions. Li-ion can diffuse and migrate through the SEI layer, but the SEI layer is impermeable to electrolytes and electrons. By monitoring the SEI resistance, we can observe the reversible formation of the SEI layers as well as identify the characteristics of the SEI layer.

R_{CT}. R_{CT} is the charge transfer resistance, which can be measured by the difficulty encountered when an electron is shifted from one compound or atom to another compound or atom. R_{CT} can be used to investigate the kinetics of the electrochemical reaction, which can be changed by the particle size, bandgap structure, phase transition, and surface coating. Monitoring the charge transfer resistance can help us to understand electrode reaction processes during the cycling processes and detect the affiliation between temperature and performance of Li-ion batteries.

W. W is the Warburg impedance, which is represented by the straight line after the semicircles and associated with the diffusion process of Li ions in the electrode. In principle, the angle of the straight line is equal to 45 degrees. Sometimes, we can see it is not 45 degrees, caused by the roughness of the electrode, state variables of electrode potential, and induce inductive resistance. Ho et al used the following equation to calculate the Li-ion diffusion speed.

$$D_{Li^+} = \frac{1}{2}\left[\left(\frac{V_M}{SF\sigma}\right) \times \left(\frac{\partial E}{\partial x}\right)\right]^2$$

where the V_M is the mole volume of active material, σ is the slope of Zimg vs. $1/\sqrt{2}\pi f$, S is the contact area between electrode and electrolyte, F is the Faraday constant, and $\partial E/\partial x$ is the slope of the straight line after the semicircles.
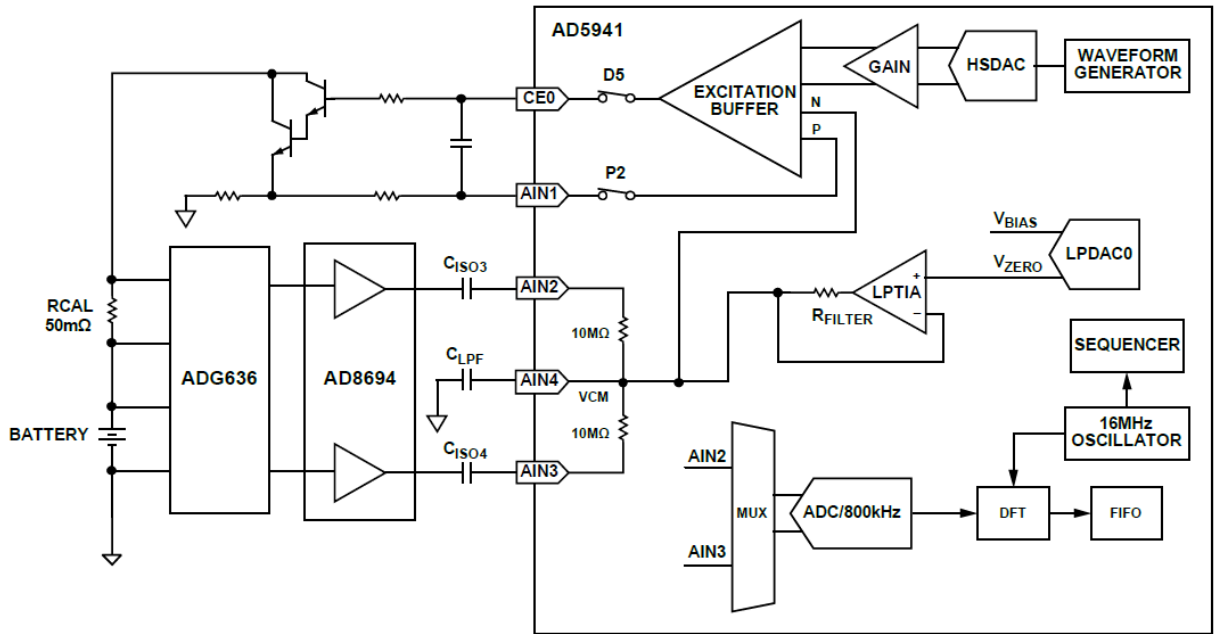
Figure 2.18. Simplified circuit block diagram of electrochemical impedance spectroscopy measurement system.
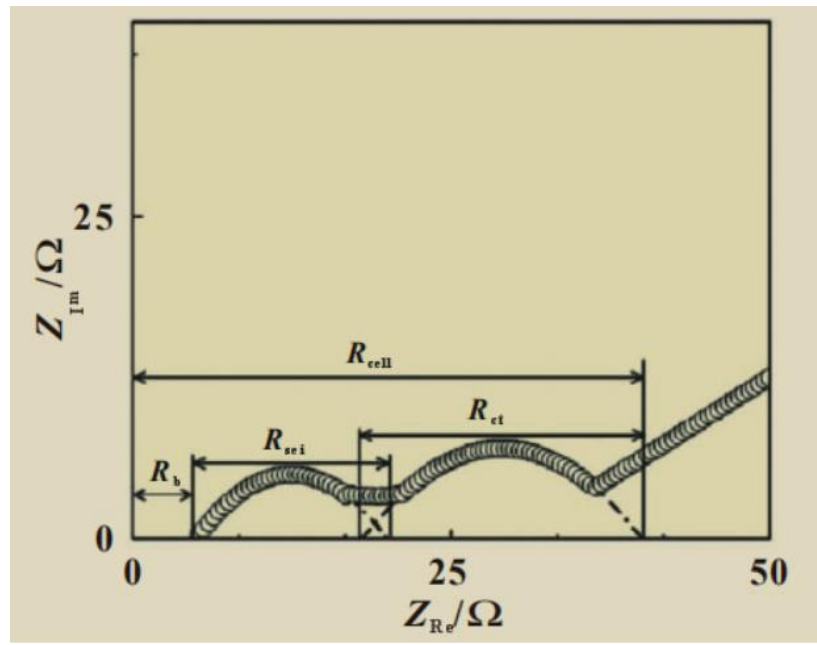
Figure 2.19. Nyquist Plot for an ideal Li-ion battery.

2.3.5 Lithium deposition behavior

Understanding the nucleation and deposition mechanism of alkali metal is essential for providing long cycle life and safe alkali metal batteries. Electrochemical deposition of Li/Na metals onto foreign substrates (such as Cu foil and carbon-based substrates) usually occurs through Volmer-Weber island growth. Volmer-Weber island growth is used to describe a mode of thin-film growth, when the atoms of a film are more strongly bonded with each other than with the substrate. In this case, 3D islands nucleate and grow on the surface. For example, during the depositing processes, the first deposited atom undergoes a random walk on the surface of the substrate. For the second deposited atom, it will first undergo a random walk and eventually meet the first atom. Due to the high mass, they will form a particle with a lower random walk velocity. (**Figure 2.20**) Subsequently deposited atoms will meet and bond with the particle, further increasing its mass, size, and stability, where these atoms are stacked like an island. During the island growth, if we increase the rate of deposition, a larger island will form. When atoms are meeting together, they will bond to their nearby atoms before migrating to a distant island. With Volmer-Weber island growth, the thickness of the islands increases before full coverage of the first layer is reached.[276-279]
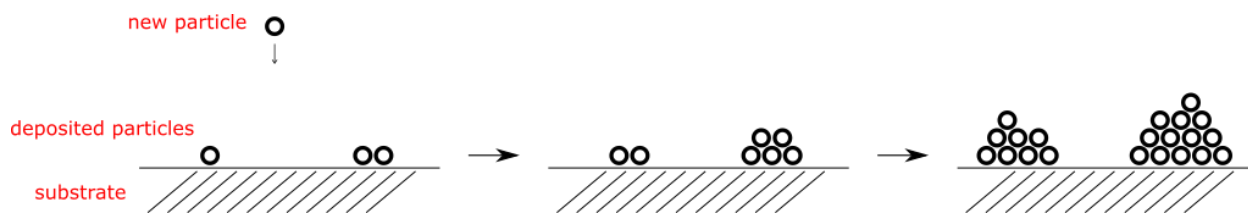
Figure 2.20. Schematic illustration of Volmer-Weber island growth.

Take lithium as an example, it is well known that Li-ions are first to close to the surface of the anode, go through the SEI layers, and react with metallic Li on the surface of the anode by a reduction reaction to form metallic Li. This reduction reaction is strongly dependent on the SEI

layer, Li-ion ionic conductivities of the electrolytes, the plating sites, and the electric conductivity of electrodes. From the first step in **Figure 2.21**, the huge volume expansion during the first Li plating processes can rupture the weak SEI layer, resulting in the growth of the dendritic structure in the cracks. According to the Volmer-Weber island growth, Li ions are inclined to deposit on the tips of the cracks, where Li dendrites will form on the surface of the anode. During the Li stripping process in the third step, Li ions are back to the cathode, and the volume contraction of the deposited layer further fractures the SEI layer, while stripping from kinks in the Li dendrite or from its roots can break the electrical contact with Li metal anode and produce dead Li. After continuous Li plating and stripping processes, the repeated process can produce a thick accumulated SEI layer, a porous Li electrode, Li dendrite structure, and dead Li, further leading to capacity fading, safety hazard, and blocked ion transport.
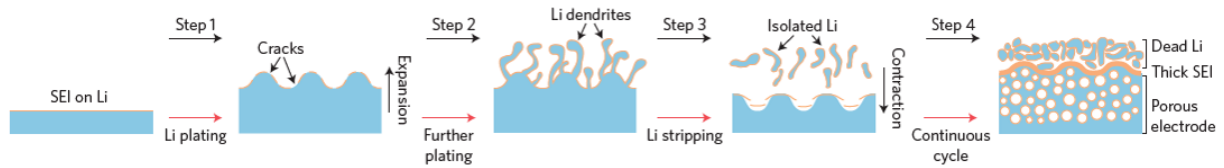
Figure 2.21. The formation of Li dendrites and dead Li during the plating process. Copyright 2017 American Chemical Society.

A fundamental mechanism for the growth of dendritic structure has further been proposed, where the growth of Li dendrite is a common occurrence during the electroplating process at a high current density. During the electroplating, a Li-ion concentration gradient can be found in the electrolyte, where a simple ambipolar diffusion equation can be used to detect the evolution of ionic concentrations:

$$\frac{\partial C}{\partial x}(x) = \frac{J\mu_a}{eD(\mu_a + \mu_{Li^+})}$$

Where μ_a is the anion mobility, μ_{Li^+} is the Li-ion mobility, J is the effective electrode current

density, D is the ambipolar diffusion coefficient, and e is the electronic charge. In the case of d_C/d_x < $2C_0/L$, the ionic concentration at the anode exhibits a steady-state with constant electrostatic potential value and concentration gradient. The deposition of Li ions on the substrate is very smooth. If d_C/d_x > $2C_0/L$,(**Figure 2.22**) the ionic concentration on the surface of Li metal anode drops to zero, the current of the system can only be sustained for a certain period, and the potential will eventually diverge at this period, where this period is called Sand's time (τ):

$$\tau = \pi D \frac{e^2 C_0^2 (\mu_a + \mu_{Li^+})^2}{4J^2 \mu_a^2}$$

$$t_a \approx 1 - t_{Li^+} = \frac{\mu_a}{\mu_a + \mu_{Li^+}}$$

Where t_a is the anionic number and t_{Li+} is the Li$^+$ transference number. When tested at a high current density, Li-ions become depleted in the electrolyte and the corresponding concentrations exhibit different behaviors, which break the electrical neutrality at the surface and lead to excessive positive charge at the anode. This builds up a local space charge inducing a large electric field and leads to the growth of Li dendrites.[276-279]
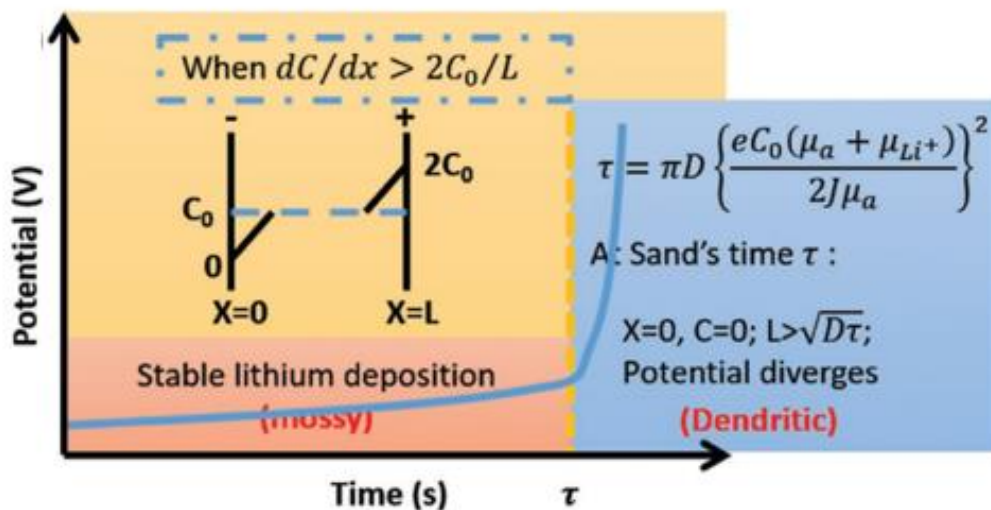
Figure 2.22. Classical mathematical model for time-dependent lithium deposition. Copyright 2018 Royal Society of Chemistry

2.3.6 Coulombic efficiency

Coulombic efficiency, also called current efficiency or faradaic efficiency, shares a direct relationship with battery efficiency. Coulombic efficiency is used to describe the charge efficiency, where electrons are transferred back and forth in the batteries. The high Coulombic efficiency means longer cycling stability or cycling life of the battery. Coulombic efficiency is also defined as the ratio between the total charge extracted from the battery and the total charge put into the battery over a full cycle.

$$\text{Coulombic efficiency} = \frac{Discharge\ capacity}{Charge\ capacitu}$$

$$= \frac{Total\ number\ of\ e^-\ back\ to\ cathode}{Total\ number\ of\ e^-\ departing\ from\ cathode}$$

$$= \frac{Total\ number\ of\ Li\ ions\ back\ to\ cathode}{Total\ number\ of\ Li\ ions\ departing\ from\ the\ cathode}$$

In an ideal cell, no side reactions will happen on the electrodes, the Coulombic efficiency is 100% and the flow of Li ions or electrons is finished through the reversible electrochemical reactions. In realistic cells, the side reactions cannot be avoided, and irreversible electron loss and decomposition of electrolytes will lead to the decline of Coulombic efficiency.

In some battery systems, the initial Coulombic efficiency is very low, which is caused by the decomposition of electrolytes, activation process, and the formation of SEI layers. The low initial Coulombic efficiency can be compensated by the additional loading of cathode materials. The initial Coulombic efficiency is a key parameter for the improvement of the redundant cathode in the full cells, which is associated with the amount of the cathode. In conventional LIBs, the specific capacity of the cathode is lower than that of the anode, so an excessive amount of cathode in the electrode must be chosen before assembling the battery, leading to an appreciable reduction of energy density. All batteries experience efficiency losses as they age. The remaining capacity in the cell after certain cycling can be effectively estimated by using the following method.

$$\text{Capacity retantion} = (Coulombic\ efficiency)^n$$

where n is the cycling number. If a cell cycled 1000 cycles delivered the capacity retention of 90%, the averaged Coulombic efficiency would be 99.99%.

Li/Li cells
Li stripping/deposition controlled by time

Li/Cu cells
Li stripping driven by over potential

Anode-free cells
Add cathode factor

Li/NMC cells
Add Li and electrolyte factor

Electrochemical window: N/A; the same capacity control for deposition and stripping
CE:
1. 100% but not meaningful
2. Over potential/polarization is affected by the electrolyte amount and Li deposition capacity
3. Useful to evaluate separator membranes and so on, if all other testing parameters at relevant scales
4. True for all symmetric metal cells, for example Mg/Mg, Zn/Zn cells.

Electrolyte: 75 µl
Cathode loading: None
Li anode: 50 µm
Li deposition: 4 mAh cm^{-2} (~20 µm)
Electrochemical window: Capacity-controlled Li deposition Li stripping till voltage >1 V
CE: Basic assessment of electrolyte properties, anode structure and interface stability.

Electrolyte: 75 µl
Cathode loading: 4 mAh cm^{-2}
Li anode: None
Electrochemical window: 2.7–4.4 V for NMC622
CE:
1. Usually low and represent the 'worst' cycling scenario of Li metal cells
2. Corresponds to minimum cycling number of LMBs
3. Estimate cycle life if SEI impedance is not high

Electrolyte: 75 µl then reduce to 13 µl
Cathode loading: 4 mAh cm^{-2}
Li anode: 50 µm
Electrochemical window: 2.7–4.4 V for NMC622
CE:
1. Higher than in anode-free cells but varies with electrolyte amount
2. Higher CE is necessary to achieve a longer cycle but cell life prediction is still not precise
3. If lean (13 µl) electrolyte is used, the results are close to those in realistic high-energy LMBs
4. Minimization of the dead volume in coin cells is needed when using lean electrolyte to ensure fully utilization of limited electrolyte content.

Figure 2.23. A coin cell protocol to measure and interpret Coulombic efficiency in Li metal batteries, where CE is defined as Coulombic efficiency.

In our thesis, CR2032-type coin cells were used as the battery case, which is assembled with Li/Na foil, Celgard separator, 80 mL electrolyte, and different current collectors. In the Li-based battery, the electrolyte is 1 M LiPF$_6$ in DEC/EC (1:1 by volume). To avoid the influence of side reactions and remove surface contamination, the galvanostatic discharging and charging processes between 0.01 V and 1.0 V (versus Li$^+$/Li) for 2-5 cycles were used to activate the different substrates. Then, different amounts of Li metal were deposited in the corresponding current collector and stripped with a cut-off voltage of 1.0 V during the repeated cycles. (**Figure 2.23**) In the Na-based battery, we choose 1 M NaClO$_4$ in DMC/EC (1:1 by volume) with 5 wt % FEC as the electrolyte. After the activated process of one galvanostatic discharging and charging process at a current density of 0.5 mA cm^{-2} between 0.01 V and 0.5 V (vs. Na$^+$/Na), a fixed amount of Na was plated onto the current collector and stripped with a cut-off voltage of 0.5 V during the repeated cycles.

2.3.7 Galvanostatic measurements

Galvanostatic measurements are an experimental technique, where a small constant current is imposed on the working electrode. The anode and cathode are often assembled in a coin cell, pouch cell, or flooded cell. The galvanostatic measurements can be used to measure the electrochemical reactions and corrosion rate. As an electrochemical measuring mode, the galvanostatic mode can be used for electrochemical analysis and the determination of electrode reaction kinetics and mechanisms based on the control of the current flowing through the battery system. The corrosion rate measurements, linear polarization measurements, and Tafel curves can be measured by this galvanostatic method. For the full cell, galvanostatic cycling performance is used to evaluate the Coulombic efficiency, specific capacity, average voltage, and capacity retention, where the Coulombic efficiency represents the reversibility of the reaction and average voltage represents the Gibbs free energy of the reaction. In the galvanostatic cycling tests, a constant current is applied to drive an electrochemical reaction, followed by a reverse current to drive the reverse reaction.

In my thesis, the Li-based full cells are assembled by CR2025-type coin cells with different cathode and Li metal anode in the glove box. The electrolyte was $LiPF_6$ in DEC/EC (1:1 by volume). For the Na-based battery, the full cells are assembled by CR2032-type coin cells with the different cathode and Na metal anode, and the electrolyte is 1 M $NaClO_4$ in DMC/EC (1:1 by volume) with 5 wt % FEC. The working voltage ranges for the LCO, LFP, LMO, NCM (1:1:1), and NCM (8:1:1) electrodes are 3.0-4.45 V, 2.5-4.0 V, 3.5-4.3 V, 2.8-4.6 V, and 3.5-4.9 V with a theoretical capacity of 274, 170, 148, 280, and 147 mAh g^{-1}, respectively.

3 SECTION I. Lithium dendrite inhibition via 3D porous lithium metal anode accompanied by inherent SEI layer

Over the past four decades, the Li-ion batteries, as one of the most advanced rechargeable batteries, are attracting much attention. The demand for Li-ion batteries increases rapidly, especially with the demand for electric vehicles. The use of Li-ion batteries to power electric vehicles calls for greater battery cycle life and higher energy density than their applications in portable electronic devices.[158] Recently, the energy density of conventional Li-ion batteries (such as graphite/LiFePO$_4$ cell and graphite/LiNiCoMnO$_2$ cell) in the market has increased from 80 to 300 Wh kg^{-1}, approaching their physicochemical limits. To increase the energy densities, metallic Li has been regarded as one of the most promising anode candidates for Li-ion batteries due to its extremely low redox potential (-3.04 V vs S.H.E.) and high theoretical capacity (3860 mAh g^{-1}).[159-165] Unfortunately, the practical application of Li anode has long been plagued by the unstable SEI layer, the large volume change, the inhomogeneous Li deposition, and uncontrollable dendrite growth during stripping/plating processes. Moreover, the growth of Li dendrites gives rise to internal short circuits and safety hazards.[170-188]

To solve the above issues of Li metal anode, great efforts have been made to prevent the growth of Li dendrites and tolerate large volume changes. Some works focus on three-dimensional (3D) porous current collectors to prevent the formation of Li dendrites. The large specific surface area of the 3D skeleton enables uniform distribution of positive charges. The 3D structure can accommodate Li during the plating process, alleviate the huge volume change, and suppress the dendrite growth.[280-295] For example, some works use 3D porous copper (Cu)-based substrates as the current collector, where a large and highly electroactive area can promote the uniform nucleation and deposition of Li metal.[286-289] However, the price and weight of the 3D Cu current collector are higher than Cu foil, resulting in high packing cost and low energy density. Recently, the development of the electrolyte components and additives has been considered as a feasible route to stabilize the SEI layers and homogenize the Li-ion flux during the plating process. However, the obtained SEI layers still cannot accommodate the morphological change during the repeated stripping and plating processes. Therefore, some artificial SEI layers as the mechanical barriers and passivation layer have been explored to inhibit the Li dendrite formation. [173-177]

In this chapter, we report a 3D Li metal anode with porous foam structure accompanied by an artificial SEI layer (inherent LDBS layer) as the Li metal anode (LMFS), realizing orientated and mitigated growth of lithium dendrites. The porous matrix served as a rigid backbone results in uniform charge distribution and thus orients the Li deposition. The LDBS layers as the stable SEI layer can prevent the formation of Li dendrites and side reactions. Moreover, the LMFS anodes exhibit excellent electrochemical performance when coupled by $LiNiCoMnO_2$ cathode with a high active material loading of 20.4 mg cm^{-2}. Besides, our prepared Li metal anodes enabled a high-performance deeply cyclable property with high area capacities up to 20.0 mAh cm^{-2}. A stable long-term plating/stripping process with low voltage hysteresis over 350 hours can be revealed by the symmetric cells, further demonstrating that our strategy can greatly inhibit the dendrite growth, minimize the electrolyte decomposition, and suppress the gassing process. These results shed fresh light on the 3D porous substrate and inherent dense SEI layer for stable Li metal anode, especially after further improvement and innovation.

3.1   Preparation of LMFS

The 2D planar Li metal was obtained from China Energy Lithium Battery Co., Ltd. Firstly, Li metal was scrubbed by the fine-tooth comb to remove the influence of the side effect product. For the preparation of the LMFS electrode, bare Li foil was immersed into the 10 ml solution of DBSA (a mixture of isomers, ≥95%) for 24 hours, and the produced bubbles were removed via vacuum treatment. The obtained LMFS anodes were washed with Propylene carbonate (anhydrous, ≥99.7%) and further dried at 50 °C in a glove box for 12 h.

3.2 Material Characterization and electrochemical measurements

The composition, morphology, and microstructure of Li metal anode were first examined using field emission SEM imaging and EDS mapping analysis by the SU8010, Hitachi, Ltd. X-ray photoelectron spectroscopy (XPS) was used for analyzing the surface chemistry of SEI layers. The XPS analysis was performed on Thermo ScientificTM ESCALAB 250Xi X-ray photoelectron spectrometer microprobe.

For cathode, the $LiNiCoMnO_2$ (80 %) were mixed with polyvinylidene difluoride (PVDF, 10%) and carbon black (10%) in N-methyl-2-pyrrolidone (NMP). The $LiNiCoMnO_2$ content in the electrode was about 3.0-20.4 mg cm^{-2}. To fabricate the 2025 type coin cells for the electrochemical measurements, a 40 μL electrolyte of 1.0 M $LiPF_6$ in EC/DEC (1:1 by volume) was used as the electrolyte. For symmetric batteries, two same Li metal anodes (such as Li foil or LMFS) were reassembled into CR2032-type coin cells with 80 mL electrolytes. A LAND galvanostatic charge-discharge instrument (Wuhan LAND Electronic Co., Ltd) and VMP3 electrochemical workstation (BioLogic Science Instrument Co., Ltd) were used to perform electrochemical measurements and the voltage range was 3.0-4.2 V.

3.3   Result and discussions
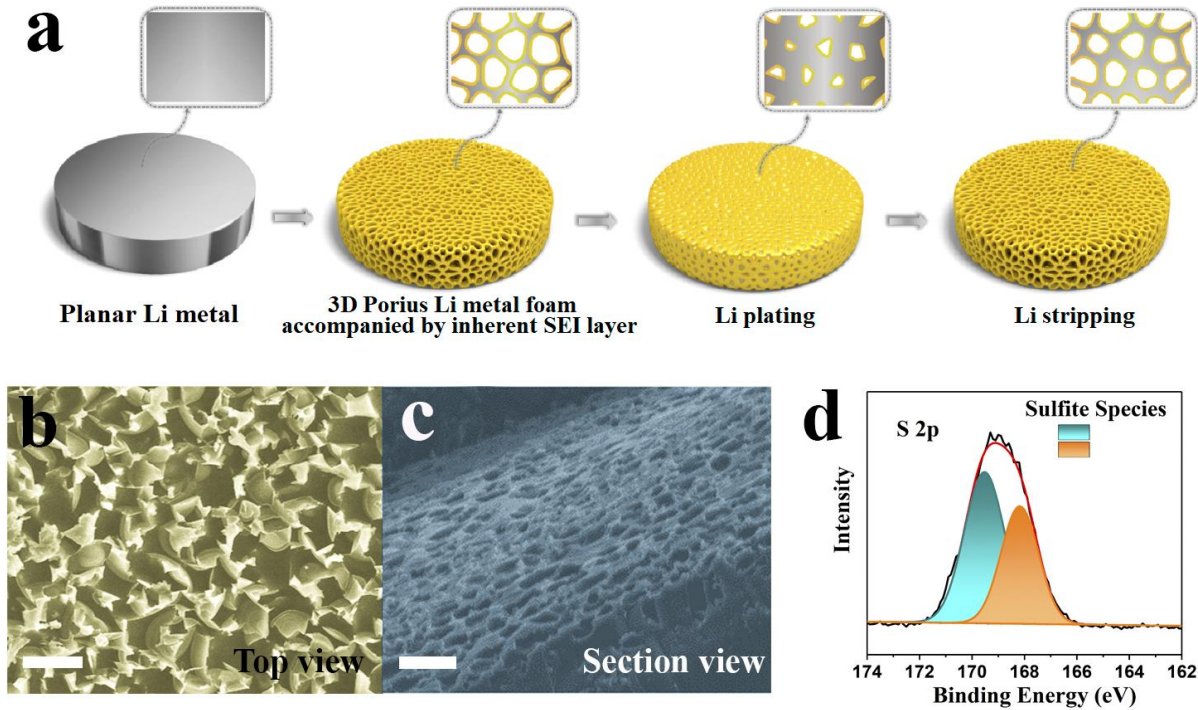
Figure 3.1. (a) Schematic diagram of the preparation process and structure of LMFS anode after Li plating and stripping processes. (b) The top-view SEM images of LMFS (c) The section-view SEM images of LMFS. . Scale bars in b and c equal to 10 μm. (d) S 2p XPS spectra of LMFS.

Figure 3.1a schematically shows the fabrication process of LMFS and its microstructure after Li plating and stripping processes. For the bare Li foil, the concentrated ion-flux could result in an uneven charge distribution, where the Li-ions tend to deposit in the form of Li dendrite and dead Li. Unlike the conventional planar Li foil, 3D Li metal anode with porous foam structure was

prepared directly via template-free chemical etching by immerging the planar Li foil into DBSA, described as follows:

2 H$_3$C(H$_2$C)$_{10}$H$_2$C—⟨benzene ring⟩—S(=O)(=O)—OH + 2 Li ⟶ 2 H$_3$C(H$_2$C)$_{10}$H$_2$C—⟨benzene ring⟩—S(=O)(=O)—O·Li + H$_2$↑

4-dodecylbenzene sulfonic acid   **lithium dodecyl benzene sulfonate**
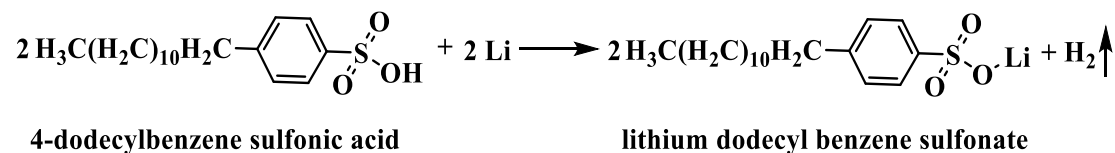
Some Li ions on the surface will react with DBSA to form a uniform LDBS layer on the surface of the porous Li skeleton. After 24 hours, 3D Li metal anode with the porous structure is yielded with the momentum of the chemical reaction. From the SEM images (**Figure 3.1b,c**), a microscopic porous structure was observed on the surface of LMFS with a thickness of 42.5 μm after the controllable template-free chemical etching process by the sulfonic acid. XPS was used to further demonstrate the successful grafting LDBS layer on the surface of the 3D porous Li matrix, where the S 2p signal can be divided into two main peaks at 168.2 eV and 169.5 eV, attributing to R-SO$_3^-$ groups. (**Figure 3.1d**)

As the unstable Li host, the traditional 2D planar Li foil provides extremely limited reaction sites for the nucleation of Li ions. The random Li nucleation behavior can be observed on the surface of the planar Li foil, leading to the indiscriminate growth of Li dendrites. Owing to the large volume change during the plating process, the broken of weak SEI layer results in the formation of some cracks on the surface of Li foil, and newly created Li metal exposure sites on the cracks re-contact with electrolyte. Li-ions tend to nucleate on antecedent reaction sites rather than fresh Li spots, further promoting the growth of Li dendrites. The repeated rupture and repair of weak SEI layer on the surface of cracks during the cycles are accompanied by the continuous consumption of Li-ions and organic electrolyte, further leading to the low Coulombic efficiency, serious gas pressure evolution, large overpotential, and short cycle life. Some Li dendrites may break and become electrically isolated from the anode after deeply plating and stripping processes, generating accumulated "dead Li". (**Figure 3.2a**) In sharp contrast to the case of the planar Li foil, the obtained Li metal anode becomes a 3D porous foam structure via template-free chemical etching, and the surface is uniformly covered with a protective artificial SEI Layer (LDBS layer), further leading to uniform charge distribution and smooth Li deposition behavior. The as-obtained porous 3D structure can tolerate the infinite volume expansion during the repeated Li

plating/stripping processes and enhance the utilization of Li ions. After the cycles, The thickness of the Li metal anode is maintained with no change, which further demonstrated that our prepared Li metal anode can effectively decrease the interface fluctuation and internal stress.
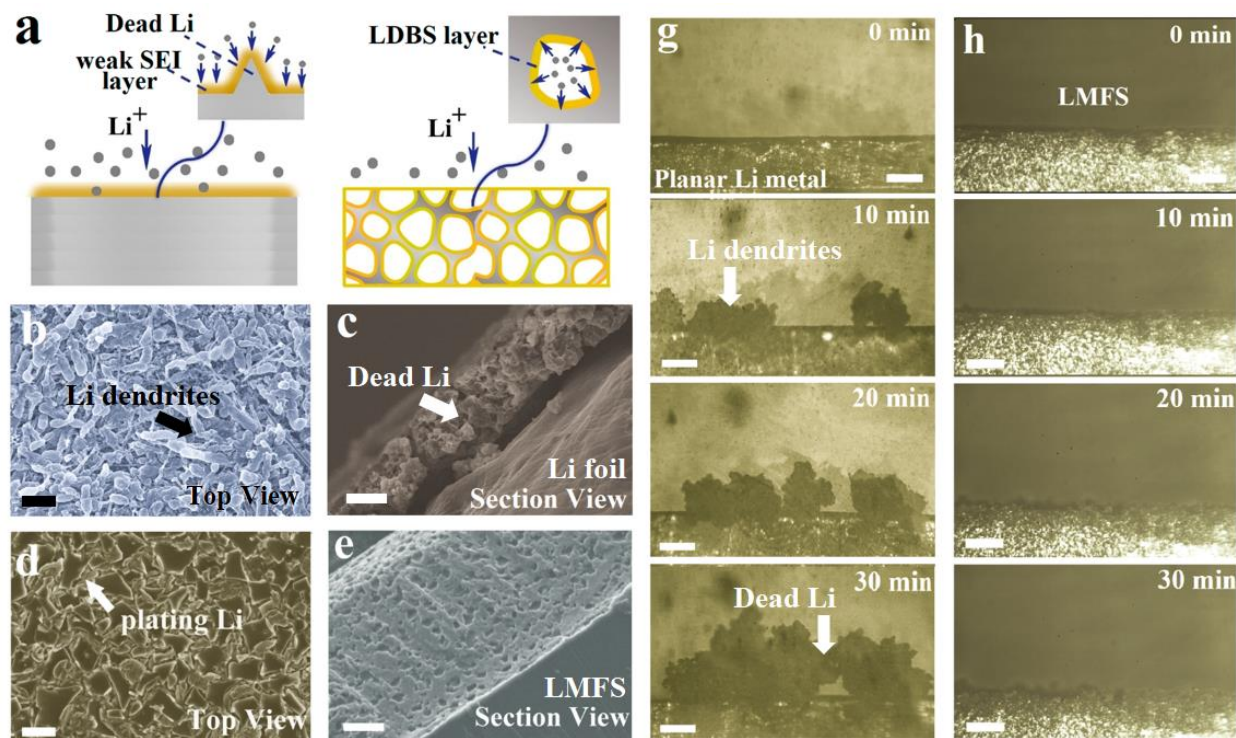
Figure 3.2. (a) Schematic illustration of planar Li foil and LMFS anode during Li plating process. The Li$^+$ flux is concentrated at the tips of Li dendrites on the surface of planar Li metal, further leading to the formation of Li dendrites and mossy Li. For the LMFS anode, Li ions are inclined to nucleate and grow at the surface of the porous foam matrix on the inner surface of the pores. (b) The top-viewSEM image of Li foil after Li plating. (c) The section-view SEM image of Li foil after Li plating. (d) The top-view SEM image of LMFS after Li plating. (e) The section-view SEM image of LMFS after Li plating. *In-situ* optical microscopy observations of Li deposition process of (g) planar Li metal and (h) LMFS. The scale bars in b, c, and e equal 10 µm, d equal 5 µm, f and g equal 100 µm.

From **Figure 3.2b,c**, the Li dendrite and dead Li can be obviously observed from the SEM image of bare planar Li foil after a nucleation area capacity of 5.0 mAh cm^{-2}. The sectional view SEM image exhibits a loose structure, corresponding to the growth of dead Li and mossy Li, which is caused by the heterogeneous distribution of the electrical field, expediting uneven deposition of Li. In contrast, the 3D porous LMFS electrode delivers a low nucleation overpotential of 3.2 mV. Homogeneous charge distribution of the electrical field and smooth Li deposition behavior were achieved. As shown in **Figure 3.2d,e**, the porous structure with many deep perforated tunnels can divide the surface of Li foil into different confinements, where Li-ions can move along the porous structure, pass through the LDBS layer, deposit on the surface, and fill the porous matrix, thus efficiently suppressing the growth of Li dendrites. A relatively flat surface and dendrite-free structure can be observed from the sectional-view SEM image of the LMFS anode after cycles. In-situ optical microscopy observation was used to exhibit the dynamic processes of the Li plating process for Li foil and LMFS anode. (**Figure 3.2g,h**) For bare Li foil, Li dendritic structure starts to grow along the surface of the anode during the Li plating process and becomes obvious over time. After only 30 min, the surface of bare Li foil is full of Li dendrites and dead Li. The growth of Li dendrites can severely penetrate through the separator, resulting in the internal short circuit of the system. In sharp contrast, the In-situ optical microscopy observation shows that the surface of the LMFS anode maintains smooth without any dendritic structure after 30 min plating process, which is in agreement with the results shown in the SEM images.

The capacity retention between Li foil and LMFS anode was measured by delithiating the electrode to 1.0 V at a current density of 1.0 mA cm^{-2}, where the obtained 3D porous LMFS anode and bare Li foil all deliver a high specific capacity of 3518 and 3679 mAh g^{-1}, respectively. The deeply cycling test was conducted by the Li∥Li and LMFS∥LMFS symmetrical cells with the continuous galvanostatic Li stripping/plating processes at the different current density between 1.0 and 20.0 mA cm^{-2}. As shown in **Figure 3.3a**, the voltage profiles of the LMFS electrode at a current density of 1.0 mA cm^{-2} with a corresponding area capacity of 1.0 mAh cm^{-2} show a very low overpotential at 25 mV, and the voltage hysteresis can maintain a balance even after cycling for 350 h. The porous matrix served as a rigid backbone leads to a more uniform charge distribution and thus orients the Li deposition. The LDBS layers as the artificial SEI layer can prevent the formation of Li dendrites and suppress the side reactions. As a contrast, the overpotential for planar Li foil (80-

100 mV) is much larger than that of LMFS, and the short circuit happens within 310 h. As shown in **Figure 3.3b**, the fluctuant voltage response can be observed from the voltage-time profiles of the Li∥Li symmetric cell at higher rates of 3.0 mA cm^{-2} or 5.0 mA cm^{-2} with a corresponding stripping/plating capacity of 2.0 mAh cm^{-2}. For LMFS∥LMFS symmetrical cell, a relatively flat and stable voltage plateau at a steady-state is achieved.

The previously reported strategies show that the conventional Li metal anode with a superfluous amount of Li is only stripping and plating at a very low area capacity of less than 2.0 mAh cm^{-2}, far from commercial applications. For commercial applications, it is important to design a stable Li metal anode with a deeply cyclable property and further realize the fast charging ability. From **Figure 3.3c**, when test at increasing current density varied from 1.0 mA cm^{-2} to 20.0 mA cm^{-2} with the corresponding area capacity from 1.0 mAh cm^{-2} to 20.0 mAh cm^{-2}, the LMFS∥LMFS symmetrical cell exhibits a low overpotential of 201 mV (at 10 mA cm^{-2}), 228 mV (at 15 mA cm^{-2}), and 453 mV (at 20 mA cm^{-2}), respectively. Electrochemical impedance measurement was further carried out to explore the interfacial stability of the different symmetrical cells before cycling at the open circuit condition. The semi-circle of the Nyquist plots is corresponding to the charge transfer resistance and interfacial resistance between electrolyte and electrode (**Figure 3.3d**). The resistance of the LMFS-based symmetrical cell (175.6 Ω) is far smaller than that of the planar Li foil-based symmetrical cell (365.3 Ω), further demonstrating the excellent Li-ion mobility after introducing the protective artificial LDBS layer (SEI layer) and 3D porous Li metal anode. During the Li stripping/plating processes, the heat generations were taken place caused by the joule heating and entropy change. The large resistance of the cell is corresponding to more heat generation. The infrared images show that the temperature of the cell with LMFS anode is only 28.2 °C after 0.5 h Li plating process at a high current density of 20.0 mA cm^{-2}, which is much smaller than that of planar Li foil-based cell (34.6 °C).
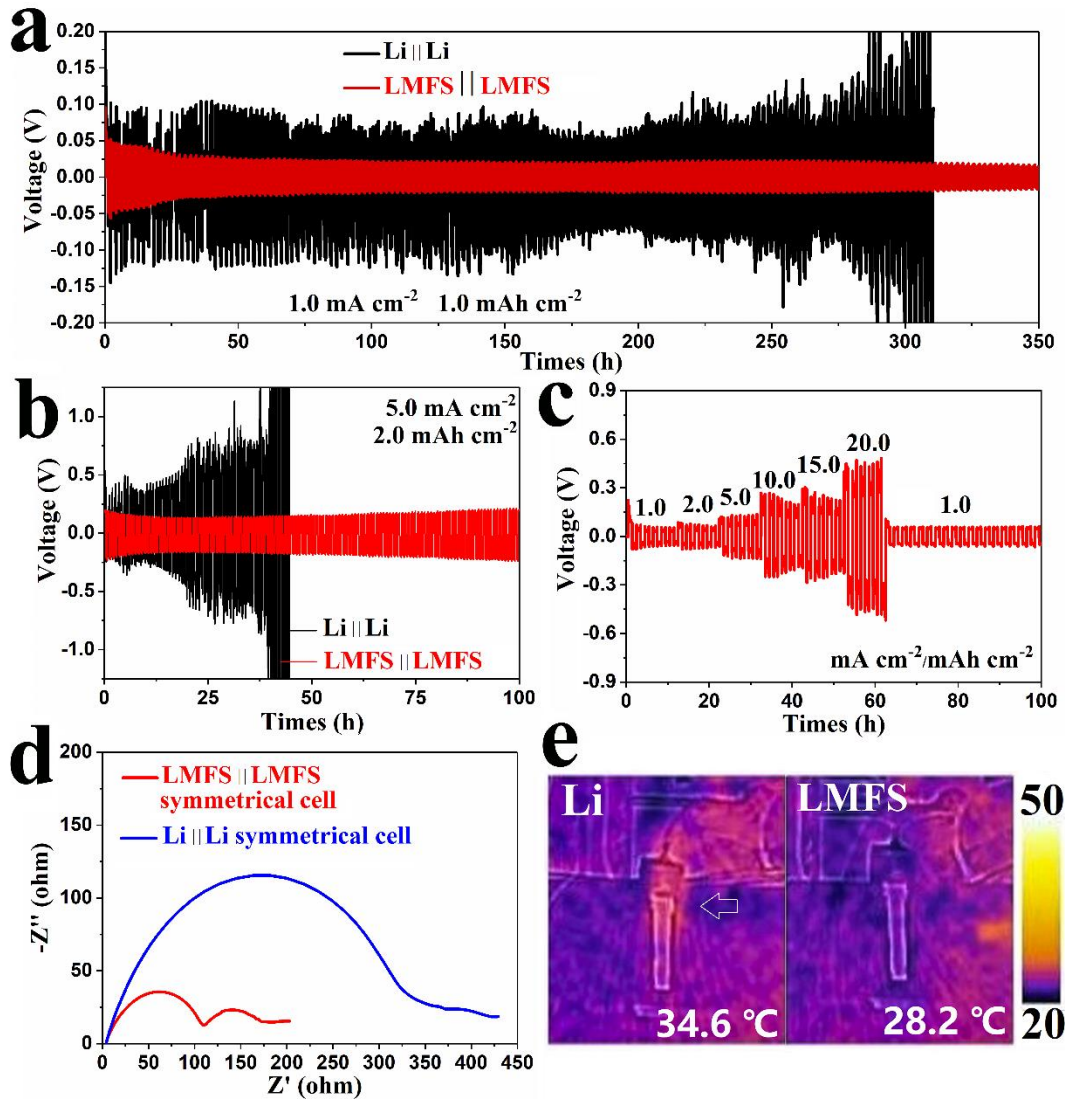
Figure 3.3. Voltage-time profiles of the Li‖Li and LMFS‖LMFS symmetric cells (a) at a current density of 1.0 mA cm^{-2} with a corresponding stripping/plating capacity of 1.0 mAh cm^{-2} and (b) at a current density of 5.0 mA cm^{-2} with a corresponding stripping/plating capacity of 2.0 mAh cm^{-2}. (c) Voltage-time profile of LMFS‖LMFS symmetric cells at different current densities and area capacity from 1.0 to 20.0 mA cm^{-2}. (d) Nyquist plots showing the impedance evolution of symmetric cells with Li foil (blue) and LMFS (red) anode. (e) IR thermal images of different cells after 30 min plating at a current density of 20.0 mA cm^{-2}.

The galvanostatic cycling performance at a high current density of 0.5 C (1 C=280 mA g^{-1}) of the full cells assembled with different Li metal anode and LiNiCoMnO$_2$ (Ni:Co:Mn=1:1:1) cathode with the active material loading of ~3.0 mg cm^{-2} was investigated to further demonstrate the

feasibility and advantages of our designed LMFS anode. The corresponding discharge-charge voltage profiles are shown in **Figure 3.4a**, and a high reversible capacity of 136.6 mAh g^{-1} was achieved. It can stabilize at a constant capacity for the subsequent cycles. The cycling performance between LMFS and bare Li foil was further evaluated at continuously varying current densities. As shown in **Figure 3.4b**, a high discharge capacity for LMFS based full cell was achieved at high rates between 0.2 and 25.0 C. When the current density suddenly back to 0.2 C after deep cycling at 25.0 C, the capacity of the cell can be largely restored during the repeated cycles. The results further certify that the LMFS anode exhibits excellent electrochemical performance during the continuous Li stripping and plating processes, which enables homogenous Li nucleation behavior and fast charge transfer for the Li/Li$^+$ reaction.
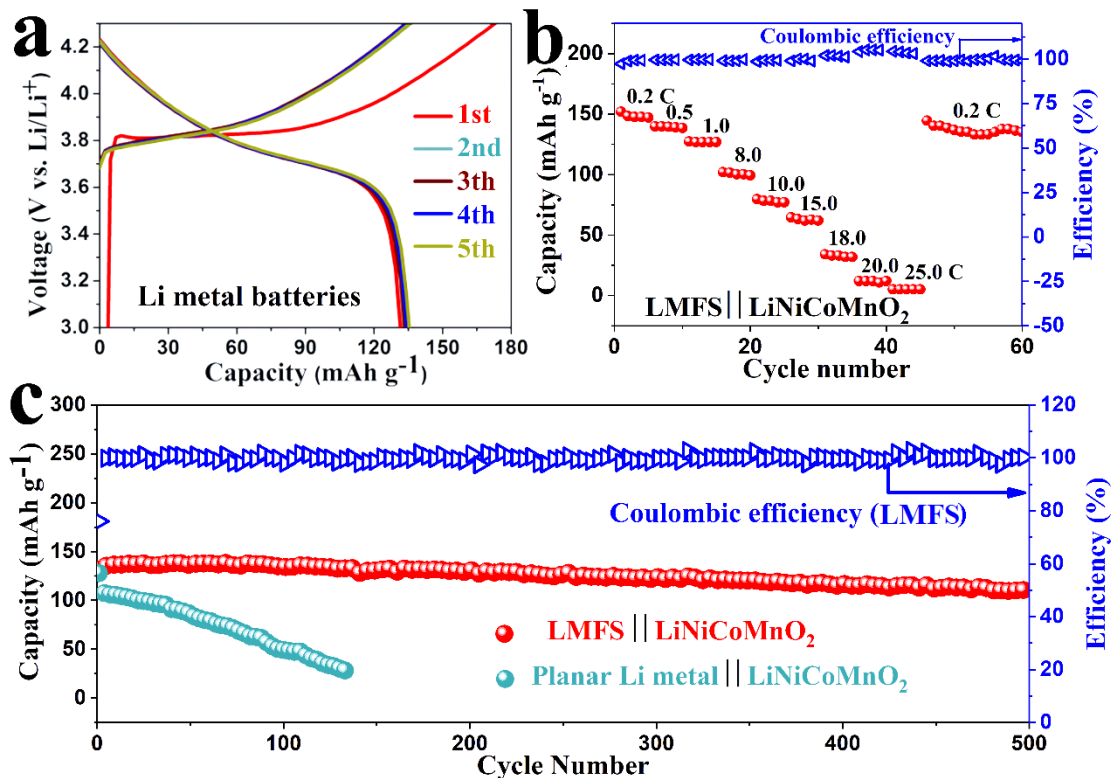
Figure 3.4. (a) The discharge and charge voltage curves of the first five cycles of LMFS and LiNiCoMnO$_2$ full cell at 0.5 C (1 C=280 mAh g^{-1}). (b) Rate performance of LMFS anode-based full cell at current densities from 0.2C to 25.0 C. (c) Long-term cycling stability with corresponding Coulombic efficiency at 0.5 C for more than 500 cycles.
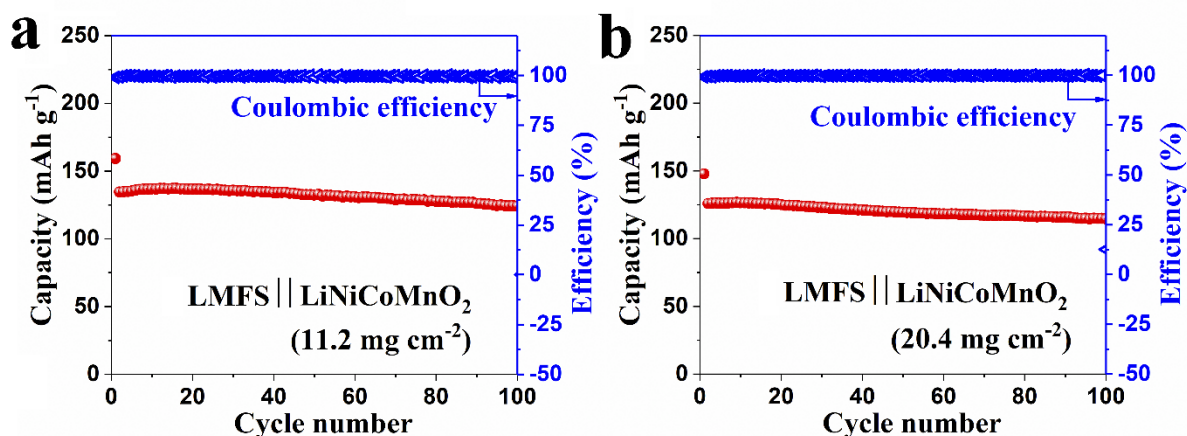
Figure 3.5. Cycling performance of LMFS anode-based full cells assembled with the high cathode material loading of (a) 11.2 mg cm^{-2} and (b) 20.4 mg cm^{-2} at 0.5 C.

To further demonstrate the advantages of the LMFS anode, we further investigated the long-term cycling stability of the full cells paired with different Li metal anodes. The full cell with LMFS anode exhibits an excellent cycling performance with high Coulombic efficiency (~100%) and high capacity retention of 84% for more than 500 cycles. This further indicates that the artificial SEI layer can prevent the continuous decomposition of the electrolyte, which contributes greatly to the excellent reversibility and achieves a great endurance capacity for high voltage. (**Figure 3.4c**) The LMFS‖LiNiCoMnO$_2$ full cell exhibits a high reversible capacity of 112.0 mAh g^{-1} at a high current density of 0.5 C. Interestingly, the cycling performance of the bare Li foil anode is also investigated under the same testing conditions. In sharp contrast, the bare Li foil exhibits a lower capacity followed by fast capacity decay within only 140 cycles. Moreover, active material loading is an important figure of merit, and more than 5.0 mg cm^{-2} for active material loading is generally required for the commercial applications of Li-based batteries. Here, we can easily adjust the areal mass density of LiNiCoMnO$_2$ cathode with a high active material loading up to 20.4 mg cm^{-2}. The charge/discharge performance of LMFS-based full cells with a high active cathode material loading of 11.2 mg cm^{-2} and 20.4 mg cm^{-2} is revealed in **Figure 3.5** at a high current density of 0.5 C with high capacities of 122.6 mAh g^{-1} and 118.3 mAh g^{-1}, respectively.
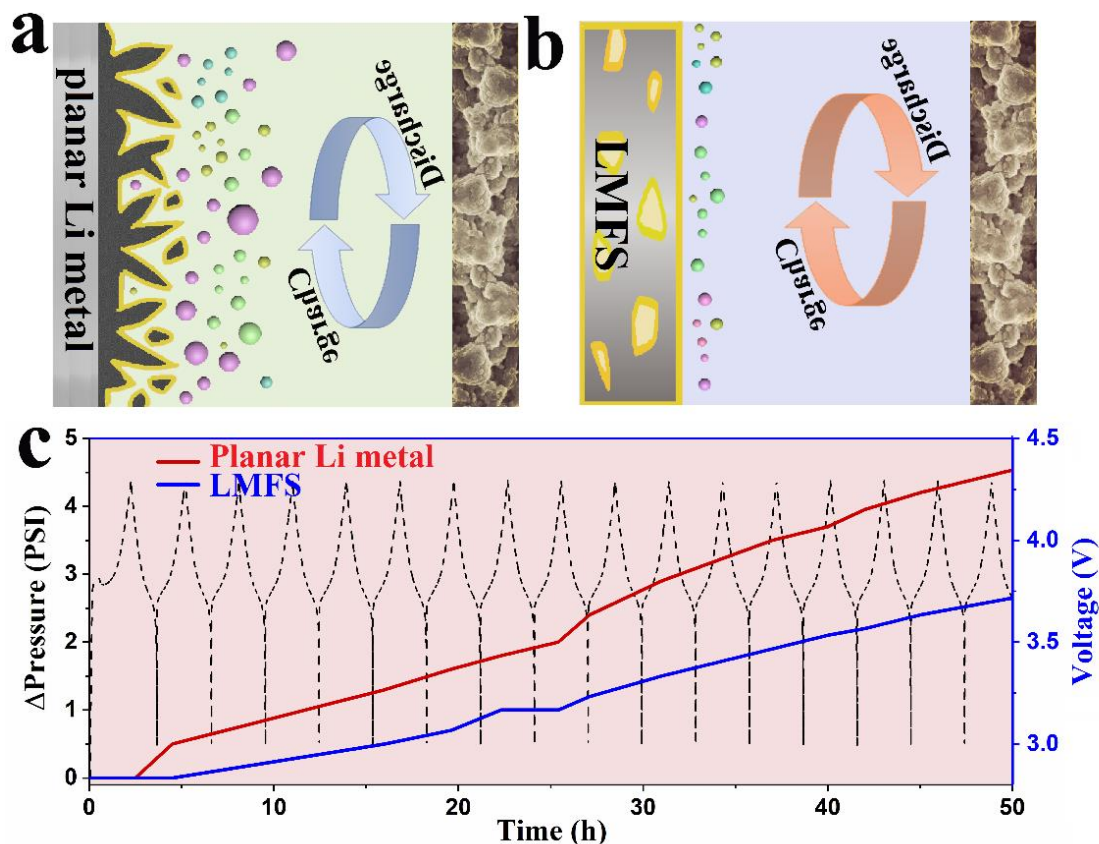
Figure 3.6. The in-situ monitoring of gas evolution of different cells during the cycles. Schematic diagram shows the produced gas inside the cells based on (a) planar Li foil and (b) LMFS anode. (c) Pressure trends with dependence on the different charge and discharge times for Li metal batteries.

In addition, the formation of SEI layer and irreversible reaction with both anode and cathode is accompanied by the consumption of Li ions and the electrolyte, accompanied by gas evolution, leading to some safety hazards (high pressure and cell explosion) and loss of initial irreversible capacities. (**Figure 3.6a,b**) Gas evolution must be effectively suppressed, which can hinder the commercial application of Li metal anode. Due to the formation of H_2 and CH_4, the gas evolution and increased pressure inside the cell can be detected, which is caused by the decomposition of the electrolyte and the formation of the SEI layer. As shown in **Figure 3.6c**, the internal gas

pressure for planar Li foil-based Li metal battery is significantly increasing to 4.6 pounds per square inch (PSI) during the initial 50-hour cycles. In sharp contrast, the LMFS anode-based cell exhibits a relatively low gas pressure of less than 2.4 PSI after 50 hours. The 3D porous Li matrix and protective artificial LDBS layer can effectively suppress the gas evolution and reduce unwanted side reactions. The results and characterization technique can be used to gain a better understanding of failure mechanisms and thus to develop a new Li metal anode to improve the safety of the energy storage system.

3.4   Conclusion

In summary, we have demonstrated a novel 3D Li metal anode with a porous foam structure accompanied by an inherent LDBS layer (artificial SEI layer) as an alternative to planar Li foil, realizing orientated and mitigated growth of lithium dendrites. The porous Li matrix served as a rigid backbone leads to a more uniform charge distribution and thus orients the Li deposition. The LDBS layers can prevent the formation of Li dendrites and side reactions. Moreover, the LMFS anodes exhibit excellent electrochemical performance when coupled by $LiNiCoMnO_2$ cathode with the active material loading up to 20.4 mg cm^{-2}. In addition, we have enabled high-performance Li metal anodes with the deeply cyclable property even tested at the high area capacities of 15.0 or 20.0 mAh cm^{-2}, and stable long-term plating/stripping process of symmetric cells with low voltage hysteresis over 350 hours are revealed, which further demonstrate that our strategy can greatly prevent dendrites from shooting out, suppress the gassing process, and minimize the electrolyte decomposition.

4   SECTION II. Single-atom and cluster Au as an usher for deeply cyclable Alkali metal anodes

As the development of energy storage devices including consumer electronics, portable electronic devices, and electric vehicles increases, so do the demands for pursuing high-energy and cost-effective multivalent metal-ion batteries, such as lithium-ion (Li-ion) and sodium-ion (Na-ion) [65-70, 121-127] However, the energy density of conventional Li-ion and Na-ion batteries is close to their theoretical limits. In this context, Li and Na metal batteries based on metallic anode are ideal candidates due to their low redox potential (-3.04 V and -2.714 V vs. the standard hydrogen electrode) and high theoretical capacity (3860 mAh g^{-1} and 1166 mAh g^{-1}).[216] However, the alkali metal anode is still facing tremendous challenges, including the large volume change, unstable SEI layers, and the uncontrolled formation of dendrites, which cause low reversible capacity and result in a short circuit or even an explosion.

To date, several achievements have been obtained to address the above issues of alkali metal anode, yet oriented control with alkali metal deposition remains elusive.[255-260] Recently, Au foil and Au particles provide a new way of heterogeneous seeded growth to control Li plating on the appointed substrates, resulting in a low nucleation barrier for Li-ions deposition. Au hosts for Li metal are expected to address the imperfection of interface instability and dendrite growth of the anode, exhibiting the great development potential for the alkali metal anode.[255] However, as the one of most common noble metals, Au is so expensive that it is unaffordable as the substrates of metal batteries. Downsizing noble metals to single atoms or clusters provides an effective way to decrease Au dosage and maximize atomic utilization efficiency. The Au single-atom or cluster modified metal anodes are analogous to Au foil anode, but, unlike many metal anodes, reaction at the active site can be understood with atomistic detail on a single atom modified metal anode. Therefore, designing a deposition matrix with single atoms makes more sense for the alkali metal anode.[268,269] Guiding metal deposition at an atomic level and inhibiting uncontrolled growth of dendrites at nucleating stages may create a new dimension to prepare the safe and efficient alkali metal anodes.

In this chapter, dendrite-free alkali metal anodes were constructed by the dispersion of single-atom and cluster Au on activated carbon cloth (SCAu-CC), which can guide alkali metal deposition

uniformly. Due to the strong affinity and interaction with Li/Na ions, introducing the single-atom and cluster Au can afford high conductivity and lithiophilicity, which can serve as Li-ion nucleation sites to favor Li metal deposition with minimized nucleation barrier. After being supported by single-atom and cluster Au, the as-obtained Li metal anode enables stable cycling in working batteries with a high plating/stripping efficiency of 99.82% for 900 cycles under 1.0 mAh cm^{-2} and deeply cyclable property at a high current density with corresponding areal capacities up to 20.0 mAh cm^{-2}. In addition, the as-obtained Na metal anode achieves a high Coulombic efficiency of 99.73% for 250 cycles and a long lifespan of more than 400 h with low overpotential. Moreover, dendritic structures are effectively inhibited and long-lifespan alkali metal batteries are successfully achieved, which shows the high Li/Na-utilization and feasibility of our strategy.

4.1   Preparation of SCAu-CC and PAu-CC

Firstly, commercial carbon cloth was treated by the modified Hummers' method. A typical three-electrode system consisting of a platinum counter electrode, an Hg/HgO reference electrode, and a working electrode was used in a mixture of 0.05 M NaCl and 0.3 mM $HAuCl_4$. The Au single-atom was deposited on the substrate by stepping the potential to -0.6 Vvs. SCE for 5 s, followed by stepping back to -0.2 V vs. SCE for 5 s for 6 cycles. The Au particles were prepared in the same way after 100 cycles.

4.2   Structure Characterizations

X-ray Absorption Near-Edge Structure (XANES) and Extended X-ray Absorption Fine Structure (EXAFS) data were collected on beamline 14W at the Shanghai Synchrotron Radiation Facility (SSRF) and on beamline 01C at the Taiwan Light Source (TLS). The microstructure of all the samples was observed by field emission scanning electron microscope (SU8010, Hitachi, Ltd) at an acceleration voltage of 10 kV and field-emission transmission electron microscopy (FEI Tecnai

$G^2$20, FEI NanoPorts, Ltd). Subangstrom-resolution aberration-corrected scanning transmission electron microscopy (STEM, FEI Titan ETEM G2 80-300) was used to characterize the dispersion and configuration of single atoms. X-ray diffraction of patterns was carried out on the D8 ADVANCE instrument (Bruker AXS GmbH Co., Ltd).

4.3 Electrochemical Measurements

For the Li-based batteries, the electrochemical performances were evaluated using coin cells (2025-type coin cells) with a Celgard separator. The electrolyte was 1 M lithium hexafluorophosphate ($LiPF_6$) in ethylene carbonate (EC)/diethyl carbonate (DEC) (1:1 by volume). For the Na-based batteries, the electrochemical performances were evaluated using coin cells (2032-type coin cells) with commercial separators (Whatmen GF/A). The electrolyte consists of 1 M sodium perchlorate ($NaClO_4$) in ethylene carbonate (EC)/dimethyl carbonate (DMC) (1:1 by volume) with 5wt% fluoroethylene carbonate. After the activation process of one cycle between 0-1 V at 0.5 mA cm^{-2}, the alkali metal anode was prepared by plating metal on the surface of different substrates. For symmetric batteries, two alkali metal anodes using various current collectors were reassembled into CR2032-type coin cells with 80 mL electrolytes. The alkali metal anode was prepared by plating alkali metal on the surface of different substrates. The $LiFePO_4$ electrodes were prepared by mixing active materials, polyvinylidene fluoride, and carbon black in the ratio 8:1:1 with N-methyl-2-pyrrolidone as the solvent. The areal mass loading of the electrode was ~12 mg cm^{-2}. The $Na_3V_2(PO_4)_3$ electrodes and were prepared by mixing active materials, polyvinylidene fluoride, and carbon black in the ratio of 8:1:1 with N-methyl-2-pyrrolidone as the solvent. The areal mass loading of the $Na_3V_2(PO_4)_3$ electrodes was 2.0-2.2 mg cm^{-2}.

4.4 Computational Details

First-principles calculations in the framework of density functional theory, including structural,

electronic performances, were carried out based on the Cambridge Sequential Total Energy Package known as CASTEP. The exchange-correlation functional under the generalized gradient approximation (GGA) with norm-conserving pseudopotentials and Perdew–Burke–Ernzerhof functional was adopted to describe the electron-electron interaction. An energy cutoff of 750 eV was used and a k-point sampling set of 5 x 5 x 1 was tested for convergence. A force tolerance of 0.01 eV Å $^{-1}$, energy tolerance of 5.0×10^{-7} eV per atom, and maximum displacement of 5.0×10^{-4} Å were considered. Each atom in the storage models was allowed to relax to the minimum in the enthalpy without any constraints. The vacuum space along the z-direction is set to be 15 Å, which is enough to avoid interaction between the two neighboring images. Then, the Li and Na atom had been absorbed on the surface of graphite, graphite+Au, graphite+Au1. Bonding energy ΔE_{bond} of Au atom on the surface of substrates was defined as:

$$\Delta E_{bond} = E_{*Au} - (E_* + E_{Au})$$

where *Au and * denote the adsorption of Au atom on substrates and the bare substrates, E_{Au} denotes the chemical potential of Au element. Adsorption energy ΔE of A group on the surface of substrates was defined as:

$$\Delta E = E_{*Au} - (E_* + E_A)$$

where *A and * denote the adsorption of Li/Na atom on substrates and the bare substrates, E_A denotes the chemical potential of Li/Na element.

4.5   Result and Discussions

The morphology, structure, and size of SCAu-CC and Au particles on CC (PAu-CC) were investigated by SEM images and TEM images in **Figure 4.1**. Firstly, the functionalized carbon cloth (CC) was prepared using the previously described procedure involving chemical oxidation and exfoliation processes, which provide a potential scaffold for firmly trapping the highly active single-atom and cluster Au in comparison to nanoparticles. As shown in **Figure 4.1a** and **4.1c**, we can see the Au nanoparticles on the surface of PAu-CC. For SCAu-CC, no nanoparticles can be

observed from **Figure 4.1b** and **4.1d**, further demonstrating that all of the Au species have existed as the single atom or cluster structure. Furthermore, elemental mapping images of SCAu-CC were used to confirm the homogeneous distributions of Au on the current collector. The high spatial resolution of aberration-corrected high-angle annular dark-field scanning transmission electron microscopy (HAADF-STEM) images illuminated the precise determination of the distribution and size of single-atom and cluster Au, which provide the local structural information about the Au species on substrates (**Figure 4.2**). The numerous bright spots are uniformly dispersed on the carbon substrate, corresponding to Au single atoms. As shown in **Figure 4.3**, XRD was further used to investigate the different crystal structures between SCAu-CC and PAu-CC**.** The strong and sharp peak at 38.2° of PAu-CC is indexed to Au. Due to the low Au content on the carbon substrate, XRD spectra for the SCAu-CC electrode shows similar peaks to amorphous carbon.
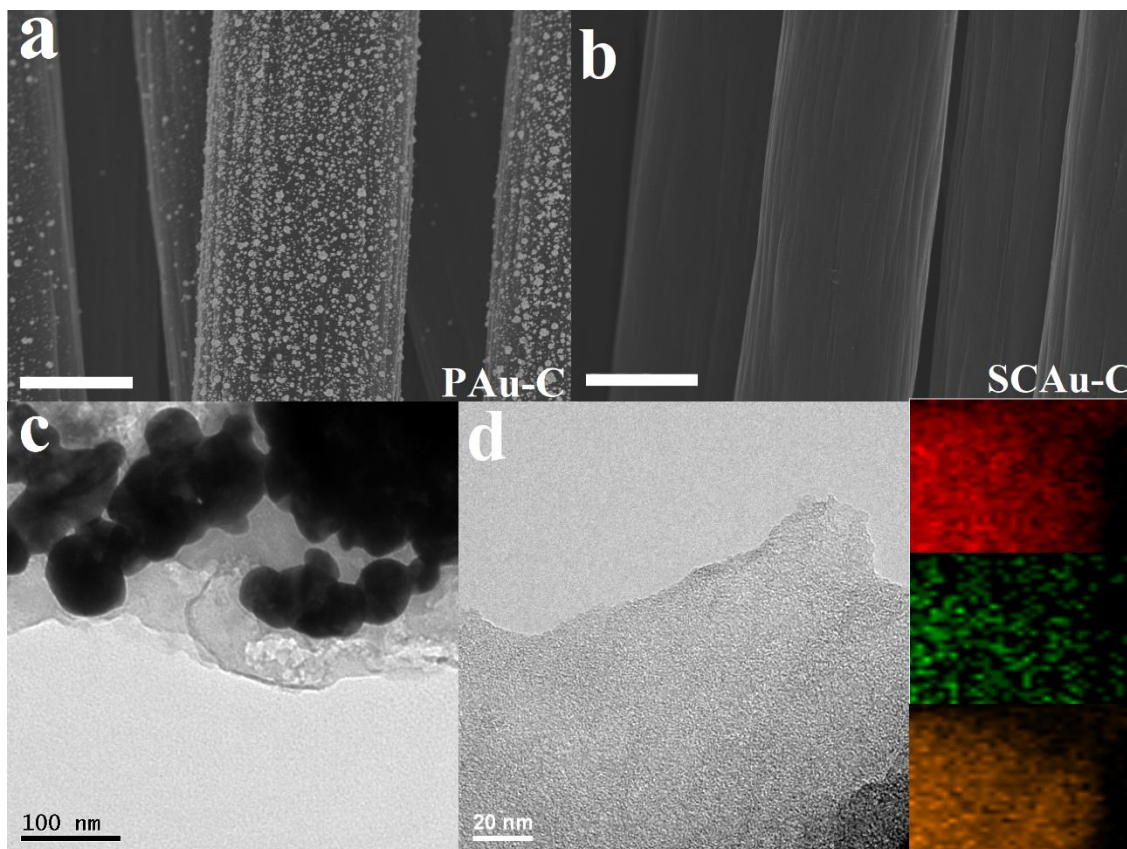
Figure 4.1. (a) The SEM images of PAu-CC. (b) The SEM images of SCAu-CC, where no Au particles can be observed. (c) The TEM images of PAu-CC. (d) The SEM images of SCAu-CC, and corresponding EDS elemental mapping results. Scale bar in a and b equal to 5 μm.
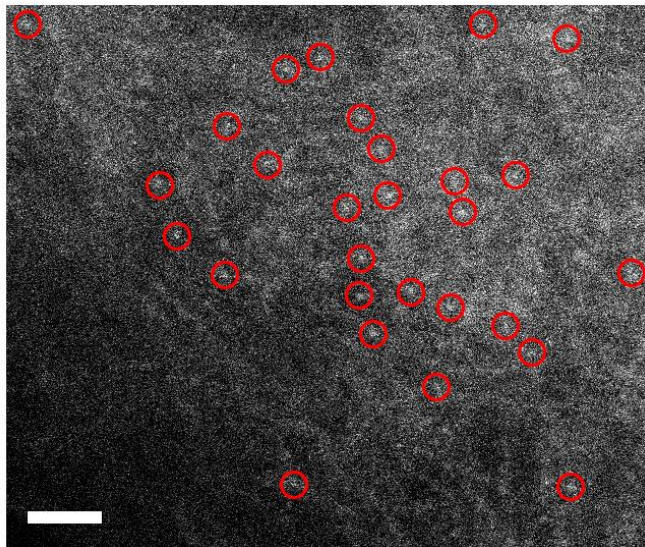
Figure 4.2. HAADF-STEM image of SCAu-CC. Scale bar, 2 nm.
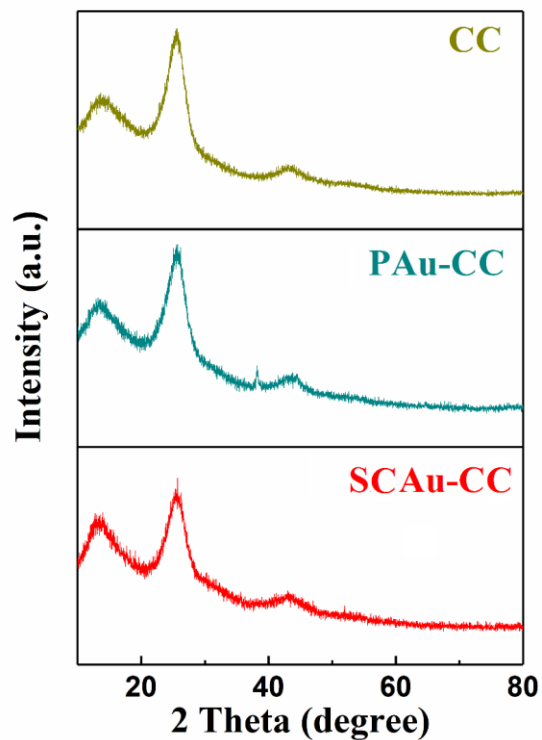
Figure 4.3. Comparison of X-ray diffraction patterns of CC, PAu-CC, and SCAu-CC. The strong and sharp peak at 38.2° of PAu-CC is indexed to Au. Due to the low Au content on carbon substrates, XRD spectra for both CC and SCAu-CC electrodes show similar peaks to amorphous carbon.

As shown in **Figure 4.4.a**, the local electronic structure and their interaction with the carbon skeleton were explored by the normalized X-ray absorption near edge structure (XANES) spectra for Au L3-edges of different substrates with comparison to a standard Au foil. Due to the completely filled 5d state of Au^0, no white-line intensity can be observed from the XANES spectrum of PAu-CC and Au foil. In sharp contrast, SCAu-CC shows the white-line intensity, suggesting that electrons prefer to transfer from the atomic Au to the carbon substrates. The increasing amount of Au-O coordination number is corresponding to the high white-line intensity, further demonstrating that the atomic-scale Au structures can significantly improve the electronic properties of Au. Furthermore, extended X-ray Absorption Fine Structure (EXAFS) data was used to further demonstrate the successful preparation of single atom and cluster Au. (**Figure 4.4.b**) From the Au foil and PAu-CC spectra, two strong peaks located at 2.56 Å and 2.14 Å represent the Au-Au peaks. One prominent peak at 1.84 Å can be observed from the Fourier transform spectra of SCAu-CC, corresponding to the Au-O contribution. A weak peak located at 2.53 Å is associated with Au-Au contributions. Compared with the PAu-CC and Au foil, the spectra of SCAu-CC shows the considerable deviation of the Au-Au bonds and significant intensity of Au-O bonds, further indicating the presence of single-atom and cluster Au.
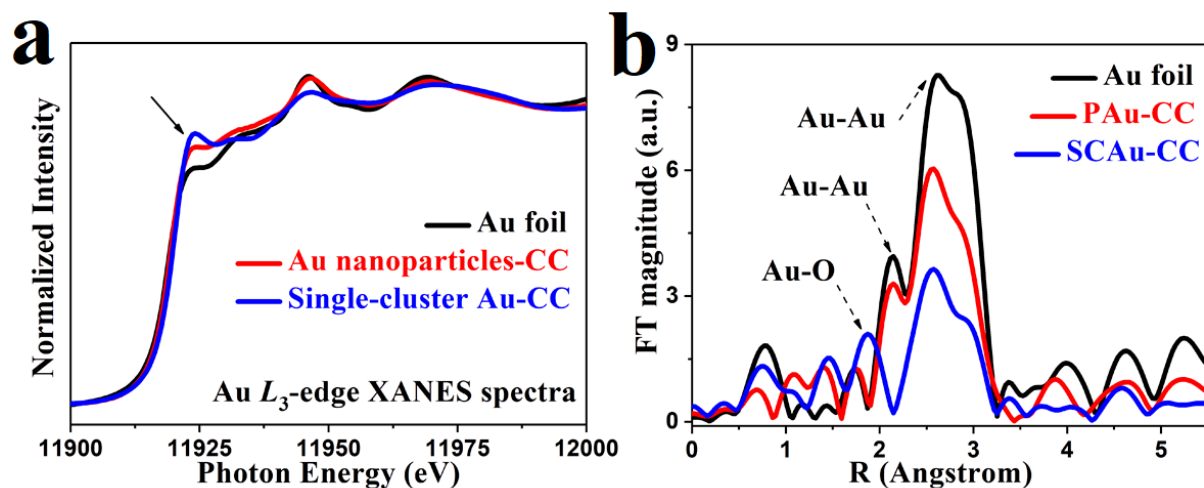
Figure 4.4. (a) Au L3-edge XANES spectra of the different substrates. (b) Fourier-transformed k3-weighted extended X-ray absorption fine structure (EXAFS) spectra.

The difference between the bottom of the voltage dip and the flat part of the voltage platform is defined as the nucleation overpotential, which becomes particularly relevant for island growth and the evolution of surface morphology. The nucleation overpotential of Li metal plating on bare Cu foil and CC substrate are ~46 mV and ~13 mV. (**Figure 4.5.a**) During the deposition process, Li ions, which are driven by the electric field, transfer from Li foil toward the current collector's surface and start nucleating. Owing to the relatively high nucleation overpotential of the substrates, the nucleation sites for Li plating on the surface of substrates are randomly distributed and isolated. After nucleation, a stable voltage value is achieved until the end of the deposition process. This phenomenon suggests that subsequent Li ions will be more inclined to nucleate on these nucleation sites, leading to the growth of dendrites due to the uneven electric field distribution. In sharp contrast, SCAu-CC exhibits a similar Li metal nucleation behavior as for the Au foil, and the 0 mV nucleation overpotential is achieved for the SCAu-CC substrate, which can guide Li to deposit on even-distributed single-atom and cluster Au. Sharing a working principle similar to Li metal anodes, the deposition behavior of Na metal on different substrates is similar to that of Li, and the Na nucleation overpotentials for the Cu, CC, PAu-CC, and SCAu-CC are 82 mV, 26 mV, 0 mV, and 0 mV, respectively. (**Figure 4.5.b**) Due to the enhanced Na affinity after introducing single-atom and cluster Au, Na ion is selectively nucleated on SCAu-CC substrate with minimized nucleation barrier. The minimized nucleation overpotential after introducing atomic-scale Au on the substrate implies that the single-atom and cluster Au active sites play an important role in Li-ion and Na ion plating behavior, which is in agreement with the results of DFT calculations.

The binding energy, electron density distribution, and interaction between the single Au atom with Li/Na atom were further used to demonstrate that Li/Na nucleation is induced by single-atom and cluster Au, promoting the uniform and selective deposition of alkali metal on the substrate. The diffusion speed of electrophilic Li-ion is slower than the transfer speed of the electron, and the distribution process is stochastic. The distribution and diffusion of Li ions near the surface of the current collector construct the morphology after Li metal deposition. As shown in **Figure 4.5.c,d**, the dispersive charge distribution on the bare CC substrate means that Li/Na ions remain scattered throughout the carbon skeleton, causing an uneven accumulation of the alkali metal. In addition, the binding energies between the carbon skeleton and Li or Na atom are only 0.14 and 0.72 eV, respectively. Compared with the binding energy between SCAu-CC and Li/Na atom, these values

are very low, which implies that the alkali metal can easily detach from the carbon skeleton, leading to the growth of dendritic structure.
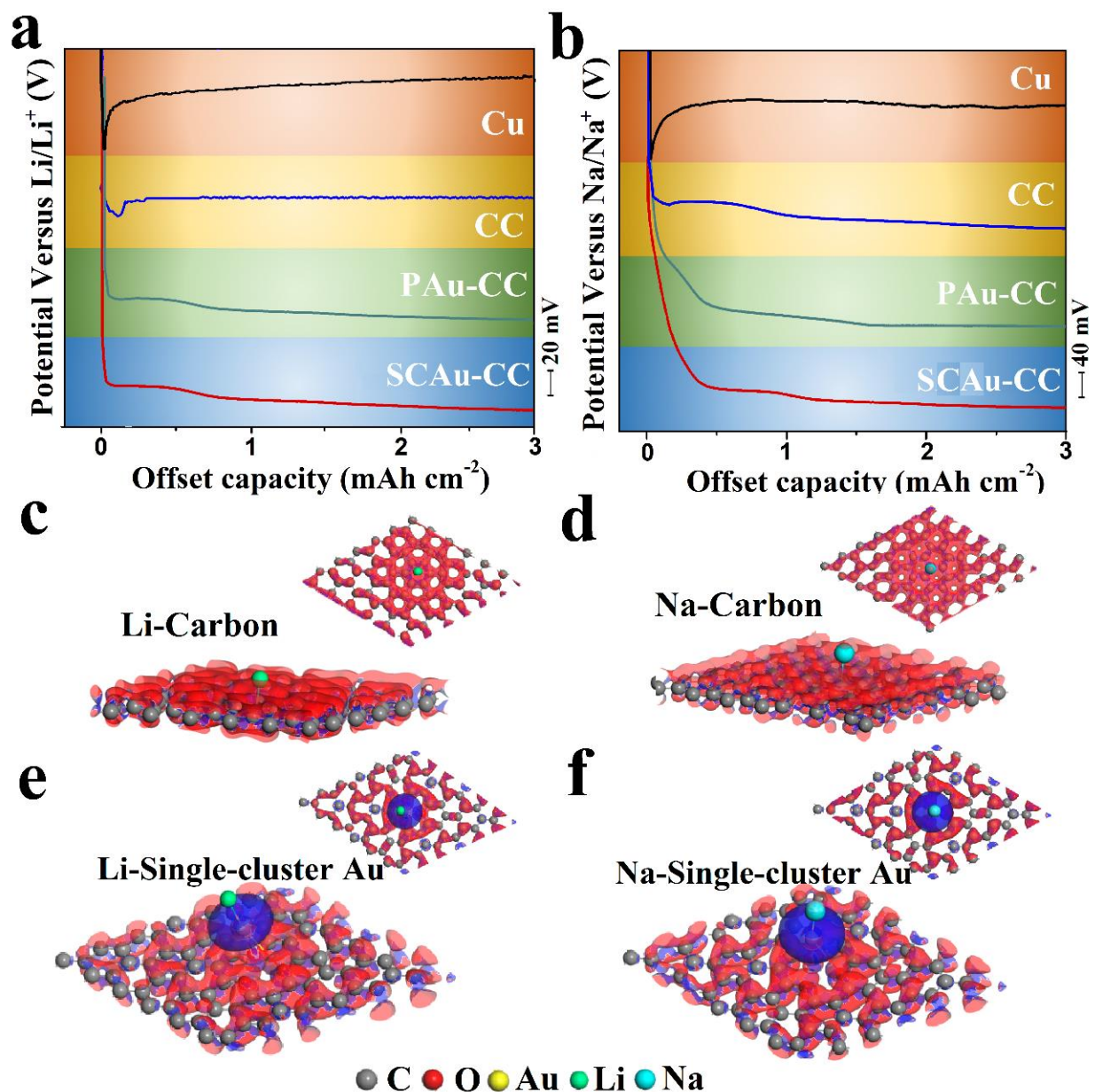
Figure 4.5 Demonstration of the strong interaction between single-atom and cluster Au and Li/Na metal. Voltage profiles of galvanostatic (a) Li and (b) Na deposition on Cu foil, CC, PAu-CC, and SCAu-CC. Electron density distribution and binding energy of the stable configurations with (c) Li atom and (b) Na atom adsorbed on the carbon skeleton, and (e) Li atom and (f) Na atom adsorbed on SCAu-CC.
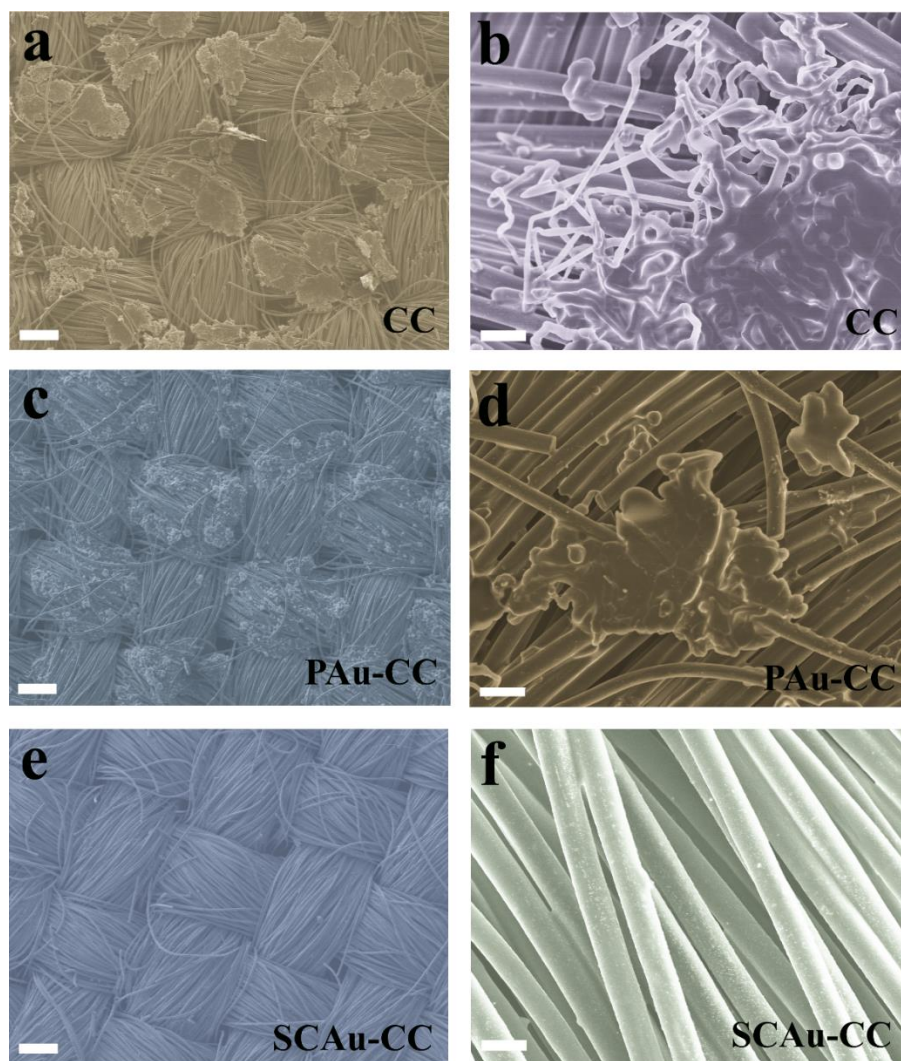
Figure 4.6. Morphology characterization of (a,b) CC, (c,d) PAu-CC and (e,f) SCAu-CC after plating 6.0 mAh cm^{-2} of Li metal. Scale bar, 500 μm and 50 μm.

As shown in **Figure 4.5.e,f**, the distribution of π electrons tend to accumulate in the region around Au single atoms, and high binding energy about 0.52 and 0.94 eV are achieved between Au atom and Li or Na atom. Therefore, the strong interactions between Au and Li/Na and the charge localization effectively enhance the affinity for alkali metal ions and regulate alkali metal nucleation during the plating processes. In addition, Single-atom and cluster Au can endow the

substrate with lithiophilic/sodiophilic nature to attract Li/Na ions to obtain multiple Li_xAu or Na_xAu alloy phases, which will be beneficial for the following deposition processes. The selective deposition of alkali metal ions on the surface of the SCAu-CC leads to a dendrite-free structure of as-obtained alkali metal anode, where no uncontrolled and amplified alkali metal deposition processes occur.

4.6   Electrochemical performance in Li-based battery

In the field of Li metal batteries, SEM images were first used to investigate the morphology of different substrates after 6.0 mAh cm^{-2} Li metal deposition. As shown in **Figure 4.6a,b**, the obvious Li cluster with a dendritic structure can be observed from the bare CC current collector, which grows vertically outside of current collectors. For PAu-CC current collector, Li dendritic structure still can be observed from the SEM images. (**Figure 4.6c,d**) The growth of Li dendrites can electronically connect the anode and cathode, leading to the internal short circuit, thermal runaway, and safety concerns. In sharp contrast, **Figure 4.6e,f** show that no apparent pancake-like Li deposits can be observed from the SEM images of SCAu-CC, where the controllable deposition of Li metal on single-atom and cluster Au with uniform distribution can form a well-regulated Li covering layer without recognizable Li dendrites. Due to the superior flexibility and robust mechanical properties of SCAu-CC, the structural integrity of the substrate after Li plating remained well preserved.

To investigate the morphology during the Li deposition process, we record the dynamic process of Li deposition for different substrates at a current density of 5 mA cm^{-2} by *in situ* optical microscopy, which further demonstrates that our strategy can suppress the growth of Li dendrites and guide the Li metal plating uniformly. As shown in **Figure 4.7a**, protrusions and dendrites start to appear along the edges of the bare CC current collector and become more and more obvious over time. After 60 min, the surface is full of Li dendrites and dead Li. For the PAu-CC current collector, some Li filaments still grow on the edge during the Li plating process, and the obvious mossy-like dendrites can be found on the surface after 60 min. In contrast, no Li dendrites and dead Li can be observed during the plating process, and the edge of the SCAu-CC current collector

remains smooth. (**Figure 4.7b**) All of these phenomena are in agreement with the SEM images and electrochemical performance.
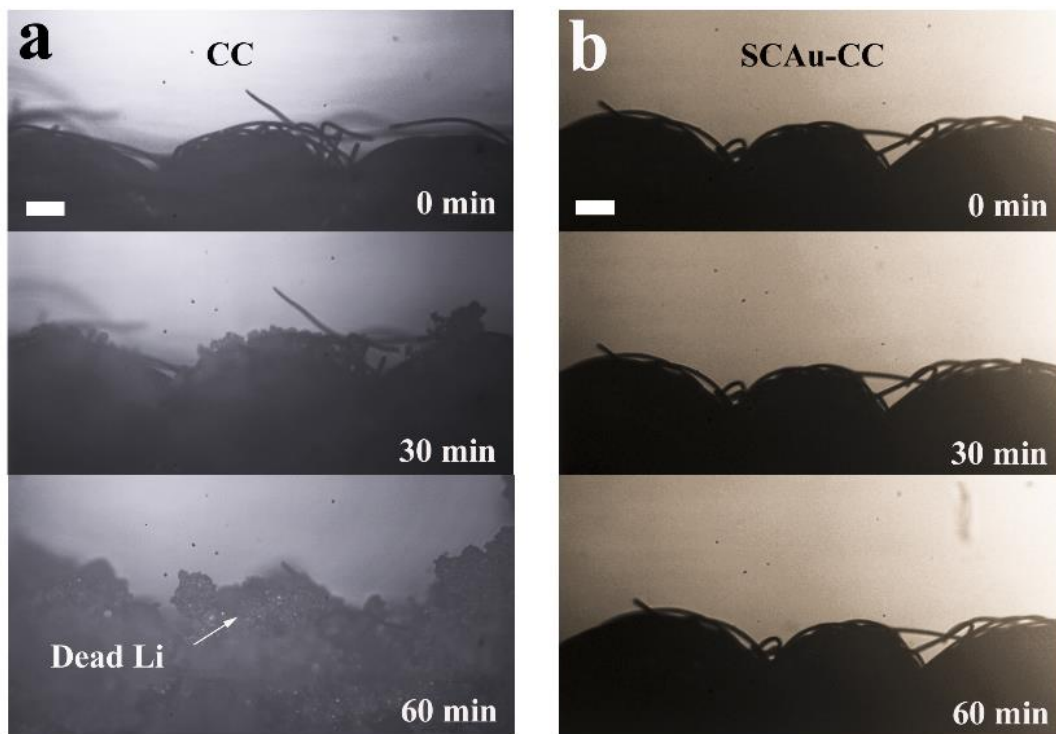
Figure 4.7. In situ optical microscopy observations of the Li deposition process with (a) CC and (b) SCAu-CC. Scale bar, 500 μm

Coulombic efficiency shares a direct relationship with battery efficiency, which can be used to evaluate the sustainability of the anode. The ratio of the total charge extracted from the battery (Li stripping capacity) to the total charge put into the battery over a full cycle (Li plating capacity) is defined as the Coulombic efficiency. During the test of Coulombic efficiency, the galvanostatic plating process of Li metal was operated at the different current densities of with different areal capacities and followed by the stripping process of Li metal to a cutoff voltage of 1.0 V versus Li^+/Li. When tested at a high current density of 4 mA cm^{-2} with corresponding areal capacities of 10.0 and 12.0 mAh cm^{-2}, half cell based on SCAu-CC substrates achieve a high average Coulombic

efficiency, further exhibiting excellent stability of the deeply cyclable Li stripping/plating behavior (**Figure 4.8a**). Compared with the Au nanoparticles, single-atom and cluster Au shows a lower diameter and more surface atoms. Single-atom and cluster Au are evenly distributed on the surface of the carbon skeleton with high surface activity, which serves as the lithiophilic sites to guide the uniform deposition of lithium ions. Furthermore, introducing single-atom and cluster Au may enhance the rate of electron transport while influencing the structural stability of the substrates, both effects potentially leading to enhanced surface reactivity. During the deeply charge-discharge cycles, it can be found that a stable Coulombic efficiency is achieved for the SCAu-CC current collector with a high areal capacity of 15 mAh cm^{-2}. The SCAu-CC current collector exhibits high Coulombic efficiency varies by about 99.91%-99.17%, when evaluated by continuously varying current densities from 0.5 to 5.0 mA cm^{-2} with the corresponding areal capacity from 1.0 to 10.0 mAh cm^{-2}. (**Figure 4.8b**) Even at the high current density of 7.5 and 10.0 mA cm^{-2} with the corresponding areal capacity of 15.0 and 20.0 mAh cm^{-2}, respectively, the average Coulombic efficiencies of cells were 98.23% and 95.90%.

When tested at a narrow condition (under a current density of 0.5 mA cm^{-2} with an areal capacity of 1.0 mAh cm^{-2}), the average Coulombic efficiency for SCAu-CC current collector is about 99.82% for 900 cycles. (**Figure 4.8c**) In contrast, the fluctuating Coulombic efficiency can be observed for CC current collector after initial 283 cycles with a relatively lower Coulombic efficiency of 99.3%, which could be attributed to the decomposition of electrolyte to reform the weak SEI layer during the repeated Li stripping/plating cycles. The battery using CC current collector shows a rapid decay of Coulombic efficiency to less than 88.4% after only 21 cycles when tested at a current density of 3.0 mA cm^{-2}. After 50 cycles, the battery using PAu-CC current collector exhibits a fluctuating Coulombic efficiency. In sharp contrast, the battery using SCAu-CC current collector maintains a stable Coulombic efficiency up to 99.23% for over 80 cycles with a high areal capacity of 6.0 mAh cm^{-2} (**Figure 4.8d**). The SCAu-CC current collector performs superior plating/stripping stability at a high current density of 4.0 mA cm^{-2} with an areal capacity of 10.0 mAh cm^{-2}, which exhibits a high average Coulombic efficiency of 99.16%. All of these indicate that our SCAu-CC current collector can realize deep cycling at the higher current densities and capacities without compromising other electrochemistry properties such as the long-term cycling performance and Coulombic efficiency, which is suitable for commercial large-scale applications of quick-charging systems.

The long-term electrochemical cycling stability of different Li metal anode (with 8 mAh cm^{-2} Li deposit) was explored by testing Li, Li-CC, Li-PAu-CC, and Li-SCAu-CC based symmetrical cells. As shown in **Figure 4.8e**, the Li-based symmetrical cell exhibits much worse performance, which shows the random voltage oscillations with a large overpotential over 168 mV during the repeat cycles at a current density of 2.0 mA cm^{-2} and capacity of 1.0 mAh cm^{-2}. The dendrite-induced short circuit occurs after 70 h, signaled by voltage fluctuations. Li-CC-based symmetrical cell and Li-PAu-CC based symmetrical cell exhibit a fluctuant overpotential of 120.0 mV and 89.8 mV, indicating an uneven Li deposition. For Li-SCAu-CC based symmetrical cell, excellent cycling stability for more than 500 h with a stable and low overpotential of 37.0 mV is achieved. Moreover, the fluctuant overpotential can be observed from Li, Li-CC, and Li-PAu-CC based symmetric cells at a higher current density of 3.0 mA cm^{-2}. It should be noted that Li-SCAu-CC based symmetric cell exhibits stable voltage profiles over 350 h with low hysteresis. Consequently, this indicates that single-atom and cluster Au can seed the nucleation and growth of Li metal, where Li metal can be deposited into the carbon skeleton uniformly and reversibly, further mitigating the degradation of Li metal during repeated cycles.

Li||LiFePO$_4$ cell was first assembled to evaluate the full-cell performance of SCAu-CC based Li metal anode (Li-SCAu-CC anode), as the commercialized LiFePO$_4$ cathode is relatively stable. Li metal anode was predeposited on the surface of the SCAu-CC electrode to prepare the Li-SCAu-CC anode, and the cathode active materials mass of the LiFePO$_4$ electrode is 10.9 mg cm^{-2}. When galvanostatically cycled between 2.5 and 4.0 V, each profile shows the one discharge and charge voltage plateaus corresponding to the two-phase reaction. (**Figure 4.10a**) This is in agreement with the traditional LiFePO$_4$ cell. The specific capacity of Li-SCAu-CC||LiFePO$_4$ cell reaches 124.3 mAh g^{-1} with an average Coulombic efficiency of 99.6% during the cycles at a current density of 0.1 C (1.0 C = 170 mA g^{-1}), which can satisfy the requirements for commercial manufacturing. Such a superior Li-SCAu-CC anode is also employed in the full cell with active LiFePO$_4$ cathode materials mass of 2.6 mg cm^{-2}. As shown in **Figure 4.10c**, a very stable cycling performance over 200 cycles can be observed. The Li-SCAu-CC||LiFePO$_4$ cell exhibits a high specific capacity of 161.5 mAh g^{-1} with a tiny capacity reduction of 0.14% per cycle, which was very close to its theoretical capacity, and a high average Coulombic efficiency near 99.86% is achieved.
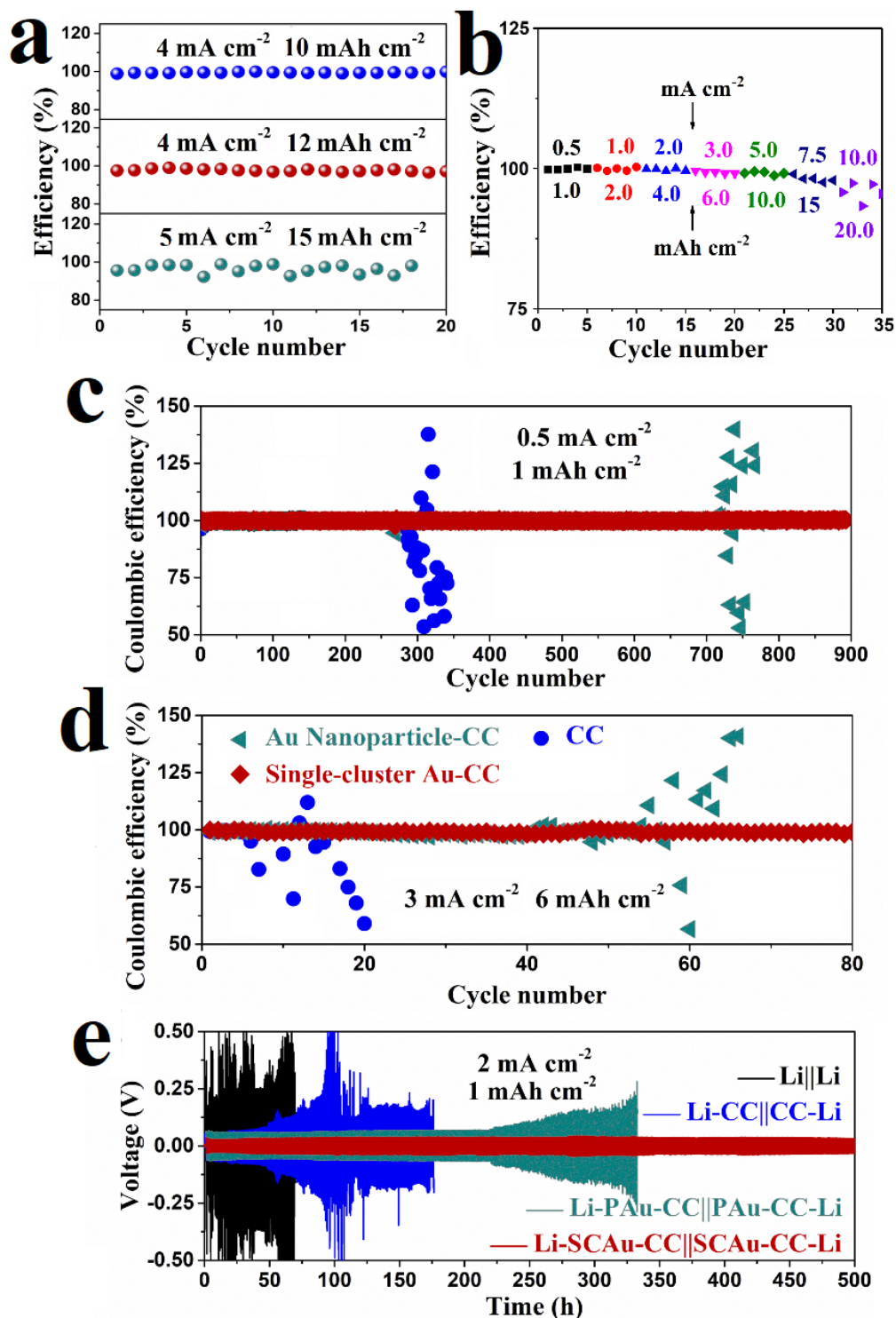
Figure 4.8. Deeply cyclable electrochemical behavior of Li metal batteries. (a) Coulombic efficiency from SCAu-CC electrode under 10.0-15.0 mAh cm⁻². (b) The rate capability of Coulombic efficiency at different areal capacities from 1.0 to 20 mAh cm⁻². Comparison of Coulombic efficiency of Li plating/stripping at current density of (c) 0.5 mA cm⁻² and (d) 3.0 mA cm⁻² with areal capacity of 1.0

mAh cm^{-2} and 6.0 mAh cm^{-2}, respectively. (e) Cycling performance of different symmetric cells at the current density of 2.0 mA cm^{-2} for more than 500 h.
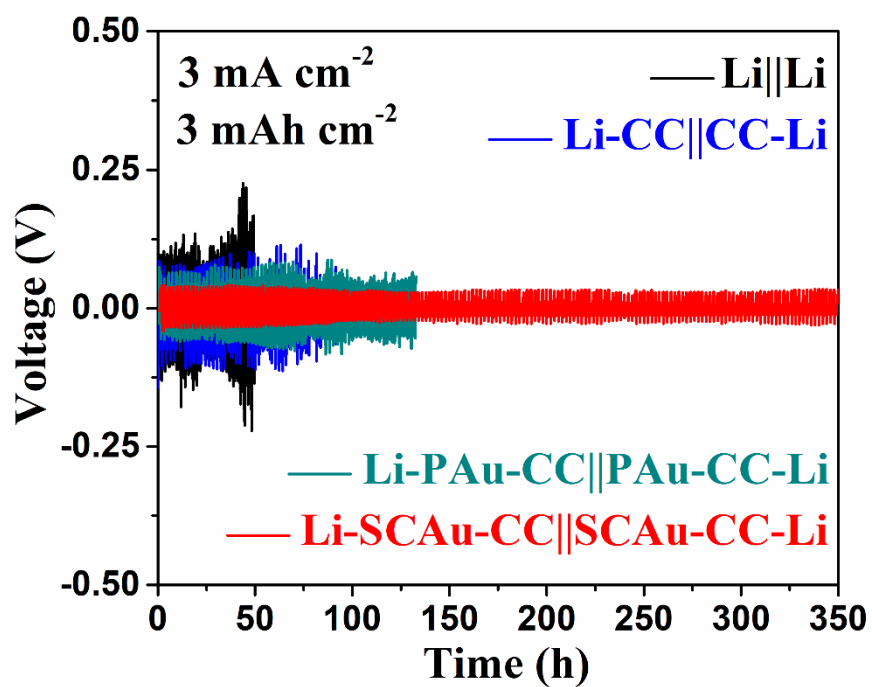
Figure 4.9. Galvanostatic Li plating/stripping profiles of symmetric cells with different anode with the areal capacity of 3.0 mA cm^{-2} at a current density of 3.0 mA cm^{-2}.
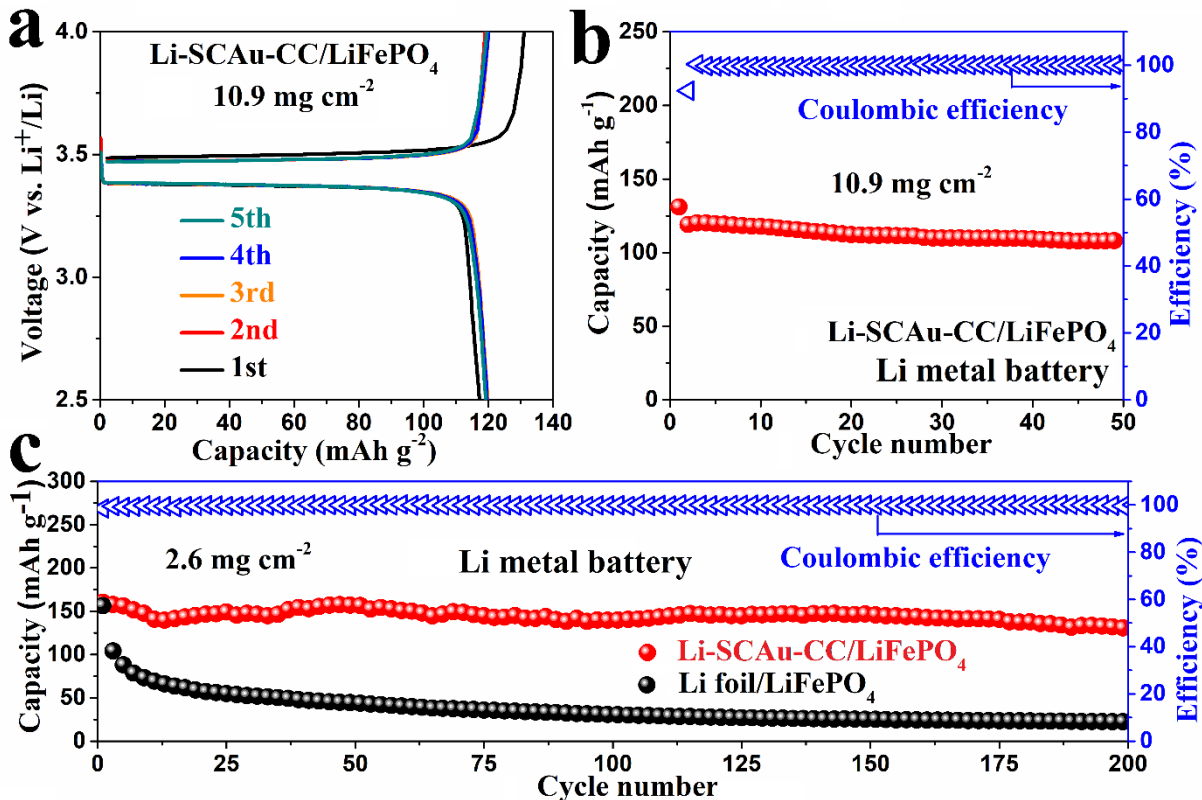
Figure 4.10. High Li metal utilization. (a) Galvanostatic charge-discharge profiles and (b) cycling performance of Li-SCAu-CC/LiFePO₄ metal batteries with the active material loading up to 10.9 mg cm⁻². (c) Long-term cycling performance of Li metal batteries.

4.7   Electrochemical performance in Na-based battery

In the field of Na metal-based batteries, the deposition process of Na deposits was recorded by *in situ* optical microscopy at a current density of 3.0 mA cm⁻². Due to the enhanced local current density, Na-ion flux is more concentrated on the tip of the rough bare Cu foil, known as the "tip effect". The rupture of SEI and unavoidable defects of the Cu foil surface can be acted as the dendritic nucleation seeds and promote the growth of Na dendrites. As shown in **Figure 4.11a**, the dendritic and mossy Na is formed after 30 min plating process on the bare Cu surface. With the continuous deposition of the nuclei, the roughness of the SEI layer amplifies and the Na dendrite proliferates. The uncontrolled growth of Li dendrites becomes more serious with time. For CC

substrates, Na suffers from a relatively high nucleation barrier, and Na nuclei tend to form at the junctions (**Figure 4.11b**). Upon the formation of nuclei, they tended to rapidly grow into Na agglomerates and finally "dead Na" emerged from the agglomerates. In sharp contrast, the introducing Au single-atom on the substrate can regulate Na nucleation and growth during Na plating, and the SCAu-CC substrates show the uniform Na deposition during the 60 min plating process, free from the Na dendrites and "dead Na" (**Figure 4.11c**).
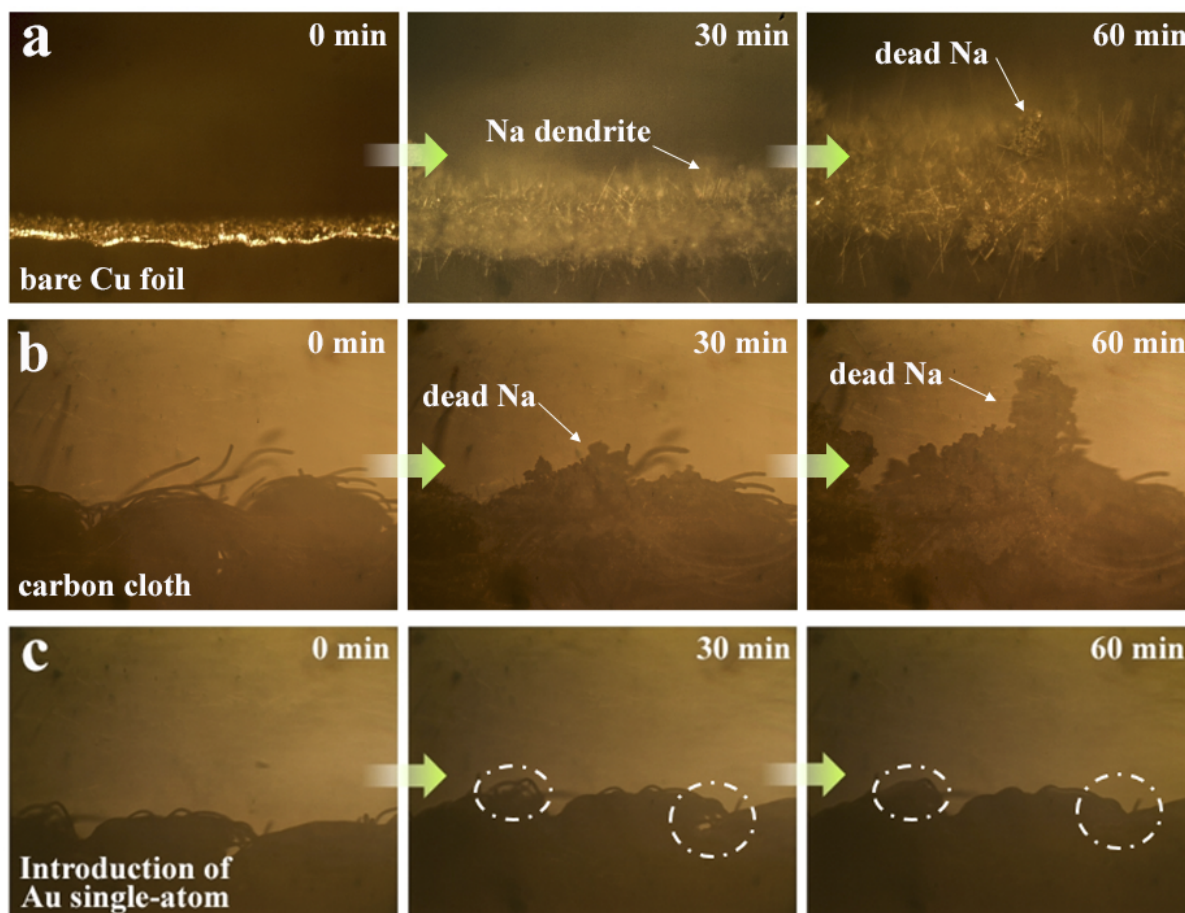
Figure 4.11. Patterned deposition of Na metal. In situ optical microscopy observations of Na deposition process on (a) bare Cu foil, (b) carbon cloth, and (c) SCAu-CC at 3.0 mA cm^{-2}.
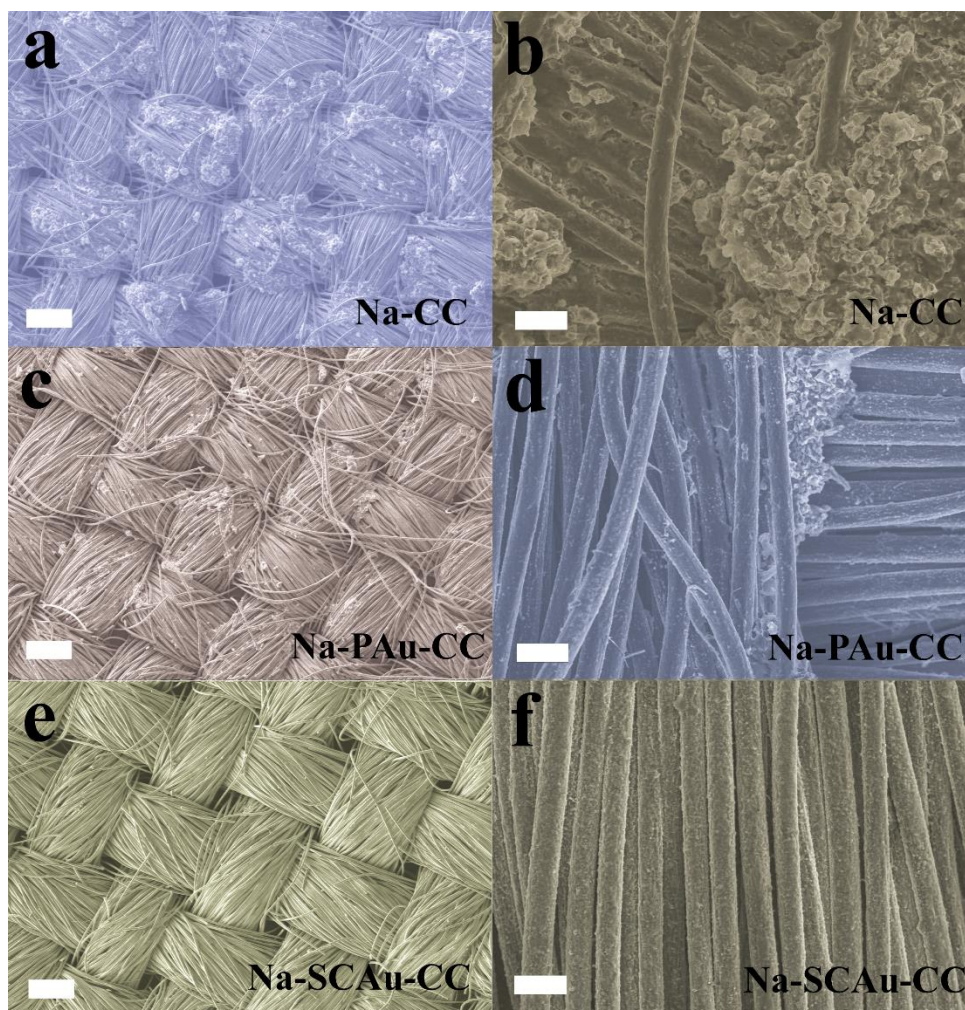
Figure 4.12. Morphology characterization of (a,b) CC, (c,d) PAu-CC and (e,f) SCAu-CC after plating 4.0 mAh cm^{-2} of Na metal. Scale bar, 500 μm and 50 μm.

These observations from *in situ* optical microscopy are also in agreement with SEM analysis of substrate surface after deposition 4.0 mAh cm^{-2} of Na metal. As shown in **Figure 4.12a, b**, many dendritic Na particles can be observed from the SEM images of CC substrates, which are related to the nonuniform ionic flux during cycling. For PAu-CC, mossy Na and a smaller fraction of dendrites are growing on the periphery of the carbon skeleton (**Figure 4.12c, d**). The Au particles are unevenly distributed on the surface of the carbon fiber network, and part of the particles are stacked and held together. The stack will become the hot spot for Na plating under repeated cycling conditions, leading to nonuniform Na nucleation/growth. In contrast, it can be clearly observed

95

that the SCAu-CC network is uniformly coated with metallic Na, and no Na dendrite or mossy Na can be observed (**Figure 4.12d, e**). Introducing single-atom and cluster Au can result in a uniform Na plating and suppress the Na dendrite formation. Notably, the structural integrity of the Na-SCAu-CC anode still maintains its fibrous morphology, further indicating the superior flexibility and robust mechanical property.
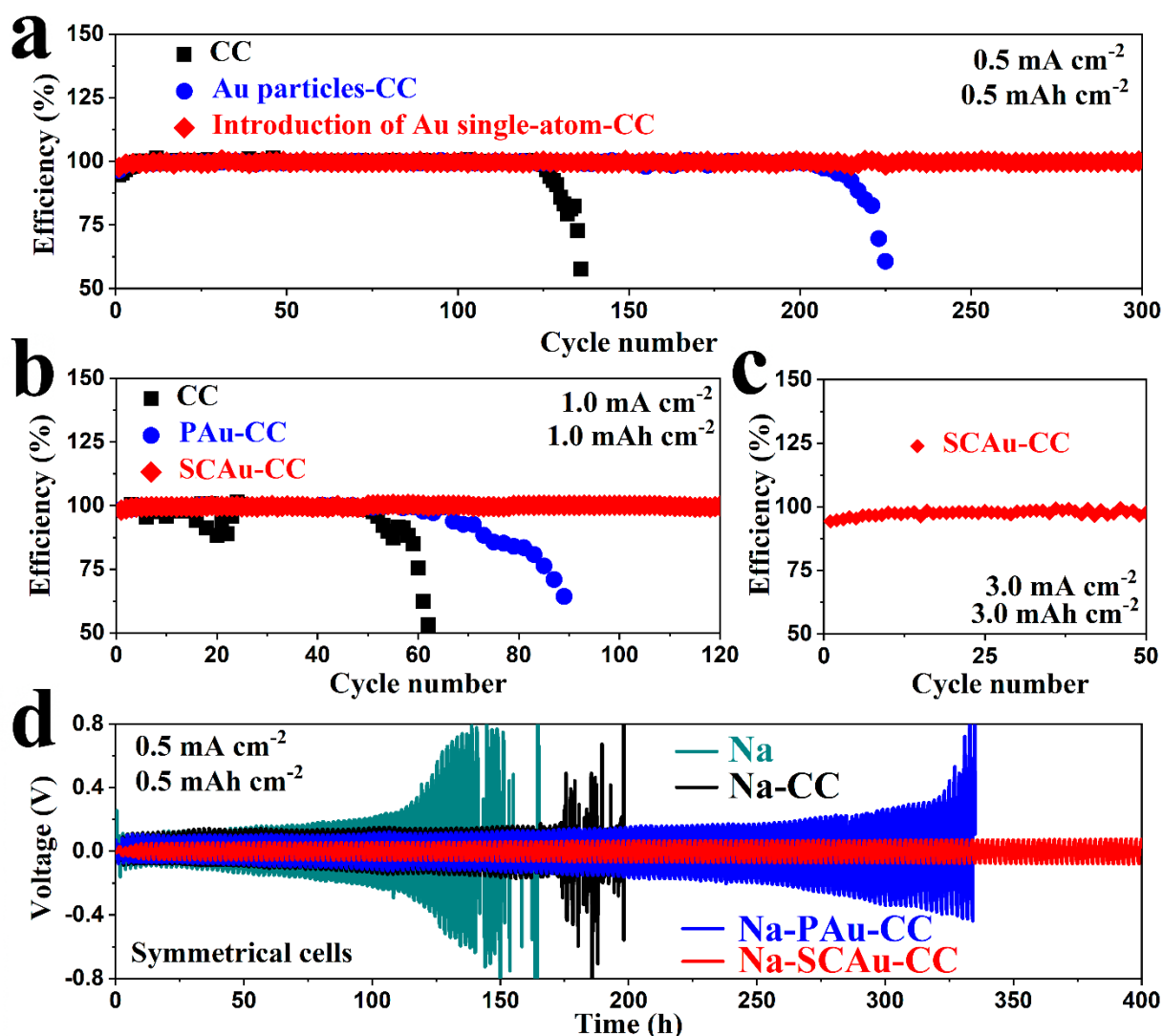
Figure 4.13. Cycling stability of Na plating/stripping process. The Coulombic efficiency of CC, PAu-CC, and SCAu-CC substrates (a) at a current density of 0.5 mA cm^{-2} and a deposition capacity of 0.5 mAh cm^{-2} and (b) at a current density of 1.0 mA cm^{-2} and a deposition capacity of 1.0 mAh cm^{-2}. (c)

Coulombic efficiency of Na deposition at a current density of 3.0 mA cm^{-2} and a deposition capacity of 3.0 mAh cm^{-2}. (d) Comparison of the cyclability of a symmetric cell assembled by Na foil, CC, PAu-CC, and SCAu-CC substrates with a limited Na source of 4.0 mAh cm^{-2}.

Figure 4.13a shows the Coulombic efficiency of the CC current collector obtained at the current density of 0.5 mA cm^{-2} with the corresponding area capacity of 0.5 mAh cm^{-2}, which starts at ~94.6% and quickly decays to 57.8 % within 120 cycles. Similarly, the PAu-CC shows rapid decay of Coulombic efficiency after 202 cycles. By contrast, the SCAu-CC electrode exhibits a long cycle life of more than 300 cycles with an average Coulombic efficiency as high as 99.73%. Then, when elevating at the area capacity of 1 mAh cm^{-2} and a high current density of 1.0 mA cm^{-2}, a fluctuant Coulombic efficiency of the CC current collector can be observed, and followed by a sudden dip (**Figure 4.13b**). The Coulombic efficiency of the PAu-CC electrode starts at about 96.1% but drastically decays after only 65 cycles. Impressively, the SCAu-CC electrode still delivers a fairly stable and high Coulombic efficiency of 99.54% for 120 cycles, and the corresponding plating/stripping curves are shown in **Figure 4.14a**. The above results further suggest that the introduction of Au single-atom can regulate the local Na ion flux distribution and reduce the local current density, promoting even deposition of Na and improving electrochemical performance. With the increase of the current density up to 3.0 mA cm^{-2}, the Coulombic efficiency of the SCAu-CC electrode could still maintain about 99.5% for 50 cycles (**Figure 4.13c**). The Au single atoms on the substrates can maintain a stable and high Coulombic efficiency for long cycling, which not only has great affinity and interaction with Na ions in the electrolyte but also serves as the sodiophilic sites to favor Na plating with minimum nucleation barrier, providing the stable and dendrite-free Na deposition.

Electrochemical impedance measurements were carried out to study the interfacial stability of symmetrical cells at the open circuit condition prior to electrochemical cycling. The semi-circle of the Nyquist plots is corresponding to the SEI resistance and the charge transfer resistance at the anode surface (**Figure 4.14b**). 4.0 mAh cm^{-2} Na deposits were restored into the electrode to prepare the Na-SCAu-CC and Na-CC electrodes. Owing to the formation of passivation films, the symmetrical cell of bare Na foil shows a large interfacial resistance of 1280 Ω. The interfacial

resistances of Na-SCAu-CC symmetrical cell (224 Ω) are much lower than that of Na-CC symmetrical cell (337 Ω). Specifically, **Figure 4.13d** shows the Voltage-time profiles of the symmetric cells using Na-SCAu-CC||Na-SCAu-CC, Na-CC||Na-CC, and Na||Na electrodes. Due to the particular property of single Au atoms, the consistently low overpotential of Na-SCAu-CC||Na-SCAu-CC symmetrical cell is only about 54 mV when measured at the current density of 0.5 mA cm^{-2} with an area capacity of 0.5 mAh cm^{-2}. The voltage hysteresis can be retained even after cycling for 400 h, which is excellent than the previously reported results, suggesting that SCAu-CC electrodes prevent the cyclic regeneration efficiently. In contrast, Na||Na cells exhibit a dramatic overpotential increase followed by an internal short circuit, and Na-CC||Na-CC cells show a continuous increase in overpotential from 57 mV to 153 mV.
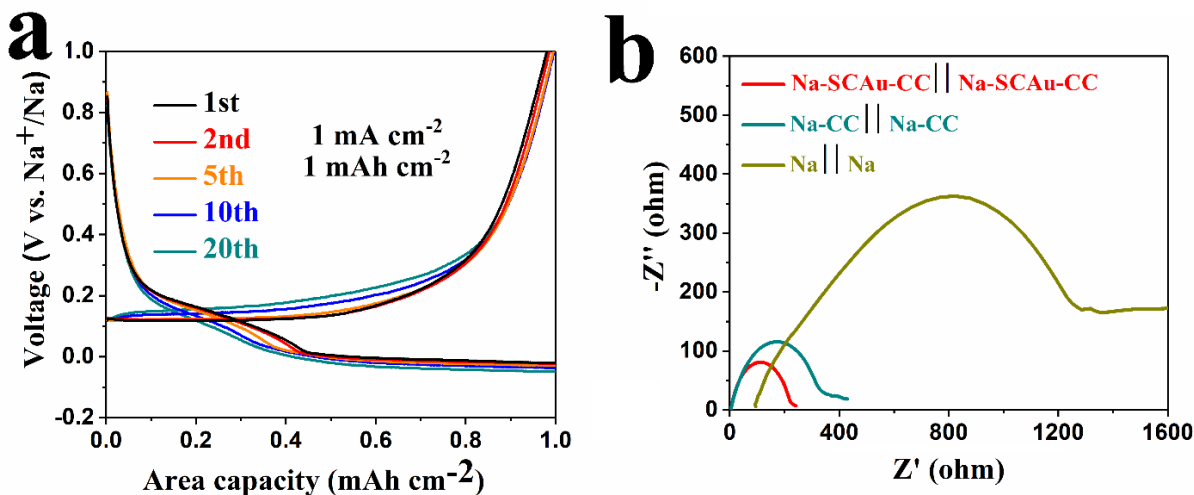
Figure 4.14. (a) Voltage profiles of the Na plating/stripping process of the first five cycles with the areal capacity of 1.0 mAh cm^{-2} at a current density of 1.0 mA cm^{-2}. (b) EIS Nyquist plots of the symmetric cells.
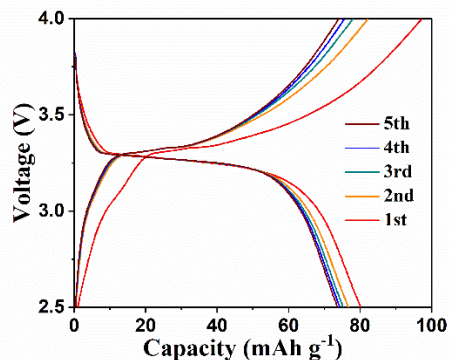
Figure 4.15. Voltage profiles of the charge/discharge process for the full cell.

The high Coulombic efficiency and small voltage hysteresis of Na stripping/plating within the SCAu-CC electrode allow us to fabricate Na-SCAu-CC anode with a limited amount of Na deposits, and so potentially realize a high energy density full cells with an excellent cycling life. In order to further confirm the advantages of SCAu-CC substrates, a proof-of-concept study was conducted on full cells using Na-SCAu-CC as anode and $Na_3V_2(PO_4)_3$ (NVP) as the cathode (**Figure 4.16a**). Different capacities of Na metal were predeposited on the substrates to prepare the Na-SCAu-CC and Na-CC anodes. The full cell was galvanostatically cycled between 2.5 and 4.0 V with the active material loading of 2.0-2.2 mg cm^{-2}. **Figure 4.15** shows the charge-discharge profiles of the full cells at 0.5 C. A couple of the oxidation and reduction peaks that are attributed to the V_4^+/V_3^+ redox couples can be clearly seen for the first five cycles. As shown in **Figure 4.16b**, 4.0 mAh cm^{-2} Na deposit was restored into the SCAu-CC electrode, and the full cell delivered an initial capacity of 79.6 mAh g^{-1} at a current density of 0.5 C (1 C = 117.6 mA g^{-1}). Furthermore, the full cell can be cycled for more than 1000 cycles with a tiny capacity reduction of 0.016% per cycle, and the Coulombic efficiency remains at around 99.76 %, manifesting a much-prolonged cycling lifetime. The cycling stability of the full cell with a Na deposit of 2.0 mAh cm^{-2} is further demonstrated in **Figure 4.16c**. Na-SCAu-CC‖NVP full cell can deliver a capacity of 78.4 mAh g^{-1} up to 200 cycles with a Coulombic efficiency of ~99.4%. Na-CC‖NVP full cell is able to offer a low capacity of only 63.4 mAh g^{-2} at 0.5 C. Additionally, the capacity of Na-CC‖NVP and Na-Cu‖NVP full cell starts to decay drastically after only 64 and 35 cycles, respectively, owing to the

complete consumption of excess Na metal. Similar behavior can be observed with an extra-low Na areal capacity of 1.0 mAh cm^{-2}, which exhibits high utilization of Na for Na-SCAu-CC electrode. (**Figure 4.16d**)
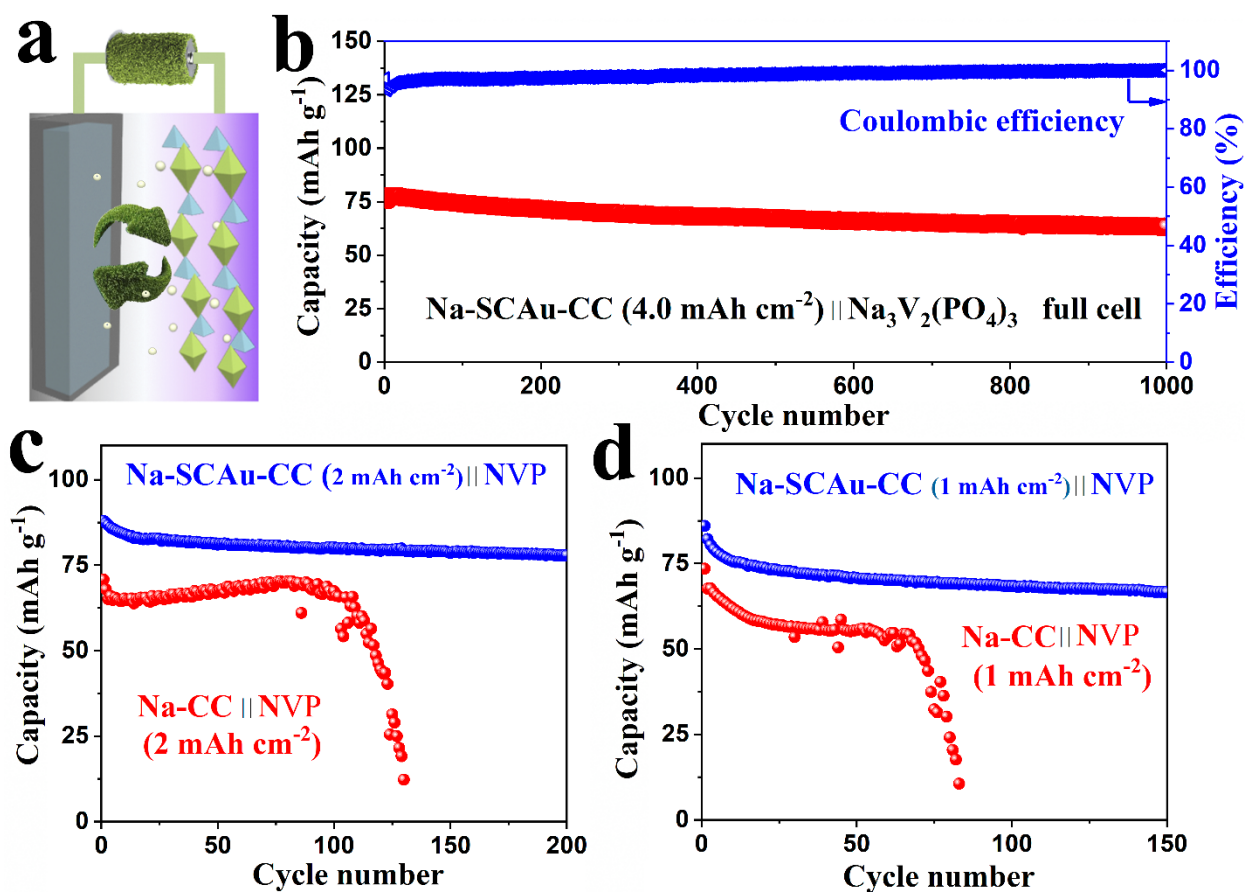
Figure 4.16. High Na utilization adapts to full cell. (a) The schematic illustration of full cell assembled with Na-SCAu-CC as the anode (with different limit Na source) and Na$_3$V$_2$(PO$_4$)$_3$ (NVP) as the cathode. **(b)** The long-term cycling stability of full cell using 4.0 mAh cm^{-2} Na on SCAu-CC. The cycling stability comparison of SCAu-CC and CC electrode using **(c)** 2.0 mAh cm^{-2} and **(d)** 1.0 mAh cm^{-2} Na.

4.8   Conclusions

In conclusion, we introduce single-atom and cluster Au as a novel "loadstone" of alkali metal on a modified carbon substrate, which can seed the metallic Li/Na nucleation and suppress uncontrolled dendrite formation at an atomic level. DFT calculation predicts the higher binding energy, revealing the guiding function between atomic-scale Au and the alkali metal. *In situ* optical microscopy observations are used to exhibit the substrate-dependent metal nucleation processes during their electrochemical plating process, where Li/Na ions are seeded to form smooth alkali-metal anode without any dendritic problems. In our approach, the obtained Li metal anode exhibits excellent long-term cycling stability of more than 900 cycles and deeply cyclable performance with a high area capacity of 20.0 mAh cm^{-2}. The Li-SCAu-CC||LiFePO$_4$ full cell exhibit excellent cycling stability with high specific capacity for more than 200 cycles. Meanwhile, for Na metal batteries, it also achieves high Coulombic efficiency of 99.73% for 250 cycles and a long lifespan of more than 400 h with low overpotential. Compared with the conventional current collector, our works provide s a sustainable and low-cost route for modified alkali metal anode by atomic metal with dendrite-free structure and high utilization, which promote the realization of large-scale energy storage applications.

5 SECTION III. Mega high utilization of sodium metal anodes enabled by single zinc atom sites

Over the past four decades, Li-ion batteries have attracted attention due to their lowest redox potential and small ionic size of Li. High energy and low-cost Li-ion batteries are promising for large-scale energy storage devices such as consumer electronics, portable electronics, electric vehicles, and grid energy storage.[21-23] However, the energy density of commercial Li-ion batteries (such as graphite/$LiFePO_4$ cell and graphite/$LiNiCoMnO_2$ cell) has increased from 80 $Wh\ kg^{-1}$ to 300 $Wh\ kg^{-1}$, approaching to their physicochemical limits.[67-73] High energy densities Li-based batteries, such as Li metal batteries, become the study focus due to their high theoretical capacity (3860 $mAh\ g^{-1}$) and extremely low redox potential (-3.04 V vs S.H.E.), which is ten times higher than graphite-based battery.[159-164] Unfortunately, the uncontrolled formation of dendrites, the unstable SEI layer, and large volume change during charging and discharging processes hinder the commercial applications of Li metal anodes, which reduce the cycling life and further lead to safety hazards such as thermal runaway and internal short circuits. Due to the uneven distribution and shortage of Li-containing resources, the continuous rise in the cost of Li-ion batteries (LIBs) has spurred research efforts in battery systems using other alkali metal ions, such as Al^{3+}. Mg^{2+}, Na^+, and K^+. Among them, following a similar mechanism and chemical property of LIBs, Na-ion-based batteries (NIBs) have drawn considerable interest, and sodium minerals are more abundant and available than lithium resources.[122-126] Conventional Na-S battery system offers a high energy density and theoretical capacity and of 1230 $Wh\ kg^{-1}$ and 1672 $mAh\ g^{-1}$, but they need to be operated at a high temperature over 300 °C, leading to the decline of the energy efficiency and some safety issues related to the highly reactive molten Na metal and corrosive molten sulfur. As a result, room temperature NIBs are beginning to garner interest in the scientific community. Pairing Na metal anodes with oxygen (O_2) or sulfur (S) based cathodes, the assembled room temperature Na-O_2 or Na-S battery system can exhibit high theoretical specific energies of 1605 and 1274 $Wh\ kg^{-1}$, which are triple or quadruple times larger than that of corresponding Li based batteries.[222-226] However, Na metal anodes are still facing tremendous challenges, similar to that reported in Li metal anode. Metallic Na can easily react with carbonate electrolytes, resulting in the formation of a weak SEI layer. Owing to its high reactivity, uncontrollable side reactions, and continuous consumption of both Na and electrolyte

can cause poor electrochemistry performance and uncontrolled Na dendritic growth, leading to safety hazards such as internal short-circuiting, thermal runaway, or explosion.[226-233]

To date, to address the stability issue of the Na metal anode, several achievements have been obtained, which are inspired by the improvement of the Li metal anode. Some works have shown that the deposition behavior and interface stability of alkali metal anodes can be greatly reinforced by modifying the electrolyte and additives, engineering protective interface layers, and constructing three-dimensional (3D) host structures. Among various approaches, 3D host structures, such as carbon paper and copper (Cu) foam, have attracted considerable interest, as they can reduce the local current density, regulate the metal deposition, inhibit the dendrite growth, and homogenize the ion flux. However, Li deposition in 3D Cu or Carbon-based structure is hampered by their poor affinity for Li metal, where Li shows poor wettability on these substrates and nucleation overpotentials occur during Li nucleation, further indicating the unfavorable Li deposition on Cu/Carbon-based substrates.[285-294]

Recently, Cui and co-workers studied the overpotentials of various materials (Au, Ag, Mg, Zn, Cu, Ni, Pt, Si, C, Al, and so on) on Li nucleation and concluded that the formation of a solid solution with lithium would help lithium nucleation because of the reduced Li/host interfacial energy.[250-255] No overpotential was needed to nucleate Li metal on Au, Ag, Zn, or Mg. Au and Ag particles providing a new way of heterogeneous seeded growth to control Li plating on the appointed substrates, resulting in a low nucleation barrier for Li-ions deposition. Noble metal hosts for Li metal are expected to address the imperfection of dendrite growth and interface instability of the anode, exhibiting the great development potential for Na metal anode. However, as one of the most common noble metals, Au and Ag are so expensive that they would be unaffordable as the substrates of metal batteries for large-scale production. Downsizing noble metals to single atoms or clusters provide an effective way to decrease Au/Ag dosage and maximize atomic utilization efficiency. The single atom or cluster modified metal anodes are analogous to noble metal foil anode, but, unlike many metal anodes, reaction at the active site can be understood with atomistic detail on a single atom modified metal anode.[260-267] Therefore, designing a Na deposition matrix with single atoms makes more sense for the Na metal anode. Guiding Na deposition at an atomic level and inhibiting uncontrolled growth of Na dendrites at nucleating stages may open up a new dimension for the design of safe and efficient Na metal anodes.

5.1 Synthesis of Na Metal Anodes

A novel Na metal anode with record-high utilization and long-term cycling stability is designed, using carbon-substrate-supported nitrogen-anchored zinc (Zn) single atoms as a current collector (Zn_{SA}-N-C). Typically, 1.875 g 2-methylimidazole was also dissolved in methanol (40 mL); meanwhile, 1.0 g $Zn(NO_3)_2 \cdot 6H_2O$ was dissolved in methanol (40 mL). Subsequently, two solutions were mixed together and transferred to a Teflon-lined stainless steel autoclave with a piece of carbon cloth (CC, 2×2 cm^2). The materials were maintained at 120 °C for 6 h, and the obtained Zn-ZIFs-C were thoroughly washed with ethanol several times. Then, the product was annealed in a quartz tube under the protection of the N_2 atmosphere (100 sccm) at a heating rate of 5 °C min^{-1} with a high temperature of 900 °C for 1 h.

The Zn_{SA}-N-C was used as the working electrode, and Na foil was used as the counter electrode. The electrolyte was 1 M sodium perchlorate ($NaClO_4$) in ethylene carbonate (EC)/dimethyl carbonate (DMC) (1:1 by volume) with 5 wt % fluoroethylene carbonate (FEC). After the activation process of one cycle between 0-1 V (versus Na$^+$/Na) at 0.5 mA cm^{-2}, Na was deposited on the Zn_{SA}-N-C at the current density of 1.0 mAh cm^{-2} by a galvanostatic discharging process.

5.2 Synthesis of NVP Cathode

2.5 g $NH_4H_2PO_4$, 1.32g V_2O_5, 1.41 g Na_2CO_3, and 0.4 g 3-hydroxytyramine hydrochloride were used in stoichiometric proportions to form a mixed solution by stirring in 50 mL distilled water. This mixture was then dried at 50 °C via forced-air drying. The precursor was preheated at 350 °C in flow argon for 4 h, reground, and re-fired at 700 °C in an argon atmosphere for 8 h.

The NVP electrodes were prepared by making thoroughly mixed by 70 wt% active materials (dried NVP), 20 wt% acetylene black, and 10 wt% polytetrafluoroethylene (60 wt% dispersion in water)

on the Al foil (0.1 mm). After being dried in a vacuum at 60 °C for 6 h, the battery was made in Glovebox (Shanghai Mikrouna Mech. Tech. Co., Ltd), where the electrolyte was 1.0 M $NaClO_4$ in EC+DMC (1:1 by volume), and FEC (5%).

5.3   Electrochemical Measurement

In the Na metal battery, the cathode electrode was composed of active material, carbon black, and polyvinylidene fluoride in a ratio of 8:1:1 by using N-methyl-2-pyrrolidone as the solvent and an aluminum foil as the current collector. CR2032-type coin cells were employed in an argon-filled glove box, with the addition of 1.0 M $NaClO_4$ in EC:DMC (1:1 by volume) with FEC (5 wt%). For symmetric batteries, two same Na metal anodes using various current collectors were reassembled into CR2032-type coin cells with 80 mL electrolyte and a Waterman separator. The full-cell assembled with Na-ZnSA-N-C‖$Na_3V_2(PO_4)_3$ and half-cell assembled with ZnSA-N-C‖Na foil were tested on a CT2001A cell test instrument (Wuhan LAND Electronic Co., Ltd) and VMP3 (BioLogic Science instrument Co., Ltd) electrochemical workstation, respectively. For the measurement of Coulombic efficiency, a fixed amount of Na was plated onto the substrates and stripped when charging to 1.0 V during each cycle.

5.4   Material Characterization

X-ray Absorption Near-Edge Structure (XANES) and Extended X-ray Absorption Fine Structure (EXAFS) data were collected on beamline 14W at the Shanghai Synchrotron Radiation Facility (SSRF) and on beamline 01C at the Taiwan Light Source (TLS). The microstructure of all the samples was observed by field emission scanning electron microscope (SU8010, Hitachi, Ltd) at

an acceleration voltage of 10 kV and field-emission transmission electron microscopy (FEI Tecnai $G^2$20, FEI NanoPorts, Ltd). Subangstrom-resolution aberration-corrected scanning transmission electron microscopy (STEM, FEI Titan ETEM G2 80-300) was used to characterize the dispersion and configuration of single atoms. X-ray diffraction of patterns was carried out on the D8 ADVANCE instrument (Bruker AXS GmbH Co., Ltd).

5.5 Computational Details

The Gaussian 09[3] suite of the program is used to simulate their covalent interaction, where is performed by utilizing the model and the density-functional theory (DFT). All the atoms are simulated by using the 6-31G (d+p) basis set, and the gas-phase Gibbs free energy is used during all the present discussions. The stationary points as local minima or transition states are characterized by analyzing vibrational frequency within the same theoretical level. The binding energy (E) was defined as the energy difference between Na ion with different substrates (E_t) and the summation of corresponding substrates (E_1) and Na ion (E_2): E = E_1+E_2-E_t. Basis set superposition error had been considered in the calculation of binding energy.

5.6 Results and Discussions

The original intention of this chapter by introducing single atoms is to spontaneously regulate Na deposition and explore the nucleation behavior of Na. First, we use carbon cloth as the substrate. Initially, the tetrahedral framework topologies of zinc contained zeolitic imidazolate frameworks (Zn-ZIFs) were uniformly covered the surface of the carbon-based skeleton with different polyhedral morphology of ca. 50-100 nm in diameter by a solvent thermal method (**Figure 5.1**),

where the metal centers are connected by four imidazolate linkers. Zn metal precursors were trapped in the cage of the resultant Zn-ZIFs, incorporated as the nodes of MOF skeleton, and single Zn atom sites were obtained after pyrolysis under the protection of the N_2 atmosphere owing to the corresponding cage confinement, long distances between adjacent metal nodes, and strong coordination strength. **Figure 5.2a,b** show the SEM and TEM images of Zn_{SA}-N-C, where no Zn nanoparticles can be observed. High-angle annular dark-field scanning transmission electron microscopy (HAADF-STEM) was used to discern individual heavy atoms. The formation of Zn single atoms is further confirmed by the HAADF-STEM image, and the single Zn atom sites appear as bright spots due to the high Z-contrast. **Figure 5.2c** clearly shows that the bright spots corresponding to Zn single atoms are uniformly dispersed on the surface of the substrate.

The chemical state and crystal structure of different substrates were further investigated by XPS and XRD. From **Figure 5.3a,** XRD patterns show the difference between CC, Zn-ZIFs-C, and Zn_{SA}-N-C, where the XRD pattern of Zn-ZIFs-C between 10 and 20° matches well with the corresponding pattern of ZIF-7. Similar XRD patterns can be observed between CC and Zn_{SA}-N-C. The atomic structure of the Zn_{SA}-N-C substrate shows that a weak intensity corresponding to Zn 2p can be detected in the corresponding XPS survey spectra (**Figure 5.3b**). All the above observations indicate that Zn species in Zn_{SA}-N-C substrates are mainly distributed in the form of single-atom sites in our strategy.
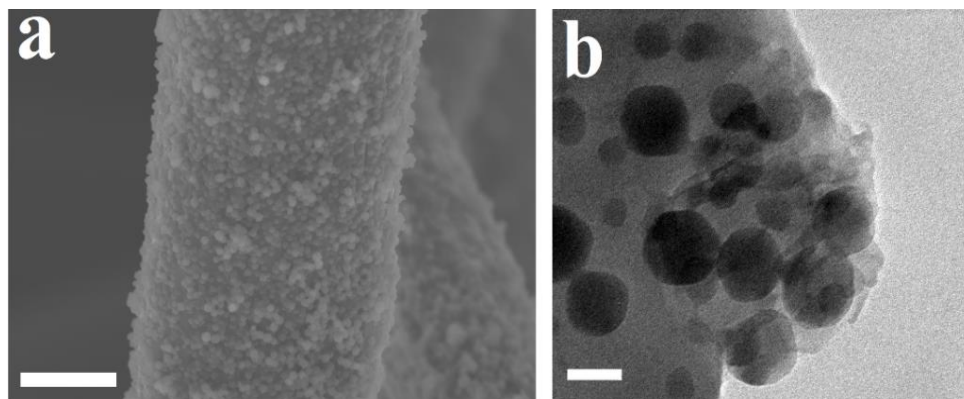
Figure 5.1. (a) SEM and (b)TEM images of Zn-ZIFs-C, where particles are dispersed on the surface. Scale bar, 5 μm, and 50 nm.
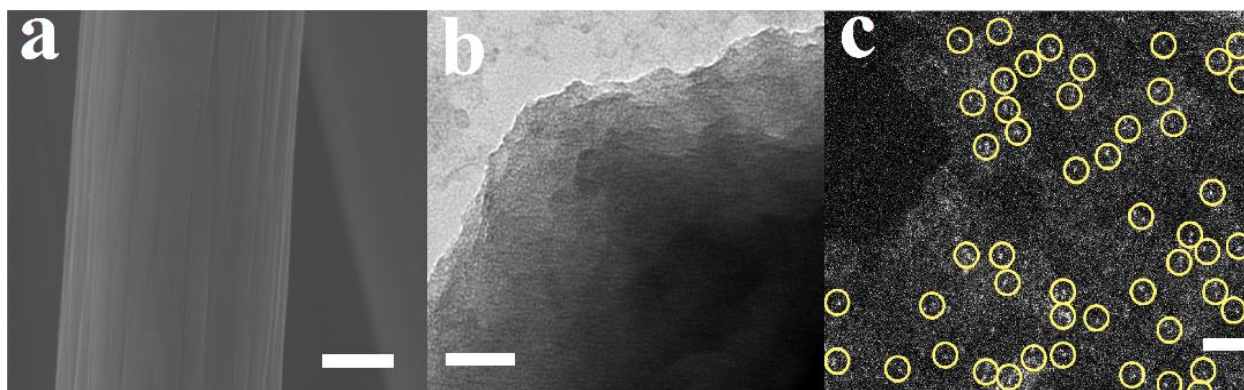
Figure 5.2. (a) SEM, (b) TEM, and (c) HAADF-STEM images of Zn$_{SA}$-N-C, and Zn Single atoms are highlighted in yellow circles. Scale bar in a, b, and c equal to 5 μm, 50 nm, and 2 nm.

To further elucidate the existence form of the zinc species in Zn$_{SA}$-N-C, the extended X-ray absorption fine structure (EXAFS) spectra and normalized X-ray absorption near edge structure (XANES) spectra for Zn K-edges with the comparison to a standard ZnO foil were used to probe the local structure of Zn in Zn$_{SA}$-N-C. As shown in **Figure 5.3c,** the XANES curve of Zn$_{SA}$-N-C exhibits near-edge absorption energy close to those of ZnO foil, where the white-line intensity of Zn$_{SA}$-N-C is similar to ZnO foil, implying that Zn single atoms carry positive charges close to +2. The electrons are inclined to transfer from Zn single atoms to CC substrates, further demonstrating that the electronic property of the system can be effectively tuned after introducing single atoms. More information of the Zn atomic structure in Zn$_{SA}$-N-C can be revealed from the Fourier transformed k-weighted χ(k) function of EXAFS spectra. As shown in **Figure 5.3d**, the Zn$_{SA}$-N-C only exhibits a single main peak at 1.58 Å, attributed to the Zn-N/Zn-O scattering paths, while the Zn-Zn peak at 2.92 Å is not observed, further indicating the successful synthesis of Zn single atoms.
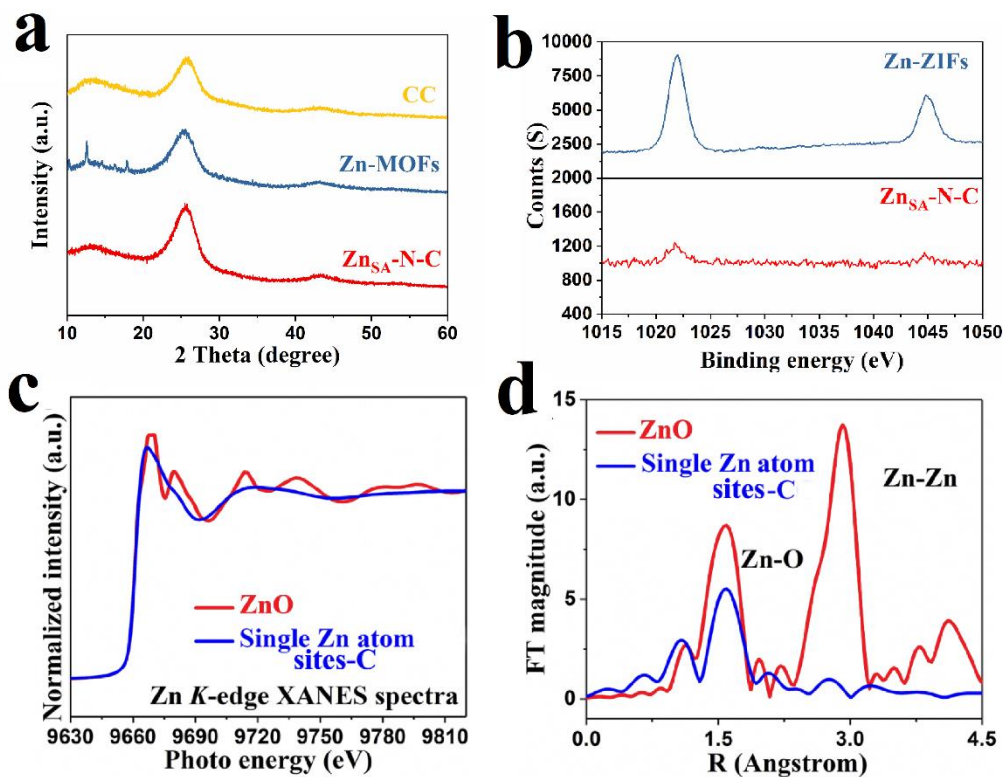
Figure 5.3. (a) The XRD profiles of different substrates. (b) Zn 2p spectra of Zn-ZIFs and Zn$_{SA}$-N-C. (c) Zn K-edge XANES spectra of the samples. (d) Zn K-edge Fourier transformed EXAFS spectra.

Na plating behavior is similar to Li plating behavior. From **Figure 5.4a**, the rough surface with many micro-structured bumps could result in uneven charge distribution on the surface of traditional Cu foil, where the Na ions can deposit faster on the tips rather than the Cu surface due to the concentrated ion flux. The newly generated Na deposits aggravate the roughness of the surface and further promote the growth of the dendritic structures by the same mechanism. On the other hand, the uneven structures on the surface are often accompanied by unstable SEI layers, which in turn accelerates the growth of the Na dendritic structure. The carbon cloth-based substrate shows lower nucleation barriers than that of Cu foil, but still hamper Na deposition on them, resulting in locally enhanced Na ion flux and promoting the growth of Na dendrites (**Figure 5.4b**). The formation of Na dendrites, even dead Na, cannot join the cycles, which can reduce the

Coulombic efficiency. Moreover, the uncontrolled growth of Na dendrites and unstable SEI layers ineluctably plague the practical applications of Na metal anode, further leading to some safety issues, such as thermal runaway, fires, or explosions. In contrast, a uniform Na deposit layer without any dendritic structure is expected for Zn_{SA}-N-C from **Figure 5.4c**. First, the single Zn atom sites are uniformly dispersed on the carbon cloth-based substrate which is confirmed by EDS mapping images and HAADF-STEM images, which serve as the sodiophilic nucleation sites to guide Na ion deposition. The as-produced numerous Na nuclei directly guide the following Na deposition process. The boundaries of Na deposits are drawn together, and finally, a smooth Na deposit layer is formed.
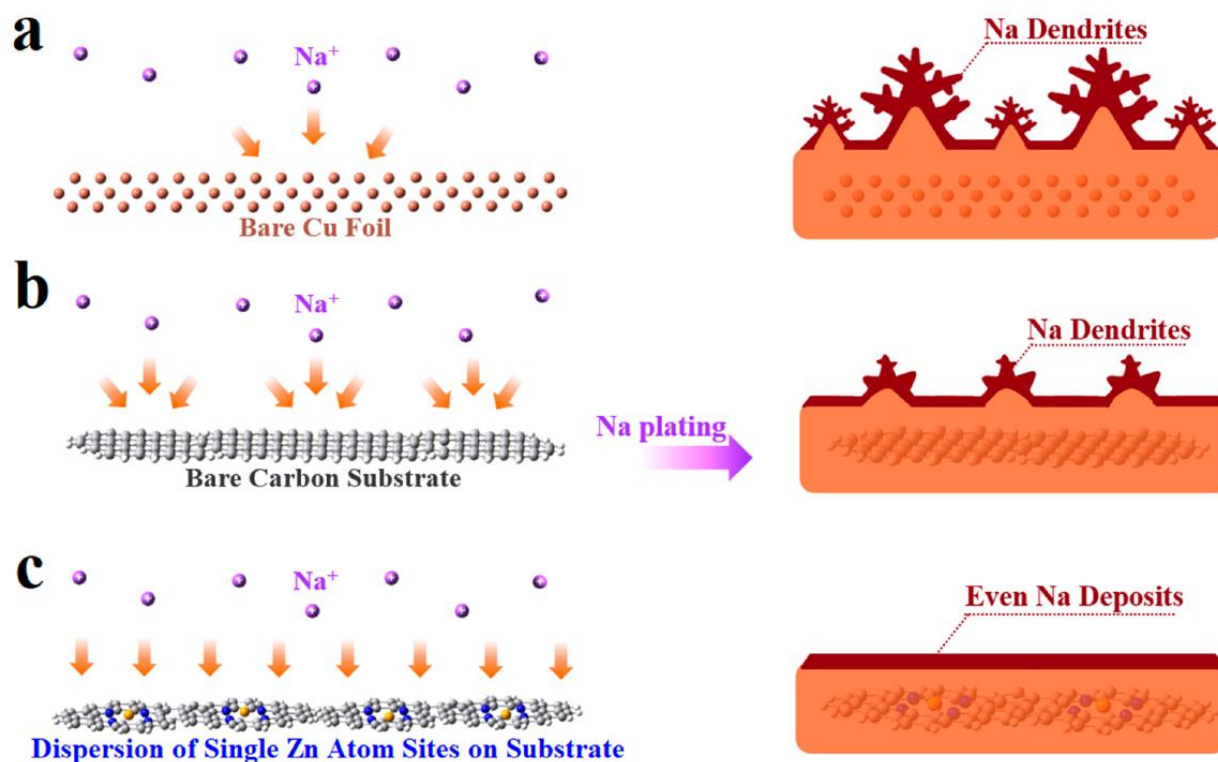
Figure 5.4. Schematic illustration of Na plating behavior on (a) Cu foil, (b) carbon substrate, and (c) Zn_{SA}-N-C electrodes. Serious Na dendrites form on the surface of bare Cu foil, which will pierce through the separator and form dead Na, causing the shorting between two electrodes. For carbon substrate, there are still some Na dendrites growing on the surface. In contrast, Na metal is selectively nucleated on uniform single Zn atom sites with a negligible nucleation overpotential, and the edge of the substrate remains smooth, free from pulverization or Na dendrites.
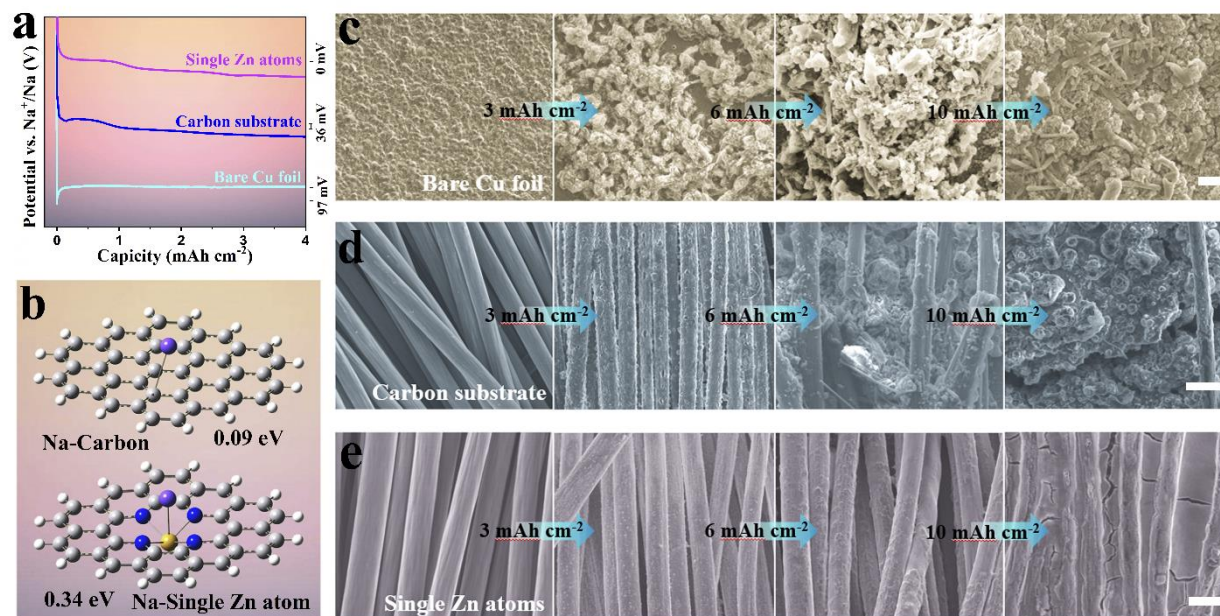
Figure 5.5 Strong interaction and patterned deposition between single Zn atoms and Na metal. (a) Voltage profiles of galvanostatic Na deposition on different substrates. (b) DFT calculations on the affinity between carbon and single Zn atom sites based substrates, to evaluate the strong interaction for Na ions. Na is expected to nucleate from single Zn atoms. SEM images of (c) Na-Cu, (d) Na-CC, and (e) Na-Zn$_{SA}$-N-C electrode, which is plating Na metal with different nucleation capacities in advance. Scale bar, 5 μm.

Sodium metal plating is a critical safety issue in Na metal batteries, and contributes significantly to aging, drastically limiting the lifetime and inducing capacity loss. From **Figure 5.5a**, the voltage profiles for Cu foil show a sharp voltage dip at the beginning of the Na deposition process and followed by a flat voltage plateau. In these voltage profiles, the nucleation overpotential is defined by the difference between the sharp tip voltage at which Na starts to nucleate and the later flat voltage for further Na deposition, which become particularly relevant for island growth and the evolution of surface morphology. The nucleation overpotential of Na metal plating on bare Cu foil and bare carbon cloth (CC) substrate is about 97 mV and 26 mV, respectively, which is used to overcome the heterogeneous nucleation barrier due to the large thermodynamic mismatch between Na and Cu or Carbon. By contrast, the voltage profile for the Na deposition process on Zn$_{SA}$-N-C is quite different. The corresponding voltage profile does not show a dip and the nucleation

overpotential is 0 mV. As validated by DFT calculations for Zn$_{SA}$-N-C, a relatively large binding energy of 0.34 eV with Na ion is achieved. (**Figure 5.5b**) In contrast, the binding energy between the carbon skeleton and Na ion and is only 0.09 eV, which is 3.8 times smaller than that of Zn$_{SA}$-N-C. Enhanced surface binding energy with minimized nucleation barrier regulates uniform Na deposition for stable Na metal anodes, which could conveniently guide Na ions to deposit on the surface of single Zn atom sites, offering uniform nucleation sites and suppressing the growth of Na dendrite.

The top-view ex-situ SEM characterization of Cu, CC, and Zn$_{SA}$-N-C was used to investigate the controlled Na nucleating and plating processes on different substrates. In this characterization, Na metal was plated on different substrates with a current density of 1.0 mA cm^{-2} and an increased area capacity from 3.0 mAh cm^{-2} to 10.0 mAh cm^{-2}. As shown in **Figure 5.5c**, the surface of the bare Cu foil is full of Na dendrites and some small particles. The growth of Na dendrites can cause the dendrite-induced internal short circuit inside the battery, leading to a safety hazard. For CC substrate in **Figure 5.5d**, Na metal is still suffering from a relatively high nucleation barrier due to the serious lattice mismatch between hexagonal carbon and body-centered cubic structured sodium. Na particles are preferentially formed at the junctions of carbon substrates, where the crossed fibers met to minimize the energy barrier. During the continuous deposition process, the formed Na particles are inclined to grow into different kinds of Na agglomerates and fill the rough surface with the isolated Na dendrites that emerged from the agglomerates. Different from the CC and Cu foil, the uniform dispersion of single Zn atoms on the carbon substrate can serve as the homogenously distributed nucleation sites to guide Na metal deposition, firstly promoting the uniform nucleation. When the surface of Zn$_{SA}$-N-C substrate is covered by a certain amount of Na metal, the as-produced numerous Na nuclei during the initial nucleation stage directly guide the following Na plating process. Furthermore, the 3D structure of the carbon cloth can accommodate Na metal to deposit inside its interspace and tolerate the volume change during the cycles. Even after plating 10.0 mAh cm^{-2} Na metal, the surface of Zn$_{SA}$-N-C remains smooth without any dendritic structure. (**Figure 5.5e**).

We further use *In situ* optical microscopy to keep a close watch on the dynamic process of Na plating at a high current density. From **Figure 5.6a**, the dendritic and mossy Na is formed along the edges of bare Na foil, and the uncontrolled growth of Na dendrites becomes more serious with

time. After 30 min, the surface of bare Na foil is full of Na dendrites and dead Na. For CC substrates, the deposition process is still suffering from a relatively high nucleation barrier. Due to the minimized nucleation barrier, the Na nuclei tend to form at the junctions of the crossed fibers. (**Figure 5.6b**) During the continuous deposition process, Na agglomerates are the main structure of the Na deposits and the surface is filled by the isolated Na dendrites. In sharp contrast, the introduction of Zn single atoms on the substrate can regulate Na deposition, free from the Na dendrites and "dead Na" (**Figure 5.6c**). After 30 min, we cannot see any signals corresponding to any dendritic structure.

Coulombic efficiency is an important tool that can provide a way to quantify parasitic reactions occurring within cells. High Coulombic efficiency usually indicates a long battery cycle life, which was defined as the ratio between Na stripping capacity and Na plating capacity. The half cells are assembled by bare Na foil (as the counter electrode) and carbon substrate or Zn_{SA}-N-C (as the working electrodes). Galvanostatic plating of Na was investigated at the current density of 0.5 mA cm^{-2} with the areal capacity of 0.5 mAh cm^{-2} and followed by stripping of Na to a cutoff voltage of 0.5 V versus Na^+/Na. The Zn atomic structure on the carbon-based substrate can significantly improve Coulombic efficiency during the repeated Na stripping/plating processes. When elevated at a low current density of 0.5 mA cm^{-2} with the corresponding area capacity of 0.5 mAh cm^{-2}, the half cell based on Zn_{SA}-N-C electrodes exhibits a high and stable average Coulombic efficiency up to 99.8% for more than 350 cycles (**Figure 5.7a,b**). Even when tested at a current density of 0.5 mA cm^{-2} with a high corresponding area capacity of 1.0 mAh cm^{-2}, the half cell still delivers a high average Coulombic efficiency up to 99.65 for more than 150 cycles (**Figure 5.7c**). The high Coulombic efficiencies and superior cycling stability during the repeated Na stripping/plating processes are benefitting from the high surface activity after introducing single Zn atoms, which provides numerous active sites for adsorption of Na ions. As shown in **Figure 5.7d**, the Coulombic efficiency for half cell with Zn_{SA}-N-C electrodes varies of 99.4%, 98.9%, and 98.5%, while cycled at a high current density varies of 2.0, 3.0, to 4.0 mA cm^{-2}, respectively. By contrast, a fluctuating Coulombic efficiency for the initial 155 cycles and a following rapid decay can be observed by the half cell using CC as the electrode, which could be attributed to the continual reaction between the electrolyte and exposed Na metal to reform the weak SEI layer during the repeated Na stripping/plating process. In my work, the designed Na metal anode based on single Zn atom sites and carbon substrate outperform than most of the previously reported modified current collectors.

114

(**Table 3**) From the voltage profile of the Na plating process, the upper plateau over 0 V at the incipient 0.2 mAh cm^{-2} capacity is attributed to the formation of multiple NaZn$_X$ alloy phases. Even when tested under a high areal capacity of 0.5 and 2.0 mAh cm^{-2}, the capacity of the voltage plateau over 0 V with limited 0.2 mAh cm^{-2} capacity is still maintained, corresponding to the formation of the multiple NaZn$_X$ alloy phases. (**Figure 5.8**) With the deepening of the Na plating process, the voltage plateau below 0 V corresponding to the typical Na deposition process can be observed until the end of the step, which is similar to the voltage profile of half cell based on Cu foil.
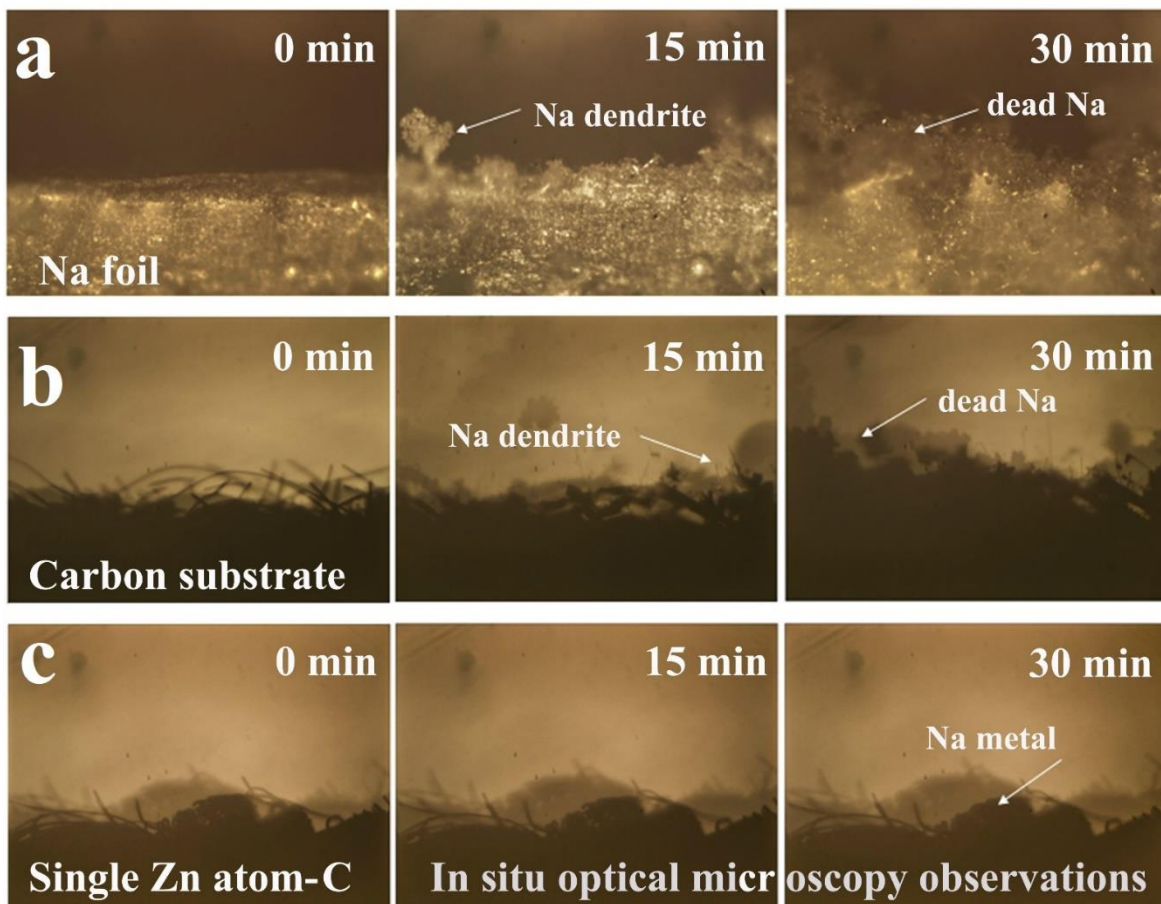
Figure 5.6. In situ optical microscopy observations of the Na plating process with (a) Na foil, (b) CC, and (c) Zn$_{SA}$-N-C.

Table. 3. Summary of the reported literature on different types of Na metal anode.

Na metal anode	Na deposits on substrate	Maximum area capacity	CE /lifetime	Polarization /lifetime	Full cells
Na metal deposited on Ag nanopaper	4.0-6.0 mAh cm^{-2}	1.0 mAh cm^{-2}	93.9-100% /50cycles	800h	-
SnO$_2$ carbon fiber /Na foil composite	excess	1.0 mAh cm^{-2}	-	300h	-
Al$_2$O$_3$ artificial SEI layer on Na foil	excess	1.0 mAh cm^{-2}	-	400h	-
Flexible carbon felt /Na metal composite	excess	2.0 mAh cm^{-2}	-	500h	200 cycles (Na$_{0.67}$Ni$_{0.33}$Mn$_{0.67}$O$_2$)
Porous Cu matrix /Na metal composite	excess	3.0 mAh cm^{-2}	-	400h	100 cycles (Na$_3$V$_2$(PO$_4$)$_3$)
Na metal deposited on Al current collector	12.0 mAh cm^{-2}	0.25 mAh cm^{-2}	99.9% /50cycles	1000h	40 cycles (FeS$_2$)
Al$_2$O$_3$ protective coating on Na foil	excess	1.0 mAh cm^{-2}	-	500h	-
N/S coated carbon tube /Na metal composite	excess	1.0 mAh cm^{-2}	-	500h	-
Metallic Na into Carbonized wood	excess	1.0 mAh cm^{-2}	-	500h	-
Inorganic-organic Coating on Na foil	excess	1.0 mAh cm^{-2}	-	300h	-
Carbon fiber/ Na metal composite	excess	3.0 mAh cm^{-2}	-	450h	-
Graphene coating on Na foil	excess	2.5 mAh cm^{-2}	93.3% /150cycles	-	-
Na metal deposited on Pillared Mxene	3.0-5.0 mAh cm^{-2}	5.0 mAh cm^{-2}	98.8% /200cycles	300h	200 cycles (Na$_3$V$_2$(PO$_4$)$_3$)
Na metal deposited on reduced graphene oxide	10.0 mAh cm^{-2}	1.0 mAh cm^{-2}	-	600h	100 cycles (Na$_3$V$_2$(PO$_4$)$_3$)
Graphene film layer on Na foil	excess	3.0 mAh cm^{-2}	-	600h	-
Our strategy	**0.3-4.0 mAh cm^{-2}**	**4.0 mAh cm^{-2}**	**99.8% /350cycles**	**1000h**	**1000 cycles (Na$_3$V$_2$(PO$_4$)$_3$)**
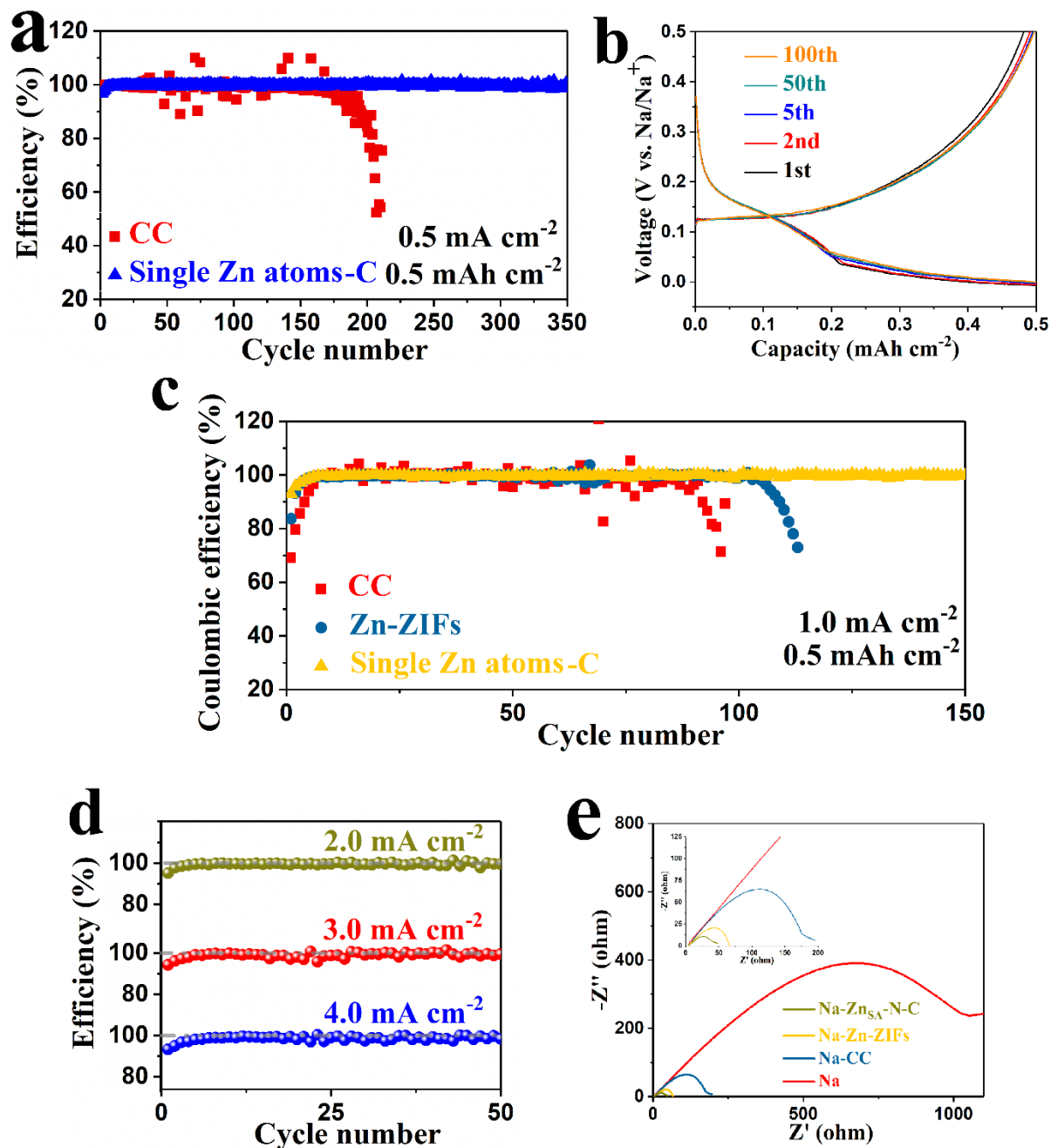
Figure 5.7. (a) Coulombic efficiency with the areal capacity of 0.5 mAh cm^{-2} at a current density of 0.5 mA cm^{-2}. (b) Voltage profiles of the Na plating/stripping process with an areal capacity of 0.5 mAh cm^{-2} at a current density of 0.5 mA cm^{-2}. (c) Comparison of Coulombic efficiency of Na plating/stripping between CC, Zn-ZIFs, and Zn$_{SA}$-N-C with the areal capacity of 1.0 mAh cm^{-2} at a current density of 0.5 mA cm^{-2}. (d) Comparison of Coulombic efficiency of Na stripping/plating at the high current density of 2.0, 3.0, and 4.0 mA cm^{-2}. (e) EIS Nyquist plots of the symmetric cells.

To evaluate the polarization performance of different Na metal anodes during galvanostatic cycling, symmetric cells with two identical electrodes were tested. Na metal anodes based on Cu foil, CC, and Zn_{SA}-N-C were synthesized by the electrodeposition of 4.0 mAh cm^{-2} Na metal on the surface of different substrates. Before cell cycling, Electrochemical impedance spectroscopy (EIS) was first conducted to evaluate the initial SEI layer formation. Only one semicircle at high frequency can be observed in **Figure 5.7e**, corresponding to the SEI resistance and charge-transfer resistance. The interfacial resistances of Na-CC‖Na-CC (189.7 Ω) cells are much lower than that of Na‖Na cell (1053.6 Ω), and the resistance of the Na-Zn_{SA}-N-C based symmetric cell (44.6 Ω)is significantly lower than any other symmetric cells, which can be attributed to the successful suppression of the growth of Na dendrites and dead Na.
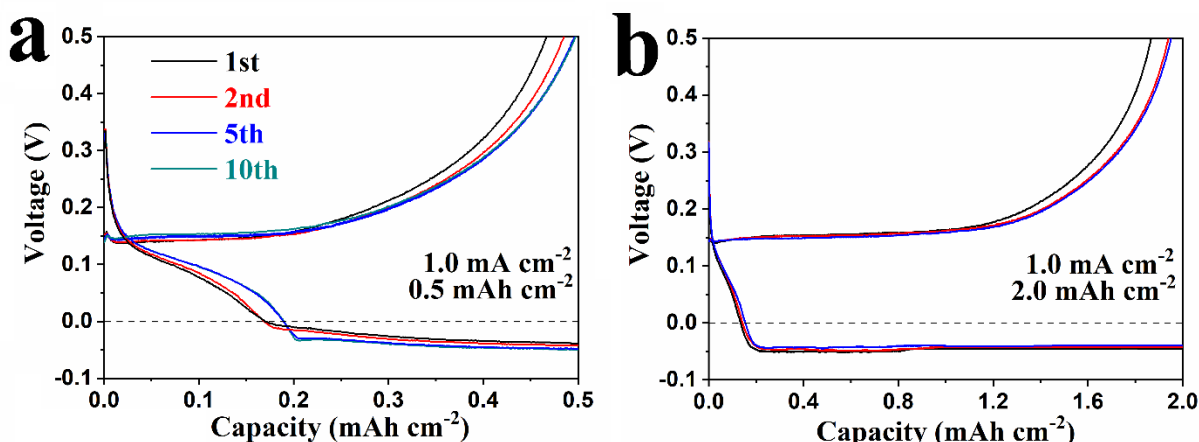
Figure 5.8. (a) Voltage profiles of different Na plating/stripping processes for Zn_{SA}-N-C at a current density of 1.0 mA cm^{-2} with an area capacity of 0.5 mAh cm^{-2}. (b) Voltage profiles of Na plating/stripping process at a current density of 1.0 mA cm^{-2} with the area capacity of 2.0 mAh cm^{-2}.

The Na utilization during the charging/discharging process is a key point in evaluating Na metal anode for commercial Na metal batteries. Similar to Li metal batteries, metallic Na foil was chosen as the counter electrode in conventional Na metal batteries. Compared with the capacity of the cathode, the capacity of counter electrode material (anode) excess is considered, which increases

the usage amount of Na metal and cost of the batteries. Among their ongoing challenges that have to be faced in the optimization process, is that the configurations irreversible Na consumption connected to electrode activation processes and SEI formation. The full cells assembled by Na-Zn$_{SA}$-N-C anode and Na$_3$V$_2$(PO$_4$)$_3$ cathode (with the areal capacity of 0.2 mAh cm^{-2}) were further investigated to demonstrate the excellent electrochemical performance of full cells and high utilization of Zn$_{SA}$-N-C electrode (**Figure 5.9a**). Different amounts of Na metal were directly deposited on the surface of the substrate to prepare the different Na-Zn$_{SA}$-N-C anodes. The galvanostatic charging/discharging curves obtained by the full cell with Na-Zn$_{SA}$-N-C anode (with the nucleation capacities of 1.0 mAh cm^{-2}) are shown in **Figure 5.9b**. The charge and discharge voltage plateau are corresponding to the V^{3+}/V^{2+} redox couple and the V^{4+}/V^{3+} redox couple. The full cell based on Na-Zn$_{SA}$-N-C anode exhibits a high capacity of 95.1 mAh g^{-1} at a current density of 0.2 C, and the subsequent cycling curves remain unaltered, further demonstrating the excellent reversibility of our strategy.

As shown in **Figure 5.9c**, the cycling performance was further investigated by the full cell (with Na-utilization of 20%) assembled by Na metal anodes based on the different substrates with the limited 1.0 mAh cm^{-2} nucleation capacities. For Cu and CC substrates, Na deposits are grown in the form of Na dendrites and dead Na, and only a small part is effective during the cycles. The discharge capacities for Na metal anode based on Cu foil and CC substrate are severely deteriorated after few cycles, which is caused by the limited reversibility, continuous consumption of electrolytes, and repeated formation of SEI layers. The Na ions in the Na dendrites cannot join the cycles and the amount of activated Na ions on the system decreases rapidly, leading to serious capacity fading. A similar phenomenon can be observed in **Figure 5.9d,** when the nucleation capacities of Na metal are decreased from 0.5 mAh cm^{-2} (with Na-utilization of 40%) to 0.2 mAh cm^{-2} (with Na-utilization of 100%), where the serious capacity decay can be observed for the Na-CC based full cell. For Na metal anode based on Zn$_{SA}$-N-C substrates, the full cell (with Na-utilization of 40%) delivers a stable and high reversible capacity of 93.8 mAh g^{-1} after 120 cycles at a current density of 0.2 C. A similar phenomenon can be observed by the full cell with Na-utilization of 60%. The dendrite-free structure can improve the reversible utilization of Na metal during the cycles. Due to the excellent Na electroactivity and directional deposition, the full cell with the record-breaking high Na-utilization of 100% still exhibits a very stable cycling performance with a high specific capacity over 120 cycles. Furthermore, the cycling life of the Na-

Zn_{SA}-N-C electrode can be broadened to 1000 cycles at a current density of 0.5 C simultaneously and delivers a high average capacity of 79.6 mAh cm^{-2} with high Coulombic efficiency of about 100%. (**Figure 5.9e**)
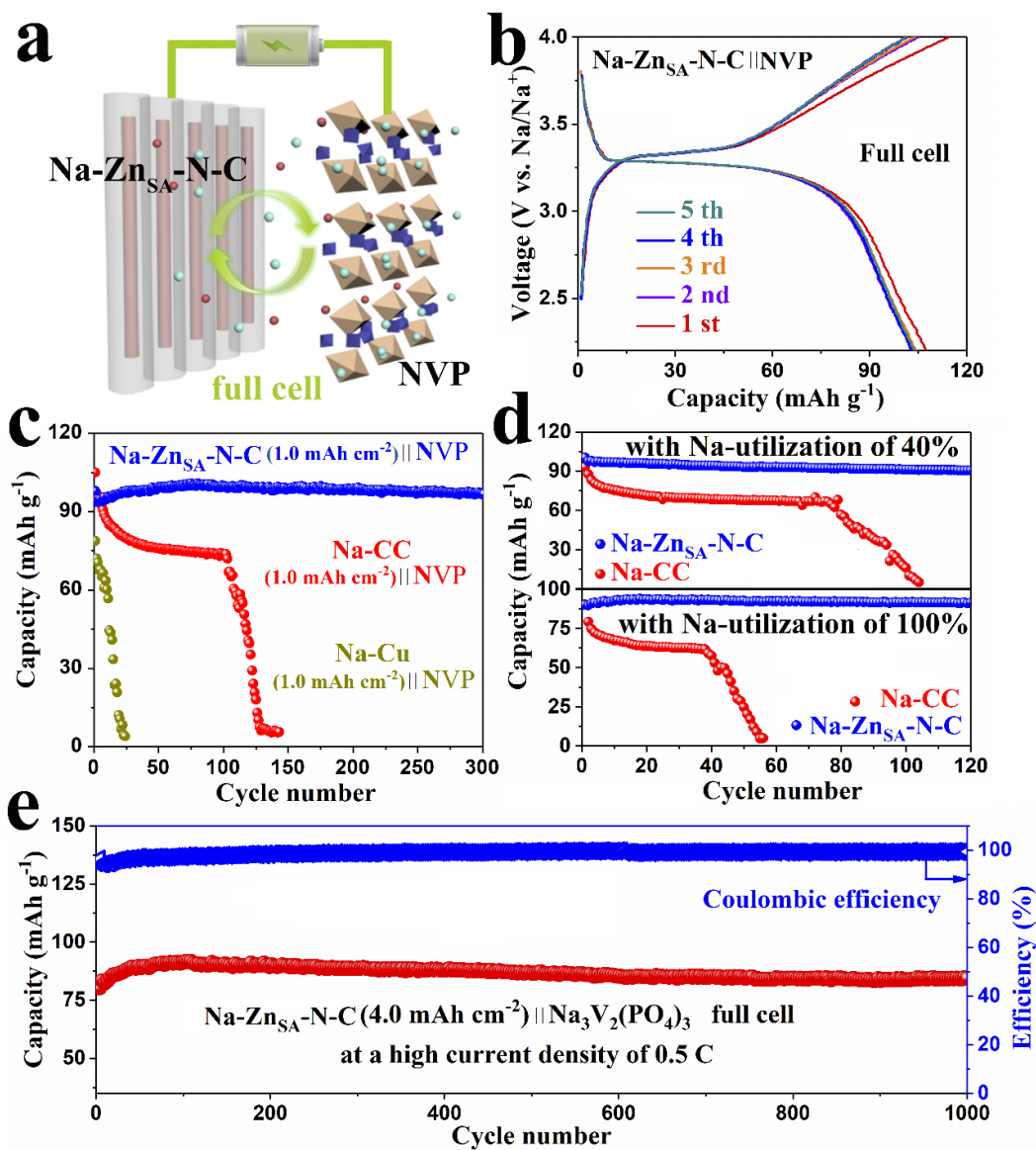
Figure 5.9 Different nucleation capacities of Na are first predeposited on Zn_{SA}-N-C for the preparation of the Na-Zn_{SA}-N-C electrode. (a) Full cells are assembled with $Na_3V_2(PO_4)_3$ as the cathode and Na-Zn_{SA}-N-C as the anode. (b) voltage profiles of the charge/discharge process for the full cell. (c) Comparison for cycle performance of different electrode (1.0 mAh cm^{-2}) at 0.2 C. (d) Cycling performance of Na- Zn_{SA}-N-C anode and Na-CC anode with high Na-utilization of 40% (top) and 100% (bottom). (e) Long cycling stability with high Coulombic efficiency almost 100% at 0.5 C.

5.7 Conclusions

In summary, we have demonstrated a novel design of single Zn atoms dispersed on the carbon cloth substrate as the basis for Na metal anode, which can successfully suppress the growth of Na dendrites by controlling Na deposition over both positions and morphology. The current collector modified by single Zn atoms can favor Na deposition with minimized nucleation energy barrier and fully tap the potential for the high utilization of Na during cycles. The half cell exhibits a high Coulombic efficiency up to 99.8% for more than 350 cycles, and the Na symmetrical cell using such Na metal anode can run steadily for over1000 hours with a lower overpotential of 56 mV. This method of introducing single atoms to guide Na ion deposition provides an effective way to conquer the intrinsic deficiencies of Na metal anode. The full cell (with high Na utilization of 100%) assembled by $Na_3V_2(PO_4)_3$ cathode and Na-Zn$_{SA}$-N-C anode with the minimized Na deposits can keep steady for more than 1000 cycles with a high Coulombic efficiency near 100%. Our work presents a facile strategy for stable Na metal anode by a brand-new atomic modified route and opens a new avenue for the development of next-generation high-energy-density Na metal batteries with high Na utilization and low cost.

6 CONCLUSION AND PERSPECTIVES

6.1 Conclusion

First, we have successfully synthesized the Zn single atoms and single-atom and cluster Au on the appropriate substrate by electrochemical deposition and pyrolysis at high temperatures. At the maximum limit of metal dispersion, single atoms and clusters generate great interest owing to their potential for closer structural resemblance, increased active sites, and maximized atomic utilization efficiency. The electronic properties of metal particles should strongly change when going below 1.0 nm, and the size of a single atom is less than 0.1 nm. Therefore, it could be expected that the single atoms and clusters-based materials would interact differently with reactants, exhibiting distinct reactivity with respect to nanoparticles. By using HAADF-STEM, XANES, and EXAFS, we can clearly see single atoms and clusters formed by a few atoms, and investigate their electronic properties.

In **Part I** for 3D porous Li metal foam with artificial SEI layer: Metallic Li is strongly considered as the alternatives of graphite anode due to its extremely low redox potential (-3.04 V vs standard hydrogen electrode) and ten times higher theoretical specific capacity (3860 mAh g^{-1}) than those of graphite. The application of rechargeable Li metal-based batteries is hindered by several serious challenges that have puzzled researchers for half a century. Artificial SEI layers and 3D porous host are used to address the challenging issue, but they still meet the barrier of low energy density, additional side reactions, and unstable combination. Thus far almost all of the electrochemical measurements on Li metal anodes have been limited to shallow cycling with a low depth of only 0.5-1.0 mAh cm^{-2}. It is critical to develop deeply cyclable Li metal anodes and further realize high-capacity Li-metal full cells. In this part, we tackle this issue by introducing a 3D porous lithium metal anode accompanied by an inherent SEI layer, which can buffer the volume change, guide Li deposition inside its porous structure, uniform the diffusion of Li-ion on the interface and enable deeply deposited Li metal. There are three novel features reported in this manuscript that make our work of great interest to the broad researchers:

1) Freestanding porous Li metal anode accompanied by an inherent SEI layer has been constructed via template-free chemical etching. The 3D porous Li matrix can buffer the volume change and guide Li deposition inside its porous structure. The dense protective

SEI layers are strongly anchored on a freestanding 3D porous Li matrix accompanied by the etching at the same time, leading to a uniform diffusion of Li ions on the interface and suppress the formation of Li dendrites and side reactions.

2) Benefiting from the unique deposition kinetics, the Li plating/stripping process based on our strategy can be deeply cycled at a high current density between 1.0 and 20.0 mA cm^{-2} with low overpotential and achieve a long lifetime up to 350 h. Moreover, Li metal batteries with LiNiCoMnO$_2$ cathode exhibit excellent electrochemical performance at a high current density and active materials loading for more than 20.4 mg cm^{-2}.

3) In terms of the combination of both porous Li matrix and inherent dense SEI layer, our cell greatly suppresses the gassing process and reduces heat generation, further demonstrating the reliability and security of the remarkable Li metal anode.

In **Part II** for Li metal anode: high energy and cost-effective Li-ion batteries are promising for large-scale energy storage applications such as electric vehicles, consumer electronics, and grid energy storage. However, traditional Li-ion batteries are approaching their theoretical energy density limits. In this context, Li metal anodes are ideal candidates due to their low redox potential (-3.04 V vs. the standard hydrogen electrode) and high theoretical specific energy (3860 mAh g^{-1}). Unfortunately, the uncontrolled formation of dendrites, the large volume change, and the unstable interface during the electrochemical cycling hinder the applications of Li metal anodes. In this context, we tackle this issue by introducing single-atom and cluster Au, which can induce Li plating with zero nucleation overpotential due to the optimized electron field distribution of the carbon skeleton. There are three novel features reported in this part that make our work of great interest to the broad researcher:

1) We report single-atom and cluster Au uniformly dispersed on the activated carbon cloth as a model to control directed Li deposition and suppress the Li dendrite growth. Single-atom and cluster Au not only favors Li deposition with zero overpotential similar to Au nanoparticles, but also has great affinity and interaction with Li ions in the electrolyte, providing stable adsorption positions for Li atoms, which are further confirmed by density

functional theory (DFT) calculations.

2) Stable and reversible Li metal anodes were achieved by virtue of the single-atom and cluster Au, exhibiting excellent cycling stability for more than 900 cycles with almost 100% Coulombic efficiency and deeply cyclable behavior at high areal capacity up to 20 mAh cm^{-2}.

3) The Li anodes can maintain a good plating/stripping efficiency of 99.82% for 900 cycles under 1 mAh cm^{-2}, and be deeply cycled at a high current density and areal capacities of 15.0 and 20.0 mAh cm^{-2} with high Coulombic efficiency.

In **Part II** for Na metal anode: as a promising alternative to the relatively high cost and scarce resources of lithium, metallic sodium is most appealing as an anode material for the next-generation energy storage systems due to its widespread geological distribution (1000 times more abundant than Li) and low cost. Unfortunately, Na metal anode has long been considered "unsafe" because of the uneven metallic deposition, dendritic growth, unstable solid electrolyte interphase (SEI), and large volume change upon repeated plating/stripping cycles, which cause low reversibility, internal short circuit, safety hazards, and short cycle life. In this context, we introduce single-atom and cluster Au as loadstone of Na metal, which improve the distribution of electric field and preferentially induce Na nucleation with no nucleation barrier, free from dendrite-induced short circuit or safety hazards. There are three novel features reported in this part that make our work of great interest to the broad researcher:

1) We introduce single-atom and cluster Au as a novel loadstone of Na metal on a modified carbon substrate, which can guide the metallic Na nucleation and suppress dendrite formation at the atomic level. In our approach, single-atom and cluster Au not only optimize the electronic property to favor Na deposition with no nucleation barriers, but also serve as a strong magnet for Na ions causing the metal to uniformly distribute on the substrate.

2) Stable and reversible Na metal anodes were achieved by the introduction of the single-atom and cluster Au. Compared with Au particle electrode, stable long-term

plating/stripping process of symmetric cells with low voltage hysteresis over 400 hours are demonstrated, and the Coulombic efficiency of the electrode can be maintained at 99.73% for more than 300 cycles.

3) The utilization of Na is a key point to apply Na metal anode for commercial Na ion batteries. When tested with a $Na_3V_2(PO_4)_3$ electrode, the full cell of the SCAu-CC electrode with minimum Na deposits are able to be cycled for 1000 cycles without diminishing its energy density.

In **Part III** for Na metal anode: owing to the wide availability and low cost of sodium resources, the rapid development of battery technologies based on sodium-ion batteries have emerged as one of the most promising alternatives to lithium-ion batteries. Notably, direct use of Na metal as anode shows clear advantages, which possesses a low redox potential (-2.714 V vs. the standard hydrogen electrode) and high theoretical specific energy (1166 mAh g^{-1}). Unfortunately, Na metal anode has long been considered "unsafe" because of the uneven metallic deposition, dendritic growth, unstable solid electrolyte interphase (SEI), and large volume change upon repeated plating/stripping cycles, which cause low reversibility, internal short circuit, safety hazards, and short cycle life. Furthermore, its low efficiency is still yet to be overcome. Almost all of the results are limited to shallow cycling conditions ($\leq$1 mAh cm^{-2}) and thus inefficient utilization (<1%). In this context, we tackle this issue by introducing single Zn atoms, which can guide spatially heterogeneous Na deposition with a zero nucleation overpotential and maximize the utilization of Na during cycles. In terms of both lifetime and Na-utilization, our cell significantly outperforms other laboratory-scale Na metal anodes. There are three novel features reported in this part that make our work of great interest to the broad researchers:

1) A record-high utilization and long-term cycling stability Na metal anode is reported, using single Zn atoms distributed carbon substrate as the current collector. Single Zn atom serves as a strong magnet for Na ions, which guide the metallic Na uniform nucleation free from dendrite-induced short circuit and safety hazards. Single Zn atoms not only favor Na deposition with zero nucleation overpotential, but also have great affinity and interaction with Na ions in the electrolyte, providing stable adsorption positions for Na

atoms, which are further confirmed by density functional theory (DFT) calculations.

2) Stable and reversible Na metal anodes were achieved by virtue of the single Zn atoms. Specifically, the Coulombic efficiency of the Zn_{SA}-N-C electrode can be maintained at 99.8% for 350 cycles, and the polarization of Na metal anode is limited to 56 mV with an ultralong lifespan for more than 1000 hours.

3) The utilization of Na is a key point to apply Na metal anode for commercial Na ion batteries. When paired with $Na_3V_2(PO_4)_3$ cathodes, the Na metal anode with minimum Na deposits (with the Na-utilization of 40% - 100%) performs a function similar to Na foil and indicates good cycling stability for more than 1000 cycles with high Coulombic efficiency of ~100%.

In my opinion, Li metal batteries and Na metal batteries are some of the most promising next-generation energy storage strategies with a high energy density, which can meet the rigid demands of new industries. However, the dendritic growth, unstable SEI layer, uneven metallic deposition, and infinite relative volume change still hinder the development of Li/Na metal anodes. In this thesis, we introduce single atom-based and cluster-based materials as the current collector to control Li/Na deposition and suppress the growth of dendrites. This discovery suggests an effective solution that suppressing Li/Na dendrite growth at the nucleating stages and seeding Li/Na deposition is expected to lead to a safe and efficient alkali metal battery and offer a mechanistic understanding of the working alkali metal battery as well, which is systemically elucidated by material characterization, electrochemical analyses, and density functional theory (DFT) calculations.

6.2 Perspectives

Based on the obtained results of the synthesis and application of single atoms in the field of alkali metal anode, we learned that by introducing single-atom sites in the substrate of alkali metal anode, a dendrite-free structure is achieved. Taken these advantages, part of future work will mainly focus on the modified substrate for alkali metal anode by different single atoms, such as Au/Co/Fe/Pt single atoms and Zn-Fe/Zn-Co/Pt-Ni dual single atom alloys. The preparation process of single atoms is still too complicated for the large-scale application of stable alkali metal anode. In the future, more efforts are needed to address the challenges for the revival of alkali metal anode, although there is still a long way to go before practical applications of alkali metal batteries. Furthermore, the root causes of Li dendrite growth are the Li-ion concentration gradient and non-uniformity of deposition. It is important for us to explore the mechanism of the Li dendrite growth. All of my future researches in the field of dendrite-free alkali metal anode are needed to be tested under practical conditions, such as at the large current density (more than 5.0 mA cm^{-2}) and high areal capacity (more than 5.0 mAh cm^{-2}).

The safety of alkali metal batteries is recognized as a critical performance requirement for commercial applications, especially in the field of electrical vehicles. The energy density of alkali metal batteries is increased, it is critical to achieving high battery safety if the energy is released unintentionally. Accidents related to fires and explosions of li-based batteries occur frequently worldwide. Methods to ensure alkali metal battery safety by internal protection mechanism is including the electrolyte and alkali metal anode, which can inhibit the gas release, protect the battery during the overcharging, develop a non-flammable electrolyte system, and achieve high thermal stability. For electrolytes, I will do some interesting works in the field of non-flammable electrolytes, which can stabilize the SEI layers, achieve a dendrite-free structure, and play multifunctional and synergistic roles at a minimum dose. For the alkali metal anode, I will do some interesting works in the field of air-stable alkali metal anode. Metallic Li is not stable in ambient air due to its low potential and high chemical reactivity toward moisture (H_2O), which requires to be stored in airtight containers out of heat, light, oxygen, and humidity. Ambient air is a mixture, mainly composed of several different pure substances, such as O_2, N_2, and H_2O. The dry O_2 and N_2 can help Li metal to form the passivation layers, which can improve the cycling behavior and restrain side reactions:

$$4Li + O_2 \rightarrow 2Li_2O;$$

$$6Li + N_2 \rightarrow 2Li_3N$$
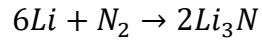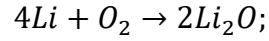
H_2O in ambient air is harmful to Li metal, which can disrupt the passivation layers and elucidate its nanoscale corrosion mechanism:

$$H_2O + Li \rightarrow LiOH + 0.5H_2;$$

$$LiOH + Li \rightarrow Li_2O + 0.5H_2$$
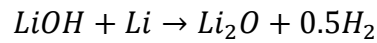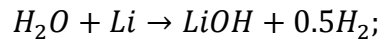
The key point of designing an air-stable alkali metal anode is how to establish a hydrophobic interface, which can stabilize alkali metal in ambient air. I will do some works to construct a protective layer on the surface of the alkali metal anode, which can isolate the alkali metal anode from the ambient air and allow reversible diffusion of Li/Na ions without any consumption.

7 BIBLIOGRAPHIE

1.   S. Chu, Y. Cui, N. Liu, The path towards sustainable energy. *Nat. Mater.* **16**, 16-22 (2016).

2.   M. S. Dresselhaus, I. L. Thomas, Alternative energy technologies. *Nature* **414**, 332-337 (2001).

3.   T. Ahmad, D. Zhang, A critical review of comparative global historical energy consumption and future demand: The story told so far. *Energy Rep.* **6**, 1973-1991 (2020).

4.   J. Eom, M. Hyun, J. Lee, H. Lee, Increase in household energy consumption due to ambient air pollution. *Nat. Energy* **5**, 976-984 (2020).

5.   M. Aydin, U. K. Pata, Are shocks to disaggregated renewable energy consumption permanent or temporary for the USA? Wavelet based unit root test with smooth structural shifts. *Energy* **207** (2020).

6.   R. York, Do alternative energy sources displace fossil fuels? *Nat. Clim. Chang.* **2**, 441-443 (2012).

7.   S. Sen, S. Ganguly, Opportunities, barriers and issues with renewable energy development – A discussion. *Renew. Sust. Energ. Rev.* **69**, 1170-1181 (2017).

8.   D. Zhang *et al.*, Present situation and future prospect of renewable energy in China. *Renew. Sust. Energ. Rev.* **76**, 865-871 (2017).

9.   F. Egli, B. Steffen, T. S. Schmidt, A dynamic analysis of financing conditions for renewable energy technologies. *Nat. Energy* **3**, 1084-1092 (2018).

10.   M. Petrović-Ranđelović, N. Kocić, B. Stojanović-Ranđelović, The importance of renewable energy sources for sustainable development. *Econ. Sustain. Dev.* **4**, 15-24 (2020).

11.   I. Khan, F. Hou, H. P. Le, The impact of natural resources, energy consumption, and population growth on environmental quality: Fresh evidence from the United States of America. *Sci. Total Environ.* **754**, 142222 (2021).

12.   G. H. Gu, J. Noh, I. Kim, Y. Jung, Machine learning for renewable energy materials. *J. Mater. Chem. A* **7**, 17096-17117 (2019).

13.   H. Lund, Renewable energy strategies for sustainable development. *Energy* **32**, 912-919 (2007).

14.   K. Hansen, C. Breyer, H. Lund, Status and perspectives on 100% renewable energy systems. *Energy* **175**, 471-480 (2019).

15.   E. Kabir, P. Kumar, S. Kumar, A. A. Adelodun, K.-H. Kim, Solar energy: Potential and future prospects. *Renew. Sust. Energ. Rev.* **82**, 894-900 (2018).

16.   D. Larcher, J. M. Tarascon, Towards greener and more sustainable batteries for electrical energy storage. *Nat. Chem.* **7**, 19-29 (2015).

17.   L. Hu *et al.*, Highly conductive paper for energy-storage devices. *Proc. Natl. Acad. Sci. U.S.A.* **106**, 21490-21494 (2009).

18.   E. Karden, S. Ploumen, B. Fricke, T. Miller, K. Snyder, Energy storage devices for future hybrid electric vehicles. *J. Power Sources* **168**, 2-11 (2007).

19.   X. Wang *et al.*, Flexible energy-storage devices: design consideration and recent progress. *Adv. Mater.* **26**, 4763-4782 (2014).

20.   H. Li, Z. Tang, Z. Liu, C. Zhi, Evaluating Flexibility and Wearability of Flexible Energy Storage Devices. *Joule* **3**, 613-619 (2019).

21.   S. Pan, J. Ren, X. Fang, H. Peng, Integration: An Effective Strategy to Develop Multifunctional Energy Storage Devices. *Adv. Energy Mater.* **6**, 1501867 (2016).

22.   Z. Song, H. Zhou, Towards sustainable and versatile energy storage devices: an overview of organic electrode materials. *Energy Environ. Sci.* **6**, 2280-2301 (2013).

23.   A. Tyagi, K. M. Tripathi, R. K. Gupta, Recent progress in micro-scale energy storage devices and future aspects. *J. Mater. Chem. A* **3**, 22507-22541 (2015).

24. L. Mai, X. Tian, X. Xu, L. Chang, L. Xu, Nanowire electrodes for electrochemical energy storage devices. *Chem. Rev.* **114**, 11828-11862 (2014).

25. M. H. Braga, N. S. Grundish, A. J. Murchison, J. B. Goodenough, Alternative strategy for a safe rechargeable battery. *Energy Environ. Sci.* **10**, 331-336 (2017).

26. P. Flowers, K. Theopold, R. Langley, Batteries and Fuel Cells. (2021), USA https://chem.libretexts.org/@go/page/38307

27. B. Ebin, M. Petranikova, B. M. Steenari, C. Ekberg, Production of zinc and manganese oxide particles by pyrolysis of alkaline and Zn-C battery waste. *Waste Manag.* **51**, 157-167 (2016).

28. Z. Wang *et al.*, Flexible zinc–carbon batteries with multiwalled carbon nanotube/conductive polymer cathode matrix. *J. Power Sources* **237**, 210-214 (2013).

29. E. Sayilgan *et al.*, Reductive leaching of manganese and zinc from spent alkaline and zinc–carbon batteries in acidic media. *Hydrometallurgy* **97**, 73-79 (2009).

30. E. Sayilgan *et al.*, A review of technologies for the recovery of metals from spent alkaline and zinc–carbon batteries. *Hydrometallurgy* **97**, 158-166 (2009).

31. K. Pourabdollah, Development of electrolyte inhibitors in nickel cadmium batteries. *Chem. Eng. Sci.* **160**, 304-312 (2017).

32. C. J. Rydh, M. Karlström, Life cycle inventory of recycling portable nickel–cadmium batteries. *Resour. Conserv. Recycl.* **34**, 289-309 (2002).

33. K. Huang, J. Li, Z. Xu, A novel process for recovering valuable metals from waste nickel-cadmium batteries. *Environ. Sci. Technol.* **43**, 8974-8978 (2009).

34. D. N. Galushkin, N. N. Yazvinskaya, N. E. Galushkin, Investigation of the process of thermal runaway in nickel–cadmium accumulators. *J. Power Sources* **177**, 610-616 (2008).

35. F. Putois, Market for nickel-cadmium batteries. *J. Power Sources* **57**, 67-70 (1995).

36. R. Ahuja, A. Blomqvist, P. Larsson, P. Pyykko, P. Zaleski-Ejgierd, Relativity and the lead-acid battery. *Phys. Rev. Lett.* **106**, 018301 (2011).

37.   P. Kurzweil, Gaston Planté and his invention of the lead-acid battery—The genesis of the first practical rechargeable battery. *J. Power Sources* **195**, 4424-4434 (2010).

38.   D. A. J. Rand, The lead/acid battery—a key technology for global energy management. *J. Power Sources* **64**, 157-174 (1997).

39.   C. Parker, Lead-acid battery energy-storage systems for electricity supply networks. *J. Power Sources* **100**, 18-28 (2001).

40.   J. F. Manwell, J. G. McGowan, Lead acid battery storage model for hybrid energy systems. *Solar Energy* **50**, 399-405 (1993).

41.   V. Aravindan, J. Gnanaraj, S. Madhavi, H. K. Liu, Lithium-ion conducting electrolyte salts for lithium batteries. *Chem. Eur. J.* **17**, 14326-14346 (2011).

42.   X. Dong *et al.*, Environmentally-friendly aqueous Li (or Na)-ion battery with fast electrode kinetics and super-long life. *Sci. Adv.* **2**, e1501038 (2016).

43.   Z. Chen *et al.*, New class of nonaqueous electrolytes for long-life and safe lithium-ion batteries. *Nat. Commun.* **4**, 1513 (2013).

44.   S.-W. Kim, D.-H. Seo, X. Ma, G. Ceder, K. Kang, Electrode Materials for Rechargeable Sodium-Ion Batteries: Potential Alternatives to Current Lithium-Ion Batteries. *Adv. Energy Mater.* **2**, 710-721 (2012).

45.   X. Liang *et al.*, Improved cycling performances of lithium sulfur batteries with LiNO3-modified electrolyte. *J. Power Sources* **196**, 9839-9843 (2011).

46.   K. Abe *et al.*, Additives-containing functional electrolytes for suppressing electrolyte decomposition in lithium-ion batteries. *Electrochim. Acta* **49**, 4613-4622 (2004).

47.   Z. Chen, W. Q. Lu, J. Liu, K. Amine, $LiPF_6$/LiBOB blend salt electrolyte for high-power lithium-ion batteries. *Electrochim. Acta* **51**, 3322-3326 (2006).

48.   H. Kim, Y. Ding, P. A. Kohl, LiSICON-ionic liquid electrolyte for lithium ion battery. *J. Power Sources* **198**, 281-286 (2012).

49. J. Kalhoff, G. G. Eshetu, D. Bresser, S. Passerini, Safer Electrolytes for Lithium-Ion Batteries: State of the Art and Perspectives. *ChemSusChem* **8**, 2154-2175 (2015).

50. E. J. Plichta, W. K. Behl, A low-temperature electrolyte for lithium and lithium-ion batteries. *J. Power Sources* **88**, 192-196 (2000).

51. G. Zhang *et al.*, The Radical Pathway Based on a Lithium-Metal-Compatible High-Dielectric Electrolyte for Lithium-Sulfur Batteries. *Angew. Chem. Int. Ed. Engl.* **57**, 16732-16736 (2018).

52. L. Yu, X. Zhou, L. Lu, X. Wu, F. Wang, Recent Developments of Nanomaterials and Nanostructures for High-Rate Lithium Ion Batteries. *ChemSusChem* **13**, 5361-5407 (2020).

53. C. Wang *et al.*, Overlooked electrolyte destabilization by manganese (II) in lithium-ion batteries. *Nat. Commun.* **10**, 3423 (2019).

54. Z. Zeng *et al.*, Safer lithium ion batteries based on nonflammable electrolyte. *J. Power Sources* **279**, 6-12 (2015).

55. S. S. Zhang, A review on electrolyte additives for lithium-ion batteries. *J. Power Sources* **162**, 1379-1394 (2006).

56. K. Kubota, M. Dahbi, T. Hosaka, S. Kumakura, S. Komaba, Towards K-Ion and Na-Ion Batteries as "Beyond Li-Ion". *Chem. Rec.* **18**, 459-479 (2018).

57. I. Hasa, J. Hassoun, S. Passerini, Nanostructured Na-ion and Li-ion anodes for battery application: A comparative overview. *Nano Res.* **10**, 3942-3969 (2017).

58. Y.-S. Hu, Y. Lu, 2019 Nobel Prize for the Li-Ion Batteries and New Opportunities and Challenges in Na-Ion Batteries. *ACS Energy Lett.* **4**, 2689-2690 (2019).

59. J.-M. Tarascon, Na-ion versus Li-ion Batteries: Complementarity Rather than Competitiveness. *Joule* **4**, 1616-1620 (2020).

60. S. Tan, Y. J. Ji, Z. R. Zhang, Y. Yang, Recent progress in research on high-voltage electrolytes for lithium-ion batteries. *Chemphyschem* **15**, 1956-1969 (2014).

61.   A. Ritchie, W. Howard, Recent developments and likely advances in lithium-ion batteries. *J. Power Sources* **162**, 809-812 (2006).

62.   S. Ohta, T. Kobayashi, J. Seki, T. Asaoka, Electrochemical performance of an all-solid-state lithium ion battery with garnet-type oxide electrolyte. *J. Power Sources* **202**, 332-335 (2012).

63.   R. McMillan, H. Slegr, Z. X. Shu, W. Wang, Fluoroethylene carbonate electrolyte and its use in lithium ion batteries with graphite anodes. *J. Power Sources* **81-82**, 20-26 (1999).

64.   J. Y. Luo, W. J. Cui, P. He, Y. Y. Xia, Raising the cycling stability of aqueous lithium-ion batteries by eliminating oxygen in the electrolyte. *Nat. Chem.* **2**, 760-765 (2010).

65.   L. Kong, C. Li, J. Jiang, M. Pecht, Li-Ion Battery Fire Hazards and Safety Strategies. *Energies* **11**, 2191 (2018).

66.   L. Hu, H. Wu, F. La Mantia, Y. Yang, Y. Cui, Thin, flexible secondary Li-ion paper batteries. *ACS Nano* **4**, 5843-5848 (2010).

67.   B. Scrosati, J. Hassoun, Y.-K. Sun, Lithium-ion batteries. A look into the future. *Energy Environ. Sci.* **4**, 3287-3295 (2011).

68.   N. Nitta, F. Wu, J. T. Lee, G. Yushin, Li-ion battery materials: present and future. *Mater. Today* **18**, 252-264 (2015).

69.   L. Su, Y. Jing, Z. Zhou, Li ion battery materials with core-shell nanostructures. *Nanoscale* **3**, 3967-3983 (2011).

70.   V. Etacheri, R. Marom, R. Elazari, G. Salitra, D. Aurbach, Challenges in the development of advanced Li-ion batteries: a review. *Energy Environ. Sci.* **4**, 3243-3262 (2011).

71.   H. Duan, H. Zheng, Y. Zhou, B. Xu, H. Liu, Stability of garnet-type Li ion conductors: An overview. *Solid State Ion.* **318**, 45-53 (2018).

72.   G. E. Blomgren, The Development and Future of Lithium Ion Batteries. *J. Electrochem. Soc.* **164**, A5019-A5025 (2016).

73.   N. Li, C. R. Martin, B. Scrosati, Nanomaterial-based Li-ion battery electrodes. *J. Power Sources* **97-98**, 240-243 (2001).

74.   Z. Gong, Y. Yang, Recent advances in the research of polyanion-type cathode materials for Li-ion batteries. *Energy Environ. Sci.* **4**, 3223-3242 (2011).

75.   J. L. Shi *et al.*, High-Capacity Cathode Material with High Voltage for Li-Ion Batteries. *Adv. Mater.* **30**, 1705575 (2018).

76.   S. B. Chikkannanavar, D. M. Bernardi, L. Liu, A review of blended cathode materials for use in Li-ion batteries. *J. Power Sources* **248**, 91-100 (2014).

77.   D. Chen *et al.*, Operando Investigation into Dynamic Evolution of Cathode-Electrolyte Interfaces in a Li-Ion Battery. *Nano Lett.* **19**, 2037-2043 (2019).

78.   X. Li *et al.*, The design of a high-energy Li-ion battery using germanium-based anode and LiCoO2 cathode. *J. Power Sources* **293**, 868-875 (2015).

79.   J. Cho, Y. J. Kim, B. Park, Novel $LiCoO_2$ Cathode Material with Al_2O_3 Coating for a Li Ion Cell. *Chem. Mater.* **12**, 3788-3791 (2000).

80.   J. Kim, B. Kim, J.-G. Lee, J. Cho, B. Park, Direct carbon-black coating on $LiCoO_2$ cathode using surfactant for high-density Li-ion cell. *J. Power Sources* **139**, 289-294 (2005).

81.   M. Jo, Y.-S. Hong, J. Choo, J. Cho, Effect of $LiCoO_2$ Cathode Nanoparticle Size on High Rate Performance for Li-Ion Batteries. *J. Electrochem. Soc.* **156** (2009).

82.   W.-J. Zhang, Structure and performance of $LiFePO_4$ cathode materials: A review. *J. Power Sources* **196**, 2962-2970 (2011).

83.   C. Sun, S. Rajasekhara, J. B. Goodenough, F. Zhou, Monodisperse porous $LiFePO_4$ microspheres for a high power Li-ion battery cathode. *J. Am. Chem. Soc.* **133**, 2132-2135 (2011).

84.   A. Tron, Y. N. Jo, S. H. Oh, Y. D. Park, J. Mun, Surface Modification of the $LiFePO_4$ Cathode for the Aqueous Rechargeable Lithium Ion Battery. *ACS Appl. Mater. Interfaces* **9**, 12391-12399 (2017).

85.   L. Liao *et al.*, Effects of temperature on charge/discharge behaviors of $LiFePO_4$ cathode for Li-ion batteries. *Electrochim. Acta* **60**, 269-273 (2012).

86.   Y. Li *et al.*, Co-coating effect of $GdPO_4$ and carbon on $LiFePO_4$ cathode surface for lithium ion batteries. *Adv. Powder Technol.* **30**, 1442-1449 (2019).

87.   S. Cui *et al.*, Optimized Temperature Effect of Li-Ion Diffusion with Layer Distance in $Li(Ni_xMn_yCo_z)O_2$ Cathode Materials for High Performance Li-Ion Battery. *Adv. Energy Mater.* **6**, 1501309 (2016).

88.   X. Zhou, Y. X. Yin, L. J. Wan, Y. G. Guo, Facile synthesis of silicon nanoparticles inserted into graphene sheets as improved anode materials for lithium-ion batteries. *Chem. Comm.* **48**, 2198-2200 (2012).

89.   P. Roy, S. K. Srivastava, Nanostructured anode materials for lithium ion batteries. *J. Mater. Chem. A* **3**, 2454-2484 (2015).

90.   X. Zhou, L. J. Wan, Y. G. Guo, Binding SnO_2 nanocrystals in nitrogen-doped graphene sheets as anode materials for lithium-ion batteries. *Adv. Mater.* **25**, 2152-2157 (2013).

91.   W.-M. Zhang, X.-L. Wu, J.-S. Hu, Y.-G. Guo, L.-J. Wan, Carbon Coated Fe_3O_4 Nanospindles as a Superior Anode Material for Lithium-Ion Batteries. *Adv. Funct. Mater.* **18**, 3941-3946 (2008).

92.   W. Qi *et al.*, Nanostructured anode materials for lithium-ion batteries: principle, recent progress and future perspectives. *J. Mater. Chem. A* **5**, 19521-19540 (2017).

93.   L. Zhang, H. B. Wu, X. W. D. Lou, Iron-Oxide-Based Advanced Anode Materials for Lithium-Ion Batteries. *Adv. Energy Mater.* **4**, 1300958 (2014).

94.   T. Yang *et al.*, A new approach towards the synthesis of nitrogen-doped graphene/MnO_2 hybrids for ultralong cycle-life lithium ion batteries. *J. Mater. Chem. A* **3**, 6291-6296 (2015).

95.   S. Yang *et al.*, Fabrication of cobalt and cobalt oxide/graphene composites: towards high-performance anode materials for lithium ion batteries. *ChemSusChem* **3**, 236-239 (2010).

96.   Y. P. Wu, E. Rahm, R. Holze, Carbon anode materials for lithium ion batteries. *J. Power Sources* **114**, 228-236 (2003).

97.   P. Nie *et al.*, Prussian blue analogues: a new class of anode materials for lithium ion batteries. *J. Mater. Chem. A* **2**, 5852-5857 (2014).

98.   J. Wang *et al.*, Accurate control of multishelled Co_3O_4 hollow microspheres as high-performance anode materials in lithium-ion batteries. *Angew. Chem. Int. Ed. Engl.* **52**, 6417-6420 (2013).

99.   L. Wang *et al.*, Nano-structured phosphorus composite as high-capacity anode materials for lithium batteries. *Angew. Chem. Int. Ed. Engl.* **51**, 9034-9037 (2012).

100.   C. Wang *et al.*, A Hollow-Shell Structured V_2O_5 Electrode-Based Symmetric Full Li-Ion Battery with Highest Capacity. *Adv. Energy Mater.* **9**, 1900909 (2019).

101.   N. Mahmood, T. Tang, Y. Hou, Nanostructured Anode Materials for Lithium Ion Batteries: Progress, Challenge and Perspective. *Adv. Energy Mater.* **6**, 1600374 (2016).

102.   C. Ma, X. Shao, D. Cao, Nitrogen-doped graphene nanosheets as anode materials for lithium ion batteries: a first-principles study. *J. Mater. Chem.* **22**, 8911-8915 (2012).

103.   W. Luo *et al.*, Surface and Interface Engineering of Silicon-Based Anode Materials for Lithium-Ion Batteries. *Adv. Energy Mater.* **7**, 1701083 (2017).

104.   Z. Liu *et al.*, Silicon oxides: a promising family of anode materials for lithium-ion batteries. *Chem. Soc. Rev.* **48**, 285-309 (2019).

105.   X. H. Liu, J. Y. Huang, In situ TEM electrochemistry of anode materials in lithium ion batteries. *Energy Environ. Sci.* **4,** 3844-3860 (2011).

106.   N. Liu *et al.*, A yolk-shell design for stabilized and scalable li-ion battery alloy anodes. *Nano Lett.* **12**, 3315-3321 (2012).

107.   W. Li, X. Sun, Y. Yu, Si-, Ge-, Sn-Based Anode Materials for Lithium-Ion Batteries: From Structure Design to Electrochemical Performance. *Small Methods* **1**, 1600037 (2017).

108.   M. Endo, C. Kim, K. Nishimura, T. Fujino, K. Miyashita, Recent development of carbon materials for Li ion batteries. *Carbon* **38**, 183-197 (2000).

109.   Y. Deng, L. Wan, Y. Xie, X. Qin, G. Chen, Recent advances in Mn-based oxides as anode materials for lithium ion batteries. *RSC Adv.* **4**, 23914-23935 (2014).

110.   A. Eftekhari, Low voltage anode materials for lithium-ion batteries. *Energy Stor. Mater.* **7**, 157-180 (2017).

111.   J. Zhang, J. Lee, A review on prognostics and health monitoring of Li-ion battery. *J. Power Sources* **196**, 6007-6014 (2011).

112.   Z. Zeng *et al.*, Visualization of electrode-electrolyte interfaces in $LiPF_6$/EC/DEC electrolyte for lithium ion batteries via in situ TEM. *Nano Lett.* **14**, 1745-1750 (2014).

113.   Y. Yamada *et al.*, Unusual stability of acetonitrile-based superconcentrated electrolytes for fast-charging lithium-ion batteries. *J. Am. Chem. Soc.* **136**, 5039-5046 (2014).

114.   J. Ming *et al.*, New Insight on the Role of Electrolyte Additives in Rechargeable Lithium Ion Batteries. *ACS Energy Lett.* **4**, 2613-2622 (2019).

115.   W. Li *et al.*, A PEO-based gel polymer electrolyte for lithium ion batteries. *RSC Adv.* **7**, 23494-23501 (2017).

116.   M. L. Lazar, B. L. Lucht, Carbonate Free Electrolyte for Lithium Ion Batteries Containing γ-Butyrolactone and Methyl Butyrate. *J. Electrochem. Soc.* **162**, A928-A934 (2015).

117.   IEA, Global EV Outlook 2020, *IEA* (2020), Paris https://www.iea.org/reports/global-ev-outlook-2020

118.   U.S. Geological Survey, Mineral commodity summaries 2020: U.S. Geological Survey, 200 p. (2020), https://doi.org/10.3133/mcs2020.

119.   M. D. Slater, D. Kim, E. Lee, C. S. Johnson, Sodium-Ion Batteries. *Adv. Funct. Mater.* **23**, 947-958 (2013).

120.   V. Palomares *et al.*, Na-ion batteries, recent advances and present challenges to become low cost energy storage systems. *Energy Environ. Sci.* **5**, 5884-5901 (2012).

121.   M. Miroshnikov *et al.*, Nature-Derived Sodium-Ion Battery: Mechanistic Insights into Na-Ion Coordination within Sustainable Molecular Cathode Materials. *ACS Appl. Energy Mater.* **2**, 8596-8604 (2019).

122.   J. Y. Hwang, S. T. Myung, Y. K. Sun, Sodium-ion batteries: present and future. *Chem. Soc. Rev.* **46**, 3529-3614 (2017).

123.   W. Deng *et al.*, A low cost, all-organic Na-ion battery based on polymeric cathode and anode. *Sci. Rep.* **3**, 2671 (2013).

124.   D. Kundu, E. Talaie, V. Duffort, L. F. Nazar, The emerging chemistry of sodium ion batteries for electrochemical energy storage. *Angew. Chem. Int. Ed. Engl.* **54**, 3431-3448 (2015).

125.   A. Bauer *et al.*, The Scale-up and Commercialization of Nonaqueous Na-Ion Battery Technologies. *Adv. Energy Mater.* **8**,1702869 (2018).

126.   S. T. Dacek, W. D. Richards, D. A. Kitchaev, G. Ceder, Structure and Dynamics of Fluorophosphate Na-Ion Battery Cathodes. *Chem. Mater.* **28**, 5450-5460 (2016).

127.   J. Ding *et al.*, $KVOPO_4$: A New High Capacity Multielectron Na-Ion Battery Cathode. *Adv. Energy Mater.* **8**, 1800221 (2018).

128.   X. Guo *et al.*, Design Principles for Aqueous Na-Ion Battery Cathodes. *Chem. Mater.* **32**, 6875-6885 (2020).

129.   M. H. Han, E. Gonzalo, G. Singh, T. Rojo, A comprehensive review of sodium layered oxides: powerful cathodes for Na-ion batteries. *Energy Environ. Sci.* **8**, 81-102 (2015).

130.   L. Wang *et al.*, A superior low-cost cathode for a Na-ion battery. *Angew. Chem. Int. Ed. Engl.* **52**, 1964-1967 (2013).

131.   J. Wang *et al.*, A High-Energy NASICON-Type Cathode Material for Na-Ion Batteries. *Adv. Energy Mater.* **10**, 1903968 (2020).

132.   B. Su *et al.*, Na$_2$SeO$_3$: A Na-Ion Battery Positive Electrode Material with High Capacity. *J. Electrochem. Soc.* **166**, A5075-A5080 (2018).

133.   J. Song, M. Xu, L. Wang, J. B. Goodenough, Exploration of NaVOPO$_4$ as a cathode for a Na-ion battery. *Chem. Commun.* **49**, 5280-5282 (2013).

134.   J. W. Somerville *et al.*, Nature of the "Z"-phase in layered Na-ion battery cathodes. *Energy Environ. Sci.* **12**, 2223-2232 (2019).

135.   Y. U. Park *et al.*, A new high-energy cathode for a Na-ion battery with ultrahigh stability. *J. Am. Chem. Soc.* **135**, 13870-13878 (2013).

136.   Z. Liu *et al.*, Local Structure and Dynamics in the Na Ion Battery Positive Electrode Material Na$_3$V$_2$(PO$_4$)$_2$F$_3$. *Chem. Mater.* **26**, 2513-2521 (2014).

137.   A. Langrock *et al.*, Carbon coated hollow Na$_2$FePO$_4$F spheres for Na-ion battery cathodes. *J. Power Sources* **223**, 62-67 (2013).

138.   J. M. Clark, P. Barpanda, A. Yamada, M. S. Islam, Sodium-ion battery cathodes Na$_2$FeP$_2$O$_7$ and Na$_2$MnP$_2$O$_7$: diffusion behaviour for high rate performance. *J. Mater. Chem. A* **2**, 11807-11812 (2014).

139.   W. Luo *et al.*, Na-Ion Battery Anodes: Materials and Electrochemistry. *Acc. Chem. Res.* **49**, 231-240 (2016).

140.   T. Yang *et al.*, A Sustainable Route from Biomass Byproduct Okara to High Content Nitrogen-Doped Carbon Sheets for Efficient Sodium Ion Batteries. *Adv. Mater.* **28**, 539-545 (2016).

141.   T. Yang *et al.*, Half and full sodium-ion batteries based on maize with high-loading density and long-cycle life. *Nanoscale* **8**, 15497-15504 (2016).

142.   D. Su, S. Dou, G. Wang, Bismuth: A new anode for the Na-ion battery. *Nano Energy* **12**, 88-95 (2015).

143. S. Rubio *et al.*, Superior electrochemical performance of TiO_2 sodium-ion battery anodes in diglyme-based electrolyte solution. *J. Power Sources* **432**, 82-91 (2019).

144. K.-H. Nam, C.-M. Park, 2D layered Sb_2Se_3-based amorphous composite for high-performance Li- and Na-ion battery anodes. *J. Power Sources* **433** (2019).

145. Y. Liu *et al.*, Tin-coated viral nanoforests as sodium-ion battery anodes. *ACS Nano* **7**, 3627-3634 (2013).

146. H. Jin *et al.*, Synergy of Black Phosphorus-Graphite-Polyaniline-Based Ternary Composites for Stable High Reversible Capacity Na-Ion Battery Anodes. *ACS Appl. Mater. Interfaces* **11**, 16656-16661 (2019).

147. A. Chaturvedi *et al.*, Two Dimensional TiS_2 as a Promising Insertion Anode for Na-Ion Battery. *ChemistrySelect* **3**, 524-528 (2018).

148. Y. Bai *et al.*, Hard carbon originated from polyvinyl chloride nanofibers as high-performance anode material for Na-ion battery. *ACS Appl. Mater. Interfaces* **7**, 5598-5604 (2015).

149. A. Ponrouch, E. Marchante, M. Courty, J.-M. Tarascon, M. R. Palacín, In search of an optimized electrolyte for Na-ion batteries. *Energy Environ. Sci.* **5** (2012).

150. Z. Yu *et al.*, Synthesis and understanding of $Na_{11}Sn_2PSe_{12}$ with enhanced ionic conductivity for all-solid-state Na-ion battery. *Energy Stor. Mater.* **17**, 70-77 (2019).

151. G. Yan *et al.*, A New Electrolyte Formulation for Securing High Temperature Cycling and Storage Performances of Na-Ion Batteries. *Adv. Energy Mater.* **9**, 1901431 (2019).

152. L. Suo *et al.*, "Water-in-Salt" Electrolyte Makes Aqueous Sodium-Ion Battery Safe, Green, and Long-Lasting. *Adv.Energy Mater.***7,** 1701189 (2017).

153. A. Ponrouch *et al.*, Towards high energy density sodium ion batteries through electrolyte optimization. *Energy Environ. Sci.* **6**, 2361-2369 (2013).

154. Y. Li *et al.*, Ultralow-Concentration Electrolyte for Na-Ion Batteries. *ACS Energy Lett.* **5**, 1156-1158 (2020).

155. X. Li *et al.*, The importance of solid electrolyte interphase formation for long cycle stability full-cell Na-ion batteries. *Nano Energy* **27**, 664-672 (2016).

156. L. Jiang *et al.*, High-Voltage Aqueous Na-Ion Battery Enabled by Inert-Cation-Assisted Water-in-Salt Electrolyte. *Adv. Mater.* **32**, e1904427 (2020).

157. C. Bommier, X. Ji, Electrolytes, SEI Formation, and Binders: A Review of Nonelectrode Factors for Sodium-Ion Battery Anodes. *Small* **14**, e1703576 (2018).

158. G. Harper *et al.*, Recycling lithium-ion batteries from electric vehicles. *Nature* **575**, 75-86 (2019).

159. Y. Guo, H. Li, T. Zhai, Reviving Lithium-Metal Anodes for Next-Generation High-Energy Batteries. *Adv. Mater.* **29**, 1700007 (2017).

160. C. Fang *et al.*, Quantifying inactive lithium in lithium metal batteries. *Nature* **572**, 511-515 (2019).

161. K.-H. Chen *et al.*, Dead lithium: mass transport effects on voltage, capacity, and failure of lithium metal anodes. *J. Mater. Chem. A* **5**, 11671-11681 (2017).

162. D. Lin, Y. Liu, Y. Cui, Reviving the lithium metal anode for high-energy batteries. *Nat. Nanotechnol.* **12**, 194-206 (2017).

163. B. Li, Y. Wang, S. Yang, A Material Perspective of Rechargeable Metallic Lithium Anodes. *Adv. Energy Mater.* **8**, 1702296 (2018).

164. W. Xu *et al.*, Lithium metal anodes for rechargeable batteries. *Energy Environ. Sci.* **7**, 513-537 (2014).

165. C. Z. Zhao *et al.*, An ion redistributor for dendrite-free lithium metal anodes. *Sci. Adv.* **4**, eaat3446 (2018).

166. Y. T. Weng *et al.*, An ultrathin ionomer interphase for high efficiency lithium anode in carbonate based electrolyte. *Nat. Commun.* **10**, 5824 (2019).

167.	B. Zhou *et al.*, A High-Performance Li-O$_2$ Battery with a Strongly Solvating Hexamethylphosphoramide Electrolyte and a LiPON-Protected Lithium Anode. *Adv. Mater.* **29** 1701568 (2017).

168.	J. He, A. Manthiram, Long-Life, High-Rate Lithium-Sulfur Cells with a Carbon-Free VN Host as an Efficient Polysulfide Adsorbent and Lithium Dendrite Inhibitor. *Adv. Energy Mater.* **10**, 1903241 (2019).

169.	H. Zheng *et al.*, Intrinsic Lithiophilicity of Li-Garnet Electrolytes Enabling High-Rate Lithium Cycling. *Adv. Funct. Mater.* **30**, 1906189 (2019).

170.	G. Zheng *et al.*, High-Performance Lithium Metal Negative Electrode with a Soft and Flowable Polymer Coating. *ACS Energy Lett.* **1**, 1247-1255 (2016).

171.	J. Zhao *et al.*, Air-stable and freestanding lithium alloy/graphene foil as an alternative to lithium metal anodes. *Nat. Nanotechnol.* **12**, 993-999 (2017).

172.	R. Zhang *et al.*, Lithiophilic Sites in Doped Graphene Guide Uniform Lithium Nucleation for Dendrite-Free Lithium Metal Anodes. *Angew. Chem. Int. Ed. Engl.* **56**, 7764-7768 (2017).

173.	X. X. Zeng *et al.*, Reshaping Lithium Plating/Stripping Behavior via Bifunctional Polymer Electrolyte for Room-Temperature Solid Li Metal Batteries. *J. Am. Chem. Soc.* **138**, 15825-15828 (2016).

174.	B. Zhu *et al.*, Poly(dimethylsiloxane) Thin Film as a Stable Interfacial Layer for High-Performance Lithium-Metal Battery Anodes. *Adv. Mater.* **29**, 1603755 (2017).

175.	Q. Xu *et al.*, Air-Stable and Dendrite-Free Lithium Metal Anodes Enabled by a Hybrid Interphase of C$_{60}$ and Mg. *Adv. Energy Mater.* **10**, 1903292 (2019).

176.	J. Xie *et al.*, Incorporating Flexibility into Stiffness: Self-Grown Carbon Nanotubes in Melamine Sponges Enable A Lithium-Metal-Anode Capacity of 15 mA h cm^{-2} Cyclable at 15 mA cm^{-2}. *Adv. Mater.* **31**, e1805654 (2019).

177.	J. Wen *et al.*, Highly Adhesive Li-BN Nanosheet Composite Anode with Excellent Interfacial Compatibility for Solid-State Li Metal Batteries. *ACS Nano* **13**, 14549-14556 (2019).

178. L. Wang *et al.*, Identifying the components of the solid-electrolyte interphase in Li-ion batteries. *Nat. Chem.* **11**, 789-796 (2019).

179. J. Wang *et al.*, Improving cyclability of Li metal batteries at elevated temperatures and its origin revealed by cryo-electron microscopy. *Nat. Energy* **4**, 664-670 (2019).

180. Y. Sun *et al.*, Stabilized Li3N for efficient battery cathode prelithiation. *Energy Stor. Mater.* **6**, 119-124 (2017).

181. S. B. Son *et al.*, An artificial interphase enables reversible magnesium chemistry in carbonate electrolytes. *Nat. Chem.* **10**, 532-539 (2018).

182. P. Shi *et al.*, Lithiophilic LiC_6 Layers on Carbon Hosts Enabling Stable Li Metal Anode in Working Batteries. *Adv. Mater.* **31**, e1807131 (2019).

183. D. Rehnlund *et al.*, Lithium trapping in alloy forming electrodes and current collectors for lithium based batteries. *Energy Environ. Sci.* **10**, 1350-1357 (2017).

184. K. Park, J. B. Goodenough, Dendrite-Suppressed Lithium Plating from a Liquid Electrolyte via Wetting of Li_3N. *Adv. Energy Mater.* **7**, 1700732 (2017).

185. Z. Lu *et al.*, Graphitic Carbon Nitride Induced Micro-Electric Field for Dendrite-Free Lithium Metal Anodes. *Adv. Energy Mater.* **9**, 1803186 (2019).

186. Y. Liu *et al.*, An Ultrastrong Double-Layer Nanodiamond Interface for Stable Lithium Metal Anodes. *Joule* **2**, 1595-1609 (2018).

187. Y. Liu *et al.*, Making Li-metal electrodes rechargeable by controlling the dendrite growth direction. *Nat. Energy* **2**, 17083 (2017).

188. Y. Liu *et al.*, An Artificial Solid Electrolyte Interphase with High Li-Ion Conductivity, Mechanical Strength, and Flexibility for Stable Lithium Metal Anodes. *Adv. Mater.* **29**, 1605531 (2017).

189.   X. Liu, J. Liu, T. Qian, H. Chen, C. Yan, Novel Organophosphate-Derived Dual-Layered Interface Enabling Air-Stable and Dendrite-Free Lithium Metal Anode. *Adv. Mater.* **32**, e1902724 (2020).

190.   W. Liu, D. Lin, A. Pei, Y. Cui, Stabilizing Lithium Metal Anodes by Uniform Li-Ion Flux Distribution in Nanochannel Confinement. *J. Am. Chem. Soc.* **138**, 15443-15450 (2016).

191.   W. Liu *et al.*, Core-Shell Nanoparticle Coating as an Interfacial Layer for Dendrite-Free Lithium Metal Anodes. *ACS Cent. Sci.* **3**, 135-140 (2017).

192.   K. Liu *et al.*, Lithium Metal Anodes with an Adaptive "Solid-Liquid" Interfacial Protective Layer. *J. Am. Chem. Soc.* **139**, 4815-4820 (2017).

193.   K. Liu *et al.*, Oxygen-rich carbon nanotube networks for enhanced lithium metal anode. *Energy Stor. Mater.* **15**, 308-314 (2018).

194.   J. Liu *et al.*, Pathways for practical high-energy long-cycling lithium metal batteries. *Nat. Energy* **4**, 180-186 (2019).

195.   H. Liu *et al.*, Plating/Stripping Behavior of Actual Lithium Metal Anode. *Adv. Energy Mater.* **9**, 1902254 (2019).

196.   A. C. Kozen *et al.*, Stabilization of Lithium Metal Anodes by Hybrid Artificial Solid Electrolyte Interphase. *Chem. Mater.* **29**, 6298-6307 (2017).

197.   P. J. Kim, V. G. Pol, High Performance Lithium Metal Batteries Enabled by Surface Tailoring of Polypropylene Separator with a Polydopamine/Graphene Layer. *Adv. Energy Mater.* **8**, 1802665 (2018).

198.   M. S. Kim *et al.*, Langmuir-Blodgett artificial solid-electrolyte interphases for practical lithium metal batteries. *Nat. Energy* **3**, 889-898 (2018).

199.   E. Kazyak, K. N. Wood, N. P. Dasgupta, Improved Cycle Life and Stability of Lithium Metal Anodes through Ultrathin Atomic Layer Deposition Surface Treatments. *Chem. Mater.* **27**, 6457-6462 (2015).

200.   Y. Jin *et al.*, Self-healing SEI enables full-cell cycling of a silicon-majority anode with a coulombic efficiency exceeding 99.9%. *Energy Environ. Sci.* **10**, 580-592 (2017).

201.   H. Huo *et al.*, Design of a mixed conductive garnet/Li interface for dendrite-free solid lithium metal batteries. *Energy Environ. Sci.* **13**, 127-134 (2020).

202.   S. Choudhury *et al.*, Electroless Formation of Hybrid Lithium Anodes for Fast Interfacial Ion Transport. *Angew. Chem. Int. Ed. Engl.* **56**, 13070-13077 (2017).

203.   W. Deng, X. Zhou, Q. Fang, Z. Liu, Microscale Lithium Metal Stored inside Cellular Graphene Scaffold toward Advanced Metallic Lithium Anodes. *Adv. Energy Mater.* **8**, 1703152 (2018).

204.   Y. Gao *et al.*, Polymer-inorganic solid-electrolyte interphase for stable lithium metal batteries under lean electrolyte conditions. *Nat. Mater.* **18**, 384-389 (2019).

205.   X. B. Cheng *et al.*, Nanodiamonds suppress the growth of lithium dendrites. *Nat. Commun.* **8**, 336 (2017).

206.   D. Lu *et al.*, Failure Mechanism for Fast-Charged Lithium Metal Batteries with Liquid Electrolytes. *Adv. Energy Mater.* **5**, 1400993 (2015).

207.   F. Qiu *et al.*, A Concentrated Ternary-Salts Electrolyte for High Reversible Li Metal Battery with Slight Excess Li. *Adv. Energy Mater.* **9**, 1803372 (2018).

208.   X. Ren *et al.*, High-Concentration Ether Electrolytes for Stable High-Voltage Lithium Metal Batteries. *ACS Energy Lett.* **4**, 896-902 (2019).

209.   F. Shi *et al.*, Lithium metal stripping beneath the solid electrolyte interphase. *Proc. Natl. Acad. Sci. U.S.A.* **115**, 8529-8534 (2018).

210.   C. Yang *et al.*, Continuous plating/stripping behavior of solid-state lithium metal anode in a 3D ion-conductive framework. *Proc. Natl. Acad. Sci. U.S.A.* **115**, 3770-3775 (2018).

211.   H. Ye, S. Xin, Y.-X. Yin, Y.-G. Guo, Advanced Porous Carbon Materials for High-Efficient Lithium Metal Anodes. *Adv. Energy Mater.* **7**, 1700530 (2017).

212.   R. Zhang *et al.*, Advanced Micro/Nanostructures for Lithium Metal Anodes. *Adv. Sci.* **4**, 1600445 (2017).

213.   P. Liu *et al.*, Dendrite-Free Potassium Metal Anodes in a Carbonate Electrolyte. *Adv. Mater.* **32**, e1906735 (2020).

214.   L. Fan, X. Li, Recent advances in effective protection of sodium metal anode. *Nano Energy* **53**, 630-642 (2018).

215.   B. Lee, E. Paek, D. Mitlin, S. W. Lee, Sodium Metal Anodes: Emerging Solutions to Dendrite Growth. *Chem. Rev.* **119**, 5416-5460 (2019).

216.   S. Li *et al.*, Hierarchical Co_3O_4 Nanofiber-Carbon Sheet Skeleton with Superior Na/Li-Philic Property Enabling Highly Stable Alkali Metal Batteries. *Adv. Funct. Mater.* **29**, 1808847 (2019).

217.   Y. Zhao, K. R. Adair, X. Sun, Recent developments and insights into the understanding of Na metal anodes for Na-metal batteries. *Energy Environ. Sci.* **11**, 2673-2695 (2018).

218.   Y. Zhao *et al.*, Superior Stable and Long Life Sodium Metal Anodes Achieved by Atomic Layer Deposition. *Adv. Mater.* **29**, 1606663 (2017).

219.   J. Zheng *et al.*, Extremely Stable Sodium Metal Batteries Enabled by Localized High-Concentration Electrolytes. *ACS Energy Lett.* **3**, 315-321 (2018).

220.   Y. Zheng *et al.*, High-Capacity All-Solid-State Sodium Metal Battery with Hybrid Polymer Electrolytes. *Adv. Energy Mater.* **8**, 1801885 (2018).

221.   S. Wheeler, K. Hurlbutt, M. Pasta, A New Solid-State Sodium-Metal Battery. *Chem* **4**, 666-668 (2018).

222.   Y. Xu *et al.*, Honeycomb-like porous 3D nickel electrodeposition for stable Li and Na metal anodes. *Energy Stor. Mater.* **12**, 69-78 (2018).

223.   Z. Xu *et al.*, Stable Na Metal Anode Enabled by a Reinforced Multistructural SEI Layer. *Adv. Funct. Mater.* **29**, 1901924 (2019).

224.   H. Ye *et al.*, Realizing a highly stable sodium battery with dendrite-free sodium metal composite anodes and O_3-type cathodes. *Nano Energy* **48**, 369-376 (2018).

225.   C. Zhang *et al.*, 2D Materials for Lithium/Sodium Metal Anodes. *Adv. Energy Mater.* **8**, 1802833 (2018).

226.   Y. Wang *et al.*, Developments and Perspectives on Emerging High-Energy-Density Sodium-Metal Batteries. *Chem* **5**, 2547-2570 (2019).

227.   T.-S. Wang, Y. Liu, Y.-X. Lu, Y.-S. Hu, L.-Z. Fan, Dendrite-free Na metal plating/stripping onto 3D porous Cu hosts. *Energy Stor. Mater.* **15**, 274-281 (2018).

228.   H. Sun *et al.*, A safe and non-flammable sodium metal battery based on an ionic liquid electrolyte. *Nat. Commun.* **10**, 3302 (2019).

229.   S. Tang *et al.*, A room-temperature sodium metal anode enabled by a sodiophilic layer. *Nano Energy* **48**, 101-106 (2018).

230.   H. Tian *et al.*, Theoretical Investigation of 2D Layered Materials as Protective Films for Lithium and Sodium Metal Anodes. *Adv. Energy Mater.* **7**, 1602528 (2017).

231.   Q. Wang *et al.*, Stabilizing a sodium-metal battery with the synergy effects of a sodiophilic matrix and fluorine-rich interface. *J. Mater. Chem. A* **7**, 24857-24867 (2019).

232.   Y. Tian *et al.*, Reactivity-Guided Interface Design in Na Metal Solid-State Batteries. *Joule* **3**, 1037-1050 (2019).

233.   S. Song *et al.*, A hybrid polymer/oxide/ionic-liquid solid electrolyte for Na-metal batteries. *J. Mater. Chem. A* **5**, 6424-6431 (2017).

234.   B. Sun *et al.*, Dendrite-Free Sodium-Metal Anodes for High-Energy Sodium-Metal Batteries. *Adv. Mater.* **30**, e1801334 (2018).

235.   B. Sun *et al.*, Design Strategies to Enable the Efficient Use of Sodium Metal Anodes in High-Energy Batteries. *Adv. Mater.* **32**, e1903891 (2020).

236.   H. Wang, C. Wang, E. Matios, W. Li, Facile Stabilization of the Sodium Metal Anode with Additives: Unexpected Key Role of Sodium Polysulfide and Adverse Effect of Sodium Nitrate. *Angew. Chem. Int. Ed. Engl.* **57**, 7734-7737 (2018).

237.   N. D. K. Tu *et al.*, Co-solvent induced piezoelectric γ-phase nylon-11 separator for sodium metal battery. *Nano Energy* **70**, 104501 (2020).

238.   J. Qian *et al.*, Protecting lithium/sodium metal anode with metal-organic framework based compact and robust shield. *Nano Energy* **60**, 866-874 (2019).

239.   L. Schafzahl, I. Hanzu, M. Wilkening, S. A. Freunberger, An Electrolyte for Reversible Cycling of Sodium Metal and Intercalation Compounds. *ChemSusChem* **10**, 401-408 (2017).

240.   Z. W. Seh, J. Sun, Y. Sun, Y. Cui, A Highly Reversible Room-Temperature Sodium Metal Anode. *ACS Cent. Sci.* **1**, 449-455 (2015).

241.   J. Lee *et al.*, Ultraconcentrated Sodium Bis(fluorosulfonyl)imide-Based Electrolytes for High-Performance Sodium Metal Batteries. *ACS Appl. Mater. Interfaces* **9**, 3723-3732 (2017).

242.   L. Ma *et al.*, Dendrite-free lithium metal and sodium metal batteries. *Energy Stor. Mater.* **27**, 522-554 (2020).

243.   T. C. Mendes *et al.*, Supported Ionic Liquid Gel Membrane Electrolytes for a Safe and Flexible Sodium Metal Battery. *ACS Sustain. Chem. Eng.* **7**, 3722-3726 (2019).

244.   Y. J. Kim *et al.*, Enhancing the Cycling Stability of Sodium Metal Electrodes by Building an Inorganic-Organic Composite Protective Layer. *ACS Appl. Mater. Interfaces* **9**, 6000-6006 (2017).

245.   D. Lei *et al.*, Cross-linked beta alumina nanowires with compact gel polymer electrolyte coating for ultra-stable sodium metal battery. *Nat. Commun.* **10**, 4244 (2019).

246.   W. Luo *et al.*, Ultrathin Surface Coating Enables the Stable Sodium Metal Anode. *Adv. Energy Mater.* **7**, 1601526 (2017).

247.   X. Chi *et al.*, A high-energy quinone-based all-solid-state sodium metal battery. *Nano Energy* **62**, 718-724 (2019).

248.   S.-S. Chi, X.-G. Qi, Y.-S. Hu, L.-Z. Fan, 3D Flexible Carbon Felt Host for Highly Stable Sodium Metal Anodes. *Adv. Energy Mater.* **8**, 1702764 (2018).

249.   S. Liu *et al.*, Porous Al Current Collector for Dendrite-Free Na Metal Anodes. *Nano Lett.* **17**, 5862-5868 (2017).

250.   K. Yan *et al.*, Selective deposition and stable encapsulation of lithium through heterogeneous seeded growth. *Nat. Energy* **1**, 16010 (2016).

251.   C. Yang *et al.*, Ultrafine Silver Nanoparticles for Seeded Lithium Deposition toward Stable Lithium Metal Anode. *Adv. Mater.* **29**, 1702714 (2017).

252.   J. Xiang *et al.*, Improved Rechargeability of Lithium Metal Anode via Controlling Lithium-Ion Flux. *Adv. Energy Mater.* **8**, 1802352 (2018).

253.   W. Ye *et al.*, Stable Nano-Encapsulation of Lithium Through Seed-Free Selective Deposition for High-Performance Li Battery Anodes. *Adv. Energy Mater.* **10**, 1902956 (2020).

254.   J. Pu *et al.*, Interlayer Lithium Plating in Au Nanoparticles Pillared Reduced Graphene Oxide for Lithium Metal Anodes. *Adv. Funct. Mater.* **28**, 1804133 (2018).

255.   A. C. Kozen *et al.*, Next-Generation Lithium Metal Anode Engineering via Atomic Layer Deposition. *ACS Nano* **9**, 5884-5892 (2015).

256.   W. Chen *et al.*, Lithiophilic montmorillonite serves as lithium ion reservoir to facilitate uniform lithium deposition. *Nat. Commun.* **10**, 4973 (2019).

257.   R. Zhang *et al.*, Coralloid Carbon Fiber-Based Composite Lithium Anode for Robust Lithium Metal Batteries. *Joule* **2**, 764-777 (2018).

258.   P. Yin *et al.*, Single Cobalt Atoms with Precise N-Coordination as Superior Oxygen Reduction Reaction Catalysts. *Angew. Chem. Int. Ed. Engl.* **55**, 10800-10805 (2016).

259.   X. F. Yang *et al.*, Single-atom catalysts: a new frontier in heterogeneous catalysis. *Acc. Chem. Res.* **46**, 1740-1748 (2013).

260.   H. Wei *et al.*, FeOx-supported platinum single-atom and pseudo-single-atom catalysts for chemoselective hydrogenation of functionalized nitroarenes. *Nat. Commun.* **5**, 5634 (2014).

261.   S. Sun *et al.*, Single-atom Catalysis Using Pt/Graphene Achieved through Atomic Layer Deposition. *Sci. Rep.* **3**, 1775 (2013).

262.   B. Qiao *et al.*, Single-atom catalysis of CO oxidation using Pt_1/FeO_x. *Nat. Chem.* **3**, 634-641 (2011).

263.   S. Mitchell, E. Vorobyeva, J. Perez-Ramirez, The Multifaceted Reactivity of Single-Atom Heterogeneous Catalysts. *Angew. Chem. Int. Ed. Engl.* **57**, 15316-15329 (2018).

264.   M. D. Marcinkowski *et al.*, Pt/Cu single-atom alloys as coke-resistant catalysts for efficient C-H activation. *Nat. Chem.* **10**, 325-332 (2018).

265.   X. Li *et al.*, Single-Atom Pt as Co-Catalyst for Enhanced Photocatalytic H_2 Evolution. *Adv. Mater.* **28**, 2427-2431 (2016).

266.   T. E. James, S. L. Hemmingson, C. T. Campbell, Energy of Supported Metal Catalysts: From Single Atoms to Large Metal Nanoparticles. *ACS Catal.* **5**, 5673-5678 (2015).

267.   N. Cheng *et al.*, Platinum single-atom and cluster catalysis of the hydrogen evolution reaction. *Nat. Commun.* **7**, 13638 (2016).

268.   P. Zhai *et al.*, Uniform Lithium Deposition Assisted by Single-Atom Doping toward High-Performance Lithium Metal Anodes. *Adv. Energy Mater.* **9**, 1804019 (2019).

269.   K. Xu *et al.*, Dendrite-tamed deposition kinetics using single-atom Zn sites for Li metal anode. *Energy Stor. Mater.* **23**, 587-593 (2019).

270. B. J. Ford, D. C. Joy, B. J. Ford. Scanning electron microscope. *Encyclopedia Britannica*, 30 Oct. 2019, https://www.britannica.com/technology/scanning-electron-microscope.

271. B. J. Ford, D. C. Joy, B. J. Ford. Transmission electron microscope. *Encyclopedia Britannica*, 23 Sep. 2019, https://www.britannica.com/technology/transmission-electron-microscope.

272. M. T. Otten, High-Angle annular dark-field imaging on a tem/stem system. *J. Electron Microsc. Techn.* **17**, 221-230 (1992).

273. J.J. Rehr, A.L. Ankudinov, Progress in the theory and interpretation of XANES. *Coord. Chem. Rev.* **249**, 131-140 (2005).

274. F. D. Groot, High-Resolution X-ray Emission and X-ray Absorption Spectroscopy. *Chem. Rev*. **101**, 1779-1808 (2001).

275. J. B. Allen, R. F. Larry, Electrochemical methods fundamentals and applications. *John Wiley & Sons, Inc.* (2001).

276. J. Xiao, How lithium dendrites form in liquid batteries. *Science* **366**, 426-427 (2019).

277. H. Wang, E. Matios, J. Luo, W. Li, Combining theories and experiments to understand the sodium nucleation behavior towards safe sodium metal batteries. *Chem. Soc. Rev.* **49**, 3783-3805 (2020).

278. A. Pei, G. Zheng, F. Shi, Y. Li, Y. Cui, Nanoscale Nucleation and Growth of Electrodeposited Lithium Metal. *Nano Lett.* **17**, 1132-1139 (2017).

279. P. Bai, J. Li, F. R. Brushett, M. Z. Bazant, Transition of lithium growth mechanisms in liquid electrolytes. *Energy Environ. Sci.* **9**, 3221-3229 (2016).

280. A. M. Hafez *et al.*, Stable Metal Anode enabled by Porous Lithium Foam with Superior Ion Accessibility. *Adv. Mater.* **30**, e1802156 (2018).

281. X. B. Cheng, R. Zhang, C. Z. Zhao, Q. Zhang, Toward Safe Lithium Metal Anode in Rechargeable Batteries: A Review. *Chem. Rev.* **117**, 10403-10473 (2017).

282. K. Tantratian *et al.*, Stable Li Metal Anode Enabled by Space Confinement and Uniform Curvature through Lithiophilic Nanotube Arrays. *Adv. Energy Mater.* **10**, 1902819 (2019).

283.   Y. Li *et al.*, Robust Pinhole-free Li₃N Solid Electrolyte Grown from Molten Lithium. *ACS Cent. Sci.* **4**, 97-104 (2018).

284.   D. Cao *et al.*, 3D Printed High-Performance Lithium Metal Microbatteries Enabled by Nanocellulose. *Adv. Mater.* **31**, e1807313 (2019).

285.   Q. Wang *et al.*, Stable Li metal anode with protected interface for high-performance Li metal batteries. *Energy Stor. Mater.* **15**, 249-256 (2018).

286.   T. T. Zuo *et al.*, Graphitized Carbon Fibers as Multifunctional 3D Current Collectors for High Areal Capacity Li Anodes. *Adv. Mater.* **29**, 1700389 (2017).

287.   C. Zhang *et al.*, Incorporating Ionic Paths into 3D Conducting Scaffolds for High Volumetric and Areal Capacity, High Rate Lithium-Metal Anodes. *Adv. Mater.* **30**, e1801328 (2018).

288.   H. Qiu, T. Tang, M. Asif, X. Huang, Y. Hou, 3D Porous Cu Current Collectors Derived by Hydrogen Bubble Dynamic Template for Enhanced Li Metal Anode Performance. *Adv. Funct. Mater.* **29**, 1808468 (2019).

289.   F. Pei *et al.*, Robust Lithium Metal Anodes Realized by Lithiophilic 3D Porous Current Collectors for Constructing High-Energy Lithium-Sulfur Batteries. *ACS Nano* **13**, 8337-8346 (2019).

290.   Q. Li, S. Zhu, Y. Lu, 3D Porous Cu Current Collector/Li-Metal Composite Anode for Stable Lithium-Metal Batteries. *Adv. Funct. Mater.* **27**, 1606422 (2017).

291.   L. Fan *et al.*, Enabling Stable Lithium Metal Anode via 3D Inorganic Skeleton with Superlithiophilic Interphase. *Adv. Energy Mater.* **8**, 1802350 (2018).

292.   P. Li *et al.*, Anchoring an Artificial Solid-Electrolyte Interphase Layer on a 3D Current Collector for High-Performance Lithium Anodes. *Angew. Chem. Int. Ed. Engl.* **58**, 2093-2097 (2019).

293.   G. Liang *et al.*, Commencing an Acidic Battery Based on a Copper Anode with Ultrafast Proton-Regulated Kinetics and Superior Dendrite-Free Property. *Adv. Mater.* **31**, e1905873 (2019).

294.   D. Lin *et al.*, Conformal Lithium Fluoride Protection Layer on Three-Dimensional Lithium by Nonhazardous Gaseous Reagent Freon. *Nano Lett.* **17**, 3731-3737 (2017).

295.   K. Liu *et al.*, Stretchable Lithium Metal Anode with Improved Mechanical and Electrochemical Cycling Stability. *Joule* **2**, 1857-1865 (2018).

8 ANNEXE

8.1 First and Co-First Authored Publications

1. **Tingzhou Yang**, Tao Qian, Mengfan Wang, Jie Liu, Jinqiu Zhou, Zhouzhou Sun, Muzi Chen and Chenglin Yan, A new approach towards the synthesis of nitrogen doped graphene/MnO_2 hybrids for ultralong cyclelife lithium ion batteries, *Journal of Materials Chemical A*, **2015**, 3, 6291-6296.

2. **Tingzhou Yang**, Tao Qian, Mengfan Wang, Xiaowei Shen, Na Xu, Zhouzhou Sun, and Chenglin Yan, A Sustainable Route from Biomass Byproduct Okara to High Content Nitrogen-Doped Carbon Sheets for Efficient Sodium Ion Batteries, *Advanced Materials*, **2016**, 28, 539-545.

3. **Tingzhou Yang**, Xiaoying Niu, Tao Qian, Xiaowei Shen, Jingqiu Zhou, Na Xu and Chenglin Yan, Half and full sodium-ion batteries based on maize with high-loading density and long-cycle life, *Nanoscale*, **2016**, 8, 15497-15504.

4. **Tingzhou Yang**, Tao Qian, Jie Liu, Na Xu, Yutao Li, Nicholas Grundish, Chenglin Yan, and John B. Goodenough, A New Type of Electrolyte System To Suppress Polysulfide Dissolution for Lithium−Sulfur Battery, *ACS Nano*, **2019**, 13, 9067-9073.

5. **Tingzhou Yang**, Tao Qian, Xiaowei Shen, Mengfan Wang, Sisi Liu, Jun Zhong, Chenglin Yan and Federico Rosei, Single-cluster Au as an usher for deeply cyclable Li metal anodes, *Journal of Materials Chemical A*, **2019**, 7, 14496-14503.

6. **Tingzhou Yang**, Tao Qian, Yawen Sun, Jun Zhong, Federico Rosei, and Chenglin Yan, Mega High Utilization of Sodium Metal Anodes Enabled by Single Zinc Atom Sites, *Nano Letters*, **2019**, 19, 7827-7835.

7. Yawen Sun[1], **Tingzhou Yang[1]**,(Co-first author) Haoqing Ji, Jinqiu Zhou, Zhenkang Wang, Tao Qian, and Chenglin Yan, Boosting the Optimization of Lithium Metal Batteries by Molecular Dynamics Simulations: A Perspective, *Advanced Energy Materials*, **2020,** 10, 2002373.

8. **Tingzhou Yang,** Yawen Sun, Tao Qian, Jie Liu, Xuejun Liu, Federico Rosei, and Chenglin Yan, Lithium dendrite inhibition via 3D porous lithium metal anode accompanied by inherent SEI layer, *Energy Storage Materials*, **2020**, 26, 385-390.

9. **Tingzhou Yang**, Sai Wang, Daniele Benetti, Kanghong Wang, Yawen Sun, Haoqing Ji, Tao Qian, Chenglin Yan, Federico Rosei, Efficient solar domestic and industrial sewage purification via polymer wastewater collector, *Chemical Engineering Journal*, **2022**, 428, 131199.

8.2 Co-Authored Publications

1. Tao Qian, Na Xu, Jinqiu Zhou **Tingzhou Yang**, Xuejun Liu, Xiaowei Shen, Jiaqi Liang, and Chenglin Yan, Interconnected three-dimensional V_2O_5/polypyrrole network nanostructures for high performance solid-state supercapacitors, *Journal of Materials Chemistry A*, **2015**, 3, 488-493.

2. Jinqiu Zhou, Tao Qian, **Tingzhou Yang**, Mengfan Wang, Jun Guo, and Chenglin Yan, Nanomeshes of highly crystalline nitrogen-doped carbon encapsulated Fe/Fe$_3$C electrodes as ultrafast and stable anodes for Li-ion batteries, *Journal of Materials Chemistry A*, **2015**, 3, 15008-15014.

3. Tao Qian, Jinqiu Zhou, Na Xu, **Tingzhou Yang**, Xiaowei Shen, Xuejun Liu, Shishan Wu, and Chenglin Yan, On-chip supercapacitors with ultrahigh volumetric performance based on electrochemically co-deposited CuO/polypyrrole nanosheet arrays, *Nanotechnology*, **2015**, 26, 425402.

4. Yu Chen, Lifeng Liu, Jie Xiong, **Tingzhou Yang**, Yong Qin, and Chenglin Yan, Porous Si nanowires from cheap metallurgical silicon stabilized by a surface oxide layer for lithium ion batteries, *Advanced Functional Materials*, **2015**, 25, 6701-6709.

5. Xiaowei Shen, Tao Qian, Jinqiu Zhou, Na Xu, **Tingzhou Yang**, and Chenglin Yan, Highly Flexible Full Lithium Batteries with Self-Knitted α-MnO$_2$ Fabric Foam, *ACS applied materials & interfaces*, **2015**, 7, 25298-25305.

6. Na Xu, Jiaqi Liang, Tao Qian, **Tingzhou Yang**, and Chenglin Yan, Half-cell and full-cell applications of horizontally aligned reduced oxide graphene/V$_2$O$_5$ sheets as cathodes for high stability lithium-ion batteries, *RSC Advances*, **2016**, 6, 68581-98587.

7. Mouping Fan, Yu Chen, Yihao Xie, **Tingzhou Yang**, Xiaowei Shen, Na Xu, Haiying Yu, and Chenglin Yan, Half-Cell and Full-Cell Applications of Highly Stable and Binder-Free Sodium Ion Batteries Based on Cu$_3$P Nanowire Anodes, *Advanced Functional Materials*, **2016**, 26, 5019-5027.

8. Wei Chen, Tao Qian, Jie Xiong, Na Xu, Xuejun Liu, Jie Liu, Jinqiu Zhou, Xiaowei Shen, **Tingzhou Yang**, Yu Chen, and Chenglin Yan, A new type of multifunctional polar binder: toward practical application of high energy lithium sulfur batteries, *Advanced Materials*, **2017**, 29, 1605160.

9. Jinqiu Zhou, Mengfan Wang, Tao Qian, Sisi Liu, Xuecheng Cao, **Tingzhou Yang**, Ruizhi Yang, Chenglin Yan, Porous yolk–shell microspheres as N-doped carbon matrix for motivating the oxygen reduction activity of oxygen evolution oriented materials, *Nanotechnology*, **2017**, 28, 365403.

10. Dan Li, Jie Liu, Na Xu, Mengfan Wang, Xuejun Liu, **Tingzhou Yang**, Tao Qian, and Chenglin Yan, Stabilizing cathodes of lithium-sulfur batteries by the chemical binding of sulfur and their discharge products to carbon nanofibers, *New Journal of Chemistry*, **2019**, 43, 15267-15274.

11. Heng Zhang, Yuan Meng, Yufeng Cao, Yong Yao, Dongli Fan, **Tingzhou Yang**, and Tao Qian, Form-stable phase change materials based on polyolefin elastomer and octadecylamine-functionalized graphene for thermal energy storage, *Nanotechnology*, **2020**, 31, 245402.

12. Jie Liu, Yufeng Cao, Jinqiu Zhou, Mengfan Wang, Hongli Chen, **Tingzhou Yang**, Yawen Sun, Tao Qian, and Chenglin Yan, Artificial Lithium Isopropyl-Sulfide Macromolecules as an Ion-Selective Interface for Long-Life Lithium-Sulfur Batteries, *ACS Applied Materials & Interfaces*, **2020**, 12, 54537-54544.

13. Tariq Ali, Niaz Muhammad, **Tingzhou Yang**, and Chenglin Yan, Advanced Layered Double Hydroxide-Based Electrocatalysts for Electrocatalytic Oxygen Evolution Reaction, *General Chemistry*, **2020**, 6, 200001.

8.3   Patents

1. Chenglin Yan, Xuejun Liu, Tao Qian, Tingzhou Yang, Method for preparing spiral asymmetric supercapacitor (ZL 2015 1 0338669.6)

2. Chenglin Yan, Tingzhou Yang, Tao Qian, Method for preparing carbon-based material for sodium ion battery by using okara (ZL 2015 1 0152359.5).

3. Chenglin Yan, Tingzhou Yang, Tao Qian, High Coulombic efficiency lithium-sulfur battery electrolyte and preparation method (ZL 2017 1 0472347.X)